UNIVERSITÉ DE STRASBOURG

ÉCOLE DOCTORALE de Physique et Chimie Physique

(À l'Institut de Physique et Chimie des Matériaux de Strasbourg)

THÈSE présentée par :

Silvia ZANETTINI

Soutenue le **23 mars 2015**

pour obtenir le grade de : **Docteur de l'Université de Strasbourg**

Discipline/ Spécialité : Physique de la matière condensée

High mobility materials for Organic Spintronic applications

THÈSE dirigée par :
M. B. DOUDIN, Université de Strasbourg

RAPPORTEURS :

M. F. BISCARINI	Professeur, Università di Modena e Reggio Emilia
M. J-Ph. ANSERMET	Professeur, Ecole Polytecnique Fédérale de Lausanne

---

AUTRES MEMBRES DU JURY :

Mme S. BEGIN-COLIN	Professeur, Université de Strasbourg
M. T. EBBESEN	Professeur, Université de Strasbourg
M. G. CHASTANET	Chargé de Recherche, Cnrs (ICMCB) - Bordeaux

Acknoledgements

In first place I would like to acknowledge Prof. Fabio Biscarini (Università di Modena e Reggio Emilia) and Prof. Jean-Philippe Ansermet (Ecole Polytechnique Federale de Lausanne) for having been the referees of my thesis manuscript, and Prof. Sylvie Begin-Colis, Prof. Thomas Ebbesen and Dr. Guillaume Chastanet for having participated to my defense in quality of jury members. I really enjoyed the scientific discussion with all of you.

The most important 'thank you' is for my thesis supervisor, Prof. Bernard Doudin. Prof. Doudin has put in my hand a thesis project challenging and exciting, at the edge of today's research on Electronics. I esteem him as a scientist and as person; the attention and care of my supervisor under the human point of view has always touched me. Besides the knowledge he transmitted me, he gave me the opportunity to access to a very efficient cleanroom facility and build a solid experience in nanofabrication, which will be useful forever. We had difficult times during my doctorate, but thanks to these experiences that I learned which type of researcher I want to be.

The relevance of the topic he assigned to me has surely been one of the criteria allowing me to win the prestigious prize L'Oreal - Unesco '*Pour les Femmes et la Science*', which has been an unforgettable experience and a considerable financial help. So thanks again to my thesis supervisor for the support in this adventure, and to Foundation L'Oreal – Unesco for the amazing prize.

An enormous 'merci' to three persons whose continuous help during these four years have been of priceless value: Fabien Chevrier for the technical help in the lab, Romain Bernard and Sabine Siegwald for the assistance in the cleanroom, and their 24/7 cheerfulness.

Thanks to my colleague and friend Dr. Jean-François Dayen for the interesting scientific discussions and thinking we had together, and for having taught me how to use a cryogenic system. I would like to acknowledge the other permanent members of the group, Bohdan Kundays, Stéphane Berciaud and Hicham Majjad: you have always been helpful and source of good advices for me. Thanks to Alain Carvalho for introducing me in the world of electron microscopy imaging.

Thanks to Nicolas Leclerc, our polymer synthesizer, to people from iCube institute (Thomas Heiser, Patrick Lévêque) for the project on electrochemical-gating of polymer thin films and people from ISIS institute (Emanuele Orgiu, Artur Ciesielski, Sebastien Haar, Paolo Samori). It has always been a pleasure to collaborate and exchange with you.

Thanks to all the persons of IPCMS which, during all these years, have given me a smile or a kind word along the corridors: Manuel Acosta, Daniel Spor, Christophe Kieber (merci pour Labview!), Jacek Arabsky, Veronique Wernher, Xavier Ledoux, Dominique Quince and many others. Thanks to Prof. Gallani for the time he dedicated to teach me how to use the Langmuir-Blodgett set-up. Thanks to Brigitte, Rosemarie, Geneviève and Angelique for having introduced me to the art of needlework. Thanks to ADDEPT association for the amusing social activities they have organized for our institute and to which it has always been a pleasure to participate. Thanks to the group of ladies of 'Femme et Science - Alsace', leaded by Marie-Claire Cadeville and Veronique Pierron-Bonnes, for the interesting activities they organize to support the role of women working in science: it was a very enriching experience.

I probably could not have managed to finish writing my thesis without the help of my 'office-mates': Dominik, Florian, Ather, Celine and Tindara. You have been so patient and supportive all along this hard period and I appreciated all your attentions immensely ('le gateau de soutien'!). Thanks to

Manuel, Gael and Christian for one of the best surprise I ever had: I will be thankful forever for your coming (from another state!) to celebrate my PhD! *Place du Café* was born with Christian's machine and a street panel souvenir bought in the South of France… and it has become a 'family' for me here in Strasbourg. Ondrej, Guillaume, François, Nicolas.. thanks for all the nice moments we spent together. A special acknowledgement goes to Michael for the inestimable psychological support to my broken heart during the 'writing-thesis' months: you came 'late' in 'my' Strasbourg, but thanks God you came; I don't know how it would have been without you. I feel the same type of gratitude for my two amazing flat-mates, Victor and my 'amiga' Nathalie: you have given me tranquility, help and friendship (and the most memorable crémaillère of my life!) during these last and hard months of my PhD, you have been my 'home', and not everybody would have been so lucky like I was. Thanks a lot for everything.

Owing to the active support of my thesis director to 'women in science', I have had the luck to find on the workplace not one, not two, but even three of the best girl-friends I have ever had. Vina you have been my guide when I was a naïve first-year PhD student, from you I learned not only science but mostly the right way to behave with colleagues, and this has been extremely precious to fully enjoy my years of thesis. I am so glad to destiny for having put you on my way. From Céline I also learned so much, a girl of endless skills, the kindest and my favorite 'trouble-shooter'. I'm very happy you decided to come to Strasbourg and I'll remember forever all the experiences we lived together during these years, at work and outside work. The last arrived in the lab, Tindara, you are an exceptional friend and one of the strongest girl I've ever met. I hope future will be shining for you, because you really deserve it. Even though I did not have the chance to work with them directly, I should mention and thank here Dimitra, Ingrid, and Kerstin which are three other amazing scientists and sweet girl-friends: hopefully I had the luck to find you on my way. It is so exceptional having the chance to work with friends and I pray I'll have the same luck in the future.

Thanks to Matteo, the first Italian I met in IPCMS, for a simple car sharing which has become a nice friendship. Thanks to Monica, my Brazilian friend, for having helped me lowering the average age of Cnrs fitness lessons and for having defended before me (and thus transmitted all the know-how on manuscript and defense preparation!). Thanks also to Guillaume Chaumy who is in charge of the follow-up of part of my thesis project: I'm happy it went in the hands of a talented master student!

Last but not least, my family of course, because they accepted and sustained my departure for another country, even though I know it was difficult for them. Thanks to my sweet hometown friends because I never felt too far from you, our friendship has survived the distance and it will always do. There's another person without which this thesis would not even exists, and without which I would have never been in Strasbourg, and I would probably be a different person. Even though we are no more flying together Alessio, you gave me wings, and for this I'll be thankful forever.

Silvia ZANETTINI, PhD

Linkedin, www.ipcms.unistra.fr

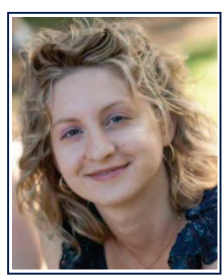

EXPERIENCE

PhD student - Cnrs (France)

Institut de Physique et Chimie des Matériaux de Strasbourg (IPCMS), Strasbourg.

October 2011 – March 2015

- **WET-PROCESSING**
  - Deposition of organic materials on pre-patterned electrodes: self-assembly of supramolecular nanowires triggered by light, spin-coating of polymer semiconductors, drop-casting/Langmuir-Blodgett of a graphene 'ink' (liquid-phase exfoliated). Experience with glove-box environment.
- **ELECTRICAL CHARACTERIZATION** (materials&devices)
  - Electronic transport measurements at low temperatures (1.4 K) and under magnetic field (7 Teslas) (magnetoconductance, Hall effect, contact resistance). Experience with cryogenic set-up.
  - Programming of NI Labview routines for remote control of Keithley instruments.
- **NANO-FABRICATION**

  Optical lithography. Metals and dielectrics thin film deposition. Drawing masks for optical litho (software: Cadence).
- **OTHERS**

  Scanning electron microscopy for sample imaging (Microscope: Zeiss Supra 40). Electrochemistry (notions).

Post-graduate researcher - Cnrs (France)

Institut de Physique et Chimie des Matériaux de Strasbourg (IPCMS), Strasbourg.

January 2011 – July 2011

Performed key control experiments for the publication of an article submitted to Nature Chemistry. Optimization of lithography fabrication process for sub-100 nanometer gaps.

Intern Master student - CNR (Italy)

Istituto dei Materiali per l'Elettronica e il Magnetismo (IMEM), Parma.

April 2010 – November 2010

- **PHOTOVOLTAICS**
  - Growth of ZnS and $(Zn_{1-x}Mg_x)O$ thin films by Pulsed Electron Deposition (PED) for integration in $CuInGa(Se)_2$ photovoltaic cells. PED technique consists in a high-power electron-beam ablation of a bulk material (target). Goal: replacement of the cadmium sulphide (CdS) buffer layer between the p-type CIGS absorber and the n-type layer (ZnO:Al).

    Morphological and electrical characterization: thickness (UV-visible spectroscopy), cristallinity (X-ray diffraction), chemical composition (EDX chemical analysis inside SEM); electronic properties: van der Pauw measurements.
  - In-depth analysis of dye sensitized solar cells functioning mechanism.

EDUCATION

University of Strasbourg, France | **PhD** in **Condensed Matter Physics** | March 2015

Very good / Excellent

University of Parma, Italy | **Master degree** in **Advanced Material Science and Technology** | November 2010

110/110 with distinction

University of Parma, Italy | **Bachelor degree** in **Material Science and Technology** | November 2008

110/110 with distinction

PUBLICATIONS & PATENTS

- S. Zanettini, JF. Dayen, C. Etrillard, N. Leclerc, M. Venkata Kamalakar, B. Doudin, *"Magnetoconductance anisotropy of a polymer thin film at the onset of metallicity"*, **Appl. Phys. Lett**. 106, 6, 063303 (**2015**).

- **European patent** F644/367 EP, *"A device for controlling a chemical reaction by a magnetic field and different uses of said device*." B. Doudin, S. Zanettini, V. Faramarzi, R. Hertel, C. Andreas, P. Lunca Popa. (registered November **2013**).

- V. Faramarzi, F. Niess, E. Moulin, M. Maaloum, JF. Dayen, JB. Beaufrand, S. Zanettini, B. Doudin, N. Giuseppone, "*Light triggered self-fabrication of supramolecular organic nanowires as metallic interconnects*", **Nature Chemistry** 4, 485–490 (**2012**).

- S. Zanettini, F. Bissoli, L. Nasi, P. Ranzieri and E. Gilioli, *"Low temperature Pulsed Electron Deposition and characterization of ZnS films for application in solar cells"*, **Cryst. Res. Technol**. 46, No. 8, 881 – 884 (**2011**).

AWARDS

Bourse L'Oréal France - UNESCO "Pour les Femmes et la Science"

October 2013

25 fellowships of 15´000 € each are given every year to 25 young female researchers working in the field of natural sciences (biology, medicine, chemistry, physics and mathematics) by L'Oréal-France Foundation and UNESCO French Commission to reward the quality of their study and to encourage them to pursue a brilliant career in science. The evaluation jury is composed by members of the French 'Académie des Sciences' (450 candidates in 2013).

Participation at the LERU Doctoral Summer School (for Strasbourg University)

April 2015

The League of European Research Universities (LERU), headquartered in Leuven, organizes this year a doctoral school on the topic "Sharing excellence: the value of knowledge exchange" in Oxford (13 – 17 July 2015). 42 places are available for candidates coming from more than 20 European universities. I have been chosen as one of the three representatives for Strasbourg University to attend this unique opportunity of professional and personal development.

CONFERENCES & COMMUNICATIONS

As PhD student:

- International Conference on Nanoscience + Technology, Vail (Colorado, USA), July 2014. **Oral presentation**.
- 10th International Conference of Organic Electronics, Modena (Italy), June 2014.
- School "Introductory Course on Magnetic Random Access Memory", Grenoble (France), July 2013.
- International Conference of Molecular Electronics, Grenoble (France), December 2012. **POSTER PRIZE**.
- School "Magnetism and Spintronics in Molecular Nanostructures", Porquerolles (France), September 2012.

As Master student:

- Italian Crystal Growth 2010 Congress, Parma (Italy), November 2010.
- 2nd Meeting of the Italian and Spanish Crystallographic Associations**,** Oviedo (Spain), July 2010.

LANGUAGES

English, French: proficient.

Italian: native language.

ADDITIONAL INTERESTS

Member of Materials Research Society. Volunteering for events organized by association "Femmes et Science – Alsace" dedicated to promote scientific disciplines among teenagers.

Matériaux à haute mobilité électrique pour des applications en Electronique de Spin Organique

Incipit

Ce travail de thèse est porté sur l'étude du transport électronique dans différents matériaux organiques semi-conducteurs, considérés comme candidats potentiels pour des applications en Electronique de Spin Organique.

Le temps de vie des porteurs de spin dans les semi-conducteurs organiques est généralement très long, dû au fait que les interactions causant le reversement de l'état de spin sont très faibles. Pour cette raison, les semi-conducteurs organiques sont considérés comme très prometteurs pour la fabrication de dispositifs pour l'Electronique de Spin.

Toutefois, pour rendre possible la diffusion d'un courant polarisée en spin à l'intérieur d'un canal semi-conducteur (injection-transport-détection), le mécanisme de transport de charge et la mobilité des porteurs, ainsi que la nature et la valeur de la résistance de contact de l'interface séparant semi-conducteur et électrodes métalliques ferromagnétiques, doivent répondre à des critères très stricts. La difficulté à répondre à ces critères soulève en fait des doutes sur l'origine réelle des signaux de magnétorésistance (MR) observé pour les vannes de spin organiques reportés en littérature jusqu'au présent.

Trois candidats ont été analysés au cours de ce travail de thèse : des nano-fils unidimensionnels de molécules de triarylamine formés par auto-assemblage, des flocons de graphène de taille nanométrique exfolié en phase liquide, et un polymère semi-conducteur fortement dopé. Tous les trois ont été déposés à partir de matériau en solution, en utilisant des techniques de déposition par voie liquide. Nous avons choisi de travailler avec des dispositifs en géométrie latérale, pour avoir aussi la possibilité d'interagir avec le matériau organique au moyen de stimula externes comme par exemple la lumière ou un champ électrique (électrode de grille) afin de créer des dispositifs multifonctionnels.

La fabrication de dispositifs de type 'vannes de spin' reste notre objectif ultime, mais aucune vanne de spin n'a été réalisée au cours de cette thèse. Les trois matériaux ont été étudiés en termes de propriétés de transport de charge (conductivité, mobilité et mécanisme de transport: par saut ou délocalisé) et de la résistance de contact avec les électrodes métalliques (Au, Ni). La compréhension du transport de charge du semi-conducteur organique est essentielle pour déterminer sa capacité à transporter le spin.

Le manuscrit est structuré comme suit. Nous allons d'abord réviser les concepts de base de l'Electronique de Spin, soulignant clairement quelles sont les caractéristiques souhaitées du matériel organique à utiliser (Introduction). Le reste de la thèse a comme objectif principal de vérifier la

correspondance de différents matériaux organiques analysés à ces conditions. Dans la poursuite de cet objectif, la thèse présente un parcours scientifiques très varié, allant de dispositifs auto-assemblés ‘bottom-up’ pour l'électronique supramoléculaire (Chapitre 2) à une enquête sur la physique fondamentale de semi-conducteurs de polymères conjugués (Chapitre 4), en passant par l'un des matériaux les plus discutés de l'électronique d'aujourd'hui, le graphène, utilisé avec une approche compatible à la déposition du matériau de solution typique de l'électronique organique (Chapitre 3). Ce travail a abouti à la fabrication de nouveaux dispositifs et à d’importantes découvertes.

Motivations
(Chapitre 1)

L'électronique de spin nait avec la découverte de l'effet de magnétorésistance géante (GMR, Giant MagnetoResistance) en 1988 et de l'effet de magnétorésistance à effet tunnel (TMR, Tunnel MagnetoResistance) en 1995. La magnétorésistance géante se manifeste en faisant passer une courant électrique dans de multicouches de métaux magnétiques/non-magnétiques et tournant l'aimantation respective des couches magnétiques. La magnétorésistance à effet tunnel exploite aussi l'orientation de l'aimantation de couches ferromagnétiques, mais se produit quand le matériau intermédiaire est une barrière de matériau isolant très fin. La configuration typique de dispositifs de GMR et TMR est illustrée en Figure 1(a). L'exploitation de ces deux effets a produit une véritable révolution dans la technologie du stockage de mémoire.

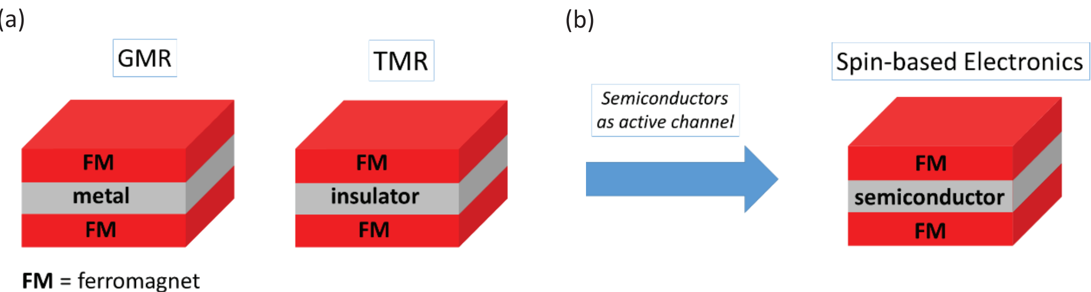

Figure 1. (a) Dispositifs (à géométrie verticale) exploitant les effets de magnétorésistance géante et magnétorésistance à effet tunnel: la couche entre les deux métaux ferromagnétiques est constituée respectivement d'un métal non-magnétique (GMR) et d'une barrière isolante (TMR). (b) Utilisation des matériaux semi-conducteurs comme canal actif pour développer une 'Electronique de Spin' avec des applications en dehors du simple stockage de mémoire.

Le prochain défi pour la 'Spintronique' est l'exploitation de la fonctionnalité de spin non seulement pour des applications dans le stockage de mémoire, mais aussi pour l'exécution des processus de calcul. Pouvoir manipuler le spin et la charge de l'électron dans le même dispositif (combiner le magnétisme à la microélectronique) promet un large éventail de nouvelles applications et apportera des avantages aux nouveaux appareils électroniques tels que l'augmentation de la vitesse de traitement de données, la diminution de la consommation d'énergie et une densité d'intégration plus élevée par rapport aux dispositifs à semi-conducteurs utilisés jusqu'à maintenant [1]. Pour atteindre cet objectif, il faut utiliser comme canal actif des matériaux semi-conducteurs (Figure 1b).

A cet effet, un contrôle optimal sur l'injection, le transport, la manipulation et la détection de courants polarisés en spin doit être maîtrisés à l'intérieur des semi-conducteurs. L'optimisation de ces différents mécanismes nécessite la maximisation de la durée de vie du spin de l'électron τ_s et de sa longueur de diffusion λ_s. Le temps de vie τ_s est la période pendant laquelle un électron maintient son

état de spin inchangé. Le longueur de diffusion λ_s du spin est la distance que l'électron peut parcourir pendant τ_s. λ_s et τ_s sont liés par la relation:

$$\lambda_s = \sqrt{D \cdot \tau_s} \quad (1)$$

où D est le coefficient de diffusion des électrons (ou trous), qui est proportionnel à la mobilité électrique μ selon la relation $D = \mu \cdot kBT/e$ [2].

λ_s atteint des valeurs de plusieurs centaines de nanomètres dans les métaux légers non magnétiques (~ 600 nm pour l'aluminium), mais elle raccourcit à < 50 nm dans les métaux magnétiques (Co, Ni) ou dans les alliages magnétiques (Py) [3]. Au contraire, λ_s est beaucoup plus longue dans les semi-conducteurs comme le Silicium et le GaAs et peut arriver à une longueur de plusieurs micromètres [4],[5],[6]. Ceci est dû au long temps de vie τ_s, combiné avec les mobilités électriques μ remarquables des semi-conducteurs inorganiques.

Les semi-conducteurs organiques (Organic Semiconductors, OSC) sont des candidats intéressants pour l'électronique de spin parce que la durée de vie du spin τ_s est censée être considérablement plus longue que dans les semi-conducteurs inorganiques. Cette caractéristique est due au fait que le couplage spin-orbite et l'interaction hyperfine (causes principales de la perte de mémoire de spin) sont très faibles dans les OSC. Le couplage spin-orbite est faible parce que les OSCs sont formés par des éléments très légers (hydrogène, carbone, azote, soufre, etc.), car l'effet est proportionnel à Z^4 (où Z est le nombre atomique). L'interaction hyperfine est généralement faible parce que le ^{12}C, l'isotope le plus commun du carbone, a un moment magnétique nucléaire nul, n'influençant pas l'état de spin des porteurs. Même s'il reste encore à comprendre lequel des deux mécanismes de relaxation de spin est le plus fort, les données spectroscopiques nous disent que τ_s peut atteindre des valeurs de 10^{-6} secondes jusqu'à 10^{-3} secondes pour les organiques (plus longues à des températures basses) [7]. Cette raison, ainsi que la flexibilité chimique et le coût relativement faible des matériaux organiques, a été la force motrice principale pour le développement de l'électronique de spin organique il y a 10 - 15 ans.

Cependant, les semi-conducteurs organiques sont souvent limités par une mobilité électronique μ faible et un mécanisme de transport par sauts (hopping). Par conséquent, même si leur temps de vie de spin τ_s est très long, la longueur de diffusion du spin λ_s est courte, souvent au-dessous de 20 nm [2].

C'est ainsi que matériaux organiques à haute mobilité, dans lesquels les porteurs de charge sont délocalisés sur des distances plus importantes et le transport par sauts est minimisé (on parle plutôt de transport continu), sont très recherchés afin de prolonger la distance à laquelle l'information de spin peut être transportée. Ceci est la motivation principale de ce travail de thèse.

De plus, une grande longueur de diffusion de spin λ_s du semi-conducteur organique n'est pas la seule condition nécessaire pour la fabrication d'une vanne de spin qui soit efficace. L'injection de spin

dans un semi-conducteur se fait normalement à partir d'un métal ferromagnétique. Le contrôle de la résistance de contact et de la polarisation en spin de l'interface constituent une deuxième problématique expérimentale importante [8]. Le Chapitre 5 est dédié à cette problématique.

Le dispositif final envisagé pour l'exploitation de ces matériaux est une vanne de spin (Figure 2). Il s'agit d'un dispositif où deux électrodes ferromagnétiques (FM) permettent d'injecter et de détecter un courant électrique polarisé en spin (leur aimantation polarise la courant) passant à travers d'une épaisseur d'un semi-conducteur organique. La résistance totale du dispositif varie selon les directions respectives d'aimantation des deux électrodes. L'état magnétique de l'un peut donc être connu en appliquant un potentiel entre les deux électrodes et en mesurant le courant, principe qui est à la base de la lecture de « bits » de mémoire.

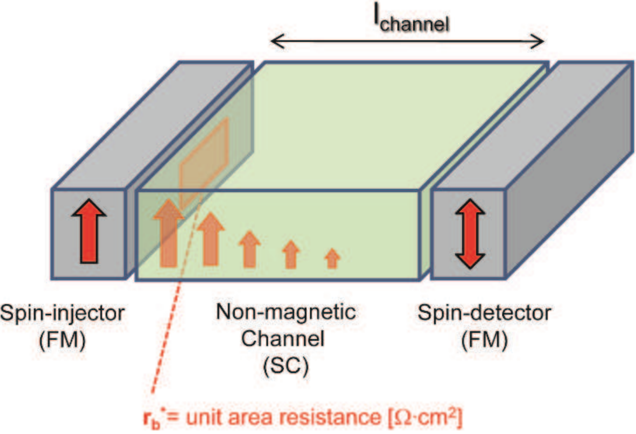

Figure 2. Dispositif de type 'vanne de spin' à géométrie latérale. Les flèches rouges indiquent respectivement l'aimantation des deux électrodes (le detector, à droite, peut être aimanté 'up' ou 'down') et la relaxation du courant polarisé en spin pendant son transport le long du canal semi-conducteur.

Le canal semi-conducteur atteint généralement une centaine de nanomètres de long. Pour notre étude, la géométrie latérale présente des avantages significatifs:

• nous pouvons décider la longueur du canal $l_{channel}$ à partir du processus de nanofabrication;

• nous pouvons ajouter une électrode de grille, et ajuster la conductivité du canal à notre convenance;

• nous pouvons garder un accès à l'échantillon par le haut, afin de *i.* l'imager (si nécessaire) et *ii.* interagir avec des stimuli externes différents du champ électrique transversal de grille (par exemple lumière, pH, etc.)

• nous évitons le problème de court-circuit entre les deux électrodes métalliques, un problème qui concerne plutôt les dispositifs à géométrie verticale et qui est dû aux infiltrations de métal à travers l'épaisseur organique pendant le dépôt de l'électrode supérieure.

Nano-fils supramoléculaires de triarylamines auto-assemblées (Chapitre 2)

Le premier matériau analysé est constitué de nano-fibres supramoléculaires formées par des molécules de triarylamine. Les triarylamines ont déjà été utilisées dans les dispositifs d'électronique organique (comme les OLED et les cellules photovoltaïques 'dye-sensitized'), sous forme de couches minces amorphes. Nos collaborateurs Moulin *et al*. [9] ont démontré que ces molécules, solubilisées dans un solvant chloré et irradié avec une lumière blanche, sont capables de s'empiler et créer des fils unidimensionnels, comme en Figure 3(a). La nucléation de la fibre supramoléculaire commence grâce à la formation d'une petite quantité de radicaux de triarylamonium, déclenchée par l'absorption de lumière, et à leur assemblage initial. Ensuite, les fibres se construisent en ajoutant des molécules neutres de triarylamine une par une. A la fin du procès, les nano-fils peuvent atteindre plusieurs centaines de nanomètres de longueur; ils sont stabilisés chimiquement par les interactions π–π entre les orbitaux des atomes d'azote centraux et par d'autres liens supramoléculaires comme des ponts à hydrogène. Au centre de ces nano-fils, la densité électronique est partagée (délocalisée) le long de la chaine moléculaire grâce au π–π stacking.

Notre équipe a réussi à reproduire cet auto-assemblage entre deux électrodes métalliques de manière à en faire une interconnexion supramoléculaire capable de conduire un courant électrique, comme représenté en Figure 3(b) [10]. Les deux électrodes métalliques sont séparées de 80 nanomètres. La Figure 3(c) montre le comportement de la résistance d'un de ces dispositifs pendant les différentes étapes de l'assemblage: une goutte de la solution contenant les triarylamines est déposée sur les électrodes; après 10 secondes d'irradiation lumineuse, la résistance diminue de cinq ordres de grandeur (10 MΩ → 600 Ω), signe que les nano-fils ont terminé leur croissance et ont mis en connections les deux électrodes de source et drain.

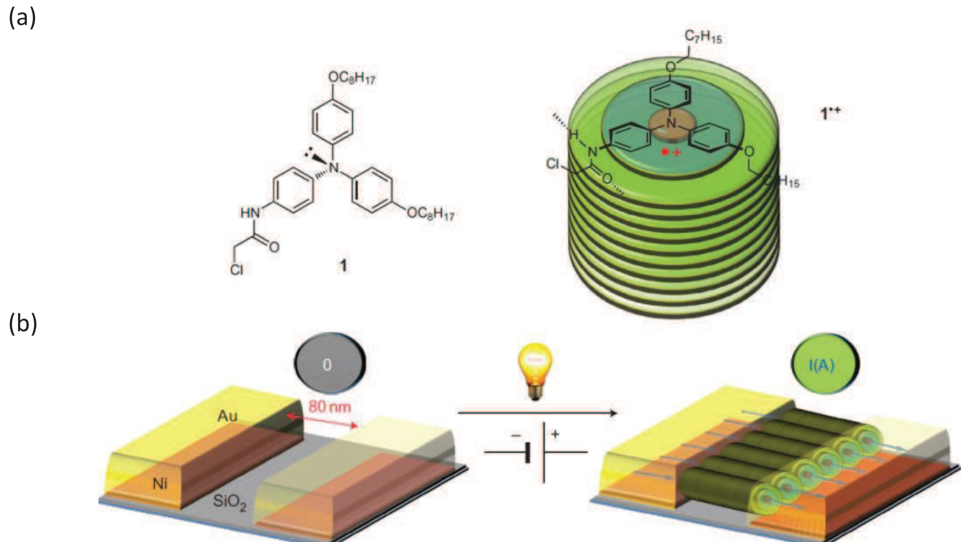

(c)

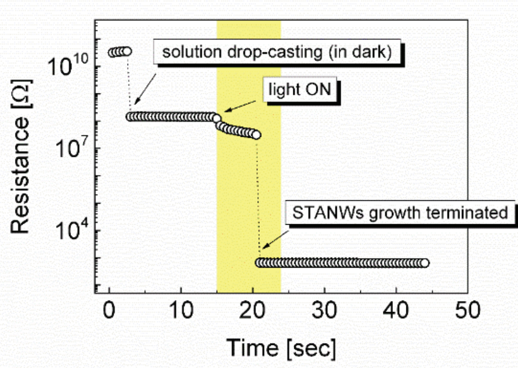

Figure 3. Processus d'auto-assemblage de triarylamines entre les électrodes. (a) Triarylamine spécifique utilisée (concentration : 1 mg/ml dans $C_2H_2Cl_4$) et empilement des molécules le long de l'assemblage. (b) Déroulement schématique de l'auto-assemblage dans la nano-tranchée: une goutte de solution est déposée sur la nano-tranchée dans l'obscurité, une différence de potentiel est appliquée entre les deux électrodes et une lumière blanche est irradiée sur la goutte pendant environ 10 secondes. Il en résulte la construction des fibres alignées d'une électrode à l'autre. (c) Variation de la résistance de la nano-tranchée aux différentes étapes du processus d'auto-assemblage (V_{sd} = 1 V). 'STANWs signifie 'Self-assembled TriArylamines NanoWires'.

Les mesures de transport électrique en fonction de la tension source-drain et en fonction de la température indiquent que les nano-fils forment des interconnexions de type métallique, possédant une conductivité parmi les meilleures pour un composant organique, jusqu'à 3 S·cm^{-1}. En premier lieu, le système électrode/nano-fils/électrode est caractérisé par une courbe I-V parfaitement ohmique (Figure 4(a)). Encore plus surprenant, la Figure 4(b) nous montre que la résistance des nano-fils diminue pendant un refroidissement de la température, ce qui est un trait sans équivoque de la nature métallique du transport, ce qui a été rarement trouvé chez des matériaux organiques.

(a)

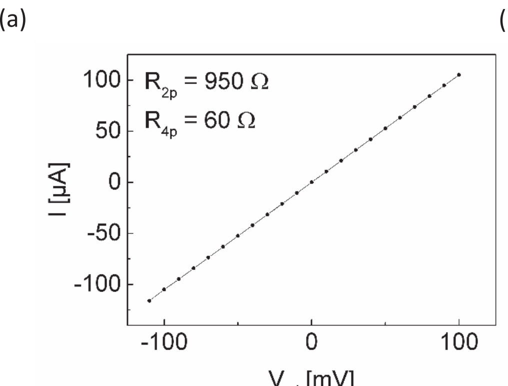

(b)

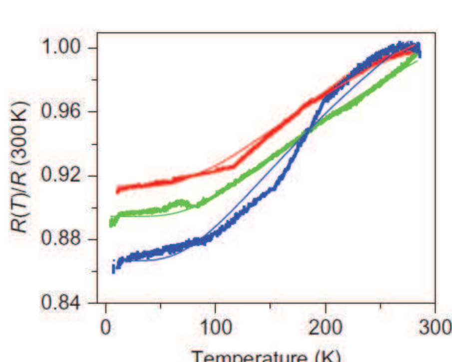

Figure 4. (a) Courbe courant-voltage d'une nano-tranchée après auto-assemblage et rinçage à l'acétone et éthanol: la courbe est parfaitement ohmique. R_{2p} et R_{4p} représentent la résistance totale du dispositif, respectivement avec et sans la résistance des électrodes métalliques en série (~ 900 Ω). (b) Mesures de Résistance - Température de trois différents dispositifs (de température ambiante à 1,5 K). Les valeurs de résistances initiales à 300 K pour chaque échantillon sont: 22 Ω (rouge), 45 Ω (vert), 360 Ω (bleu). Chaque courbe expérimentale a été interpolé en utilisant un modèle de transport quasi-unidimensionnel.

La mobilité est plutôt difficile à évaluer en raison d'une incertitude sur la densité des porteurs de charge; toutefois on l'estime autour de 1 – 10 cm^2/V·s, valeur confirmée par des études théoriques menées ensuite [11]. Encore plus remarquable, la résistance d'interface entre l'extrémité de la fibre et l'électrode est très faible.

En plus de leur conductivité exceptionnelle, l'avantage de ces nano fils est leur capacité à s'assembler d'eux-mêmes là où on le souhaite, bien plus facilement que des nanotubes de carbone, pour lesquels un positionnement contrôlé est un défi technique majeur. Ces résultats ont abouti à une publication dans Nature Chemistry (2012) et ils ont eu un large impact dans la communauté scientifique.

Le processus de lithographie développé par notre groupe pour la fabrication des nano-tranchées a été un élément clef de la réussite de cette brillante découverte. Notre processus de fabrication fait usage de la lithographie optique standard pour créer ces espacements plus petit de 100 nanomètres, sur des très longues distances (10 – 100 μm) [12]. La dénomination 'nano-tranchée' est due au rapport important entre la largeur et la longueur de l'interstice. Les détails du procédé de lithographie sont représentés en Figure 5. L'astuce principale est de garder l'échantillon incliné lors du dépôt de la deuxième électrode, de sorte que le bord de la première électrode (déjà déposé) fasse ombre et crée l'espacement.

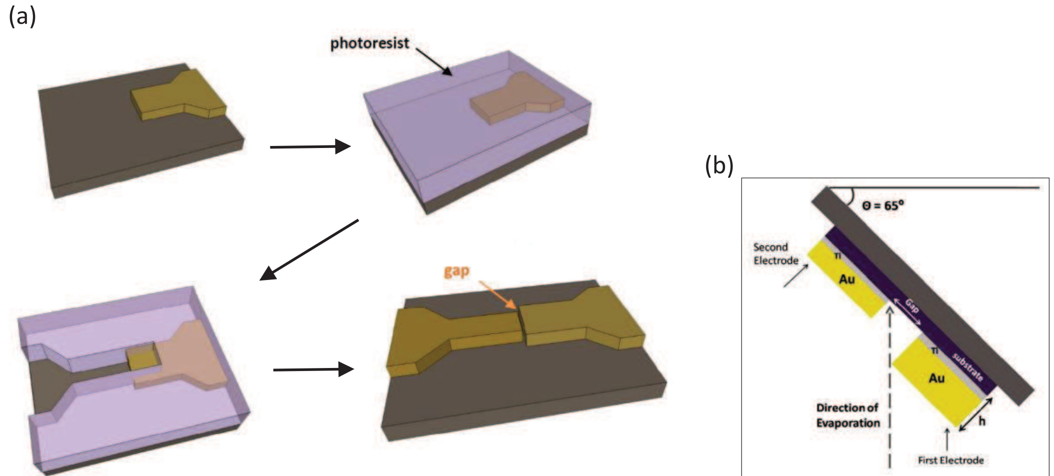

Figure 5. Schéma du processus de lithographie pour la fabrication des nano-tranchées. (a) La première électrode est modelée et déposée; puis la résine photosensible est déposée partout et ouverte par irradiation en superposition partielle avec la première électrode; le dépôt de métal de la deuxième électrode est fait avec l'échantillon incliné à un angle spécifique, comme illustré en (b). L'ombre de la première électrode forme la nano-tranchée entre les deux.

Cette méthode de nanofabrication nous permet de réaliser des nano-tranchées uniformes tout le long de la largeur micrométrique et de manière reproductible. La productivité est considérablement ameliorée par rapport à la lithographie par faisceau d'électrons (e-beam lithography), qui est la technique normalement utilisée pour la fabrication d'espacements aussi petits.

Nano-flocons de graphène exfolié en phase liquide (Chapitre 3)

Nous avons ensuite examiné les propriétés de transport d'une encre à base de graphène exfolié en phase liquide. La conductivité exceptionnelle de la monocouche de carbone et sa capacité à atteindre des valeurs de mobilité électronique jusqu'à 10000 $cm^2/V\cdot s$ sont déjà connues depuis sa découverte en 2004. Des longueurs de diffusion de spin de dizaines de micromètres ont été démontrées expérimentalement pour des flocons de graphène de haute qualité [13]. On décide donc de tester le graphène comme candidat pour la fabrication de vannes de spin, mais tout de même en adoptant une approche similaire à celui de l'électronique organique connu comme « wet chemistry », consistant à déposer le matériau sur des grande surfaces par voie liquide. En poursuivant cet objectif, on choisit d'utiliser du graphène obtenu par exfoliation mécanique à partir du graphite en phase liquide. La dispersion du graphène en solvant organique (N-méthyl-2-pyrrolidone, NMP) est fournie par nos collaborateurs du groupe de Prof. Samori (ISIS, Strasbourg) [14]. Elle est constituée principalement de flocons de taille nanométrique (200 – 300 nm maximum). Le matériel est déposé en utilisant diffèrentes techniques comme Langmuir-Blodgett ou « drop-casting ».

A la fin du processus de déposition, les nano-flocons de graphène connectent les électrodes espacées de 80 nm et leurs propriétés de transport électronique peuvent être sondées, à l'aide de l'application d'une tension de grille par électrolyte. La Figure 6(a) représente l'échantillon avec plusieurs nano-tranchées recouvertes par l'électrolyte (ion-gel = gel contenant des ions mobiles) et (b) un vue de profil des nano-flocons suspendus connectant les deux électrodes de la nano-tranchée.

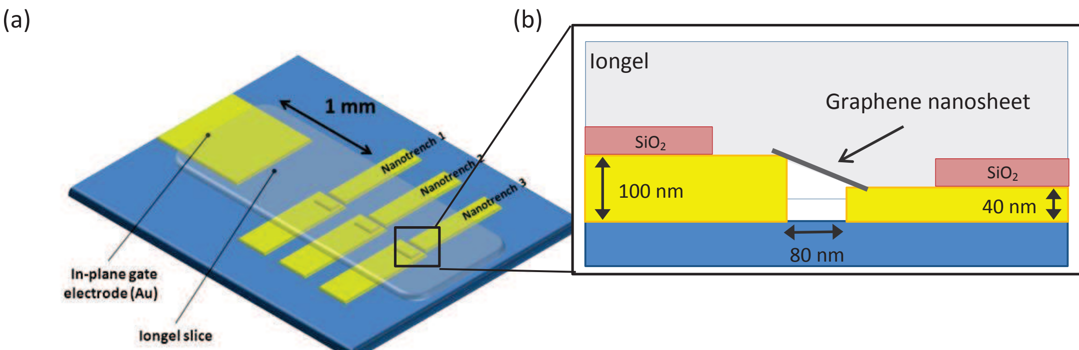

Figure 6. Schéma de l'échantillon pour l'étude des propriétés de transport de nano-flocons de graphène suspendus. (a) Vue en perspective de l'échantillon : plusieurs nano-tranchées sont présentes sur la même puce, la tranche de ion-gel couvre toutes les nano-tranchées et est en contact avec l'électrode de grille. (b) Vue de profil d'un flocon de graphène qui fait le pont entre les deux électrodes de la nano-tranchées (écart : 80 nm). Une couche de recouvrement de SiO_2 (en rouge) protège les électrodes de source et de drain du contact direct avec l'iongel.

En Figure 7 on peut voir une image des nano-flocons déposés sur la nano-tranchée prise au microscope électronique.

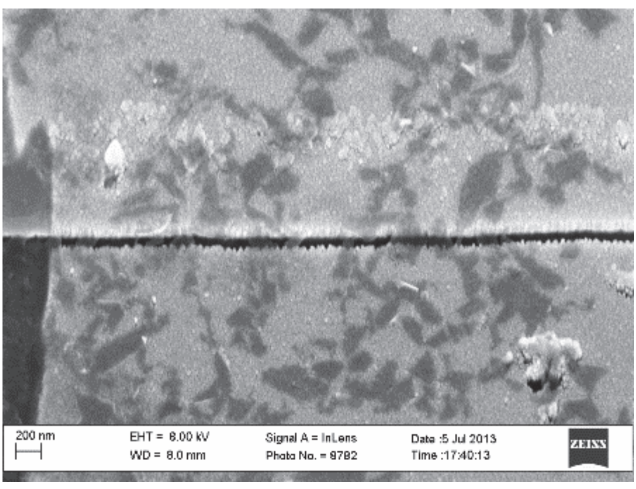

Figure 7. Image prise au microscope électronique d'une nano-tranchée couverte par des nano-flocons de graphène exfolié par voie liquide. Sur cet échantillon, le graphène a été déposé par Langmuir-Blodgett.

La Figure 8(a) illustre les connections électriques au dispositif et (b) le résultat de la mesure. Le point de Dirac (maximum de résistance en variant la tension de grille) et une conduction de type ambipolaire ont pu être détectés sur plusieurs dispositifs, ce qui est remarquable en considérant la taille nanométrique du canal. On estime une mobilité des électrons et des trous supérieur à 1 cm^2/V·s. Par rapport aux fibres supramoléculaires de triar(b) nines, la résistance de contact est plus haute, car le graphène est simplement posé sur les électrodes et non lié chimiquement au métal. La valeur de mobilité est par conséquent sous-estimée.

(a)

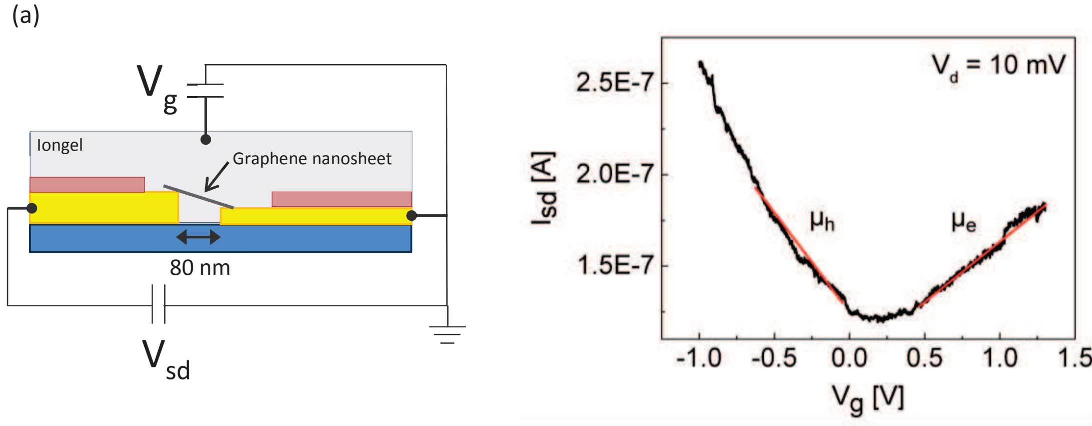

Figure 8. Mesures de transport. (a) Schéma des connections : V_{sd} = différence de potentiel entre source et drain, V_g = tension de grille. (b) Courbe de transfer : courant passant entre source et drain I_{sd} en fonction de la tension de grille V_g (avec un V_{sd} = 10 mV).

Le handicap majeur de ce système et du système de nano-fils supramoléculaires est l'impossibilité de connaitre exactement leur résistance d'interface avec les électrodes métalliques. Leur échelle nanométrique empêche l'utilisation des méthodes classiques pour la mesure de la résistance de contact, par exemple le Transmission Line Method (TLM, dans laquelle on varie la

distance séparant électrodes source et drain) ou la méthode à quatre points (dans laquelle on insère deux points de mesures de chute de potentiel) [15].

Couche mince d'un polymère semi-conducteur fortement dopé (Chapitre 4)

Nous étudions par conséquence un autre matériau, organique et à haute mobilité, pour lequel nous pouvons mesurer la résistance de contact, afin de savoir si elle satisfait les conditions pour avoir une injection de spin significative. Il s'agit d'un polymère semi-conducteur, notamment poly(2,5-bis(3-dodecyl-2-yl)-thieno[3,2-*b*]thiophene (C12-PBTTT) [16] (Figure 9(a)), déposé par spin-coating sous forme de couche mince (25 - 30 nm). Bien que le PBTTT est déjà connu pour son degré de cristallinité élevé et sa bonne mobilité électrique (0.1 $cm^2/V\cdot s$), on le soumet à un dopage électrochimique important. Le dopage sert à augmenter la densité de porteurs de charge du semi-conducteur jusqu'à que le niveau de Fermi se trouve en proximité des états de conduction « délocalisés », c'est-à-dire caractérisés par une longueur de conjugaison supérieure (environ 25 nm contre le 5-10 nm typiques). Le but est de surmonter un type de transport « par sauts », qui est typique des matériaux organiques désordonnés et dérive de la localisation des fonctions d'onde (due à l'absence/carence d'un ordre cristallin – '*localisation d'Anderson*'), et parvenir à un mécanisme de transport « de bande ». Autrement dit, on cherche à produire sur le matériau une transition d'un état isolant à un état métallique. La concrétisation de cet objectif ambitieux serait non seulement importante pour exploiter ce polymère semi-conducteur en électronique de spin, mais aussi une conquête historique pour le domaine de l'électronique organique elle-même.

L'étude de propriétés de transport électronique du PBTTT en fonction du dopage a été effectué en utilisant une géométrie de type 'barre de Hall', comme en Figure 9(b): cette géométrie permet de réaliser de mesures à 4 point (par lesquelles on peut distinguer la résistance intrinsèque du matériau de la résistance de contact), ainsi que de vérifier la génération d'un signal de Hall en présence d'un champ magnétique externe (ceci serait indication d'un type de transport plus 'délocalisé). Le dopage électrochimique se fait en utilisant un électrolyte comme grille, dans une configuration similaire à celle utilisée pour l'expriment avec le graphène exfolié en phase liquide (paragraphe précédent). La Figure 9(c) montre la géométrie de l'échantillon, avec la tranche de gel ionique en contact avec l'électrode de grille latéral et la barre de Hall.

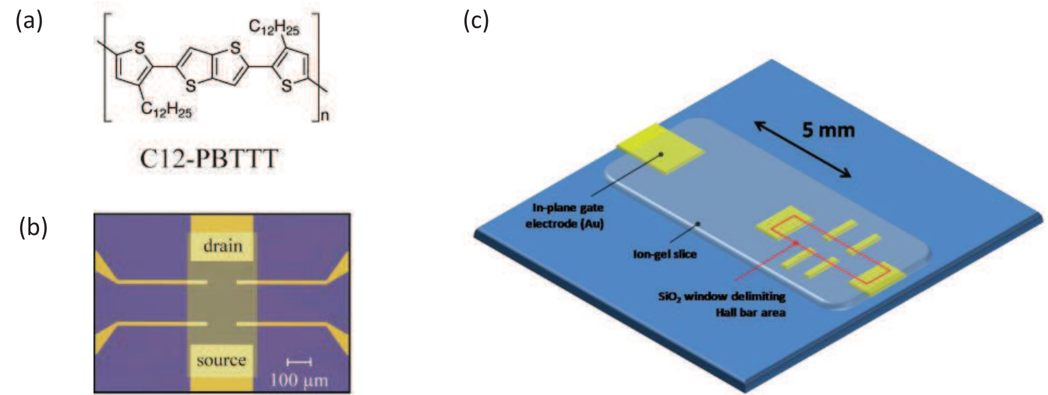

Figure 9. (a) Formule chimique du poly(2,5-bis(3-dodecyl-2-yl)-thieno[3,2-b]thiophene (C12-PBTTT). (b) Image au microscope optique d'une barre de Hall, avant le spin-coating du PBTTT. La barre de Hall mesure 400 µm de longueur et 300 µm de largeur. (c) Vue de l'échantillon en perspective: la tranche de ion-gel couvre tout le canal actif de la barre de Hall et touche l'électrode de grille.

Le dopage électrochimique du semi-conducteur organique est obtenu quand les ions du gel ionique commencent à pénétrer dans la couche mince du polymère. Ça correspond au Régime III représenté en Figure 10(a). Ce régime est accessible en imposant une tension de grille importante pendant un temps long (minutes). Un des grands avantages d'une grille électrolytique est de fonctionner avec de tensions de grille relativement faibles, de quelque Volts. Comme visible en Figure 10(b), le couche mince de PBTTT arrive à conduire un courant source-drain de 0.1 µA et atteint des valeurs de conductivités > 1000 $S{\cdot}cm^{-1}$ (à température ambiante) par l'application de seulement -3.5 V de tension de grille. Les numéros de 1 à 6 sur la Figure 10(b) indiquent les six échantillons à dopage croissant dont les propriétés de transport ont été analysées en fonction de la température et en présence d'un champ magnétique.

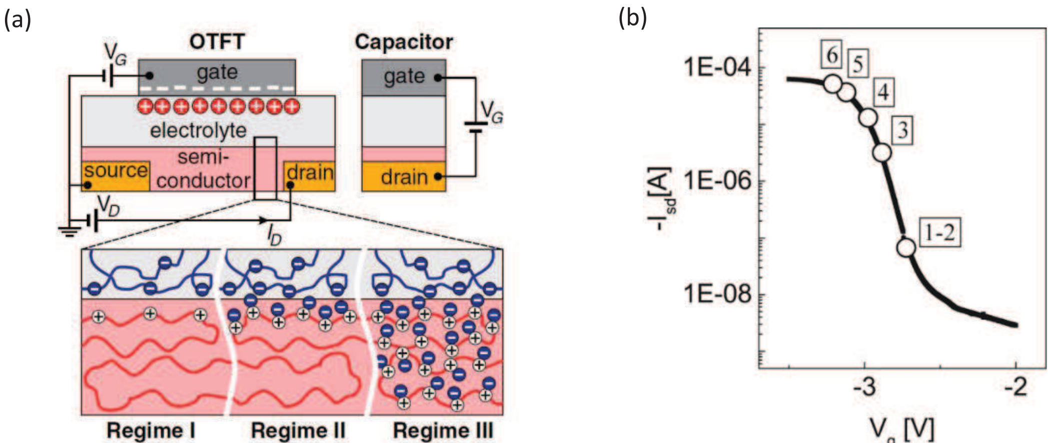

Figure 10. (a) Illustration schématique des trois différents régimes de fonctionnement d'un OFET avec grille électrolytique (mode d'accumulation dans un semi-conducteur de type p). Régime I: purement électrostatique, comme une grille diélectrique standard (SiO_2 per exemple). Régime II : «mixte» (pas purement électrostatique, mais le dopage est limitée à la première monocouche proche de l'interface). Régime III : électrochimique (les ions pénètrent sur toute l'épaisseur

de la couche de semi-conducteur). Reproduit à partir de [17]. (b) Courbe de transfer : courant passant entre source et drain I_{sd} en fonction de la tension de grille V_g (avec une tension source-drain de V_{sd} = -50 mV)

Les mesures en fonction de la température (1 K – 300 K) et en fonction du champ magnétique ont révélé que les couches les plus fortement dopées (correspondant aux échantillons 5 et 6) présentent deux signatures typiquement associé à l'état métallique de la matière: *i.* une conductivité résiduelle à la température de zéro absolu (T = 0 K), en Figure 11(a) et *ii.* une augmentation de la conductivité en présence d'un champ magnétique externe (à baisse température, entre 12 K et 4.5 K), en Figure 11(b), que nous interprétons comme la manifestation de l'effet de localisation faible.

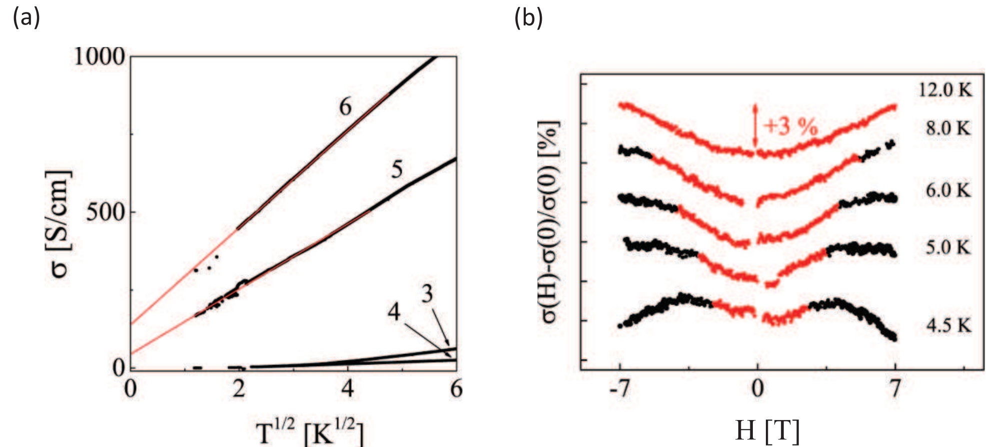

Figure 11. (a) Extrapolation de la conductivité électrique à zero kelvin (lignes rouges). Les deux échantillons plus dopés, 5 et 6, montrent une valeur non-nul de conductivité: ça constitue une forte indication de 'metallicité' du polymère. (b) Magneto-conductivité d'un échantillon fortement dopé à basse température en variant le champ magnétique entre - 7 Teslas et + 7 Teslas. La couche mince de polymère est perpendiculaire à la direction du champ magnétique.

La localisation faible est un phénomène d'origine quantique (interférence constructive entre fonctions d'onde) qui se vérifie quand le type de transport des charges est cohérant sur des distances importantes (= phase de la fonction d'onde du porteur de charge conservé pendant le trajet). L'effet de localisation faible est généralement observé dans des couches minces des métaux conventionnels et n'est pas compatible avec un type de transport 'par sauts'.

La mobilité électrique des porteurs de charge dans le PBTTT fortement dopé arrive à ~ 10 $cm^2/V \cdot s$, 100 fois plus haute que dans le PBTTT non dopé. Ces valeurs sont extrêmement prometteuses et désignent ce polymère semi-conducteur comme le meilleur parmi les trois candidats examinés, sous un point de vue de propriétés électroniques intrinsèques.

Le problème de la résistance de contact organique/métal (Chapitre 5)

Les mesures de résistance de contact du PBTTT avec des électrodes d'or et nickel montrent une valeur exceptionnellement basse par rapport aux valeurs typiquement reportées pour des dispositifs d'électronique organique. La résistance de contact est environ 10 Ω·cm, 100 à 1000 fois plus basse que les valeurs minimales de dispositifs utilisant un matériau diélectrique standard comme grille. Une telle valeur est surtout due à l'action de dopage que la grille électrolytique exerce sur la zone proche à l'interface.

Cependant la résistance de contact reste encore trop élevée si analysée en relation à la capacité d'injecter (et détecter) efficacement une courant polarisée en spin aux interfaces métal/organique. Le modèle d'injection (et détection) du spin dans un semi-conducteur en régime de transport diffusive (délocalisée) développé par Fert et Jaffrès [18] indique que la valeur de résistance de contact r_b* doit être comprise entre une limite inférieure et une limite supérieure. Les courbes à forme de cloche en Figure 12 représentent la fenêtre de 'bons' valeurs pout obtenir l'amelioration du signal de magnétorésistance $\Delta R/R^P$ pour la vanne de spin simulé ferromagnétique/semi-conducteur/ferromagnétique (ou, une meilleure performance du dispositif). Les 'bons' valeurs sont exprimés en termes du rapport entre la résistance de contact r_b* e la résistance du canal r_N. Le signal $\Delta R/R^P$ plus haut corresponds à un rapport r_b*/r_N égal à l'unité.

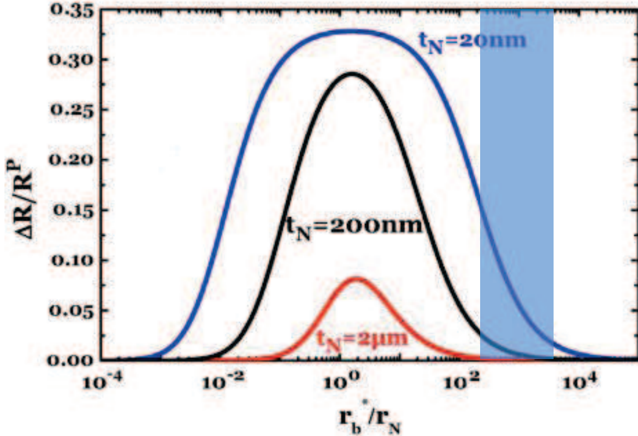

Figure 12. Signal de magnétorésistance $\Delta R/R^P$ en fonction du rapport r_b*/r_N, où $r_N = \rho_N \cdot \lambda_s$ (produit de la résistivité pour la longueur de diffusion du spin). Les simulations théoriques sont présentées pour différentes longueurs du canal t_N de la vanne de spin: 2 μm (rouge), 200 nm (noir) et 20 nm (bleu). Le signal de magnétorésistance $\Delta R/R^P$ le plus élevé est associé à la voie la plus courte et à un rapport $r_b*/r_N \approx 1$.

Le rectangle bleu indique l'intervalle où les données experimentales du system PBTTT/Nickel se placent: évidemment elles sont situées très loin du centre de la courbe de 'bons' valeurs. En deux mots, la diminution de résistance d'interface atteint par dopage électrochimique ne permet pas de compenser l'énorme chute de conductivité intrinsèque du matériau.

En résumé, trois matériaux très différent ont été examinés, en utilisant à la fois des circuits à l'échelle nanométrique (pour l'expérience avec les fibres supramoléculaires et les nano-flocons de graphene) ou micrométriques (pour l'expérience avec le PBTTT). Nous avons mis en place une technique de grille électrolytique afin d'étudier les propriétés électroniques en fonction de la densité de porteurs de charge, qui a permis de varier la conductivité des matériaux et atteindre des valeurs remarquables, approchant celles des métaux. Nos trois candidats ont montré des mobilités électriques au moins supérieur à 1 $cm^2/V{\cdot}s$, ce qui est remarquable pour des matériaux organiques. Cependant, une analyse des circuits injecteur et détecteur de spin montrent des possibilités limitées de réaliser des vannes de spin, essentiellement à cause des valeurs de résistances d'interface trop importantes.

[1] S. A. Wolf, D. D. Awschalom, R. A. Buhrman, J. M. Daughton, S. von Molnár, M. L. Roukes, A. Y. Chtchelkanova, and D. M. Treger, "Spintronics: A Spin-Based Electronics Vision for the Future," *Science*, vol. 294, no. 5546, pp. 1488–1495, Nov. 2001.

[2] G. Szulczewski, S. Sanvito, and M. Coey, "A spin of their own," *Nat. Mater.*, vol. 8, no. 9, pp. 693–695, Sep. 2009.

[3] J. Bass and W. P. Pratt Jr, "Spin-Diffusion Lengths in Metals and Alloys, and Spin-Flipping at Metal/Metal Interfaces: an Experimentalist's Critical Review," *ArXivcond-Mat0610085*, Oct. 2006.

[4] I. Appelbaum, B. Huang, and D. J. Monsma, "Electronic measurement and control of spin transport in silicon," *Nature*, vol. 447, no. 7142, pp. 295–298, May 2007.

[5] J. M. Kikkawa and D. D. Awschalom, "Lateral drag of spin coherence in gallium arsenide," *Nature*, vol. 397, no. 6715, pp. 139–141, Jan. 1999.

[6] S. A. Crooker, M. Furis, X. Lou, C. Adelmann, D. L. Smith, C. J. Palmstrøm, and P. A. Crowell, "Imaging Spin Transport in Lateral Ferromagnet/Semiconductor Structures," *Science*, vol. 309, no. 5744, pp. 2191–2195, Sep. 2005.

[7] M. Warner, S. Din, I. S. Tupitsyn, G. W. Morley, A. M. Stoneham, J. A. Gardener, Z. Wu, A. J. Fisher, S. Heutz, C. W. M. Kay, and G. Aeppli, "Potential for spin-based information processing in a thin-film molecular semiconductor," *Nature*, vol. 503, no. 7477, pp. 504–508, Nov. 2013.

[8] A. Fert, J.-M. George, H. Jaffres, and R. Mattana, "Semiconductors Between Spin-Polarized Sources and Drains," *IEEE Trans. Electron Devices*, vol. 54, no. 5, pp. 921 –932, May 2007.

[9] E. Moulin, F. Niess, M. Maaloum, E. Buhler, I. Nyrkova, and N. Giuseppone, "The Hierarchical Self-Assembly of Charge Nanocarriers: A Highly Cooperative Process Promoted by Visible Light," *Angew. Chem. Int. Ed.*, vol. 49, no. 39, pp. 6974–6978, Sep. 2010.

[10] V. Faramarzi, F. Niess, E. Moulin, M. Maaloum, J.-F. Dayen, J.-B. Beaufrand, S. Zanettini, B. Doudin, and N. Giuseppone, "Light-triggered self-construction of supramolecular organic nanowires as metallic interconnects," *Nat. Chem.*, vol. 4, no. 6, pp. 485–490, Apr. 2012.

[11] A. Akande, S. Bhattacharya, T. Cathcart, and S. Sanvito, "First principles study of the structural, electronic, and transport properties of triarylamine-based nanowires," *J. Chem. Phys.*, vol. 140, no. 7, p. 074301, Feb. 2014.

[12] J. F. Dayen, V. Faramarzi, M. Pauly, N. T. Kemp, M. Barbero, B. P. Pichon, H. Majjad, S. Begin-Colin, and B. Doudin, "Nanotrench for nano and microparticle electrical interconnects," *Nanotechnology*, vol. 21, p. 335303, 2010.

[13] B. Dlubak, M.-B. Martin, C. Deranlot, B. Servet, S. Xavier, R. Mattana, M. Sprinkle, C. Berger, W. A. De Heer, F. Petroff, A. Anane, P. Seneor, and A. Fert, "Highly efficient spin transport in epitaxial graphene on SiC," *Nat. Phys.*, vol. 8, no. 7, pp. 557–561, Jul. 2012.

[14] A. Ciesielski, S. Haar, M. El Gemayel, H. Yang, J. Clough, G. Melinte, M. Gobbi, E. Orgiu, M. V. Nardi, G. Ligorio, V. Palermo, N. Koch, O. Ersen, C. Casiraghi, and P. Samorì, "Harnessing the Liquid-Phase Exfoliation of Graphene Using Aliphatic Compounds: A Supramolecular Approach," *Angew. Chem. Int. Ed.*, p. n/a–n/a, Jul. 2014.

[15] D. Natali and M. Caironi, "Charge Injection in Solution-Processed Organic Field-Effect Transistors: Physics, Models and Characterization Methods," *Adv. Mater.*, vol. 24, no. 11, pp. 1357–1387, 2012.

[16] I. McCulloch, M. Heeney, C. Bailey, K. Genevicius, I. MacDonald, M. Shkunov, D. Sparrowe, S. Tierney, R. Wagner, W. Zhang, M. L. Chabinyc, R. J. Kline, M. D. McGehee, and M. F. Toney, "Liquid-crystalline semiconducting polymers with high charge-carrier mobility," *Nat. Mater.*, vol. 5, no. 4, pp. 328–333, Mar. 2006.

[17] A. Laiho, L. Herlogsson, R. Forchheimer, X. Crispin, and M. Berggren, "Controlling the dimensionality of charge transport in organic thin-film transistors," *Proc. Natl. Acad. Sci.*, vol. 108, no. 37, pp. 15069–15073, Aug. 2011.

[18] A. Fert, J.-M. George, H. Jaffres, and R. Mattana, "Semiconductors Between Spin-Polarized Sources and Drains," *IEEE Trans. Electron Devices*, vol. 54, no. 5, pp. 921 –932, May 2007.

Table of contents

1. INTRODUCTION 1

1.1 THE RAISE OF SPINTRONICS 1
1.2 SPINS FOR LOGIC PROCESSES: THE USE OF SEMICONDUCTORS 2
1.2.1 The resistance mismatch problem 4
1.3 ORGANIC SEMICONDUCTORS FOR SPINTRONICS: LONG SPIN LIFETIME, SHORT SPIN DIFFUSION LENGTH .. 5
1.4 THE IMPORTANCE OF CONTACT RESISTANCE 7
1.5 SEARCH FOR ADEQUATE ORGANIC MATERIALS 8
1.6 THE LATERAL GEOMETRY 10
1.7 OBJECTIVE AND STRUCTURE OF THE THESIS 12

2. SUPRAMOLECULAR TRIARYLAMINES NANOWIRES 19

2.1 SUPRAMOLECULAR ELECTRONICS 19
2.1.1 1D structures from polydisperse π-conjugated polymers 20
2.1.2 1D structures from monodisperse oligomers or molecules (self-assembly) 21
2.2 CHARGE TRANSPORT PROPERTIES OF ORGANIC 1D NANOSTRUCTURES 22
2.3 SELF-ASSEMBLY PROCESS OF TRIARYLAMINES MOLECULES IN SOLUTION 24
2.4 SELF-ASSEMBLY OF TRIARYLAMINES BETWEEN METALLIC ELECTRODES 27
2.4.1 Description of the self-assembly experiment 27
2.4.2 Imaging STANWs inside nanotrenches 30
2.4.3 A closer look on the self-assembly process 32
2.4.3.1 Light source 32
2.4.3.2 Presence of a magnetic metal in the electrodes 33
2.4.3.3 Threshold voltage potential 34
2.4.3.4 Self-assembly between electrodes spaced > 100 nm 35
2.4.4 Excluding artifacts 36
2.4.4.1 Stress tests on the electrodes 36
2.4.4.2 Blind test 37
2.4.5 Metallic temperature dependent behavior 39
2.4.6 Conductivity and contact resistance estimates 39
2.5 ELECTROLYTE-GATING OF STANWS 41
2.6 CONCLUSIONS 42

3. LIQUID EXFOLIATED GRAPHENE 47

3.1 GRAPHENE SPIN DIFFUSION LENGTH λ_S 47
3.1.1 Experimental measure of spin diffusion length λ_s in graphene 48
3.2 LIQUID-PHASE EXFOLIATION OF GRAPHITE TO GRAPHENE 49
3.2.1 Basic principle of liquid-phase exfoliation 49
3.2.1 LPE-graphene deposition techniques on substrates 51
3.3 GRAPHENE ELECTRONIC PROPERTIES FOR FET DEVICES 52
3.3.1 Quantum capacitance of graphene 53
3.3.2 Electrical properties of liquid exfoliated graphene 54
3.4 ELECTROLYTE-GATING OF SUSPENDED LPE-GRAPHENE NANOSHEETS 57
3.4.1 Samples fabrication 58
3.4.1.1 Substrate preparation: bottom Au electrodes and SiO_2 cap layer 58

3.4.1.2 LPE-graphene deposition 59
3.4.1.3 Raman analysis and TEM characterization of LPE-graphene 60
3.4.2 Optical and electrical characterization after deposition 61
3.4.2.1 Electronic microscope imaging 63
3.4.3 Electrolyte-gating experiment 64
3.4.3.1 Iongel preparation 64
3.4.3.2 Transfer curves 65
3.4.3.3 $I_g - V_g$ curves 65
3.4.4 Discussion of the results 67
3.4.4.1 Electrical double layer specific capacitance C_{EDL} 67
3.4.4.2 Mobility estimation 68
3.4.4.1 Position of the Dirac neutrality point, smoothness and hysteresis 70
3.4.4.1 I_{on}/I_{off} ratio 70
3.5 CONCLUSIONS 71

4. HIGHLY DOPED POLYMER SEMICONDUCTOR (PBTTT) 75

4.1 CRYSTALLINE CONJUGATED POLYTHIOPHENES 76
4.1.1 Molecular structure and crystalline arrangement of PBTTT 76
4.2 CHARGE TRANSPORT PHYSICS OF CONJUGATED POLYMERS (AT LOW CARRIER DENSITIES) 77
4.2.1 Gaussian Disorder Model (GDM) 79
4.2.2 Mobility edge 80
4.3 CHEMICAL DOPING OF CONJUGATED POLYMERS 81
4.3.1 Early "synthetic metals" 81
4.3.2 Electrolyte-gating: an efficient doping technique 82
4.4 CHARGE TRANSPORT PHYSICS OF CONJUGATED POLYMERS (AT HIGH CARRIER DENSITY) 83
4.4.1 Insulator-to-metal transition 85
4.5 KEY EXPERIMENTAL INSIGHTS INTO METALLICITY 86
4.6 CHARGE TRANSPORT STUDY OF HIGHLY DOPED PBTTT THIN FILMS 88
4.6.1 Sample preparation 89
4.6.1.1 Substrate fabrication 89
4.6.1.2 Spin-coating of PBTTT thin films 89
4.6.1.3 Top-gate electrolyte 90
4.6.2 Gate-voltage tuning of the conductivity 91
4.6.2.1 Cooling at constant gate bias 92
4.6.2.2 Carrier density estimate 93
4.7 CONDUCTIVITY TEMPERATURE DEPENDENCE 96
4.7.1 Interpretation of the conductivity behavior 99
4.8 MAGNETOTRANSPORT 101
4.8.1 Interpretation of the magnetotransport properties 103
4.8.1.1 Positive magnetoconductance: disruption of weak localization 103
4.8.1.2 Coherence length estimation 105
4.8.1.3 Negative magnetoconductance: electron-electron interactions 105
4.9 HALL EFFECT 107
4.9.1 Experiment 108
4.10 MOBILITY CALCULATION 110
4.11 CONCLUSIONS 112

5. CONTACT RESISTANCE OF DOPED PBTTT WITH METALS 117

5.1 SEMICONDUCTOR BETWEEN SPIN POLARIZED SOURCE-DRAIN: THE PROBLEM OF SPIN INJECTION AND DETECTION 117

5.1.1 Lower limit for interface resistance: $r_b^* > r_1$ 120

5.1.2 Upper limit for interface resistance: $r_b^* < r_2$ 121

5.1.3 Gate-tuning of the r_b^*/r^N ratio 122

5.2 THE METAL/SEMICONDUCTOR INTERFACE 123

5.2.1 Metal/inorganic semiconductor interface: the Schottky barrier 123

5.2.2 Metal/organic semiconductor interface 125

5.3 CONTACT RESISTANCE OF SOLUTION-PROCESSED ORGANIC SEMICONDUCTORS ONTO METALS 127

5.3.1 The highly doped polymer semiconductor case 128

5.3.2 Few attempts of lateral organic spinvalves with highly doped polymers 129

5.4 GATED FOUR-PROBE METHOD FOR CONTACT RESISTANCE MEASUREMENTS 130

5.5 CONTACT RESISTANCE OF PBTTT WITH METALS (AU, NI) 133

5.5.1 PBTTT/Gold electrodes 133

5.5.1.1 Contact resistance as a function of doping 133

5.5.1.2 Contact resistance as a function of temperature 135

5.5.1.3 Contact resistance versus channel resistance at high doping 136

5.5.2 PBTTT/Nickel electrodes 136

5.5.2.1 Contact resistance as a function of doping 136

5.6 CONCLUSIONS 137

5.7 POSSIBLE SOLUTIONS AND PERSPECTIVES 139

CONCLUSIONS 143

APPENDIX A - NANOTRENCHES FABRICATION 149

APPENDIX B – ELECTROLYTE-GATING 153

High mobility materials for organic spintronic applications

In this thesis we will investigate organic type spacers for the purpose of making organic spinvalves (OSVs). Even though the thesis title reads 'for organic spintronics applications', the reader should not expect to encounter experiments on the fabrication of spinvalve devices! The organic spacers are mainly investigated in terms of charge transport properties (electrical conductivity, carriers mobility) and contact resistance with metals (Au, Ni), in a geometry we consider best-suited to implement interesting spin-based devices.

During this thesis work, it became more and more evident, in fact, that stringent conditions are needed for the fabrication of organic spinvalves. If we want to make diffusive transport of a spin current inside the organic channel possible (injection-transport-detection), both the intrinsic characteristics of the organic channel (type of charge/spin transport, carriers mobility) and the interface between the organic channel and the ferromagnetic metallic electrodes should meet special criteria. The existence of these strict requirements, together with the still needed proof of detection of a spin current in non-local configuration for organic materials, raise indeed some doubts on the real origin of the magnetoresistance (MR) signals found in literature for two-terminal OSVs.

We will therefore initially remind some basics concepts of Spintronics, pointing out clearly which are the search guidelines for the suitable organic material. We believe it is necessary to verify the fulfillment of these criteria before 'blindly' trying to make spinvalves. The main scope of this thesis is thus testing different organic materials in order to find one satisfying these conditions. In pursuing this objective, the thesis presents an interesting scientific 'parcours' going from bottom-up self-assembled devices for supramolecular electronics (Chapter 2) to an in-depth plunge into the fundamental physics of conjugated polymer semiconductors (Chapter 4), passing though one of the most discussed materials of today's electronics, graphene, used with an approach more compatible with typical wet-processes of Organic Electronics (Chapter 3). This work led to new device concepts and new discoveries.

The Introduction will provide the basics of the motivations for this thesis, and we will implement some specific discussion on the properties of the organic material studied, as well as the reasoning behind our experimental strategy, at the beginning of each chapter. Hence, Chapters 2 - 5 contain an initial survey on the material characteristics and the concepts studied, followed by the experimental part.

1. Introduction

1.1 The rise of Spintronics

Circuit miniaturization by scaling down of the device size has been the main driving force for semiconductor technology for more than 40 years. In a very farsighted paper of 1965 [1], Gordon Moore foresaw that the number of devices incorporated on integrated circuits would have exponentially increased over time. This challenging prevision has been indeed fulfilled since 1970, with a doubling of the number of transistor per chip every 18 months, causing the historical trend known as “Moore’s law”. However, we arrive now to a bottleneck in device miniaturization, mostly due to problems of power dissipation which causes circuit overheating.

One alternative approach to maintain the increase of device performances by other means than just scaling the dimensions (“equivalent scaling”) is to incorporate new materials and adopt new concepts for device functioning. The exploitation of the electron spin (in addition to its charge) and the use of spin currents (instead of electric currents) for information computing in electronic devices is extremely promising. The research field aiming at efficient control and manipulation of spin-polarized currents is Spintronics.

Spintronics originates from the discovery of Giant Magnetoresistance (GMR) in 1988 [2],[3]. Less than 10 years after the discovery of this effect, GMR-based hard disk read heads revolutionized the market of magnetic mass storage. The Giant magnetoresistance effect consists in a significant change in the electrical resistance of multilayered structures of magnetic and non-magnetic metallic thin films (initially Fe/Cr, then Co/Cu), depending on whether the magnetization of adjacent ferromagnetic layers is in a parallel or antiparallel alignment. The current can flow either perpendicular to the interfaces between layers (Current Perpendicular to Plane, CPP), or parallel (Current In Plane, CIP). The magnetization direction can be controlled, for example, by applying an external magnetic field; the overall resistance is low for parallel alignment and high for antiparallel alignment. GMR effect is based on the dependence of electron scattering events on their spin orientation and it is strictly related to the multilayer structure. Because GMR considerably changed our understanding of spin-dependent transport processes (and not only in magnetic system), its discovery was awarded with the 2007 Nobel Prize in Physics to A. Fert and P. Grünberg.

Jullière discovered in 1975 the Tunnelling Magnetoresistance (TMR) [4], i.e. the effect according to which the current passing through an insulating barrier sandwiched between two magnetic layers depends on the relative magnetization of these two. The device formed by two magnetic electrodes and a non-magnetic spacer is a spinvalve. A TMR spinvalve mechanism relies on the quantum tunneling of electrons from one electrode to the other, thus the oxide thickness is restrained between 1 and 3 nanometers. Contrarily to GMR, no scattering events occur to the electron tunnelling the barrier and the magnetoresistance effect is mostly related to the different spin-polarization degree of the electrons at the Fermi level in the two magnetic electrodes. First observation of large TMR at room temperature (10 - 20 %) employing Al_2O_3 as insulating layer was reported in 1995 [5],[6]. Nowadays Fe/MgO/Fe spinvalves, exploiting additional effects due to the matching of electronic states between electrodes and insulator, reach magnetoresistance values ~ 200 % at room temperature [7],[8] (with a record report of ~ 600 % [9]). Because of these exceptional values, the effect is sometimes referred to as Giant TMR (not to be confused with GMR).

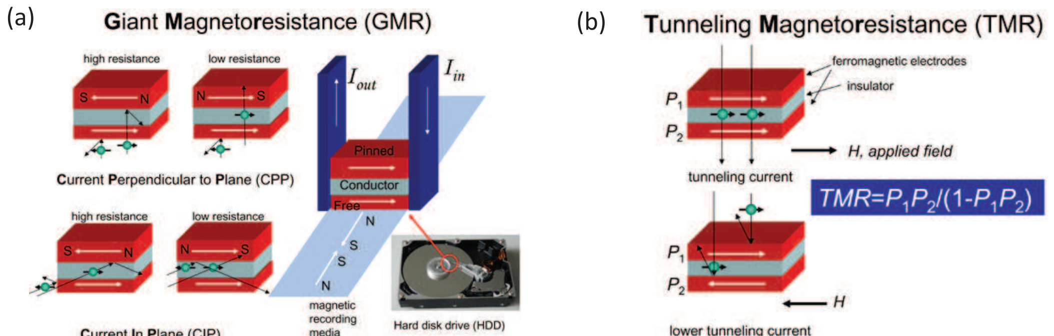

Figure 1.1 Representation of GMR and TMR mechanisms: in both cases, a considerable variation of the electrical resistance is achieved by switching the magnetization of the device's electrodes (in red) from parallel to antiparallel. a) Grey spacer is a conductor material, typically a non-magnetic metal. GMR works for both CPP and CIP geometries; a hard disk drive read-head is also illustrated. b) Grey spacer is a very thin insulator (few nanometers). P_1 and P_2 denote the spin polarization degree of the two ferromagnetic electrodes.

1.2 Spins for logic processes: the use of semiconductors

The next challenge for Spintronics is the exploitation of the spin functionality not only to build memory devices, but also to execute logic processes. Combining magnetism to microelectronics, i.e. unify spin and charge manipulation in a single device, promises a wide range of new phenomena and applications. Adding the spin degree of freedom to conventional semiconductor charge-based electronics will bring important advantages to the new electronic devices such as nonvolatility, increased data processing speed, decreased electric power consumption, and higher integration densities compared with conventional semiconductor devices [10].

For this purpose, an optimal control on the electrical injection, transport, manipulation and detection of spins (spin currents) inside semiconductors have to be mastered. Phenomena such as Rashba effect [11], spin Hall effect [12] or spin torque effect [12],[13] could be used in the short term to fabricate the first magnetologic devices. Magnetic Random Access Memories (MRAM) exploiting the spin torque effect have already been subject of considerable investments by important industrial companies (Samsung for example). Huge efforts are underway to realize the first experimental prototype of the spin Field Effect Transistor (spin-FET) proposed by Datta and Das [14] in 1990.

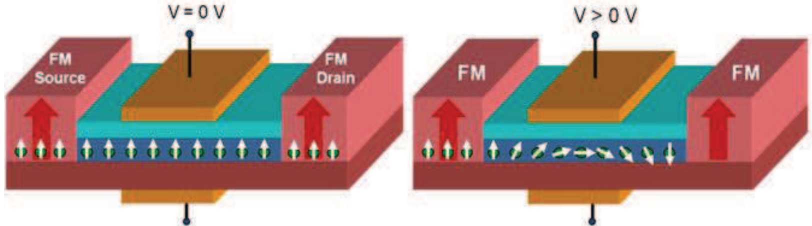

Figure 1.2 Principle mechanism of the spin Field Effect Transistor (spin-FET). Source and drain electrodes are ferromagnetic and the current injected in the semiconductor channel is spin-polarized. Rashba effect, caused by the gate electric field, makes the electrons spin to precess. When the electron spins are antiparallel to the drain magnetization, the electrons are rejected at the semiconductor/drain interface (situation on the right).

The spin-FET principle mechanism, as illustrated in Figure 1.2, is based on the Rashba effect, i.e. the precession of the electron magnetic moment in presence of an electric field. A spin-FET would allow the fine modulation of the source-drain spin current (keeping the two electrode parallel magnetized), similarly to a “classical” FET. Unlike in a spinvalve, the high and low resistance states can be switched by the gate voltage alone, leaving the magnetization of the two ferromagnetic layers unchanged.

The successful realization of spin-based electronic devices requires to maximize the spin lifetime τ_s of the conduction electrons in the semiconductor and to extend their motion along relevant length scales, i.e. to extend their spin diffusion length λ_s. The spin lifetime τ_s is the time period during which an electron keeps unvaried its spin state. The related spin diffusion length λ_s is the distance the electron can travel during τ_s, thus without undergoing any spin-flip event. λ_s and τ_s are related by the relation:

$$\lambda_s = \sqrt{D \cdot \tau_s} \qquad 1.1,$$

where D is the carriers diffusion coefficient. It must be noted that D is proportional to the carrier mobility μ, $D = (\mu \cdot k_B T)/e$. λ_s reaches values of hundreds of nanometers for light non-magnetic metals (~ 600 nm for Aluminum [15][16]), while it shortens to 1 - 50 nm for magnetic metals (Co, Ni) or magnetic alloys [17]. As revealed by the vocabulary, this simple model in spin transport in materials implies the adequacy of a diffusive model of charge transport. The body of research in this field in the last 30 years showed that such model applied remarkably well to most experiments.

Spin diffusion length in semiconductors is expected to be larger respect to metals, especially for high-quality crystalline materials of relevance for industrial applications. The first demonstration of spin injection in silicon reports detectable spin transport across 10 μm undoped Si [18]. Other experiments attribute to GaAs a spin diffusion length > 50 μm [19],[20]. Figure 1.3 shows indeed spin injection in a GaAs stripe from an iron ferromagneric electrode, imaged by means of magneto-optical Kerr effect [20].

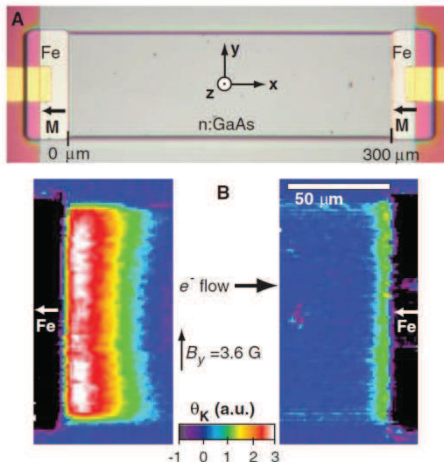

Figure 1.3 Imaging of spin transport in lateral FM/GaAs/FM structures by magneto-optical Kerr effect. The technique allows clear detecting of a spin unbalance up to ~ 50 μm from the source (left electrode). Reprinted from [20].

The long τ_s combined with remarkable carrier mobilities (μ_e up to 1500 cm^2/V·s in undoped Si and almost 10 times more for GaAs) allow spin-polarized currents to travel along important distances. In short, their intrinsic physical characteristics and the necessity to merge the existing technology,

make the employment of semiconductors essential for the fabrication of information processing spintronic devices.

1.2.1 The resistance mismatch problem

Using semiconductors adds a complication respect to all-metals GMR devices or metal-oxide TMR spinvalves: the so-called “resistance mismatch problem”. Semiconductors are employed as active channel, but the use of ferromagnetic (FM) metallic electrodes remains essential for the injection/detection of spin-polarized current (magnetic semiconductors could also be used, but they are less practical and nonexistent at room temperature).

When an electrical spin current must cross an interface between a ferromagnetic and a non-magnetic material, as represented in Figure 1.4(a), a spin-up/spin-down electrons imbalance is formed at the interface (spin accumulation) [21]. This imbalance relaxes on both sides of the interface with an exponential decay going with the spin diffusion length λ_s of the material, namely $\exp(x/\lambda_s)$, as illustrated in Figure 1.4(b).

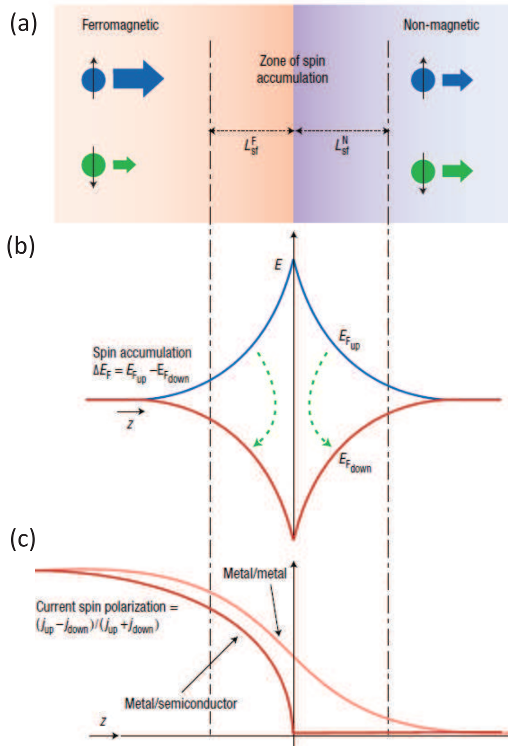

Figure 1.4 Schematic representation of the spin accumulation at an interface between a ferromagnetic metal and a non-magnetic layer. a) Spin-up and spin-down current. L^F_{sf} and L^N_{sf} are the spin diffusion lengths respectively of the FM and of the semiconductor. b) Exponential decay of spin accumulation. c) Spin polarization of the current for the case metal/metal and metal/semiconductor interface. Reprinted from [22].

If the non-magnetic material is a semiconductor, according to the theory developed by Fert and Jaffrès [23],[24], the spin polarization $(SP)_I$ of the current entering into the semiconducting channel is:

$$(SP)_I = \frac{\beta}{1 + r_N / r_F} \qquad 1.2,$$

where β is the bulk asymmetry coefficient of the FM electrode, and $r_N = \rho^{NM} \cdot \lambda_s^{NM}$ for the semiconductor ('NM' stays for non-magnetic) and $r_F = \rho^{FM} \cdot \lambda_s^{FM}$ for the ferromagnet. $(SP)_I$ is represented in Figure 1.4(c). If the semiconductor resistivity ρ^{NM} is much higher than the electrode resistivity ρ^{FM} (typical situation for a semiconductor in contact with a ferromagnetic metal), amplified by the fact that spin relaxation is easier in a ferromagnetic metal than a semiconductor ($\lambda_s^{NM} > \lambda_s^{FM}$), we have that $r_N >> r_F$. According to Equation 1.2, if $r_N >> r_F$, the spin polarization of the injected current $(SP)_I$ goes to zero. Physically this means that the spin imbalance preferentially flows back into the FM electrode and does not propagate into the semiconductor.

This issue of resistance mismatch ($\rho^{NM} >> \rho^{FM}$) is one of the main obstacles for the fabrication of efficient spin-based electronic devices. We return on the topic in paragraph 1.4.

1.3 Organic semiconductors for spintronics: long spin lifetime, short spin diffusion length

Organic semiconductors (OSCs) are interesting candidates for spin-based electronics because the spin carriers lifetime τ_s is estimated to be considerably longer than in inorganic semiconductors. Spectroscopic data tell us that τ_s in organics can reach values of 10^{-6} s to even 10^{-3} s (longer at low temperatures) [25]. This has been the main driving force for the birth and development of the research field of Organic Spintronics, together with the advantage related to chemical flexibility and relatively low production cost of organic materials [26].

The main transport mechanism of charge and spin in organic semiconductors relies on spin-1/2 polarons, which are localized electrons dressed up by a molecular deformation. Conduction occurs due to the thermally activated hopping of polarons between localized sites. Even though mechanisms for relaxation of spin polarization are not completely understood yet, it is known that spin-orbit coupling and hyperfine interaction[1] are the main causes of spin memory loss. Spin-orbit coupling is proportional to Z^4 (where Z is the atomic number), thus it is expected to be very weak in OSCs, since they are formed by very light elements (carbon, hydrogen, nitrogen, sulfur, etc). Hyperfine interaction is generally low because the most common isotope ^{12}C of carbon has zero nuclear magnetic moment.

However, a long spin lifetime does not necessarily correspond to a long spin diffusion length, and OSCs typically exhibit spin diffusion lengths not exceeding 20 nm. In fact, according to equation 1.1, a low mobility μ can strongly limit the spin diffusion length λ_s. Charge transport occurring by hopping between localized states leads indeed to very low electron/hole mobility (typically $10^{-5} < \mu < 10^{-2}$ cm^2/V·s).

In Figure 1.5 we report the graph from Szulczewski *et al*. [27] showing the correspondence between spin lifetime τ_s and spin diffusion length λ_s for different materials. The data are taken from literature and mainly derive from measurement of spinvalve devices.

[1] *Hyperfine interaction is between the electron spin and the nuclear magnetic moments.*

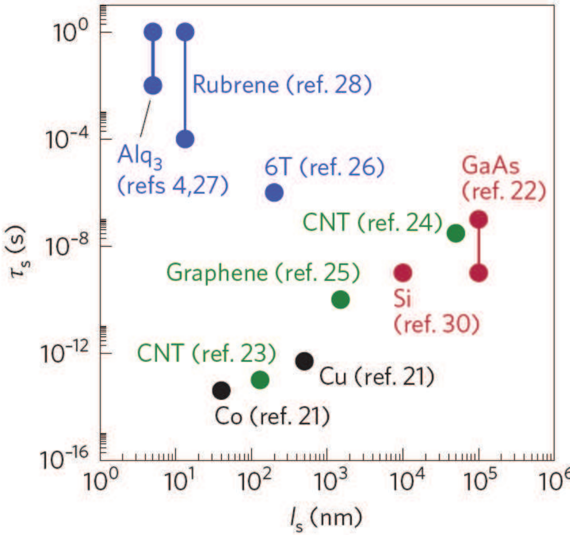

Figure 1.5 Spin lifetime τ_s *versus* spin diffusion length λ_s, for various materials. Reprinted from [27]. References indicated in the graph relate to bibliography of the source article.

Organic semiconductors are located in the top left corner of the graph. As above mentioned, their low carrier mobility limits the distance at which a carrier can travel before losing its spin memory, although the carriers spin state is preserved for a long time interval. Carbon-based materials such as graphene and carbon nanotubes (CNT) constitute an exception among organics: their low dimensionality and special band structure lead to very high mobilities, thus their λ_s can reach the micrometers range (although there are significant discrepancies in the literature about the spin diffusion length in graphene).

A clear and undoubtful demonstration of electrical spin injection in organics is still lacking. Even though magnetoresistance (MR) signals are found reproducibly in vertical organic spinvalves [28],[29], MR by itself cannot be considered as a proof of spin injection. Better indicators of electrical spin injection would be the detection of pure spin currents in a non-local geometry device and/or the observation of Hanle precession. Hanle effect is caused by the precession of the spin in the presence of a non collinear magnetic field and can be detected by observing the way in which it affects the magnetoresistance in a spinvalve device. While Hanle effect has been measured in spintronic devices fabricated with an inorganic spin transporting channel [30], and its observation established spin injection into inorganic semiconductors on a sure footing, it is still missing for organic semiconductors [31].

Just recently, in a pioneering work, Watanabe *et al*. [32] have been able to detect Hanle effect in an undoped conjugated polymer. To do so, they inject spin-polarized current by optical spin pumping (pure spin current), thus bypassing completely the problem related to metal/semiconductor resistance mismatch typical of electrical spin injection. They found an exceptionally high temperature-independent $\lambda_s \sim 200$ nm (corresponding to $\tau_s \sim 20$ ms, calculated from Equ. 1.1). They also deduce that the main source of spin scattering is the spin-orbit coupling during the hop event. This encouraging result needs however confirmation by others and the practical use of optical spin injection for organic spintronics devices remains to be shown.

In summary, the main issue for the use of organics in Spintronics is that the spin memory persists for very long time, but not over long distances, limited by the OSCs bad conductivity properties.

1.4 The importance of contact resistance

The contact resistance is the physical obstacle that an electrical current encounters when trying to pass from a material to another, due to energy barriers forming and unavoidable scattering related to the heterogeneity of the interface system. A parasitic potential drop is associated to the contact resistance in a functioning device during operation (parasitic because it just causes energy loss). In particular, metallic electrodes and semiconductor molecular materials have very different electronic properties by nature, and a significant contact resistance is a serious limitation in Organic Electronics devices [33]. Electrically poor contacts severely degrade charge injection as well as charge transport in the channel [34]. Ohmic contacts remain a big challenge for the fabrication of new transistors using organic semiconductors [33] and 2-D materials (graphene [35],[36]; molybdenum disulfide MoS_2 [37]).

The FETs lateral geometry also limits the physical area of contact between OSC and metal. For field effect transistor studies, the conductive active channel is very often a few nanometers thick only (thickness of the gate-induced accumulation layer), making the charge-injection interface essentially independent of the metal electrode and semiconductor thickness. This is why, for devices in OFET geometry, the contact resistance is expressed in $\Omega\cdot$cm (thickness of the injection area is considered negligible respect to the width W). Typical values of contact resistance in OFETs gated with conventional dielectrics are always higher than 1 k$\Omega\cdot$cm. Such highly resistive contacts become strongly constraining in devices with channel length L < 1 µm. In fact, since the channel resistance R_{ch} scales down with L while contact resistance R_c does not, interface effects are dominant in nano-size devices and constitute a major issue for technological downscaling.

In the context of Spintronics, however, the contact resistance between ferromagnetic (FM) electrodes and the semiconducting (SC) channel can help to solve the resistance mismatch problem discussed in paragraph 1.2.1. As already explained, the spin polarization of a current injected from a ferromagnet to a semiconductor goes to zero when $r_N = \rho^{NM}\cdot\lambda_s^{NM}$ is too high (Equation 1.2, [23]), because the spin current preferably flows back and relaxes inside the ferromagnet. One possible solution to restore spin accumulation inside the semiconductor (with respect to the FM) is indeed to add a spin-dependent interface resistance r_b^*. Such interface resistance re-equilibrates the spin relaxation on both the metallic and the semiconducting side. Experimentally, this interface resistance has been added typically in the form of a tunnel barrier of oxide, and it has allowed to optimize graphene [38] and metallic [39] spinvalves.

Even though a non-zero (spin-dependent) interface resistance is beneficial to spin injection, r_b^* cannot be too high neither, otherwise one falls again into the problem of spin back flow. A too high interface resistance is detrimental for injecting the spin (spin current cannot enter the semiconductor) and for detecting the spin (spin current cannot exit the semiconductor). Typical values of contact resistance at metal/organic interfaces are intrinsically very high, thus in Organic Spintronics the main difficulty is to keep r_b^* low enough.

Following [24], the interface between the semiconductor and the ferromagnetic metallic source and drain must have a contact resistance r_b^* per unit of area [$\Omega\cdot cm^2$] included in a well-defined resistance "window". Such window of optimal r_b^* values is centered around r_N (we recall that $r_N = \rho^{NM}\cdot\lambda_s^{NM}$, i.e. the product of the semiconductor resistivity and its spin diffusion length). If the ratio r_b^*/r_N is around 1, the spinvalve magnetoresistance signal $\Delta R/R^P$ reaches its maximum value, as illustrated in Figure 1.6.

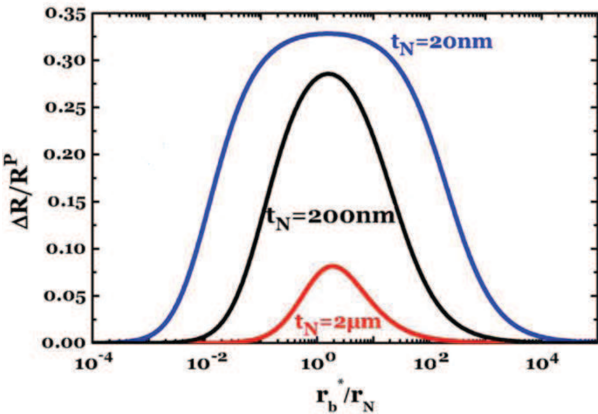

Figure 1.6 Calculated magnetoresistance signal $\Delta R/R^P$ as a function of the r_b*/r_N ratio, where $r_N = \rho^{NM} \cdot \lambda_s$ and λ_s = 2 µm. Calculation are presented for different spinvalves channel lengths t_N (2 µm, 200 nm and 20 nm): The highest MR signal is associated to the shortest channel.

1.5 Search for adequate organic materials

The two previous paragraphs give us the key requirements for the choice of the organic material suitable for application in Spintronics:

- High charge carrier mobility;
- Low interface resistance with metals.

These two requirements point towards the same type of material characteristics, in the sense that increasing the mobility of an OSC improves its conductivity, which should also result in a reduction of its interface resistance with a metal electrode. In this search for an adequate material, Organic Spintronics can take great advantage from the ongoing research in Organic Electronics, which also aims to improve the conductivity of OSCs. Furthermore, polarons in organic semiconductors are both charge and spin carriers and the understanding of spin-transport phenomena inevitably goes altogether with the comprehension of charge-transport mechanisms.

Organic Electronics witnessed a rapid development and some of its applications are already commercially available (mainly Organic Light Emitting Diodes for screens), but the study of the fundamental physics of electrical transport in conducting organic materials is not completely understood yet. The investigation on the interplay between semiconductor morphology and transport properties is a today's hot topic in Organic Electronics [40],[41],[42].

The quest for highly conductive OSCs already dates to the works carried out in the 80'-90' on doped conjugated polymers (polyaniline, polyacetilene, etc), leading to the production of the so-called "synthetic metals" [43],[44]. Nowadays, several organic semiconductors already exist exceeding the mobility of amorphous silicon (0.5 – 1 $cm^2/V \cdot s$), such as polythiophene copolymers ([45], p-type), naphthalene and perylene diimide copolymers ([46], n-type), and thieno[3,2-*b*]thiophene isoindigo (iITT) based copolymers ([47], ambipolar). OSCs are becoming competitive for low-cost field-effect transistors production [48]. One of the most conductive "new generation" doped conjugated polymer, known as PEDOT:PSS, can reach record values > 100 S/cm and investigated as potential substitute to indium tin oxide (ITO) for transparent electrodes [49].

It is by now well established that low-mobility in organic semiconductors is caused by the absence of extended delocalized electronic wavefunctions. Localization of electronic wavefunctions is

mainly caused by structural disorder, similarly to what happens introducing crystal disorder in inorganic semiconductors like silicon (amorphous silicon). This effect is referred to as Anderson localization [50]. As a consequence, when a potential difference is applied to the material, charge carriers are obliged to hop from one localized state to another in order to drift. This hopping process requires energy, thus it is thermally activated: at low temperature, localization leads to infinitely high resistances (insulating state).

One approach to improve OSCs conductivity is trying to minimize the structural disorder, and consequently to reduce the localization. Structural disorder (also called "static disorder") mainly consists in a scarce crystal arrangement or presence of impurities. In reality, highly ordered OSCs already exist in the form of organic single crystals (pentacene, rubrene, etc) and they indeed held for many years the best mobility values in Organic Electronics (> 10 $cm^2/V\cdot s$) [51],[52]. However, they lack the ease of processability required for many applications in Organic Electronics, mainly the possibility of thin film processing. The degree of crystallinity of a molecular material results from a combination of the molecule features (planarity, presence of lateral groups, etc) and the deposition technique. Nowadays chemists are working to design small molecule OSCs that maintain solution-processability and are able to organize themselves in a high-order molecular packing during thin film deposition. TIPS-pentacene [53], C_n-BTBT [54] and C_n-DNTT (where n = 8 or 10), represented in Figure 1.7, are successful examples of small molecule OSCs in which conductivity is given by the π-π stacking of molecule cores and solubility in organic solvents is guaranteed by functionalization with bulky lateral groups.

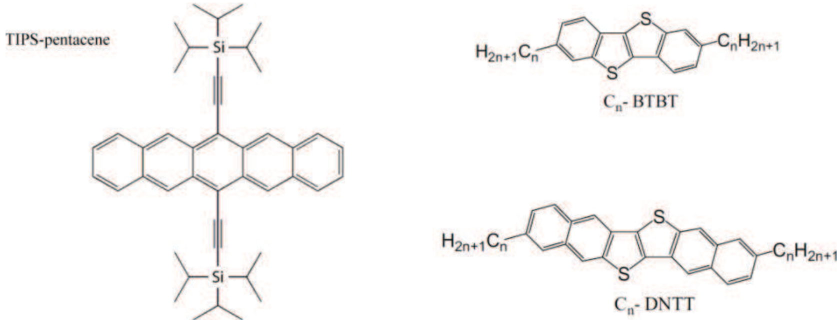

Figure 1.7 Three main examples of solution-processable small molecule organic semiconductors with mobility μ higher than 1 $cm^2/V\cdot s$.

In conjugated polymers semiconductors the situation is slightly different. π-conjugation along the polymer chain should theoretically give rise to infinitely extended 1-D electronic wavefunctions. In this case, structural disorder is due to chain defects which break the conjugation and transform the polymer chain in a series of localized-wavefunction segments [55]. The arrangement of the polymeric fibers in crystalline aggregates, as represented in Figure 1.8(a) strongly helps to reduce static disorder. This is why semi-crystalline polymers generally show higher mobility values. The presence of disordered, amorphous regions in the films does not necessarily hinder charge transport, as long as the molecular weight is large enough to provide a percolating network between the aggregates (red bold lines in Figure 1.8). Amorphous polymers, as represented in Figure 1.8 (c), present usually lower mobilities than semi-crystalline ones Figure 1.8(a).

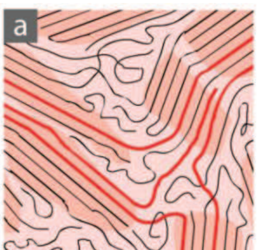

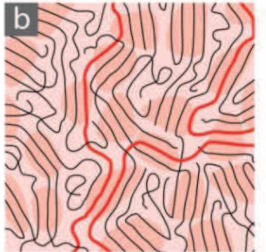

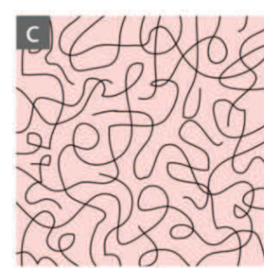

Figure 1.8 Different possible microstructures of conjugated polymer films (schematic top-view). There can be a coexistence of ordered (darker shadowed areas) and spaghetti-like amorphous regions. Polymer chains connecting different crystalline domains are shown in bold red. a) semicrystalline polymer film (for example, PBTTT); b) polymer film with smaller crystalline areas (typical of many donor-acceptor copolymers; PDPPBT, PNDI2OD-T2); c) completely amorphous polymer film. Reprinted from [56].

A second possible approach to improve the conductivity of a material is increasing its density of charge carriers (intrinsically very low in OSCs), for example by means of chemical doping. The conductivity σ is in fact proportional not only to mobility μ, but also to carrier density n ($\sigma = e \cdot \mu \cdot n$, where e is the electron charge). Chemical doping has been the very first approach to make polymers conductive (Nobel prize in Chemistry in 2000 to A. Heeger, A.G. MacDiarmid and H. Shirakawa). Chemical doping increases the carrier density n and, more importantly, enhances the mobility, by the filling of the localized trap-states in the tail of the Gaussian Density of States (DOS) typical of disordered organic semiconductors [57],[55].

1.6 The lateral geometry

We present investigations on 'lateral' planar devices, where electrodes lie flat on a substrate with the active material being a thin film separating the electrodes. This geometry is ideally suited for 'gating' purposes, with a third electrode controlling a transverse electric field acting on the semiconducting channel (Figure 1.9).

For our studies, this geometry has significant key advantages:

- we can impose the channel length L by the electrodes geometrical choices in the patterning process;
- we can gate the structure, and therefore tune the channel conductivity;
- we can reversibly dope the material, and therefore tune its conductivity;
- we can keep a top access to the sample, in order to *i.* get access to its structural properties by imaging techniques and *ii.* possibly tune its properties though external stimuli besides electric field (e.g. light, pH, etc)
- we circumvent the problem of electrical short, making thin vertical structures unreliable.

There are however unavoidable limitations to this approach:

- we cannot study the tunneling though ultra-thin films of organic materials (which is anyway highly challenging for all devices geometries);
- this 'open' geometry is sensitive to the chemical environment, and makes in particular the samples possibly air-sensitive;
- Most important: the interface resistance will be significant, as the contact area between SC and electrodes is limited by the intrinsic thickness of the conducting zone of the SC.

The other technical choice we make here involves the 'chemical' approach for making the active thin film. We deliberately use solution-processed materials, and make thin films by drop casting or controlled substrate spinning. This is an alternative to a vacuum evaporation process. We use the 'chemical' approach for convenience and team background experience reasons, keeping in mind that the simplest technical choices are also a key argument for progressing in this exploratory research.

Our group has developed experience in the fabrication of gaps of nanometric size (80 - 100 nm), both by means of edge-mediated optical lithography [58] and e-beam lithography. These so-called 'nanotrenches' have already been used by our group to study electrical transport in spin-crossover nanocrystals [59], optically switchable molecular junctions [60] and nanoparticles networks [61],[62]. You can find the fabrication details of 'nanorenches' in Appendix A.

In this thesis we take great advantage of the accessibility characterizing the lateral geometry. In Chapter 2, for example, it is shown how irradiation with a light stimulus has been essential for targeted positioning of the self-assembled supramolecular nanowires between pre-patterned metallic electrodes. Most of all, lateral geometry is exploited to apply a transverse electric field, in a bottom-gate or top-gate configuration.

In Figure 1.9 a prototypical top-gated lateral spinvalve is represented. Thanks to the gate control, we should be able to modulate on one hand the semiconductor resistivity and indirectly its spin diffusion length ($r_N = \rho \cdot \lambda_s$), on the other hand the FM/SC interface resistance r_b*. This allows us to shift the r_b*/r_N ratio along the orange arrow and reach the value for maximum MR signal. In the best case, one could think of turning on and off the magnetoresistance signal in function of the gate voltage.

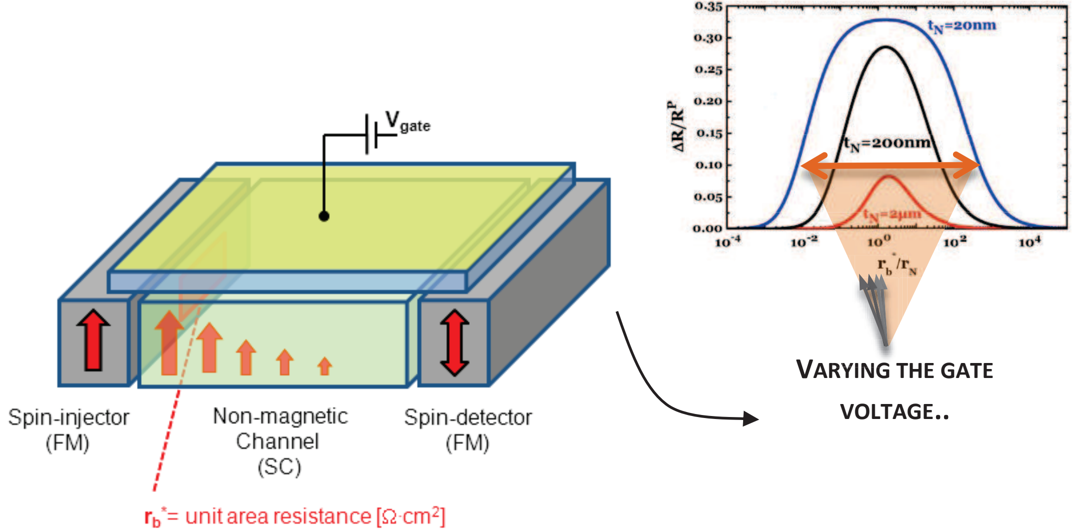

Figure 1.9 Principle of gate modulation of the r_b*/r_N ratio. A prototypical top-gated lateral spinvalve is represented. The gate is potentially able to tune both the semiconductor resistivity and the interface resistance, and the possible change in the r_b*/r_N ratio results in a displacement along the orange arrow in the MR plot.

In the context of the resistance mismatch problem, a gate electrode could be the key to adjust the r_b*/r_N ratio in order to obtain the most efficient spin injection in a spinvalve. Even though the illustration in Figure 1.9 may remind the spin field effect transistor (Figure 1.2), the functioning mechanism of our device does not correlate with the Rashba effect on which the spin-FET is based.

A gating test has been carried out for all the three materials under study. The technique adopted is electrolyte-gating: instead of using conventional thin layers of oxides, this method exploits the polarizability of electrolytes upon the application of a voltage potential through a metallic electrode. The motivations for this particular gating approach are the high capacitance (respect to standard

dielectrics) and the possibility of doping. Details on electrolyte-gating technique are given in Appendix B.

1.7 Objective and structure of the thesis

In summary, this thesis aims to study the charge transport properties of different organic materials with enhanced conductivity, with the ultimate goal of using them for the fabrication of Organic Spintronics devices. Organic Spintronics needs organic semiconductors characterized by significant carrier mobility and electrical conductivity, indication of a more 'delocalized' type of transport respect to typical hopping. Highly conductive organic materials are expected to show coherent spin transport over long distances and at the same time a reduced electrode/channel contact resistance. Since Organic Electronics also quests for highly conductive semiconductors, the results contained in this thesis might interest researchers belonging to both communities.

The three candidate materials investigated in this thesis share this common feature, even though they are quite different by nature. Due to the variety of the materials studied, each Chapter contains its own introductive part describing the main characteristics of the material, followed by the experimental part. Please refer to the sub-introductory parts of each chapter for all information concerning the synthesis/deposition of the material and a general overview of its electronic transport properties.

Chapter 2 describes the self-assembly of Supramolecular Triarylamines Nanowires (STANWs) in between metallic electrodes [63]. This experiment uses the self-organizing capabilities of supramolecular chemistry architectures to produce an excellent example of "bottom-up" construction of nanoscale circuit. The self-assembled supramolecular nanofibers are characterized by a strong π-π interaction between the cores of each triarylamine, which creates an extended electronic wavefunction. The sharing of such delocalized wavefunction with the metal electrodes (allowed by the 'in loco' construction of the fibers) leads to a surprisingly low interface resistance and gives rise to extraordinary values of conductivity for the electrode/STANWs/electrode system.

Chapter 3 contains charge transport measurements of nano-sized graphene flakes. These particular nanosheets are produced by a special method: liquid-phase exfoliation of graphite [60]. The interesting advantage of liquid-phase exfoliated graphene is its processability from solution. Liquid-phase exfoliated graphene (LPE-graphene) can be considered as a solution-processable "ink" with remarkable mobility and conductivity. Successful electrolyte-gating on the LPE-graphene nanoflakes deposited by drop-casting or Langmuir-Blodgett methods on prepatterned metallic electrodes will be presented.

Chapter 4 provide a detailed study on the charge transport properties of highly doped conjugated polymer thin films. The conjugated polymer under analysis is poly(2,5-*bis*(3-dodecyl-2-yl)-thieno[3,2-*b*]thiophene, commonly known as PBTTT, which is considered a semi-crystalline solution-processable polymer, owing to its high degree of crystallinity. We explore how extreme doping, made possible by an experimental approach using electrolyte gating, will bring these PBTTT thin films very close to the metallic state. For this purpose, we present electrical measurements as a function of temperature and in presence of magnetic field, both proving the vicinity to the insulator-to-metal transition.

The main reason driving our research towards polymer thin films has been the search for a material for which the value of interface resistance with metals was measurable, and the channel/interface resistance ratio potentially tunable with the application of electrolyte-gating. For STANWs and LPE-graphene nanosheets systems, the contact resistance was neither measurable nor

tunable, thus we could not know where we were located respect to the resistance mismatch condition of Figure 1.6.

This is why in **Chapter 5** we 'complete' Chapter 4 by illustrating the influence of electrochemical doping on the contact resistance of PBTTT with gold and ferromagnetic (nickel) electrodes.

Each Chapter contains final remarks; nevertheless at the end of the manuscript we draw a global conclusion on the future of organic materials for Spintronic. **Appendix A** explains the special lithography process for the fabrication of nanosized gaps with high aspect ratio (nanotrenches), used mostly in Chapter 2 and 3. **Appendix B** clarifies the mechanism of electrolyte-gating that has been adopted for all the three system under study.

BIBLIOGRAPHY

[1] G. E. Moore and others, “Cramming more components onto integrated circuits,” *Electronics*, vol. 38, no. 8, 1965.

[2] M. N. Baibich, J. M. Broto, A. Fert, F. N. Van Dau, F. Petroff, P. Etienne, G. Creuzet, A. Friederich, and J. Chazelas, “Giant Magnetoresistance of (001)Fe/(001)Cr Magnetic Superlattices,” *Phys. Rev. Lett.*, vol. 61, no. 21, pp. 2472–2475, Nov. 1988.

[3] G. Binasch, P. Grünberg, F. Saurenbach, and W. Zinn, “Enhanced magnetoresistance in layered magnetic structures with antiferromagnetic interlayer exchange,” *Phys. Rev. B*, vol. 39, no. 7, pp. 4828–4830, Mar. 1989.

[4] M. Julliere, “Tunneling between ferromagnetic films,” *Phys. Lett. A*, vol. 54, no. 3, pp. 225–226, Sep. 1975.

[5] T. Miyazaki and N. Tezuka, “Giant magnetic tunneling effect in Fe/Al2O3/Fe junction,” *J. Magn. Magn. Mater.*, vol. 139, no. 3, pp. L231–L234, Jan. 1995.

[6] J. S. Moodera, L. R. Kinder, T. M. Wong, and R. Meservey, “Large Magnetoresistance at Room Temperature in Ferromagnetic Thin Film Tunnel Junctions,” *Phys. Rev. Lett.*, vol. 74, no. 16, pp. 3273–3276, Apr. 1995.

[7] S. Yuasa, T. Nagahama, A. Fukushima, Y. Suzuki, and K. Ando, “Giant room-temperature magnetoresistance in single-crystal Fe/MgO/Fe magnetic tunnel junctions,” *Nat. Mater.*, vol. 3, no. 12, pp. 868–871, Dec. 2004.

[8] S. S. P. Parkin, C. Kaiser, A. Panchula, P. M. Rice, B. Hughes, M. Samant, and S.-H. Yang, “Giant tunnelling magnetoresistance at room temperature with MgO (100) tunnel barriers,” *Nat. Mater.*, vol. 3, no. 12, pp. 862–867, Dec. 2004.

[9] S. Ikeda, J. Hayakawa, Y. Ashizawa, Y. M. Lee, K. Miura, H. Hasegawa, M. Tsunoda, F. Matsukura, and H. Ohno, “Tunnel magnetoresistance of 604% at 300K by suppression of Ta diffusion in CoFeB∕MgO∕CoFeB pseudo-spin-valves annealed at high temperature,” *Appl. Phys. Lett.*, vol. 93, no. 8, p. 082508, Aug. 2008.

[10] S. A. Wolf, D. D. Awschalom, R. A. Buhrman, J. M. Daughton, S. von Molnár, M. L. Roukes, A. Y. Chtchelkanova, and D. M. Treger, “Spintronics: A Spin-Based Electronics Vision for the Future,” *Science*, vol. 294, no. 5546, pp. 1488–1495, Nov. 2001.

[11] E. Rashba, “Properties of semiconductors with an extremum loop. 1. Cyclotron and combinational resonance in a magnetic field perpendicular to the plane of the loop,” *Sov Phys Solid State*, vol. 2, pp. 1224–1238, 1960.

[12] L. Berger, “Emission of spin waves by a magnetic multilayer traversed by a current,” *Phys. Rev. B*, vol. 54, no. 13, pp. 9353–9358, Oct. 1996.

[13] J. C. Slonczewski, “Current-driven excitation of magnetic multilayers,” *J. Magn. Magn. Mater.*, vol. 159, no. 1–2, pp. L1–L7, Jun. 1996.

[14] S. Datta and B. Das, “Electronic analog of the electro-optic modulator,” *Appl. Phys. Lett.*, vol. 56, no. 7, p. 665, 1990.

[15] F. J. Jedema, H. B. Heersche, A. T. Filip, J. J. A. Baselmans, and B. J. van Wees, “Electrical detection of spin precession in a metallic mesoscopic spin valve,” *Nature*, vol. 416, no. 6882, pp. 713–716, Apr. 2002.

[16] S. O. Valenzuela and M. Tinkham, “Direct electronic measurement of the spin Hall effect,” *Nature*, vol. 442, no. 7099, pp. 176–179, Jul. 2006.

[17] J. Bass and W. P. Pratt Jr, “Spin-Diffusion Lengths in Metals and Alloys, and Spin-Flipping at Metal/Metal Interfaces: an Experimentalist’s Critical Review,” Journal of Physics: Condensed Matter 19, 183201 (2007).

[18] I. Appelbaum, B. Huang, and D. J. Monsma, “Electronic measurement and control of spin transport in silicon,” *Nature*, vol. 447, no. 7142, pp. 295–298, May 2007.

[19] J. M. Kikkawa and D. D. Awschalom, “Lateral drag of spin coherence in gallium arsenide,” *Nature*, vol. 397, no. 6715, pp. 139–141, Jan. 1999.

[20] S. A. Crooker, M. Furis, X. Lou, C. Adelmann, D. L. Smith, C. J. Palmstrøm, and P. A. Crowell, “Imaging Spin Transport in Lateral Ferromagnet/Semiconductor Structures,” *Science*, vol. 309, no. 5744, pp. 2191–2195, Sep. 2005.

[21] T. Valet and A. Fert, "Theory of the perpendicular magnetoresistance in magnetic multilayers," *Phys. Rev. B*, vol. 48, no. 10, pp. 7099–7113, Sep. 1993.

[22] C. Chappert, A. Fert, and F. N. Van Dau, "The emergence of spin electronics in data storage," *Nat. Mater.*, vol. 6, no. 11, pp. 813–823, Nov. 2007.

[23] A. Fert and H. Jaffrès, "Conditions for efficient spin injection from a ferromagnetic metal into a semiconductor," *Phys. Rev. B*, vol. 64, no. 18, p. 184420, Oct. 2001.

[24] A. Fert, J.-M. George, H. Jaffres, and R. Mattana, "Semiconductors Between Spin-Polarized Sources and Drains," *IEEE Trans. Electron Devices*, vol. 54, no. 5, pp. 921 –932, May 2007.

[25] M. Warner, S. Din, I. S. Tupitsyn, G. W. Morley, A. M. Stoneham, J. A. Gardener, Z. Wu, A. J. Fisher, S. Heutz, C. W. M. Kay, and G. Aeppli, "Potential for spin-based information processing in a thin-film molecular semiconductor," *Nature*, vol. 503, no. 7477, pp. 504–508, Nov. 2013.

[26] V. A. Dediu, L. E. Hueso, I. Bergenti, and C. Taliani, "Spin routes in organic semiconductors," *Nat. Mater.*, vol. 8, no. 9, pp. 707–716, Sep. 2009.

[27] G. Szulczewski, S. Sanvito, and M. Coey, "A spin of their own," *Nat. Mater.*, vol. 8, no. 9, pp. 693–695, Sep. 2009.

[28] Z. H. Xiong, D. Wu, Z. Valy Vardeny, and J. Shi, "Giant magnetoresistance in organic spin-valves," *Nature*, vol. 427, no. 6977, pp. 821–824, Feb. 2004.

[29] C. Barraud, P. Seneor, R. Mattana, S. Fusil, K. Bouzehouane, C. Deranlot, P. Graziosi, L. Hueso, I. Bergenti, V. Dediu, F. Petroff, and A. Fert, "Unravelling the role of the interface for spin injection into organic semiconductors," *Nat. Phys.*, vol. 6, no. 8, pp. 615–620, Jun. 2010.

[30] Y. K. Kato, R. C. Myers, A. C. Gossard, and D. D. Awschalom, "Observation of the Spin Hall Effect in Semiconductors," *Science*, vol. 306, no. 5703, pp. 1910–1913, Dec. 2004.

[31] A. Riminucci, M. Prezioso, C. Pernechele, P. Graziosi, I. Bergenti, R. Cecchini, M. Calbucci, M. Solzi, and V. Alek Dediu, "Hanle effect missing in a prototypical organic spintronic device," *Appl. Phys. Lett.*, vol. 102, no. 9, p. 092407, 2013.

[32] S. Watanabe, K. Ando, K. Kang, S. Mooser, Y. Vaynzof, H. Kurebayashi, E. Saitoh, and H. Sirringhaus, "Polaron spin current transport in organic semiconductors," *Nat. Phys.*, Mar. 2014.

[33] D. Natali and M. Caironi, "Charge Injection in Solution-Processed Organic Field-Effect Transistors: Physics, Models and Characterization Methods," *Adv. Mater.*, vol. 24, no. 11, pp. 1357–1387, 2012.

[34] L. Bürgi, T. J. Richards, R. H. Friend, and H. Sirringhaus, "Close look at charge carrier injection in polymer field-effect transistors," *J. Appl. Phys.*, vol. 94, no. 9, p. 6129, 2003.

[35] A. D. Franklin, S.-J. Han, A. A. Bol, and W. Haensch, "Effects of Nanoscale Contacts to Graphene," *IEEE Electron Device Lett.*, vol. 32, no. 8, pp. 1035–1037, Aug. 2011.

[36] J. T. Smith, A. D. Franklin, D. B. Farmer, and C. D. Dimitrakopoulos, "Reducing Contact Resistance in Graphene Devices through Contact Area Patterning," *ACS Nano*, vol. 7, no. 4, pp. 3661–3667, Apr. 2013.

[37] H. Liu, A. T. Neal, and P. D. Ye, "Channel Length Scaling of MoS2 MOSFETs," *ACS Nano*, vol. 6, no. 10, pp. 8563–8569, 2012.

[38] N. Tombros, C. Jozsa, M. Popinciuc, H. T. Jonkman, and B. J. van Wees, "Electronic spin transport and spin precession in single graphene layers at room temperature," *Nature*, vol. 448, no. 7153, pp. 571–574, Aug. 2007.

[39] Y. Fukuma, L. Wang, H. Idzuchi, S. Takahashi, S. Maekawa, and Y. Otani, "Giant enhancement of spin accumulation and long-distance spin precession in metallic lateral spin valves," *Nat. Mater.*, vol. 10, no. 7, pp. 527–531, Jun. 2011.

[40] D. Venkateshvaran, M. Nikolka, A. Sadhanala, V. Lemaur, M. Zelazny, M. Kepa, M. Hurhangee, A. J. Kronemeijer, V. Pecunia, I. Nasrallah, I. Romanov, K. Broch, I. McCulloch, D. Emin, Y. Olivier, J. Cornil, D. Beljonne, and H. Sirringhaus, "Approaching disorder-free transport in high-mobility conjugated polymers," *Nature*, Nov. 2014.

[41] H. Sirringhaus, T. Sakanoue, and J.-F. Chang, "Charge-transport physics of high-mobility molecular semiconductors," *Phys. Status Solidi B*, vol. 249, no. 9, pp. 1655–1676, 2012.

[42] S. T. Hoffmann, H. Bässler, and A. Köhler, "What Determines Inhomogeneous Broadening of Electronic Transitions in Conjugated Polymers?," *J. Phys. Chem. B*, vol. 114, no. 51, pp. 17037–17048, Dec. 2010.

[43] P. J. Nigrey, A. G. MacDiarmid, and A. J. Heeger, "Electrochemistry of polyacetylene, (CH)x: electrochemical doping of (CH)x films to the metallic state," *J. Chem. Soc. Chem. Commun.*, no. 14, pp. 594–595, Jan. 1979.

[44] R. Menon, C. O. Yoon, D. Moses, A. J. Heeger, and Y. Cao, "Transport in polyaniline near the critical regime of the metal-insulator transition," *Phys. Rev. B*, vol. 48, no. 24, pp. 17685–17694, Dec. 1993.

[45] I. McCulloch, M. Heeney, M. L. Chabinyc, D. DeLongchamp, R. J. Kline, M. Cölle, W. Duffy, D. Fischer, D. Gundlach, B. Hamadani, R. Hamilton, L. Richter, A. Salleo, M. Shkunov, D. Sparrowe, S. Tierney, and W. Zhang, "Semiconducting Thienothiophene Copolymers: Design, Synthesis, Morphology, and Performance in Thin-Film Organic Transistors," *Adv. Mater.*, vol. 21, no. 10–11, pp. 1091–1109, Mar. 2009.

[46] S. Vasimalla, S. P. Senanayak, M. Sharma, K. S. Narayan, and P. K. Iyer, "Improved Performance of Solution-Processed n-Type Organic Field-Effect Transistors by Regulating the Intermolecular Interactions and Crystalline Domains on Macroscopic Scale," *Chem. Mater.*, vol. 26, no. 13, pp. 4030–4037, Jul. 2014.

[47] I. Meager, M. Nikolka, B. C. Schroeder, C. B. Nielsen, M. Planells, H. Bronstein, J. W. Rumer, D. I. James, R. S. Ashraf, A. Sadhanala, P. Hayoz, J.-C. Flores, H. Sirringhaus, and I. McCulloch, "Thieno[3,2-b]thiophene Flanked Isoindigo Polymers for High Performance Ambipolar OFET Applications," *Adv. Funct. Mater.*, vol. 24, no. 45, pp. 7109–7115, 2014.

[48] H. Sirringhaus, "25th Anniversary Article: Organic Field-Effect Transistors: The Path Beyond Amorphous Silicon," *Adv. Mater.*, vol. 26, no. 9, pp. 1319–1335, Mar. 2014.

[49] M. V. Fabretto, D. R. Evans, M. Mueller, K. Zuber, P. Hojati-Talemi, R. D. Short, G. G. Wallace, and P. J. Murphy, "Polymeric Material with Metal-Like Conductivity for Next Generation Organic Electronic Devices," *Chem. Mater.*, vol. 24, no. 20, pp. 3998–4003, Oct. 2012.

[50] P. W. Anderson, "Absence of Diffusion in Certain Random Lattices," *Phys. Rev.*, vol. 109, no. 5, pp. 1492–1505, Mar. 1958.

[51] O. D. Jurchescu, M. Popinciuc, B. J. van Wees, and T. T. M. Palstra, "Interface-Controlled, High-Mobility Organic Transistors," *Adv. Mater.*, vol. 19, no. 5, pp. 688–692, 2007.

[52] V. C. Sundar, J. Zaumseil, V. Podzorov, E. Menard, R. L. Willett, T. Someya, M. E. Gershenson, and J. A. Rogers, "Elastomeric transistor stamps: reversible probing of charge transport in organic crystals," *Science*, vol. 303, no. 5664, pp. 1644–1646, Mar. 2004.

[53] J. E. Anthony, J. S. Brooks, D. L. Eaton, and S. R. Parkin, "Functionalized Pentacene: Improved Electronic Properties from Control of Solid-State Order," *J. Am. Chem. Soc.*, vol. 123, no. 38, pp. 9482–9483, 2001.

[54] T. Uemura, Y. Hirose, M. Uno, K. Takimiya, and J. Takeya, "Very High Mobility in Solution-Processed Organic Thin-Film Transistors of Highly Ordered [1]Benzothieno[3,2-b]benzothiophene Derivatives," *Appl. Phys. Express*, vol. 2, no. 11, p. 111501, Nov. 2009.

[55] H. Bassler, Ed., *Charge Transport in Organic Semiconductors*, vol. 312. Berlin, Heidelberg: Springer Berlin Heidelberg, 2012.

[56] R. Noriega, J. Rivnay, K. Vandewal, F. P. V. Koch, N. Stingelin, P. Smith, M. F. Toney, and A. Salleo, "A general relationship between disorder, aggregation and charge transport in conjugated polymers," *Nat. Mater.*, Aug. 2013.

[57] C. Tanase, E. J. Meijer, P. W. M. Blom, and D. M. de Leeuw, "Unification of the Hole Transport in Polymeric Field-Effect Transistors and Light-Emitting Diodes," *Phys. Rev. Lett.*, vol. 91, no. 21, p. 216601, Nov. 2003.

[58] J. F. Dayen, V. Faramarzi, M. Pauly, N. T. Kemp, M. Barbero, B. P. Pichon, H. Majjad, S. Begin-Colin, and B. Doudin, "Nanotrench for nano and microparticle electrical interconnects," *Nanotechnology*, vol. 21, p. 335303, 2010.

[59] C. Etrillard, V. Faramarzi, J.-F. Dayen, J.-F. Letard, and B. Doudin, "Photoconduction in [Fe(Htrz)2(trz)](BF4)·H2O nanocrystals," *Chem. Commun.*, vol. 47, no. 34, p. 9663, 2011.

[60] V. Faramarzi, C. Raimondo, F. Reinders, M. Mayor, P. Samori, and B. Doudin, "Optically switchable molecular device using microsphere based junctions," *Appl. Phys. Lett.*, vol. 99, no. 23, pp. 233104–233104–3, Dec. 2011.

[61] M. Pauly, J.-F. Dayen, D. Golubev, J.-B. Beaufrand, B. P. Pichon, B. Doudin, and S. Bégin-Colin, “Co-tunneling Enhancement of the Electrical Response of Nanoparticle Networks,” *Small*, vol. 8, no. 1, pp. 108–115, 2012.

[62] J.-F. Dayen, E. Devid, M. V. Kamalakar, D. Golubev, C. Guédon, V. Faramarzi, B. Doudin, and S. J. van der Molen, “Enhancing the Molecular Signature in Molecule-Nanoparticle Networks Via Inelastic Cotunneling,” *Adv. Mater.*, vol. 25, no. 3, pp. 400–404, 2013.

[63] V. Faramarzi, F. Niess, E. Moulin, M. Maaloum, J.-F. Dayen, J.-B. Beaufrand, S. Zanettini, B. Doudin, and N. Giuseppone, “Light-triggered self-construction of supramolecular organic nanowires as metallic interconnects,” *Nat. Chem.*, vol. 4, no. 6, pp. 485–490, Apr. 2012.

[64] A. Ciesielski and P. Samorì, “Graphene via sonication assisted liquid-phase exfoliation,” *Chem. Soc. Rev.*, 2013.

2. Supramolecular Triarylamines NanoWires

Nowadays, high molecular weight conjugated polymers in the form of thin plastic films and vacuum-deposited molecular crystals (pentacene, rubrene, etc) are among the most promising Organic Electronics materials for optimal device performances. Unfortunately, conjugated polymers suffer of limited crystallinity (causing localization and low mobility), while single crystals are very unpractical to process. To possibly overcome these issues, supramolecular chemistry has been proposed as a promising tool for the design of new conducting organic compounds [1]. Supramolecular chemistry, unlike 'classical' chemistry, exploits weaker and reversible non-covalent interactions between molecules, such as hydrogen bonds and van der Waals forces.

One of the first approach to *supramolecular electronics* consisted in creating individual 1D wires of already known polymeric and oligomeric π-conjugated systems (e.g. polyaniline, polyacetylene, polythiophenes, etc). After those first attempts, many new supramolecular systems have been synthetized and have made supramolecular electronics apt to bridge the gap between single molecule electronics and bulk devices. A big advantage of supramolecular nano-interconnects is the possibility of controlling the self-assembly of the molecules, and possibly pre-determine their positioning in the circuitry by means of external stimuli (light, electric field, etc). The strategy of using external stimuli to obtain addressability makes supramolecular aggregates a very promising "bottom-up" alternative also to carbon nanotubes, whose main limitation is their difficult sorting (metallic versus semiconducting nanotubes) and positioning.

In this Chapter, we describe the self-assembly of supramolecular organic nanowires between two metallic electrodes, from a solution of triarylamine derivative molecules, under the simultaneous action of light and voltage triggers. They exhibit a combination of large conductivity values (> 3 S/cm) and low interface resistance (< $2 \cdot 10^{-1}$ $\Omega \cdot$cm). Moreover, the decrease of the device resistance when the temperature is lowered to 1.5 K is the fingerprint of an intrinsic metallic behavior. This is a spectacular experimental outcome; indeed, organic materials showing metallic behavior are very seldom in literature [2]. An electrolyte-gating attempt on the suspended supramolecular fibers will also be described in the last part of the Chapter.

2.1 Supramolecular electronics

In 2005, Schenning and Meijer introduced the concept of *supramolecular electronics* [1]. Supramolecular electronics can be considered as the domain of organic electronics which targets a length scale positioned between the one of organic films (plastic electronics - µm) and single molecules (molecular electronics - Å), as schematically represented in Figure 2.1. It aims at taking advantage of self-assembly strategies to construct organic nanostructures (nanowires, nanoribbons, nanotubes, nanobelts, and nanofibers) and to integrate them in miniaturized electronic devices. Supramolecular electronics rests on the use of supramolecular chemistry as a bottom-up approach for the design of conducting components at the 5 - 100 nm scale. The challenges in this field are both the construction

of the nanostructures displaying optimized transport properties and their precise connections to electrodes.

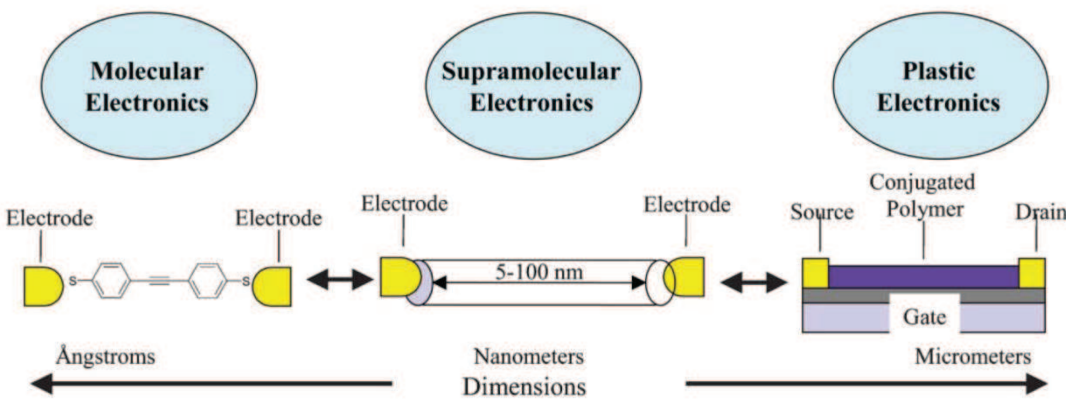

Figure 2.1 Schematic representation illustrating the gap between Molecular Electronics and Plastic Electronics, potentially filled by Supramolecular Electronics. Supramolecular electronics aims to construct and investigate supramolecular nanoarchitectures, hooked up to electrodes, in the 5 – 100 nm range. Reprinted from [1].

While traditional chemistry focuses on the covalent bond, supramolecular chemistry exploits the weaker and reversible non-covalent interactions between molecules. These forces include for example hydrogen bonding, metal coordination, hydrophobic forces, van der Waals forces, π-π interactions and electrostatic effects. This type of chemistry is notably inspired and trying to emulate biological processes, which very often rely on supramolecular forces.

2.1.1 1D structures from polydisperse π-conjugated polymers

Early approaches to supramolecular electronics relied on the fabrication of single fibers of polydisperse π-conjugated polymers, previously used in amorphous or thin film form. Some of the polymers able to give one dimensional structures are listed in

Figure 2.2(a): polyaniline, polyacetilene, polypyrrole, etc [1]. Beside those, also poly(3-hexylthiophene), P3HT, and poly(3,4-ethylenedioxythiophene), PEDOT, have been demonstrated to form nanofibers. An example of P3HT nanowires aligned by means of dropcasting in presence of an AC electric field is shown in Figure 2.2(b) [3]. The formation of 1D nanostructures from conventionally bulk polymers strongly relies on the use of special fabrication techniques. Template-assisted chemical synthesis, electrospinning, electrochemical or interfacial polymerization, flash welding or electrochemical dip-pen nanolithography (E-DPN), have been used to obtain single fibers.

The delocalization path for charge carriers in the one dimensional structure is constituted by the chain of sp^2 hybridized carbon atoms (σ-bonds + π-bonds), like in a typical π-conjugated polymer. By virtue of their high crystallinity, and often single-crystallinity, the 1D nanostructures have enhanced charge transport properties compared to polycrystalline or amorphous 2D thin films.

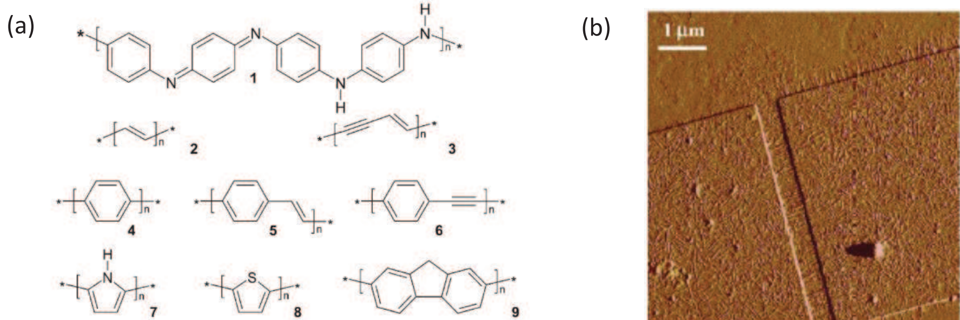

Figure 2.2 a) π-Conjugated polymers that can form nanowires: 1, polyaniline; 2, polyacetylene; 3, polydiacetylene; 4, poly(phenylene), PP; 5, poly(phenylene, vinylene), PPV; 6, poly(phenylene ethynylene), PPE; 7, polypyrrole, PPy; 8, polythiophene; 9, polyfluorene, PF. [1] b) AFM image of a device prepared by dropcasting a solution of P3HT in p-xylene applying an AC voltage (2 V, 102 kHz) resulting in aligned nanofibers [3].

2.1.2 1D structures from monodisperse oligomers or molecules (self-assembly)

In contrast to polydisperse π-conjugated polymers, a more novel approach is to use well defined oligomers (or molecules) as building blocks of stacked aggregates with perfectly tuned π–π interactions. We report in Figure 2.3 the example of self-assembled fibers of bisurea to illustrate the principle [4]. The authors insert functional entities, represented by “F” in Figure 2.3(a), in bisurea derivatives and exploit its ability to form multiple hydrogen bonds with neighboring molecules. In particular they choose a thiophene functionality (mono- or bi-thiophene, respectively n = 1 or n = 2, in Figure 2.3(b)) and they obtain elongated twisted fibers with a breadth of ~ 2 µm and lengths of tens of µm (Figure 2.3(c)). The thiophene moieties are π-stacked in the fibers and this leads to an efficient intermolecular charge transport, demonstrated by means of pulse-radiolysis time-resolved microwave conductivity (PR-TRMC) technique.

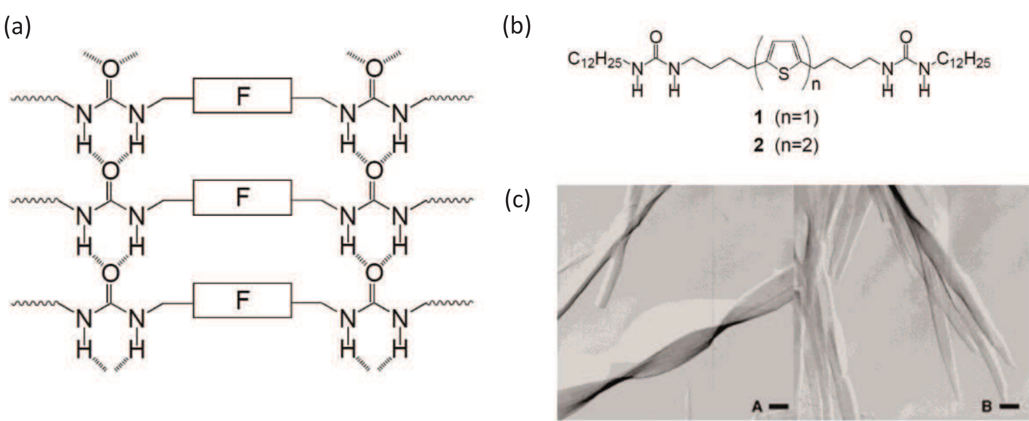

Figure 2.3 a) Representation of a ribbon of bisurea compound used for the spatial organization of functional entities F. b) Chemical formula of mono- and bithiophene bisurea. c) Electron micrographs of lamellar fibers obtained from mono- and bithiophene bisurea. The bar corresponds to 500 nm. Reprinted from [4].

After a decade of experimental developments, these concepts have proved to be of great interest for further implementations in nanotechnologies. Several other types of supramolecular

nanostructures have been created exploiting supramolecular bonds as clamps for the creation of electronic channels for free charge carriers. Detailed reviews already exist on the topic [5],[6],[7],[8].

The high conductivity of these molecular conductors originates from the π-stacked columnar structure of the donor/acceptor. Indeed, important challenges have now been addressed to improve the conductivity properties of these π-conjugated systems even more. Conductivity is enhanced by doping π-donors or π-acceptors with oxidants or reductants before/after the formation of such nanostructures, even though some nanofibers exhibit good electric conductivity in the neutral state, without any doping. One can also envision taking advantage of the intrinsic weak chemical bond specific to supramolecular chemistry, for example looking for self-healing molecular conductors. In the next paragraph we examine some examples of electrical characterization of these organic one-dimensional structures.

2.2 Charge transport properties of organic 1D nanostructures

The study of charge transport properties in soft supramolecular organic self-assemblies is of great interest for both practical and scientific reasons. On one hand, they represent a promising alternative route to low-cost and high performance organic electronics and nanoelectronics, consequently the investigation and continuous improvement of their electric performance is very important for technological applications. On the other hand, because of their more basic morphology compared to polycrystalline or amorphous thin films, studies on 1D organic nanostructures can provide a fundamental understanding of the intrinsic nature of charge transport, its limits, and structure/charge-transport relationship in organic semiconductors.

The main difficulty to get insight into the electrical properties of the supramolecular aggregates is the transfer to a solid substrate (if self-assembled in solution for example) and the connection to electrodes. The experimental methods applied to the study of the semiconductive properties of organic materials can be divided into different categories, mainly differing in the way charge carriers are introduced in the material:

a) DC and transient (Time-of-Flight) photoconductivity measurements [9].

   The material is irradiated with a light source to produce electron-hole pairs, while an electric field is applied. The electric field drifts the single charge carriers, while conductivity is measured. For DC photoconductivity the light is kept on and current is measured as a function of temperature or electric field. In transient measurements, photocurrent is induced with laser pulses and measured as a function of time at a certain distance from the irradiation zone. Charge carrier mobility is deduced by time-of-flight (TOF) experiment.

b) Measurement of the current/voltage characteristics in charge injection devices.

   Charge carriers are injected in the organic material from metallic electrodes, which act as charge reservoirs. Mobility can be extracted if a gate field effect is also applied to the device. Attention must be paid to contact-limitations due to difficult charge injection.

c) Pulse radiolysis time-resolved microwave conductivity (PR-TRMC) [10],[11].

   Mobile charge carriers are created in the organic material with a short pulse of high-energy radiation. The high penetrating power of the radiation makes it possible to uniformly ionize samples several millimetres thick irrespective of their color, chemical composition, and morphology. A change in the conductivity of the medium resulting from the radiolytic formation of mobile charge carriers is measured as a change in the power level of microwaves

which propagate through the sample. Knowing the energy deposited in the sample (measured by dosimetry), the maximum concentration of charge-carrier pairs formed during the pulse can be estimated with reasonable accuracy. This allows in turn estimates to be made of the minimum value of the sum of the charge-carrier mobilities from the end-of-pulse conductivity. The actual value of the mobility is expected to be no more than an order of magnitude higher than this minimum value.

Methods a) and b) require the preparation of a thin layer of the organic material to which electrode contacts must be applied. Conversely method c), the PR-TRMC technique, circumvent the problems associated to DC conductivity techniques by measuring the formation of mobile charge carriers (by exposure to high-energy radiation) as a change in the power level of microwaves which propagate through the sample. The main advantage of pulse radiolysis time-resolved microwave conductivity is that it permits a direct comparison of a variety of materials, for instance between the two main categories of 1D nanostructures presented in the previous paragraph, π-conjugated polymers and π-π stacked discotics.

We focus here on the current/voltage characteristic measurements, since we will use this technique to create and characterize our supramolecular triarylamines nanowires. Current/voltage studies consist in collecting I-V curves in two-electrode geometry in order to extract the conductivity σ of the organic material; gate field-effect measurements can also possibly be used to estimate the charge carriers mobility μ. Two representative examples from literature are reported in Figure 2.4. As above mentioned, one should be aware that charge injection/extraction of the organic layer at the metal electrodes is limited by metal/organic contact resistance. For this reason, conductivity and mobility values measured with current/voltage characterization methods are usually underestimated respect to the ones obtained by contactless spectroscopic techniques.

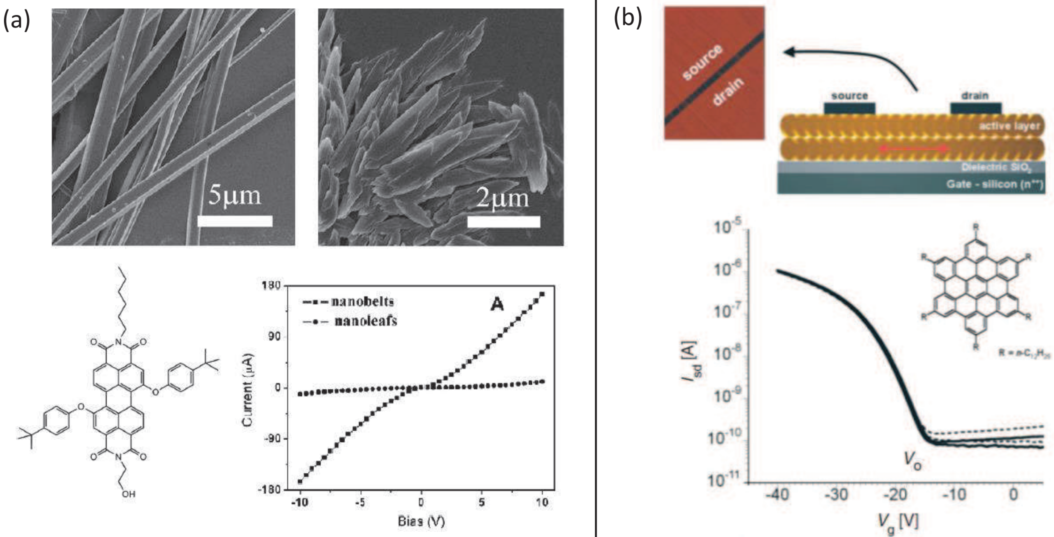

Figure 2.4 Examples of current/voltage characteristic measurements on supramolecular structures. a) Self-assembly of amphiphilic perylenetetracarboxylic diimide derivative under the form of nanobelts (in methanol, left) and nanoleaves (in n-hexane, right) and relative I-V curves taken in a bottom-contact two-terminal device. From Chen *et al*. [12]. b) Bottom-gate top-contact device for the characterization of hexa-*peri*-hexabenzocoronene (HBC) thin films. From Pisula *et al*. [13].

Chen *et al*. [12] report the self-assembly in solution of an amphiphilic perylenetetracarboxylic diimide derivative, creating nanobelts and nanoleaves structures, in Figure 2.4(a), depending on the

solvent used. The nanostructures already formed have been drop-casted on ITO interdigitated electrodes with 75 µm channel length. A conductivity value of $3.3 \cdot 10^{-3}$ S/cm and $1.2 \cdot 10^{-4}$ S/cm has been calculated from the I-V curves for nanobelts and nanoleaves respectively. The very good conductivity of the nanobelts is attributed to the long-range 1D π–π stacking structure that favors the conductivity through face-to-face intermolecular π-delocalization. Charge carrier mobility cannot be extracted using a two-terminal device.

A different device configuration has been adopted by Pisula *et al*. [13] who performed the deposition of a hexa-*peri*-hexabenzocoronene (HBC) derivative by zone-casting (solution spread by a nozzle onto a moving substrate) onto Si/SiO_2 substrates, followed by evaporation of top-contact gold electrodes, with channel length of 25 µm, in Figure 2.4(b). The as-obtained FETs show a very good on/off ratio of 10^4 and a field-effect mobility of $5 \cdot 10^{-3}$ $cm^2/V \cdot s$ in the saturation regime.

In both cases the electronic transport has been found to be improved with respect to the thin film form of the same material. The main reason is that a self-organized material presents likely a very low number of structural imperfections and in theory no impurities, thus defect-scattering of charge carriers moving through is lowered.

Despite their immense potential, the charge transport properties of these supramolecular low-dimensionality interconnects are still not exceptional and considerable efforts needs still to be done to enhance their electrical conductivity. Ultimately, achieving metallic conductivity combined with controlled positioning of these soft organic self-assemblies between electrodes remains an enormous challenge.

2.3 Self-assembly process of triarylamines molecules in solution

A recently discovered class of supramolecular 1D structures (not described in previous paragraphs) derives from triarylamine-based molecules. Triarylamine derivatives are known as hole transporting components used in organic light emitting diodes (OLEDs). Being photoactive species, they have also been incorporated as dyes in dye-sensitized solar cells (DSCs) [14] and used in xerographic process for photocopiers and printers [15]. In these applications, triarylamines are in the form of amorphous molecular materials.

In 2010 our collaborators Moulin *et al*. [16] observed that various triarylamine derivatives are able to self-assemble in solution upon light stimulation and to form one dimensional nanowires. The different triarylamine derivatives synthesized by Moulin *et al*. are shown in Figure 2.5(a). The authors observe a different ^{1}H-NMR (proton nuclear magnetic resonance) spectrum after irradiating the solution to visible light for few minutes (for compound **1** in Figure 2.5(b), A$\rightarrow$B) and the initial spectrum reappears after heating overnight at 60°C (B$\rightarrow$C). The change in ^{1}H-NMR spectra is accompanied by a color change of the solution, from light yellow to light green after exposure to light. A change in the UV/Vis-NIR absorption spectrum after light irradiation reveals the production of a small quantity of triarylammonium radicals ($\mathbf{1}^{\bullet+}$). To quantify the number of radicals, Electron Spin Resonance (ESR, or Electron Paramagnetic resonance, EPR) spectroscopy is performed on the solution before and after irradiation. ESR confirms the presence of a radical species, likely localized on the nitrogen atom of the triarylamine molecule, after light irradiation and the quantitative evolution of the number of spins is reported in Figure 2.5(c). Point A presents the state of the solution before visible light excitation; after white light irradiation (from A to B), the number of triarylammonium radicals is roughly 10 % of the total number of molecules. From B to C the amount of radicals was recorded as a function of time in the dark: a very smooth decay is observed on a period of 16 h asymptotically leading to a plateau of 6

radicals per 1000 triarylamines molecules (0.6 %). The heating of the solution at point C causes the destruction of the stabilized radicals and brings back the solution to initial state.

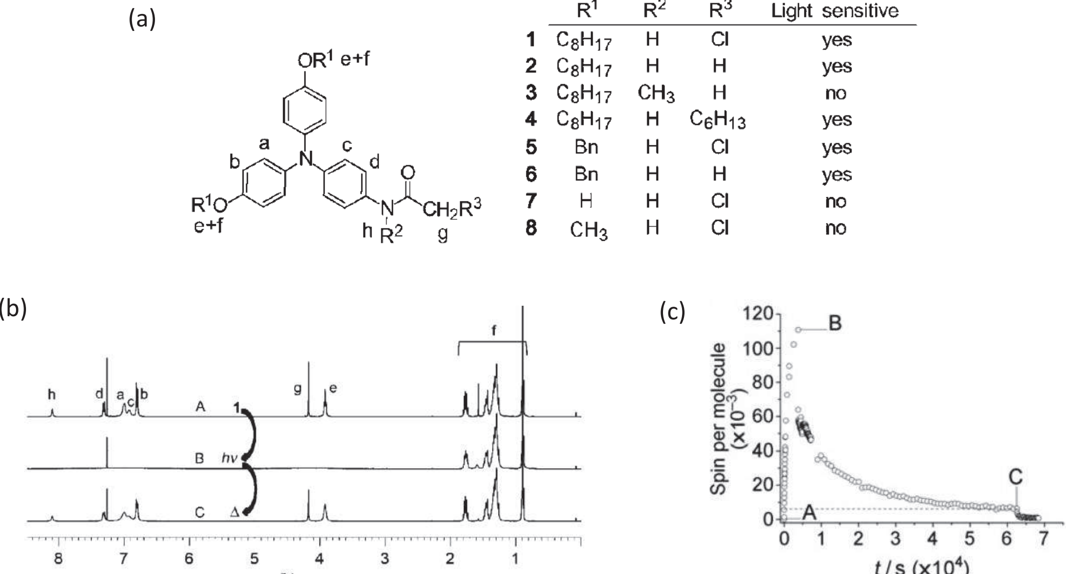

	R^1	R^2	R^3	Light sensitive
1	C_8H_{17}	H	Cl	yes
2	C_8H_{17}	H	H	yes
3	C_8H_{17}	CH_3	H	no
4	C_8H_{17}	H	C_6H_{13}	yes
5	Bn	H	Cl	yes
6	Bn	H	H	yes
7	H	H	Cl	no
8	CH_3	H	Cl	no

Figure 2.5 a) Structures of the triarylamines derivatives synthesized by Moulin *et al*. (1-8). b) ^1H NMR spectra of species 1 (A) immediately after purification, (B) after 10 min exposure to visible light and (C) after subsequent heating overnight at 60°C, demonstrating the formation and dissolution of supramolecular structures. c) Quantitative ESR data, as a function of time, showing the evolution of the ratio of the triarylammonium radical $1^{\bullet+}$ over neutral 1: without visible light excitation at RT (point A); upon visible light excitation (A→B); in the absence of light at RT (B→C); and after subsequent heating (60°C) in the dark (from C). Reprinted from [16].

The very low concentration of radicals at equilibrium and their unusual long stability, together with the ^1H-NMR spectra features after light irradiation, support the hypothesis that the radicals self-associate with their neutral counterparts (normal triarylamine molecules) in order to delocalize their charge in excess and find more chemical stability. Chlorinated solvents appear to be necessary to initiate the oxidation of the triarylamine to its radical form (the reaction transfers one electron to the solvent molecule and liberates Cl^- counterions).

Atomic Force Microscopy is used by Moulin *et al*. to confirm the presence of the hyphotesised supramolecular structures. The irradiated green solution is dried on a substrate and imaged. Fibrillar 3D aggregates are observed, characterized by a “corn-like” surface enlighted by high resolution AFM images, in Figure 2.6(a). The structures are 10-50 nm in width and 50-1000 nm in length, clearly composed by bundles of smaller 1D fibers strongly packed in a concentric-layer organization. Combining AFM images and computer modelling the most probable structure is the one depicted in Figure 2.6(a), where along the 1D fiber triarylamines are rotated 120° one respect to the other (“snowflake”) in order to minimize the steric hindrance of the aromatic rings. In this configuration inter-stack hydrogen bonds (red lines in the picture) are formed between triarylamines of neighbouring fibers. H-bonds are likely the most effective source of lateral attraction between different stacks.

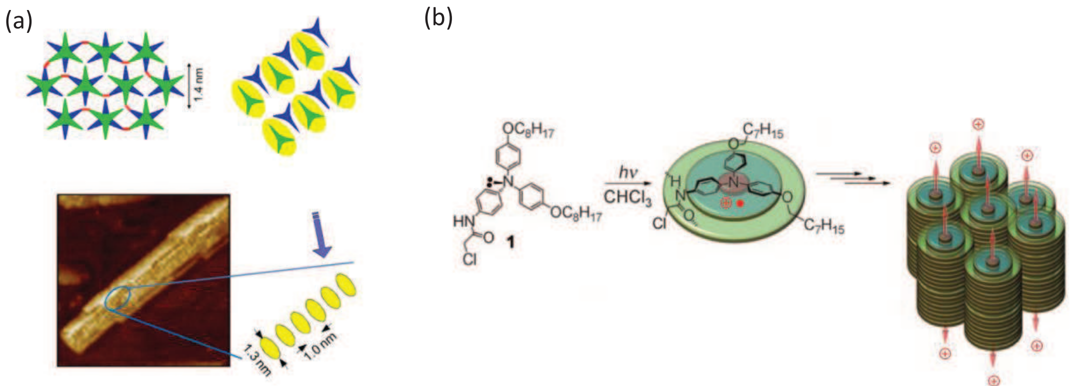

Figure 2.6 a) “Snowflake” molecule arrangement within the triarylamine multi-stack structure: green and blue are differently oriented neighbouring triarylamines within the stack, H-bonds can connect differently colored molecules only, the positions of H-bonds are shown by red segments. Bottom: Corn-like multi-stacked structure observed by AFM. b) Schematic illustration of the light-triggered self-assembly process.

In conclusion, the self-assembly process can be described as illustrated in Figure 2.6(b). An electron transfer occurs between light-excited triarylamines and the solvent, producing a small amount of triarylammonium radicals. In this electronic configuration, the charge transfer to neutral triarylamines and various supramolecular interactions (π-π stacking, H-bonds) initiate the self-assembly of 1D supramolecular polymers which combine to produce larger 3D fibers. Moulin and coworkers assume that one radical (one charge) is sufficient to stabilize the stacking of 160 triarylamine units along the axis of the self-assembled wire. It must be noted that the π-π stacking leading to delocalization of the radical charge along the fiber is located in the “center” of the wire, and the insulating lateral groups spatially separate the conduction channel from the solvent.

EXPERIMENTAL

2.4 Self-assembly of triarylamines between metallic electrodes

In this experiment, we want to trap Supramolecular Triarylamine NanoWires (STANWs) in between metallic electrodes with the aim of probing their transport properties. The strategy for trapping them between metallic contacts inherently exploits their ability of self-construction in solution.

The first successful realization of STANWs self-assembly between metallic electrodes has been carried out by Dr. Vina Faramarzi, previous PhD student in our group. The results of this experiment have been published in the article "Light triggered self-construction of supramolecular organic nanowires as metallic interconnects", V. Faramarzi *et al.*, Nat. Chem., 4, Apr. 2012 [17].

2.4.1 Description of the self-assembly experiment

Nano-sized gaps are fabricated by edge-mediated optical lithography on Si/SiO_2 substrates, as described in Appendix A. Gap length is L ~ 80 nm and gap width ranges between 10 µm < W < 100 µm. Owing to the very high aspect ratio (W/L), we call this type of samples "nanotrenches". Every sample is a 2.5*2.5 mm square containing seven nanotrenches, Figure 2.7(a); each nanotrench is connected by four metallic pads, Figure 2.7(b).

(a)

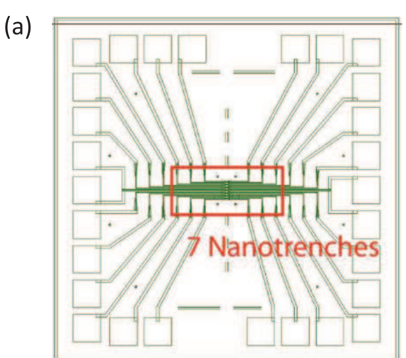

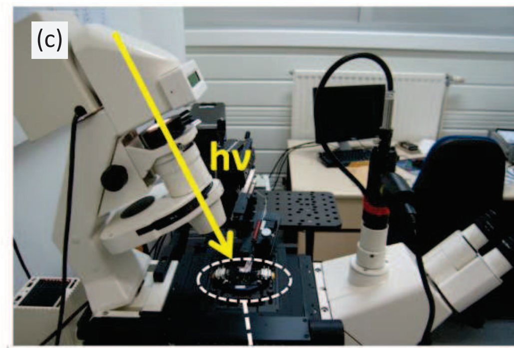

(b)

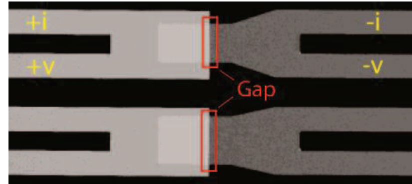

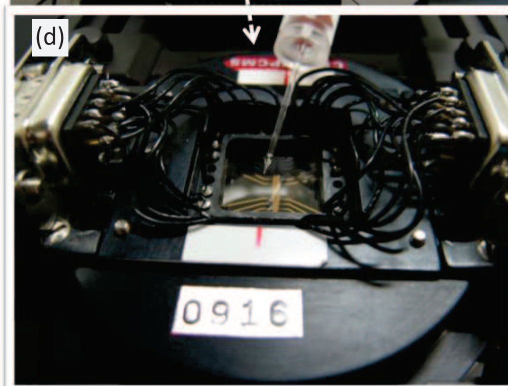

Figure 2.7 a) Plan of the 2.5*2.5 mm sample, containing seven nanotrenches (in the center) and connection pads. b) SEM image of the four pads connecting each gap and possible 'pseudo' four-probe measurements. c,d) Photograph of the inverted microscope set-up used for light irradiation (c) and of a sample placed inside the sample-holder (d). Sample holder has an aperture to permit light irradiation of the central nanotrenches zone.

The sample is positioned in a dedicated sample holder mounted on a set-up for simultaneous electrical and optical probing. We first immerse the nanotrench in a solution of triarylamine (compound 1) in 1,1,2,2-tetrachloroethane (1 mg/mL) carefully kept in the dark before the experiment. The solution drop-casting on the substrate is carried out in a dark room. A photograph of the inverted microscope set-up for light irradiation and of the sample (inserted in the sample holder) just before drop-casting are respectively shown in Figure 2.8(c) and (d).

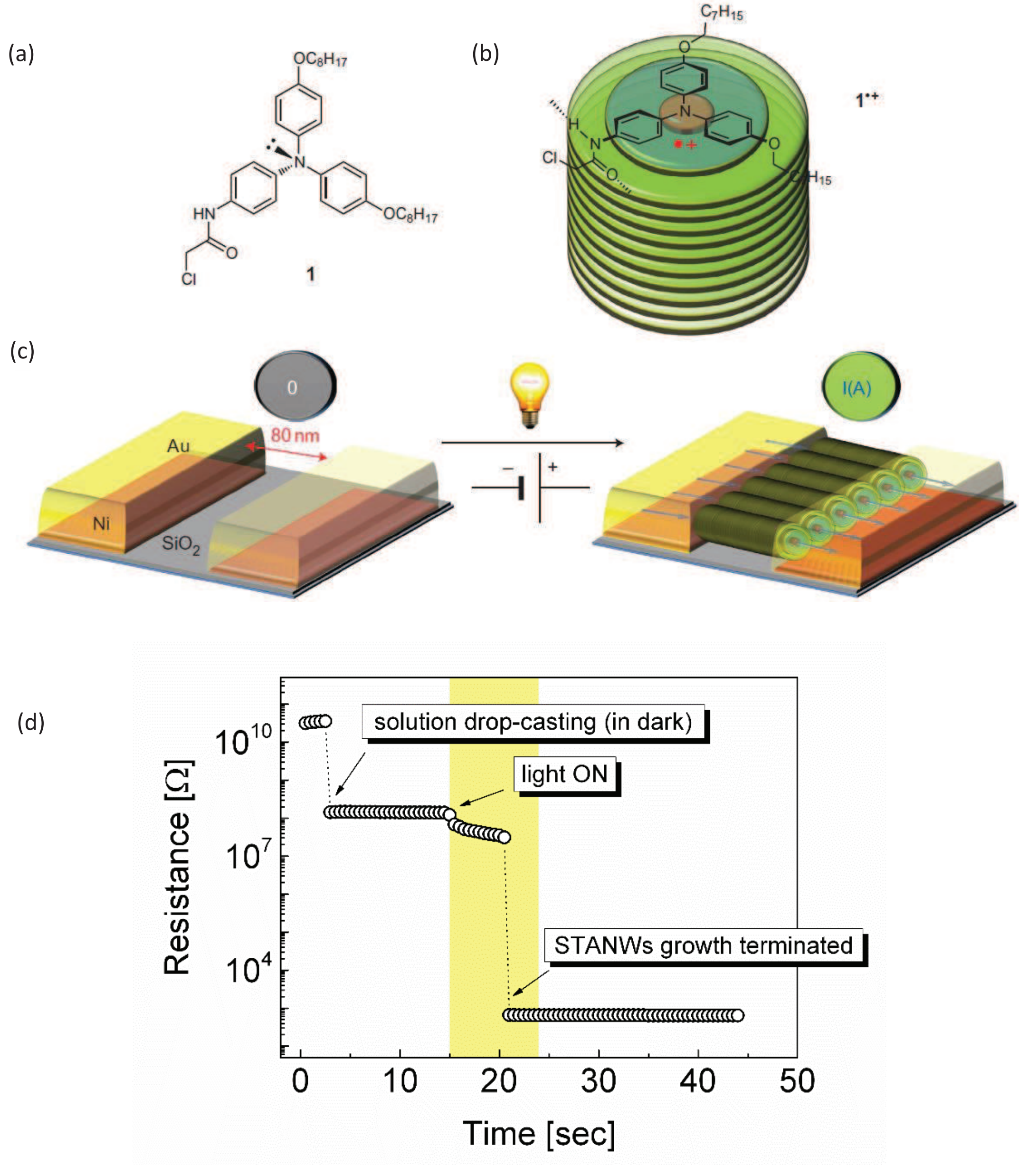

Figure 2.8 Self-assembly process between electrodes. a) Specific triarylamine used for self-assembly experiments between electrodes (1 mg/ mL in $C_2H_2Cl_4$). b) Piling up of the molecules along the assembly. c) Triggered self-construction process for STANWs in the nanotrench geometry: after solution drop-casting in the dark, the device is submitted to white light irradiation and contemporary electric field between electrodes. This results in fibers aligned in the direction of the electric field and strongly connecting the two electrodes. d) Electrical track of the self-assembly process (V_{sd} = +1 V).

A DC bias of few hundreds millivolt is applied between the two Ni/Au electrodes situated 80 nm apart, Figure 2.8(c). Tetrachloroethane is intentionally chosen among chlorinated solvents for its high boiling point (146.5°C), in order to slow down the drop evaporation. While keeping the bias voltage constant (and meanwhile measuring the current as a function of time), the sample is irradiated with a white light (halogen lamp) of 10 W/cm^2 power density. Infrared filter is present on the light path to limit the sample heating to few degrees. The irradiation time is 10 seconds. As described in paragraph 2.3, light irradiation of triarylamine molecules **1** results in the formation of a catalytic quantity of triarylaminamonium radicals $\mathbf{1}^{\bullet +}$ that to the supramolecular polymerization of the fibers aligned between the electrodes, Figure 2.8(c).

In Figure 2.8(d), all the steps of the self-assembly process are visible in the electric signal trace. The first decrease of resistance from 10^{10} Ω to 10^8 Ω corresponds to the wetting of the electrodes in the solution (in the dark), probably due to leakage current related to Cl^- and H^+ ions of the solvent. Switching on the light stimulus immediately translates in a small resistance reduction, corresponding to the formation of triarylamonium radicals and self-assembly process starting. 5 to 10 seconds later, when STANWs growth terminates with the bridging of the two electrodes, a six orders of magnitude drop in resistance occurs! The final two-probe total resistance value is normally around 1 kΩ. By subtracting the metallic pads in series, we obtain a resistance of the system metal/STANWs/metal ranging between 50 Ω and 200 Ω. The measured current can easily attain values in the milliAmpere range, sometimes reaching the compliance level set in the instrument.

I-V curves are taken at the end of the self-assembly process to confirm the gap closure and the stability of the self-assembly. One typical I-V curve is reported in Figure 2.9. The resistance value indicated as R_{4p} is not a “real” four-probe (i.e. it is not contact-resistance-free): it just refers to the source/STANWs/drain resistance subtracted of the connection pads resistance. The I-V curve shows perfect ohmicity of the system.

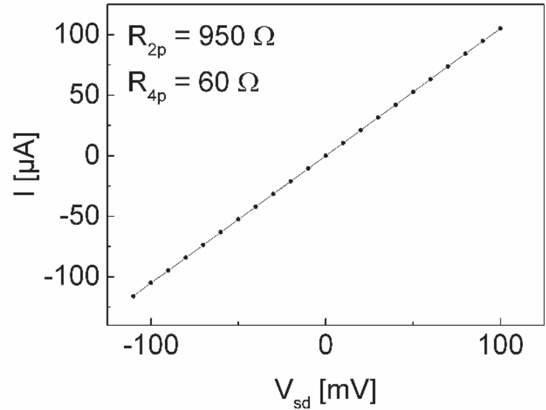

Figure 2.9 I-V ohmic characteristic of a gap filled with STANWs after rinsing with acetone and ethanol. R_{2p} and R_{4p} represent the total device resistance respectively with and without the metallic pads resistance in series (~900 Ω, for this specific gap).

We believe that a difference exists between self-assembly in solution and self-assembly between electrodes: in the first case radicals initiate the supramolecular polymerization by stacking with neutral triarylamines molecules ([16], paragraph 2.3), while in our experiment radicals are likely just protagonist. They are probably first attracted to the gap, the first radical anchors to the metal surface and discharge to it; successively, other radicals arrive and pile-up one after the other in a self-limiting

process terminating on the second electrode. The assembly between electrodes probably does not involve neutral triarylamines.

The electronic situation of a free-standing fiber is indeed very different from the one of a fiber attached to metal leads. Moulin and coworkers found out that 1 radical (1 charge) is delocalized over 160 triarylamines molecules when the nanowire is in solution. A nanowire chemically linked to the metal electrodes shares with it its electronic wavefunctions, thus charge carriers in STANWs bridging electrodes are in direct contact with the electrons reservoir of the metal.

According to computer simulations and high-resolution AFM images, the molecule density along the 1D nanowire is roughly two molecules per nanometer. This means that around 160 molecules (radicals) are needed to construct one single fiber bridging the two electrodes 80 nm apart.

2.4.2 Imaging STANWs inside nanotrenches

The devices can be rinsed after self-assembly with acetone/ethanol or chlorinated solvents and successively dried with a nitrogen flux without disruption of the fibers in the gap.

We find that AFM is the best-suited technique for imaging STANWs inside the gap. After rinsing, samples were given to our collaborator M. Maaloum and imaged. Images are shown in Figure 2.10. The AFM probes used are very sharp (< 10 nm curvature radius) and made from monolithic silicon, highly doped to dissipate static charge. Note that the topography of the sample makes the AFM imaging very challenging.

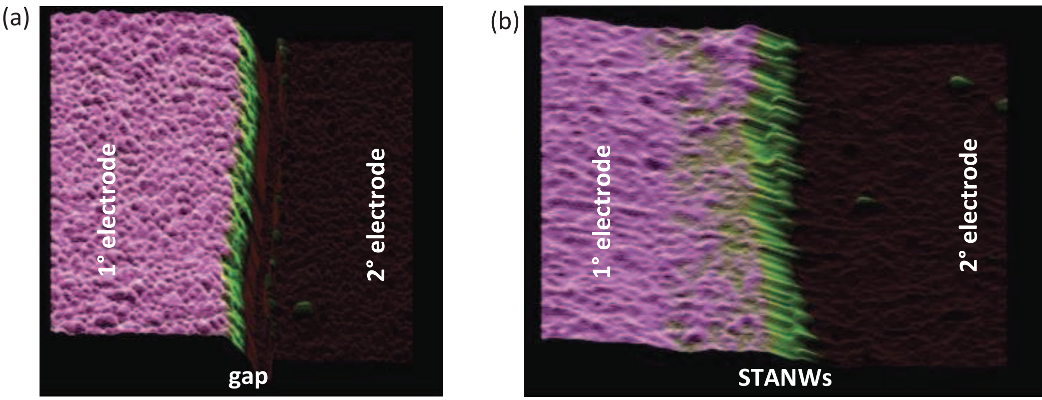

Figure 2.10 Topography of the open gap before light irradiation (a) and after light irradiation, filled with STANWs (b).

AFM imaging of the gap reveals the presence of wires similar to those observed in solution (paragraph 2.3, [16]) but with shorted length in order to match exactly the electrode gap. They are oriented inside the gap with homogeneous diameters of 12 ± 2 nm. STANWs diameters are measured taking into account the convolution of the image by the AFM tip during the imaging process. Not all the fibers are touching both electrodes: as shown by Figure 2.11, some STANWs grow just half of the gap. In general, the resolution of AFM images is considerably reduced because the two electrodes have different heights (different metal thickness, $\Delta h = h_1 - h_2 \sim 50$ nm) and the fibers make a high angle with the surface.

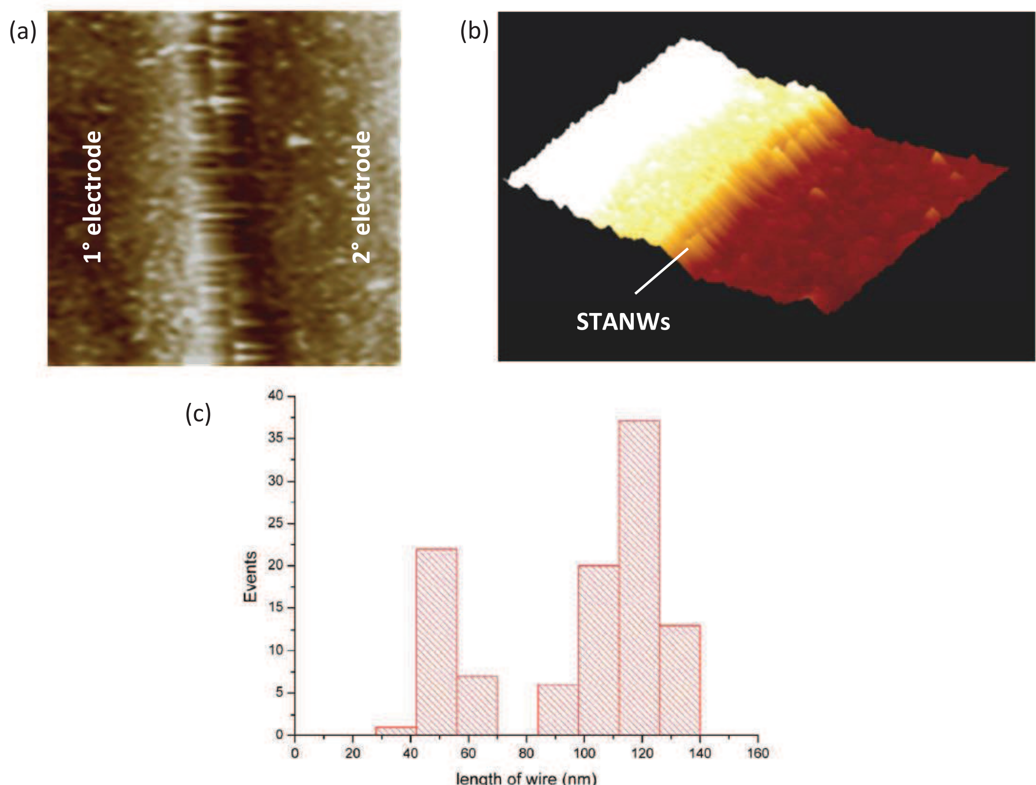

Figure 2.11 a) AFM image of the closed gap with STANWs (surface scale 500x500 nm^2). b) Topography extracted from image (a). c) Bimodal length distribution of STANWs. Short length average distribution (~ 50 nm) is due to residual non-connecting wires at the surface. Long length average distribution matches the gap length.

Extensive imaging by Scanning Electron Microscopy (SEM) has also been performed on closed gaps to check the status of electrodes (corrosion, metallic shortcuts, etc). Unfortunately STANWs do not show enough contrast at SEM to be able to see the fibers in the gap, Figure 2.12 (a,b). This is not fully surprising since SEM is not optimized for detection of light atoms structures. The same gap imaged with AFM was found to be filled with nanofibers, Figure 2.12(c). Applying a too high force to the AFM tip during imaging can cause breaking of the fibers, as it happened for Figure 2.12(d).

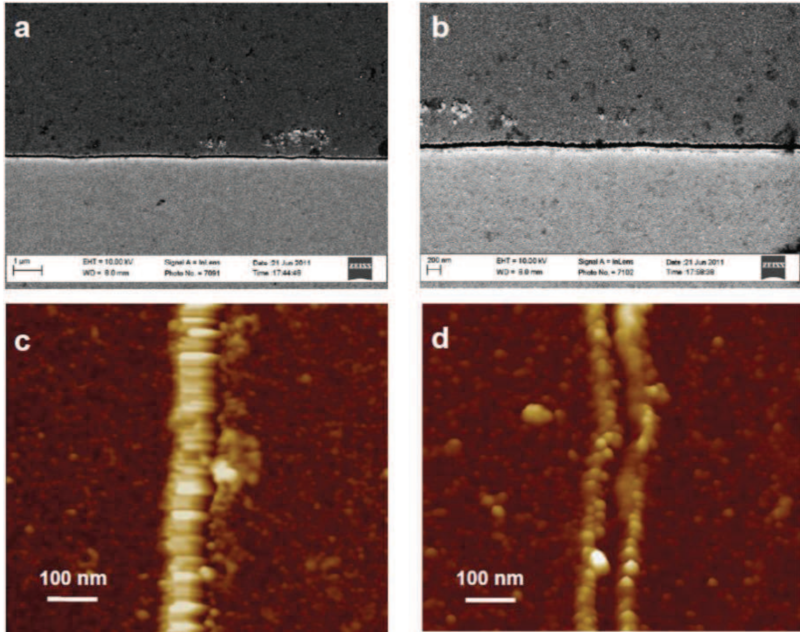

Figure 2.12 SEM (a,b) and AFM (c) imaging of a nanotrench filled with STANWs, characterized by a four-probe resistance of 50 Ω after rinsing. Evidently in the SEM images no fibers can be detected, while AFM clearly shows their presence. To take images like (c), AFM applied force value is maintained weak to preserve STANWs; a slight increase in the applied force value causes the destruction of the suspended nanofibers bridging the electrodes, as happened in (d).

2.4.3 A closer look on the self-assembly process

In this paragraph we focus on the external stimuli needed for the self-assembly process to happen, a combination of the correct photon energy, the application of a voltage potential and the presence of a strong magnetic field gradient.

2.4.3.1 Light source

Necessary condition to trigger the self-assembly process is that the spectrum of the light source matches the absorbance of neutral triarylamines. Figure 2.13(a) reports the absorbance spectrum of the triarylamines in chloroform solution; the arrows indicate the evolution of peaks intensity as a function of time [16]. The highest absorbance peak centered at 300 nm is the one associated to the formation of triarylamonium radicals.

The standard irradiation source for the self-assembly experiment is a halogen lamp, whose spectrum, zoomed in the zone of interest ($\lambda \sim 300$ - 400 nm), is shown in Figure 2.13(b) (blue line). A halogen lamp mainly emits in the visible range ($\lambda \sim 400$ - 700 nm), but the vanishing tail of its spectrum towards the ultraviolet (UV) frequencies is sufficient to trigger the production of enough triarylamonium radicals for STANWs formation. We find out that the weak intensity of the halogen lamp UV tail is actually better than irradiating with a strong UV source, mainly because it avoids electrodes corrosion. Self-assembly tests carried out with a 380 nm light emitting diode (red line in Figure 2.13(b), detector saturated) showed very unstable and irreproducible gap closure.

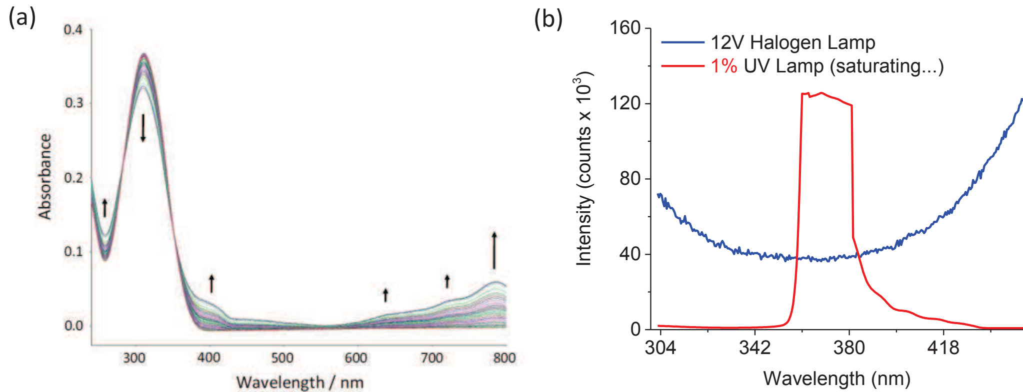

Figure 2.13 a) UV-Vis-NIR spectra obtained as a function of time of irradiation (indicated by arrows) for an initial 0.1 mM solution of triarylamines in chloroform. b) Spectra of the two light sources tested for self-assembly: blue, UV tail of halogen lamp; red, 380 nm LED (detector saturated).

2.4.3.2 Presence of a magnetic metal in the electrodes

For historical reasons related to a previous project on microspheres magnetic trapping, the typical electrodes for self-assembly experiments are made of thin film tri-layers of titanium (5 nm), nickel (35 nm) and gold (20 nm). Using this metal combination, self-assembly process between electrodes is almost 100 % successful. Later, we discover that self-assembly does not occur between electrodes made of gold or platinum only. The presence of a nickel layer (or likely, of some magnetic metals in general) seems to be a necessary condition for successful interconnects formation.

Our explanation is that the presence of a magnetic metal (Ni, Co or Py) creates a favorable magnetic gradient force for the attraction of the triarylamonium radicals inside the nanogap. The triarylamonium radical is indeed paramagnetic (because of its unpaired electron), and paramagnets are by definition attracted towards region of larger magnetic field intensity. The force attracting the radicals is proportional to the magnetic field intensity H and to its gradient ∇H. The magnetic field H is scale-independent, therefore the gradient increases linearly when reducing the size of the sample. We speculate that, because our electrodes have nanoscale dimensions, the magnetic gradient force on the radicals is high enough to influence the equilibrium of the chemical reaction related to STANWs formation. The influence of magnetic fields ionic flows or reaction rates has been already demonstrated and is studied in the field of magnetoelectrochemistry.

Nanotrenches with asymmetric magnetic electrodes of cobalt (Co) and permalloy (Py) have also been fabricated by e-beam lithography, without the gold upper layer. Self-assembly between magnetic-only electrodes is meant to test STANWs in a lateral spinvalve device. Unfortunately, experiments showed that the stability of the supramolecular fibers between Co-Py and Ni-only electrodes was often too short in time to allow spinvalve tests. Roughly, we carried out at least 40 tentative self-assembly between magnetic-only electrodes, resulting in 10 STANWs-filled gaps stable enough to be measured in the cryostat. Over these ten, just one showed a small magnetoresistance signal, which however could not be unequivocally identified as a spinvalve signal. The partial instability of STANWs between magnetic-only electrodes reveals that the gold layer plays an important role in the interconnect formation, likely being responsible for a more robust connection with STANWs. The selectivity of STANWs to the anchoring surface could be a big limitation for the use of this material in Organic Spintronics.

2.4.3.3 Threshold voltage potential

Standard experiments reveal that a threshold voltage of +0.8 V at the drain electrode is needed to successfully perform the self-assembly process. One should consider that the two electrodes are immersed in solution during self-assembly. The ions and molecules in the solution thus screen the electrode potential. This screening is total after a certain distance away from the electrode surface, which is normally few nanometers (Helmholtz layer).

To better explore the importance of the voltage needed at the electrode, we perform some electrochemistry experiment with the help of a bipotentiostat. A simple potentiostat functions by maintaining the potential of the working electrode (WE) at a constant level with respect to a reference electrode (RE); it does that by adjusting the current at an auxiliary electrode, called counter-electrode (CE). A bipotentiostat is able to control the potential of two working electrodes, WE(1) and WE(2), respect to the reference. We insert a platinum electrode in the triarylamine solution as reference electrode and we connect source and drain electrode as working electrode 1 and working electrode 2. The counter electrode is another side metallic pad present on the substrate. This 'pseudo' electrochemical cell is illustrated in the inset of Figure 2.14. In this way we are sure of the absolute value of the voltage we apply to both source and drain electrodes. First we shine light (10 s) to produce triarylamonium radicals, then we start to apply an increasing voltage difference between WE(1) and WE(2), $\Delta V_{WE(1)\text{-}WE(2)}$. Figure 2.14 shows the outcome of the bipotentiostat experiment, reporting the potential difference applied $\Delta V_{WE(1)\text{-}WE(2)}$ on the top and the corresponding current measured on the bottom. $\Delta V_{WE(1)\text{-}WE(2)}$ is imposed by keeping WE(2) at 0 V and gradually incrementing the WE(1) potential.

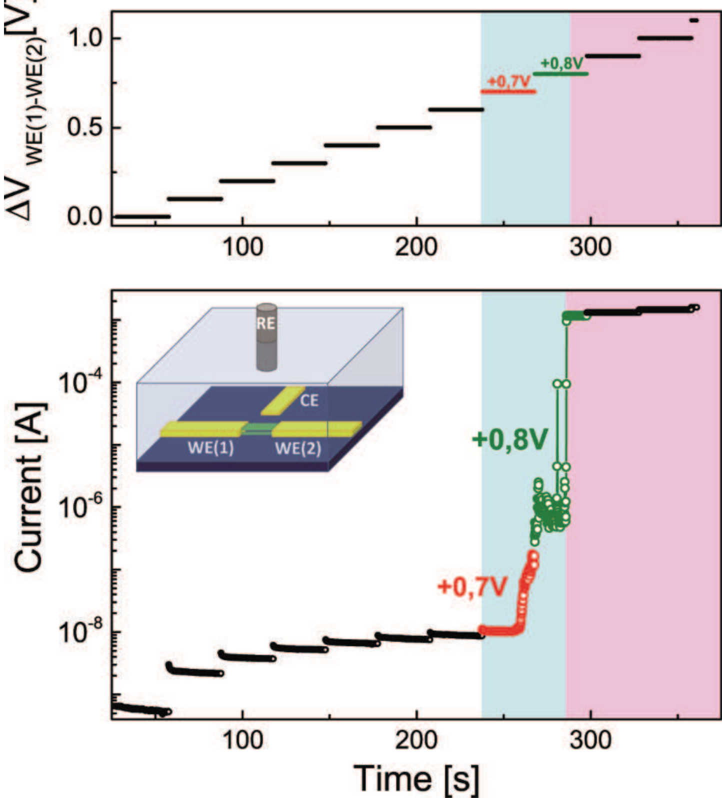

Figure 2.14 Self-assembly process conducted using a bipotentiostat as voltage potential source. Source (working electrode 2) is kept at 0 V respect to the Pt reference. Drain (working electrode 1) potential is increased step by step. Gap closure occurs in correspondence of a voltage difference equal to 0.7 – 0.8 V.

A steep increase of current starts at +0.7 V and finishes at +0.8 V, corresponding to the self-assembly process taking place. The experiment confirms the need of a +0.8 V, as observed for self-assembly experiment carried out with a simple sourcemeter.

We perform a second experiment in which the potential difference $\Delta V_{WE(1)-WE(2)}$ is maintained constant and below |0.7 V|, and WE(2) shifted respect to RE in an electrochemical window of ± 1 V. The fact that such experiment does not produce any self-assembly means that the process is not related to any electrochemical redox reaction happening at some specific potential. We also observe successful occurrence of self-assembly by applying a negative voltage to WE(1). In correspondence of -0.8 V on WE(1) and 0 V on WE(2), the usual current jump is detected (plot not shown here). This confirms that redox reactions are not involved in the anchoring of STANWs to the metal electrodes, otherwise the process would not work for both voltage polarities.

We believe that a high enough voltage difference is needed between the electrodes in order for the radicals to preferentially anchor to one electrode or the other (and start growing fibers). The local electric field acts in combination to magnetic field: the latter increases the residence time of triarylamonium radicals in the gap zone, and the first preferentially drives them on one of the two electrodes. Additionally, Petach *et al*. [18] found indications of a potential of zero charge around +0.8 V for a thin film of Au. The point of zero charge is a concept relating to the phenomenon of adsorption, and it describes the condition when the electrical charge density on a surface is zero. This could be another possible reason for the augmented affinity to the electrode manifesting at $|\Delta V_{WE(1)-WE(2)}| = 0.8$ V.

As further confirmation of the combined action of voltage and magnetic field gradient, we could manage to self-assembly at a lower voltage potential (+0.3 V) by approaching a 0.8 Teslas permanent magnet to the sample, i.e. applying an external magnetic field H. In fact, micromagnetic simulations performed by our collaborators R. Hertel and C. Andreas (in the context of another experiment with Nickel ions in solution, [19]) demonstrate that an enhanced attractive force towards the center of the gap is created when electrodes are magnetized along their long axe, Figure 2.15(a). The simulation is shown in Figure 2.15(b). The strong gradient ∇H is due to the nanometric size of the electrodes. The application of H in the direction of Figure 2.15(a) promotes the self-assembly process respect to the situation of zero external magnetic field, in which the Ni magnetic layer is randomly magnetized. We are currently investigating the influence of magnetic force gradient also for other systems.

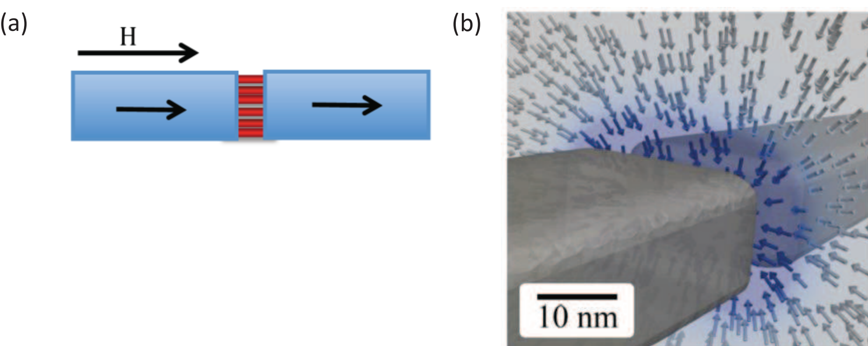

Figure 2.15 Magnetic gradient force density field for nanoscale Ni electrodes, simulated the electrodes magnetized along their axe. Gradient strongly attracts paramagnetic species towards the gap. Reprinted from [19].

2.4.3.4 Self-assembly between electrodes spaced > 100 nm

We also carried out STANWs self-assembly between electrodes patterned by e-beam lithography. Patterning the gap by e-beam lithography instead of using angle evaporation permits *i.*

to deposit two electrodes having the same height (thickness) and *ii.* to fabricate gaps with spacing above 100 nm. With this experiment we aim to self-assemble triarylamines over distances longer than 80 nm. In fact, being able to measure devices with different channel lengths L (and equal widths W) could provide insights on the contact resistance value (channel resistance scales with channel length L, while contact resistance remains constant).

The metal evaporated is again the trilayer Ti-Ni-Au. The e-beam patterned nanogaps width W is 500 nm - 1 µm (much shorter than the 10-100 µm typical of nanotrenches) because of technical lithography issues related to the proximity effect. Examples of electrodes geometries designed by e-beam (and imaged after self-assembly test) are shown in Figure 2.16.

(a)

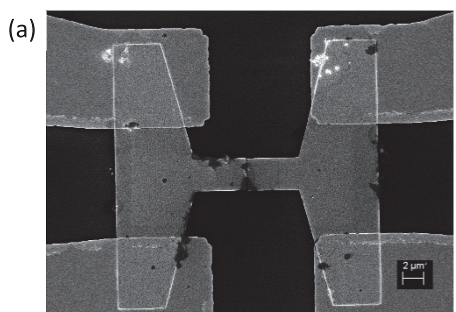

(b)

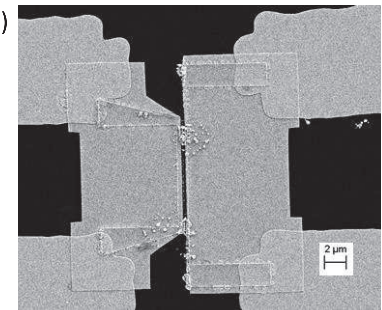

Figure 2.16 SEM images of nanogaps made by e-beam lithography after self-assembly tests.

The maximum gap length over which self-assembly results in circuit closure is ~ 160 nm. STANWs construction does not work between electrodes separated with 300 – 400 nm, not even increasing the applied voltage bias above the typical +0.8 V needed to close an 80 nm gap. Electrodes “far” apart might be a problem, not especially for the fibers formation, but rather for their positioning in the gap.

2.4.4 Excluding artifacts

Because the conductivity we observe is unexpectedly high for organic materials, we have taken great care to exclude the hypothesis of electrode metallic residues creating shortcuts.

We showed that STANWs-filled gaps, if still immersed in the chlorinated solvent, do not stand a temperature higher than 60°C; this relates to the supramolecular nature of the fibers, which can be ‘easily’ disassembled. We could re-close the same nanotrench a second and third time, by bringing back the sample to room temperature and repeating the self-assembly procedure. This is a strong evidence that our measured device is made of the supramolecular fibers.

Nevertheless we present here a series of measurements mostly aimed at checking that the observed remarkable conductivity of our samples are not experimental artifacts.

2.4.4.1 Stress tests on the electrodes

Figure 2.17 presents test measurements of nanotrenches (~ 80 nm), without the presence of organic self-assembly. Data were taken at room temperature under ambient conditions, similar to those during the self-assembly.

We observed the following:

i. As-made nanotrenches can sustain up to 5 V bias, with typical leakage currents not exceeding a few pA. The observed current in Figure 2.17(a) is mostly due to the parasitic capacitive part of the circuit.

ii. When immersed in the solvent tetrachlorioethane ($C_2H_2Cl_4$), the leakage current increases up to nA values, with applied bias exceeding 3 V, Figure 2.17(b). A possible origin for the leakage current is the water content of the solvent, which might be non-negligible under ambient atmosphere conditions.

iii. We test that illumination at power of similar magnitude to the one used for self-assembly does not create photoconduction artifacts in presence of the chlorinated solvent, Figure 2.17(c).

iv. Solutions of triarylamine molecules that do not self-assemble because of the absence of the amide responsible for hydrogen bonding (molecule 4 of Table 2.1), under illumination, showed leakage currents in the nA range (3 V bias), in Figure 2.17(d), typically seven orders of magnitude smaller than those obtained on successfully self-assembled systems.

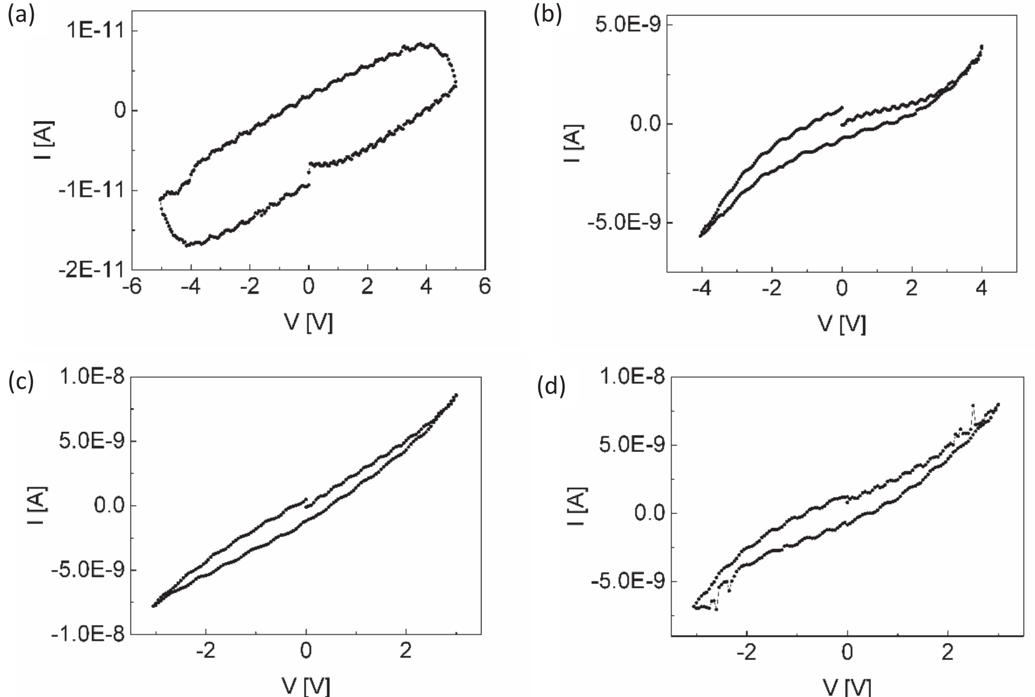

Figure 2.17 I-V measurements of the empty gap at high voltages. a) I-V of an empty reference nanotrench (width = 100 µm; length = 0.08 µm) without any solvent. b) I-V of a nanotrench immersed in $C_2H_2Cl_4$ before light irradiation. c) I-V measurements of the nanotrench immersed in $C_2H_2Cl_4$, and upon white light irradiation (density 10 $W{\cdot}cm^{-2}$). d) I-V curve of a nanotrench covered with a solution of molecule 4 (1 $mg{\cdot}mL^{-1}$ in $C_2H_2Cl_4$), after white light illumination, characteristic of a chemically and redox related sample, but without self-assembly properties.

From this series of test experiments, we can deduce that no electromigration of metal, nor photoconduction due to Ti inclusions or polluted SiO_2 substrate, occur, even under experimental conditions significantly more stressful than those used during the standard self-assembly procedure.

2.4.4.2 Blind test

Our collaborators previously described that triarylamine analogues 1-6 (Table 2.1) behave differently upon light stimulation in chlorinated solvent [16]. Indeed, they determined by ^1H NMR experiments that compounds 1-3 self-assemble in chloroform solutions upon light stimulation, while compounds 4-6 do not produce stacks. Their different behavior is due to the fact that several features

should be simultaneously operating to produce STANWs: a) a triarylamine core; b) an amide group for hydrogen bonding (the chlorine having no role in the self-assembly); and c) alkyl chains or benzylic groups on the phenols for hydrophobic or stacking secondary interactions.

We thus perform a control experiment using a blind test protocol: a person prepares the solutions and another person performs the conductivity experiments. Each vial is labeled and the label is kept coded to the second person, until the measurements are performed and analyzed. Each molecules solution is measured under the same conditions: we apply 1 V of potential difference (higher than the threshold voltage) between the electrodes immersed in solutions of triarylamines 1-6 (1 mg·mL-1), together with a 100 W irradiation at constant distance (≈ 10 W·cm^{-2}) for a period of 10 seconds. First we observe whether self-assembly occurs or not; then, I-V dependence is measured for each gap. Table 2.1 summarizes for each derivative 1 to 6 the behavior determined in solution (“Self-assembled” or “Non self-assembled”) and the result of the blind test in the column “State of the gap”. The definition “Closed” corresponds to the 6 orders of magnitude increase of the conductance.

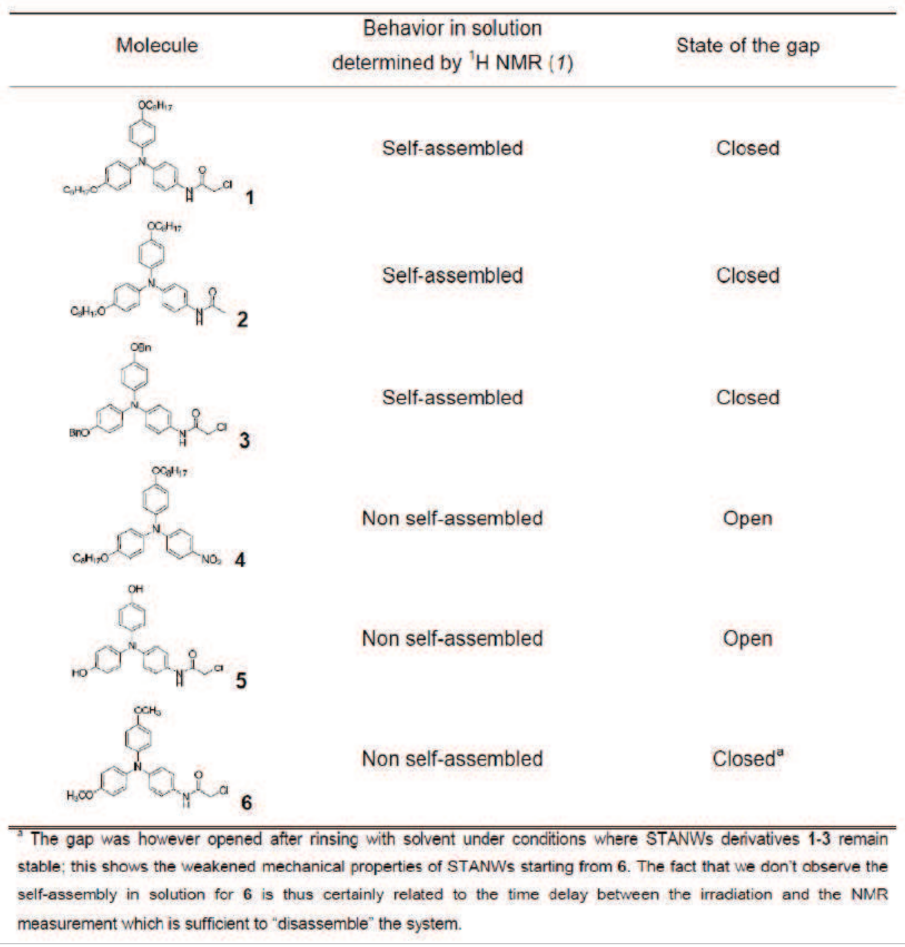

Molecule	Behavior in solution determined by ^{1}H NMR (*1*)	State of the gap
1	Self-assembled	Closed
2	Self-assembled	Closed
3	Self-assembled	Closed
4	Non self-assembled	Open
5	Non self-assembled	Open
6	Non self-assembled	Closed[a]

[a] The gap was however opened after rinsing with solvent under conditions where STANWs derivatives **1-3** remain stable; this shows the weakened mechanical properties of STANWs starting from **6**. The fact that we don't observe the self-assembly in solution for **6** is thus certainly related to the time delay between the irradiation and the NMR measurement which is sufficient to “disassemble” the system.

Table 2.1 Summary of the control experiments performed in blind test conditions to confirm that high conductivity values are associated just to molecules able to self-assembly in solution.

The clear correspondence “Self-assembled – Closed” and “Non self-assembled – Open” proves that the high conductivity values are related to STANWs formation.

In addition to stress experiments and blind test, successive self-assembly has been performed on the same gap (successive drop-casting, assembly, drying processes) without visible electrode modifications observed under high-magnification optical microscope.

2.4.5 Metallic temperature dependent behavior

The most spectacular finding is the temperature dependence of the supramolecular fibers resistivity. Several samples measured down to 1.5 K reveal resistivity values diminishing with decreasing temperatures. Decreasing resistance while cooling, in organic materials, has been a 'holy grail' for long time and only few examples are today present in literature [2],[20].

Figure 2.18(a) reports measurements for three different samples. A finite resistivity is extrapolated at $T \rightarrow 0$ K. In Figure 2.18(b) we report an I-V curve, showing the persistence of ohmic behavior at 1.5 K as well. We measure currents up to 25 mA for the lowest resistance samples submitted to a 1 V bias, under vacuum conditions (indications of sample heating have been in a slight deviation from the ohmic behavior – not shown here).

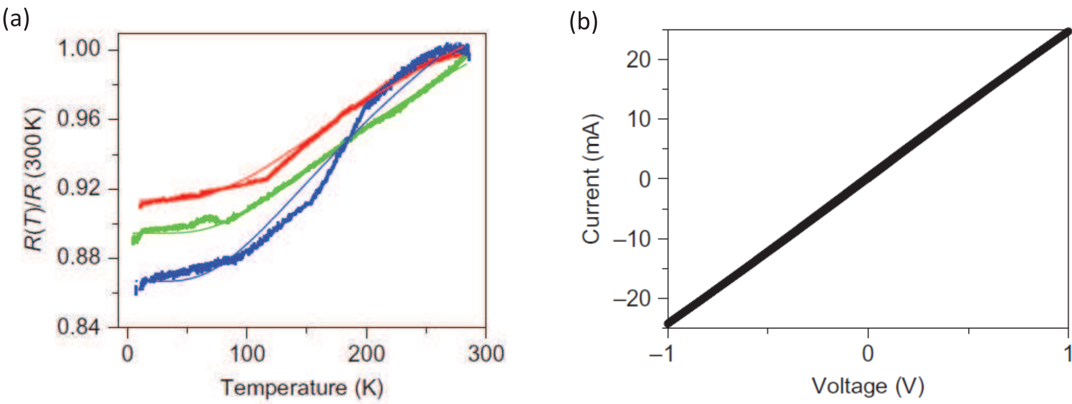

Figure 2.18 a) Normalized R(T) measurements of three independently prepared STANWs devices, between room temperature and 1.5 K (in vacuum, using an AC bridge technique). Initial resistances for each sample at 300 K: 22 (red), 45 (green), 360 (blue). Each set of data is fitted (thin lines) using a quasi-one-dimensional model of the resistance. b) I-V curve indicating current values of several tens of milliamperes at high bias (± 1V).

A tentative fitting of the normalized R(T) curves has been done following a quasi-one-dimensional model of transport elaborated by Kivelson and Heeger for conducting polymers [21] (solid lines in Figure 2.18(a)). According to this model the mean free path in the nanowires is mainly limited by chain imperfections and phonon scattering. These fits correlate with the unidirectional supramolecular shape of the wires that we initially described.

2.4.6 Conductivity and contact resistance estimates

Two-probe electrical conductance measurements do not allow separating the intrinsic material conductivity from the contact resistance contribution. We try however to provide values estimates for STANWs, in order to compare their outstanding conductivity to the one of other organic or carbon based materials.

The electrode/STANWs/electrode system can be simplified to the general scheme represented in Figure 2.19, where R_{ch} is the total intrinsic resistance of the fibers themselves, and R_S and R_D are the total contact resistances of STANWs, respectively with source and drain electrodes.

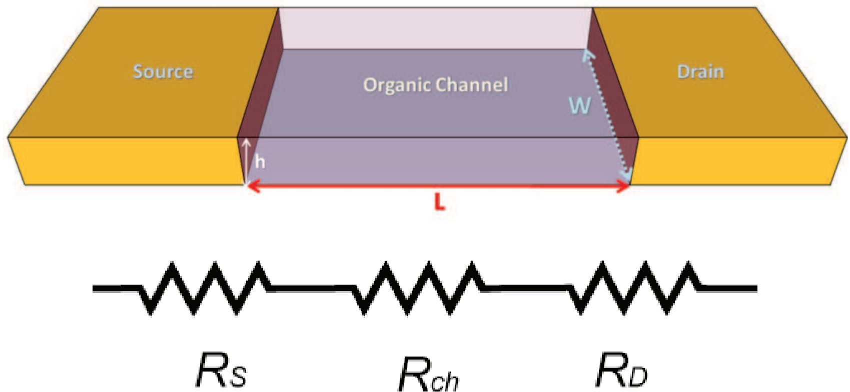

Figure 2.19 Schematic representation of a device formed by two electrodes and an organic channel in the middle.

Let us consider an average observed ($R_S + R_{ch} + R_D$) value of 50 Ω for a nanotrench 100 µm wide. If we assume that the interface resistances are negligible, one can then deduce a lower bound value of the material conductivity. Supposing that both dimensions (width W and thickness *h*) of the electrode/channel contact area are 100 % filled (W = 100 µm, *h* = 50 nm), then from Equation 2.1:

$$R_{ch} = \rho \frac{L}{W \cdot h} \tag{2.1}$$

we obtain a resistivity value ρ of 0.3 Ω·cm, which corresponds to a conductivity σ around 3 S/cm. If we consider W and *h* only 10 % filled, the conductivity estimate increases by 2 orders of magnitude: 300 S/cm. The uncertainty on the effective contact surface between metal and fibers introduces a large error bar on the extracted conductivity value σ. Most likely, the gaps are 100% filled along the width and only 10 % filled along the thickness, leading to an average value of 30 S/cm.

In a similar way we try to estimate an upper boundary value of the contact resistance. If we suppose that the sample resistance (50 Ω) is originated only by interfaces, we obtain a specific contact resistance in the range $5{\cdot}10^{-2}$ Ω·cm < R'_c < $5{\cdot}10^{-1}$ Ω·cm, depending on the width gap filling (lower value: 10 % filling, upper value: 100 %). In terms of surface contact resistance [Ω·cm^2], this corresponds to $3{\cdot}10^{-8}$ Ω·cm^2 < R_c < $3{\cdot}10^{-6}$ Ω·cm^2. To summarize, conductivity and contact resistance values estimates are reported in Table 2.2.

	Conductivity	Contact resistance
Nanotrench 100 % filled	σ < 3 S/cm	$R_c < 5{\cdot}10^{-1}$ [Ω·cm] $r_b^* < 3{\cdot}10^{-6}$ [Ω·cm^2]
Nanotrench 10 % filled	σ < 300 S/cm	$R_c < 5{\cdot}10^{-2}$ [Ω·cm] $r_b^* < 3{\cdot}10^{-8}$ [Ω·cm^2]

Table 2.2 Conductivity and contact resistance estimates for STANWs.

Akande *et al*. [22] recently reported a detailed first principle study of the structural, electronic, and transport properties of the class of triarylamine derivatives we have studied. Interestingly the authors evaluate the hole mobility using two methods, one describing more appropriately hopping conductance and the other designed for band-transport. Since the parameters deduced for STANWs (reorganization energy, intermolecular hopping, etc) do not fall in either of these limiting cases, but rather in between them, it seems reasonable to take the mobility values found in the two regimes

respectively as the lower and upper bounds for the nanowire mobility. They find a value of $\mu_h \sim 0.1$ $cm^2/V \cdot s$ considering a hopping type of transport along the fibers, against a $\mu_h \sim 12$ $cm^2/V \cdot s$ for a band-like transport. Trying to estimate mobility from our experimental results ($\mu = \sigma/e \cdot p$) is naïve because of the double incertitude on the intrinsic conductivity σ and on the density of carriers p values. However, supposing $p = 1 \cdot 10^{19}$ cm^{-3}, we obtain a hole mobility μ_h between 2 to 200 $cm^2/V \cdot s$, which is partially in agreement with the theoretical simulation. The carrier density is estimated by considering the density of radical cations stabilized within the supramolecular stacks, i.e. 6 radical cations over 1000 triarylamines (from EPR experiments in solution, paragraph 2.3, [16]) and by calculating the fibers volume accordingly the most favorable structure derived from computer modeling. Considering our experimental estimates and the calculations from Akande and coworkers, we can reasonably assert that STANWs holes mobility is included between 1 and 10 $cm^2/V \cdot s$.

The extremely low value of contact resistance is, however, the most astonishing feature of this system. R_c in the range of 10^{-2} - 10^{-1} $\Omega \cdot cm$ is at least 4 orders of magnitude lower than typical values for metal/OSC interfaces [23] in organic thin film transistors. We attribute this value to the fact that the supramolecular fibers tightly share their electronic wavefunctions with the metal electrodes. This strong hybridization with the metal surface is probably the cause of the low contact resistance and also a fundamental condition for the existence and stability of STANWs between electrodes.

2.5 Electrolyte-gating of STANWs

The experiment of self-assembling triarylamines between metallic electrodes takes great advantage of the lateral geometry of our device to access the photosensible material and built the in-situ connection. As explained in the Introduction (Chapter 1), we want to exploit lateral geometry even further by attempting the gating of STANWs. Gating the supramolecular nanofibers means to tune their charge carriers density by applying a transverse electric field. In a first place, this would allow a controllable modulation of their conductivity (eventually towards lower values, to obtain significant high I_{on}/I_{off} ratios) and additionally the possibility to measure hole mobility μ from experimental data. Ultimately, in the framework of using STANWs as organic spacer for lateral spinvalves, the gating test is an attempt to tune the interface/channel resistance ratio (r_b^*/r_N) towards its optimal value to obtain the highest spinvalve magnetoresistance signal.

The density of carrier we estimate for STANWs, 10^{19} – 10^{20} cm^{-3}, is small for a metal. One can then expect a non-negligible Debye length (electric-field screening length) extending over several nanometers, impacting therefore the density of carriers. Considering the very short channel (80 nm) and the high conductivity of the material, the ability to gate it successfully is a real challenge. For this reason, we choose to use the method of electrolyte-gating. Standard dielectric bottom gate would probably be completely uninfluent and the evaporation of ultra-thin high-ε dielectric on the top of soft organic fibers could easily break them. The principle mechanism of electrolyte-gating is explained in detail in Appendix B.

The device is shown in Figure 2.20(a). After self-assembly, the sample is rinsed (acetone, ethanol) and repositioned on the same experimental set-up. We use the ionic liquid 1-butyl-3-methylimidazolium hexafluorophosphate, $[BMIM]^+[PF_6]^-$, as electrolyte. The ionic liquid is gently drop-casted on the self-assembled gap. Thanks to its high viscosity, the contact angle is high and the drop remains pseudo-spherical. A metallic gate electrode is then put in contact with the drop. The gate electrode used is a 1 mm^2 area platinum disk electrode for electrochemistry. One should mention that successful samples require a significant stability, keeping closed 'soft' nano-interconnections after adding the ionic liquid. We had a typical 25% success rate.

A constant source-drain bias V_{sd} of +0.1 V is applied. Application of the gate voltage causes ions moving inside the electrolyte, and formation of a densely charged electrical double layer in contact with STANWs fibers (and source-drain electrodes as well). Results are reported in Figure 2.20(b). In red it is shown the value of the gate voltage applied as a function of time; in black the corresponding change of the total resistance (STANWs + metallic pads).

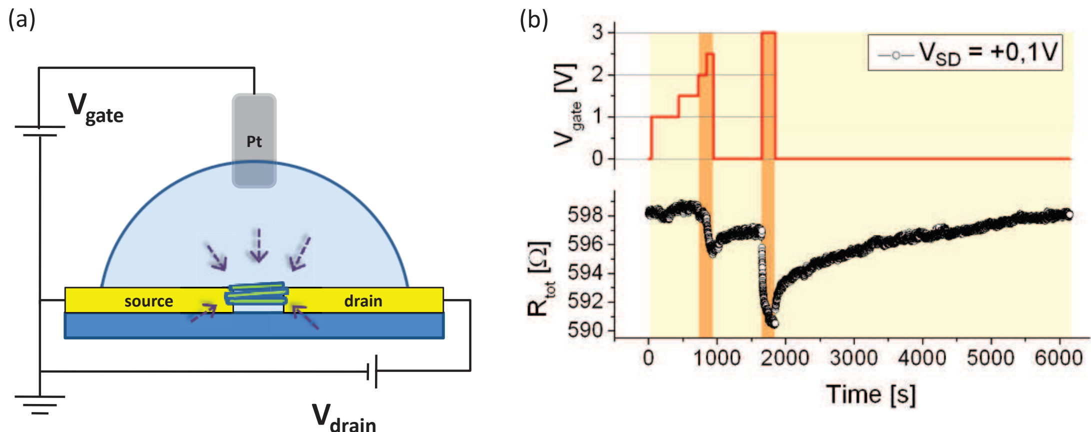

Figure 2.20 STANWs electrolyte-gating experiment. a) Schematic representation of the set-up for STANWs electrolyte-gating. 1D fibers connect source and drain electrodes. A drop of $[BMIM]^+[PF_6]^-$ covers the active channel and a large area of the connecting metallic pads (figure not in scale). Dashed arrows indicate the transvers electric field exerted on the nanofibers. b) Modulation of the total resistance R_{tot} (black points, bottom) at different gate biases V_g (red line, top), as a function of time.

The measured sample has a resistance ($R_S + R_{ch} + R_D$) around 70 Ω. Source-drain resistance starts to show a modulation just for gate biases above +2.5 V. In particular, a 7 Ω change in R_{tot} is detected in correspondence of V_g = + 3.0 V.

This test experiment provided few information:

- the equilibration time of the sample conductivity is long. This strongly limited the samples we investigated, with the presented one being the samples where several gate voltage stress values were used.
- 10 % resistance increase (7 Ω over 70 Ω) is rather small. Moreover, we should consider that ionic liquids have been demonstrated to be able to vary the conductivity of metallic thin films [24],[25],[18]. Since a large area of the metallic pads is covered by the ionic liquid drop, the total resistance modulation may be due to a tuning of the metallic thin films conductivity.

We conclude that the resistance modulation is too small to speculate on the field-effect induced on the supramolecular assembly. Device geometry should be ameliorated to reduce the ionic liquid/metal electrodes contact surface and negative gate voltages should be tried. Further experiments would be needed.

2.6 Conclusions

In this Chapter we have demonstrated the self-organization of soft supramolecular 1D nanofibers of triarylamine molecules (STANWs) for the creation of metallic interconnects. These

triarylamines nanowires constitute a unique conducting soft organic material that intrinsically exploits the potentiality of the “bottom-up” self-assembly approach that supramolecular chemistry put at the service of electronics. The necessary light-trigger and the process self-limitation enable the precise positioning of the organic electrical interconnect in determined position of a nanoscale circuitry.

The share of the electronic wavefunction of the STANWs with the metal electrode is likely the reason explaining the ohmicity of the metal/STANWs contact (down to 1 K!). In fact, if the metallicity of the organic fibers is by itself spectacular (just few examples of organic metals have been demonstrated [2]), even more astonishing is the extremely low value of contact resistance with the metallic electrodes, smaller than $5\cdot10^{-1}$ $\Omega\cdot$cm (in terms of contact resistance per unit area, $3\cdot10^{-6}$ $\Omega\cdot$cm^2). Similar values are lower than for conducting polymers, organic single crystals and even graphene. Indeed, metal/STANWs contact resistance presents the lowest value inside this thesis, respect to the one of graphene nanoflakes (Chapter 3) and of a highly doped polymer semiconductor (Chapter 5). Only metallic carbon nanotubes can exhibit less resistive interfaces with metals. Considering that nanometric devices performances are severely degraded by contact limitations, this is a strong asset for STANWs technological application.

Moreover, STANWs interconnects present an exceptional stability, both in air (not sensible to oxygen and moisture) and vacuum, which is of fundament importance for Organic Electronics.

This discovery (published in April 2012) has triggered an important impulse in the scientific community, both aiming to theoretical understanding of the astonishing values obtained [22],[26] and to reproduce the same experiment with other type of supramolecular materials [27],[28].

Concerning our ultimate goal of finding a suitable organic spacer for lateral spinvalves, the carriers mobility above 1 cm^2/V·s and the clear metallic character of STANWs strongly point towards a very long spin diffusion length (Bhattacharya *et al*. [26] predict $\lambda_s \sim 100$ nm at room temperature) and make them ideal candidates for the purpose. However, extensive spinvalve tests have been carried out, but with scarce success. The main problem is to stabilize STANWs properly between magnetic-only electrodes. The strong hybridization of the fibers wavefunction with the metal electrodes, which is surely one of the main peculiarity of the system, is also the cause of the extreme selectivity in the choice of the surface to which the fiber like to bond to.

With this system we also lack experimental insights into the channel/interface resistance ratio r_b^*/r_N, thus we do not know whether we fulfill the condition to avoid resistance mismatch or not (see discussion in the Introduction). Gating seems to be ineffective on the fibers resistivity r_N and interface resistance r_b^* cannot be varied because of the impossibility to change the interface material. For these reasons, we start to work with another material, well known for its high carrier mobility and less selective in terms of contacting interfaces: graphene.

BIBLIOGRAPHY

[1] A. P. H. J. Schenning and E. W. Meijer, “Supramolecular electronics; nanowires from self-assembled π-conjugated systems,” *Chem. Commun.*, no. 26, p. 3245, 2005.

[2] K. Lee, S. Cho, S. Heum Park, A. J. Heeger, C.-W. Lee, and S.-H. Lee, “Metallic transport in polyaniline,” *Nature*, vol. 441, no. 7089, pp. 65–68, May 2006.

[3] M. Mas-Torrent, D. Den Boer, M. Durkut, P. Hadley, and A. Schenning, “Field effect transistors based on poly (3-hexylthiophene) at different length scales,” *Nanotechnology*, vol. 15, no. 4, p. S265, 2004.

[4] F. S. Schoonbeek, J. H. van Esch, B. Wegewijs, D. B. A. Rep, M. P. de Haas, T. M. Klapwijk, R. M. Kellogg, and B. L. Feringa, “Efficient Intermolecular Charge Transport in Self-Assembled Fibers of Mono- and Bithiophene Bisurea Compounds,” *Angew. Chem. Int. Ed.*, vol. 38, no. 10, pp. 1393–1397, May 1999.

[5] F. J. M. Hoeben, P. Jonkheijm, E. W. Meijer, and A. P. H. J. Schenning, “About Supramolecular Assemblies of π-Conjugated Systems,” *Chem. Rev.*, vol. 105, no. 4, pp. 1491–1546, Apr. 2005.

[6] M. Hasegawa and M. Iyoda, “Conducting supramolecular nanofibers and nanorods,” *Chem. Soc. Rev.*, vol. 39, no. 7, pp. 2420–2427, Jun. 2010.

[7] F. S. Kim, G. Ren, and S. A. Jenekhe, “One-Dimensional Nanostructures of π-Conjugated Molecular Systems: Assembly, Properties, and Applications from Photovoltaics, Sensors, and Nanophotonics to Nanoelectronics†,” *Chem. Mater.*, vol. 23, no. 3, pp. 682–732, Feb. 2011.

[8] E. Moulin, J.-J. Cid, and N. Giuseppone, “Advances in Supramolecular Electronics - From Randomly Self-assembled Nanostructures to Addressable Self-Organized Interconnects,” *Adv. Mater.*, vol. 25, no. 3, pp. 477–487, Jan. 2013.

[9] M. Gailberger and H. Bässler, “dc and transient photoconductivity of poly(2-phenyl-1,4-phenylenevinylene),” *Phys. Rev. B*, vol. 44, no. 16, pp. 8643–8651, Oct. 1991.

[10] J. M. Warman, G. H. Gelinck, and M. P. de Haas, “The mobility and relaxation kinetics of charge carriers in molecular materials studied by means of pulse-radiolysis time-resolved microwave conductivity: dialkoxy-substituted phenylene-vinylene polymers,” *J. Phys. Condens. Matter*, vol. 14, no. 42, p. 9935, Oct. 2002.

[11] J. M. Warman, M. P. de Haas, G. Dicker, F. C. Grozema, J. Piris, and M. G. Debije, “Charge Mobilities in Organic Semiconducting Materials Determined by Pulse-Radiolysis Time-Resolved Microwave Conductivity: π-Bond-Conjugated Polymers versus π−π-Stacked Discotics,” *Chem. Mater.*, vol. 16, no. 23, pp. 4600–4609, Nov. 2004.

[12] Y. Chen, Y. Feng, J. Gao, and M. Bouvet, “Self-assembled aggregates of amphiphilic perylene diimide–based semiconductor molecules: Effect of morphology on conductivity,” *J. Colloid Interface Sci.*, vol. 368, no. 1, pp. 387–394, Feb. 2012.

[13] W. Pisula, A. Menon, M. Stepputat, I. Lieberwirth, U. Kolb, A. Tracz, H. Sirringhaus, T. Pakula, and K. Müllen, “A Zone-Casting Technique for Device Fabrication of Field-Effect Transistors Based on Discotic Hexa-peri-hexabenzocoronene,” *Adv. Mater.*, vol. 17, no. 6, pp. 684–689, Mar. 2005.

[14] Z. Ning and H. Tian, “Triarylamine: a promising core unit for efficient photovoltaic materials,” *Chem. Commun.*, no. 37, p. 5483, 2009.

[15] Y. Shirota, “Photo- and electroactive amorphous molecular materials:molecular design, syntheses, reactions, properties, and applications,” *J. Mater. Chem.*, vol. 15, no. 1, p. 75, 2005.

[16] E. Moulin, F. Niess, M. Maaloum, E. Buhler, I. Nyrkova, and N. Giuseppone, “The Hierarchical Self-Assembly of Charge Nanocarriers: A Highly Cooperative Process Promoted by Visible Light,” *Angew. Chem. Int. Ed.*, vol. 49, no. 39, pp. 6974–6978, Sep. 2010.

[17] V. Faramarzi, F. Niess, E. Moulin, M. Maaloum, J.-F. Dayen, J.-B. Beaufrand, S. Zanettini, B. Doudin, and N. Giuseppone, “Light-triggered self-construction of supramolecular organic nanowires as metallic interconnects,” *Nat. Chem.*, vol. 4, no. 6, pp. 485–490, Apr. 2012.

[18] T. A. Petach, M. Lee, R. C. Davis, A. Mehta, and D. Goldhaber-Gordon, “Mechanism for the large conductance modulation in electrolyte-gated thin gold films,” *Phys. Rev. B*, vol. 90, no. 8, p. 081108, Aug. 2014.

[19] P. L. Popa, N. T. Kemp, H. Majjad, G. Dalmas, V. Faramarzi, C. Andreas, R. Hertel, and B. Doudin, “The magnetoelectrochemical switch,” *Proc. Natl. Acad. Sci.*, p. 201322828, Jul. 2014.

[20] M. Ahlskog, M. Reghu, A. J. Heeger, T. Noguchi, and T. Ohnishi, "Electronic transport in the metallic state of oriented poly (p-phenylenevinylene)," *Phys. Rev. B*, vol. 53, no. 23, p. 15529, 1996.

[21] S. Kivelson and A. J. Heeger, "Intrinsic conductivity of conducting polylmers," *Synth. Met.*, vol. 22, pp. 371 –384, 1998.

[22] A. Akande, S. Bhattacharya, T. Cathcart, and S. Sanvito, "First principles study of the structural, electronic, and transport properties of triarylamine-based nanowires," *J. Chem. Phys.*, vol. 140, no. 7, p. 074301, Feb. 2014.

[23] D. Natali and M. Caironi, "Charge Injection in Solution-Processed Organic Field-Effect Transistors: Physics, Models and Characterization Methods," *Adv. Mater.*, vol. 24, no. 11, pp. 1357–1387, 2012.

[24] D. Daghero, F. Paolucci, A. Sola, M. Tortello, G. Ummarino, M. Agosto, R. Gonnelli, J. Nair, and C. Gerbaldi, "Large Conductance Modulation of Gold Thin Films by Huge Charge Injection via Electrochemical Gating," *Phys. Rev. Lett.*, vol. 108, no. 6, p. 066807, Feb. 2012.

[25] M. Tortello, A. Sola, K. Sharda, F. Paolucci, J. R. Nair, C. Gerbaldi, D. Daghero, and R. S. Gonnelli, "Huge field-effect surface charge injection and conductance modulation in metallic thin films by electrochemical gating," *Appl. Surf. Sci.*, vol. 269, pp. 17–22, Mar. 2013.

[26] S. Bhattacharya, A. Akande, and S. Sanvito, "Spin transport properties of triarylamine-based nanowires," *Chem. Commun.*, vol. 50, no. 50, p. 6626, 2014.

[27] A. A. Sagade, K. V. Rao, U. Mogera, S. J. George, A. Datta, and G. U. Kulkarni, "High-Mobility Field Effect Transistors Based on Supramolecular Charge Transfer Nanofibres," *Adv. Mater.*, vol. 25, no. 4, pp. 559–564, Jan. 2013.

[28] J. J. Armao, M. Maaloum, T. Ellis, G. Fuks, M. Rawiso, E. Moulin, and N. Giuseppone, "Healable Supramolecular Polymers as Organic Metals," *J. Am. Chem. Soc.*, vol. 136, no. 32, pp. 11382–11388, Aug. 2014.

3. Liquid exfoliated graphene

Graphene is certainly the 2-D material with the highest charge carrier mobility discovered up to now, with decisive advantages for devices patterning and realization. Since its earliest days it has been identified as a high interest material for spintronic and spin quantum computing, owing to the expected long spin lifetime τ_s and spin diffusion length λ_s. Its exceptional transport properties are due to unique physical characteristics (strong π-delocalization in 2-dimensions over large distances, linear dispersion of the density of states) that make it quite different from standard organic materials such as molecular crystals or polymers (weak intermolecular interactions, high effective mass of charge carriers). Graphene does not suffer from the issues of low mobility and hopping transport typical of organic materials.

Our search for a suitable candidate for organic lateral spinvalves cannot leave aside graphene. We propose to integrate it in our device using the wet-chemistry approach typical of Organic Electronics, and quite distinct from the usual way to process graphene circuits. We take advantage of the opportunity of collaboration with the group of Professor P. Samori in Strasbourg (Institute of Supramolecular Chemistry, ISIS) that masters liquid-phase exfoliation of graphite into graphene and successive deposition from solution onto substrates. The typical approach of Spintronics with Graphene is to perform non-local measurements on large graphene flakes to demonstrate spin transport over micrometers. We want instead to make a 2-terminal spinvalve with a high mobility organic material filling the nanometric channel. In our vision graphene ink is just one possible solution-processable material. It does not need to be high quality graphene, as far as it provides high enough mobility and long enough spin diffusion length. At the beginning of this project, mobility values for exfoliated 'graphene ink' were essentially unknown. The few initial works claim μ a few tens of $cm^2/V\cdot s$, much smaller than typical values of mechanically exfoliated and CVD graphene but larger than organic materials.

In this Chapter we report a study on the transport properties of liquid-phase exfoliated (LPE) graphene nanosheets. This study is preparatory for potential future fabrication of lateral spinvalves. The graphene flakes (of nanometric size) are measured in bottom-contact configuration on the nanotrench electrodes described in paragraph 3.4. Electrolyte-gating is applied to explore LPE-graphene electronic properties and to demonstrate the possibility of a gate-control.

3.1 Graphene spin diffusion length λ_s

Graphene is the name given to a flat monolayer of carbon atoms tightly packed into a two-dimensional (2-D) honeycomb lattice. Each carbon is in its sp^2 hybridized state and the third p_z electron is used to form an extended π-delocalization over the whole monolayer. Thanks to this electronic delocalization and to the typical high crystal quality, charge carriers can travel thousands of interatomic distances without scattering. Charge carrier mobility $\mu_{e/h}$ in graphene can exceed 10^5 $cm^2/V\cdot s$, even under ambient conditions. Although some inorganic semiconductors in their undoped state exhibit comparable room temperature mobilities (namely, InSb), in graphene $\mu_{e/h}$ remains high even at high carrier density n ($> 10^{12}\ cm^{-2}$) in both electrically and chemically doped devices [1].

The long τ_s expected for graphene stems from the small spin-orbit coupling of carbon atoms and the weak hyperfine interactions resulting from the absence of nuclear spins for the main ^{12}C isotope.

Its exceptional charge carrier mobility μ converts the long τ_s into very long spin diffusion length λ_s, according to Equation 1.1 (see Introduction).

3.1.1 Experimental measure of spin diffusion length λ_s in graphene

Estimates of spin diffusion length λ_s in graphene are documented in literature mostly using non-local spin diffusion measurements, combining non-local spin valve data and Hanle precession measurements. Measuring in non-local configuration consists in dissociating the electric current from the spin current by injecting/extracting spin-polarized current between two electrodes and detecting the pure spin signal with two different magnetic electrodes aside.

Hill *et al*. [2] fabricated the first local graphene spin-valve in 2006. The first non-local spin-valve measurements done on mechanically exfoliated graphene was instead presented in 2007 by Tombros *et al*. [3] (Figure 3.1) and reproduced by the same group in 2009 (Popinciuc *et al*. [4]).

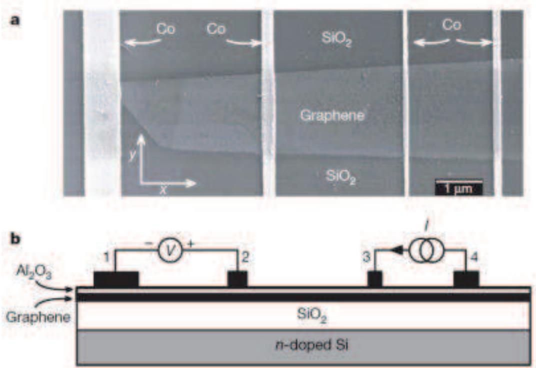

Figure 3.1 Non-local graphene spinvalve of Tombros *et al*. [3]. a) Scanning electron micrograph of a four-terminal contacted single-layer graphene on SiO_2. b) The non-local spin valve geometry. A current I is injected from electrode 3 through the Al_2O_3 barrier into graphene and is extracted at contact 4. The voltage difference is measured between contacts 2 and 1.

These first non-local measurements provide values of λ_s in graphene around 1.5 - 2.0 µm, slightly varying as a function of the gate voltage (carrier density), and spin lifetimes τ_s of 100 – 200 ps. These values refer to mechanically exfoliated graphene. Comparable values have been demonstrated for single-layers and bi-layers of graphene grown by Chemical Vapour Deposition (CVD) and transferred on SiO_2 [5] and on hexagonal boron-nitride (hBN) [6]. Exceptionally long values of λ_s, up to 200 µm, have been reported by Dlubak *et al*. [7] on graphene epitaxially grown on SiC.

In general, the estimation of λ_s for graphene in literature is still controversial, especially because spin depolarization mechanisms in graphene also necessitate deeper investigation. A low mobility graphene will certainly be characterized by a low diffusion coefficient D and a shorter λ_s. We can say that a λ_s value of 1 micron and spin flip time τ_s of the order of 150 picoseconds are established, while higher values need additional experimental evidence.

Note that much larger spin lifetime were recently reported using Electron Spin Resonance, ESR (or Electron Paramagnetic resonance, EPR) technique. Náfrádi *et al*. [8] conducted an ESR study on chemically synthesized graphene (solvothermal synthesis). Interestingly, they find that conduction electrons do not interact with localized spin in graphene at low temperatures (50 K), thus leading to unprecedentedly long spin lifetime value of 65 ns for conduction electrons. Such finding needs further experiments to show if such spin lifetime values can transfer into very long λ_s.

3.2 Liquid-phase exfoliation of graphite to graphene

Several strategies have been developed for graphene production since its first isolation by scotch-tape mechanical exfoliation in 2004 [9]. Mechanical exfoliation from graphite is a top-down approach providing very good quality and µm-sized graphene flakes, but it suffers of very low yield and it is not suitable for industrial scale-up. Chemical Vapor Deposition (CVD) from gas precursor (methane is the most common choice) on catalytically active surfaces (Cu, Ni) is a large area bottom-up technique providing graphene crystals of rather good quality [10]. CVD is the most promising technique for graphene production at the industrial level [11]. The main limitation of CVD is the necessity to transfer the graphene layer from the metallic catalyst growth substrate (usually copper) on an insulating substrate. Other bottom-up approaches have been developed, based on the organic syntheses starting from small molecular modules in liquid media [12]. These however are both size limited, because macromolecules become more and more insoluble with increasing size, and suffer from the occurrence of side reactions with increasing molecular weight.

The first top-down "chemical" way for graphene production consisted in the reduction of graphene oxide sheets, obtained upon oxidation of graphite [13]. The greatest problem of this process is that reduction cannot remove all structural defects introduced by the oxidation process. It was quickly clear that a more convenient way to obtain high quality graphene by chemical methods was the direct exfoliation of graphite in liquid environment, exploiting sonication or other external driving forces to extract individual layers. The first report of exfoliation–intercalation–expansion of graphite has been published simultaneously by two different groups, Hernandez *et al.* [14] and Li *et al.* [15], in 2008.

The synthesis and processing in liquid phase of graphene have attracted increasing interest in the last few years. The interest is driven by the possibility to scale up the synthesis of graphene making it cheaply available in large amount, enabling a wide range of applications such as large area electronics on transparent flexible/stretchable substrates, composites, catalytic systems. Besides large area covering, LPE graphitic material is also becoming very popular for the production of graphene paper and graphene-foam for flexible and ultralight supercapacitors [16],[17]. Liquid-phase exfoliation of graphite into graphene belongs to the top-down approach since chemical bonds are rather disrupted and not created, and it provides an extremely versatile and potentially up-scalable technique for massive graphene production. A detail description on the production and processing of graphene and 2d crystals is provided in the review by Bonaccorso *et al*. [18].

3.2.1 Basic principle of liquid-phase exfoliation

The liquid-phase exfoliation (LPE) process of graphite into graphene consists in three steps: dispersion of graphite in a solvent, exfoliation and purification [19]. Successful exfoliation requires the overcoming of the van der Waals attractions between the adjacent layers of graphite (interlayer distance 3.35 Å). The choice of the solvent is of primary importance to obtain significant exfoliation yield. Solvents ideal to disperse graphene are those with a low interfacial tension with it: in this case penetration of solvent molecules in between graphitic layers is promoted and inter-sheet attractive forces are immediately substituted by solvation, as soon as the graphene sheet is isolated. The most commonly used solvents are shown in Figure 3.2: N,N-dimethylformamide (DMF), N-metyl-2-pyrrolidone (NMP), ortho-dichlorobenzene (o-DCB), all characterized by a surface tension around 40 mJ m^{-2}. Unfortunately their boiling temperatures are rather high (DMF: 152°C, NMP: 202 °C, o-DCB: 180 °C), thus leading to a cumbersome complete removal of solvent residues from the graphene itself.

The liquid phase exfoliation process is not spontaneous and needs to be assisted by some external forces: this could be either sonication or application of an electrochemical potential to a graphite electrode. Sonication promotes shear forces and cavitation, i.e. the growth and collapse of the micrometer-sized bubbles or voids in liquids due to pressure fluctuations, thus helping exfoliation. Intuitively, a longer sonication time increases the quantity of material exfoliated, as shown in the concentration – sonication time plot of Figure 3.2. However, a sonication time too long consumes high energy and severely reduces the average flake size, thus limiting the graphene performances for most applications.

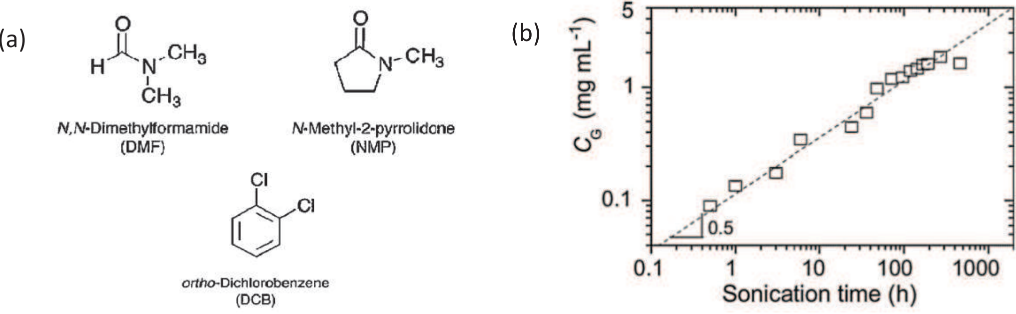

Figure 3.2 a) Best organic solvents for graphite exfoliation: DMF, NMP and DCB. b) Direct proportionality between sonication time and graphene yield (expressed in terms of concentration of graphene in the dispersion C_G) [19].

In 2013 electrochemical exfoliation has been reported [20], with exceptional production yields (1 mg/mL of graphene in DMF in few minutes). The application of a positive potential (+ 10 V) to a graphite electrode immersed in an acidic aqueous solution strongly induces the intercalation of negative ions in between graphite flakes. In few minutes, the graphite is completely expanded and it disperses in the solution. The addition of surfactants to the liquid medium can increase the production yield, in particular when such molecule has a high energy of adsorption on the basal plane of graphene, higher than the one of the solvent molecule interacting with the graphene.

Figure 3.3 illustrates the main steps of sonication-assisted exfoliation. A centrifugation step is necessary to separate mono-, bi- and tri- layer graphene from multilayers and graphite residues. After centrifugation, the filtered solution of graphene flakes is dispersed either in the original exfoliation solvent or in a solvent more compatible with the deposition technique chosen. However, solubility of graphene in other solvents is not straightforward.

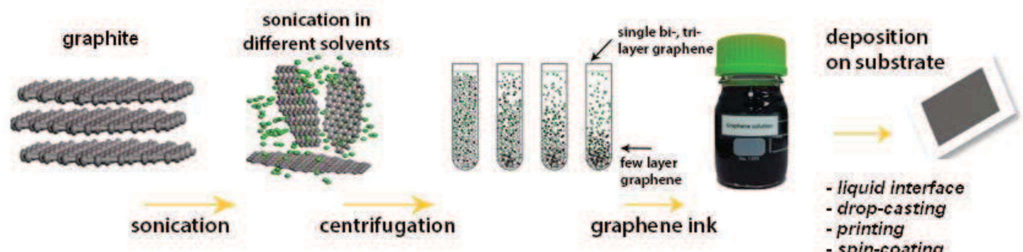

Figure 3.3 Main steps of sonication-assisted exfoliation of graphite.

Since the presence of remaining solvent can greatly impact the device performance, dispersion of graphene in low boiling solvents is preferable. Unfortunately low boiling solvents, e.g. water, ethanol and chloroform, have a surface tension unsuitable for direct exfoliation of graphene. However, new approaches based on a solvothermal-assisted exfoliation process of graphite in a highly polar

organic solvent, such as ethanol:sodium 1:1 solution [21] or acetonitrile [22], have also been developed.

3.2.1 LPE-graphene deposition techniques on substrates

One of the main advantages of liquid-phase exfoliation is making graphene solution-processable, thus allowing its deposition in a variety of environments and on different substrates, not available using mechanical cleavage or other growth methods. Langmuir-Blodgett technique [15], inkjet printing [23] or simple drop-casting [24] are some of the methods used to deposit LPE-graphene on substrates. We describe these techniques in some more detail.

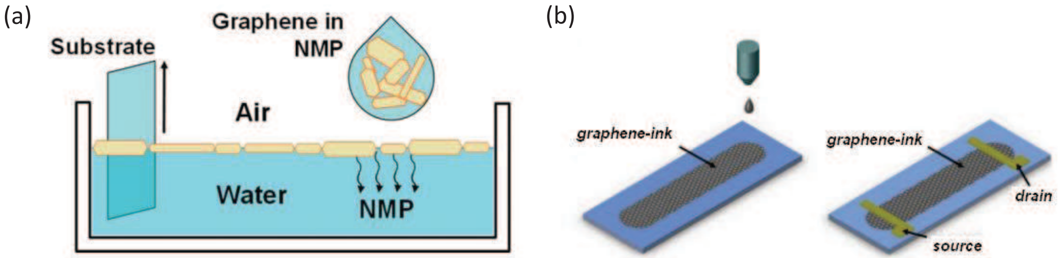

Figure 3.4 Schematic representation of a) Langmuir-Blodgett deposition of graphene on a substrate starting from a NMP graphene ink [25] and b) ink-jet printing of graphene thin film and successive evaporation of source and drain metallic electrodes [23].

➢ *Langmuir-Blodgett deposition*

The Langmuir-Blodgett deposition technique exploits the high surface tension at the air-water surface to prepare a thin layer (ideally, monolayer) of the material to deposit on a substrate. Once the material is distributed on the water surface of the bath, the substrate is immersed (or emerged) in (out of) water, while keeping a constant surface pressure with the help of mechanical barriers constantly compressing the water surface. The process can be repeated many times in order to obtain films of different thickness, as long as enough material is present on the bath surface. Langmuir-Blodgett technique has been ideated for amphiphilic molecules and would require the material to deposit to be in a low boiling point solvent, so that it easily evaporates away of the air-water surface. As illustrated in Figure 3.4(a), the method can also be applied to high boiling point solvents (NMP for example), because, as long as this solvent is miscible with water, it sinks into the bath and hydrophobic graphene flakes float on the water surface.

➢ *Inkjet printing & Drop casting*

Inkjet printing technique progressed from printing text and graphics to a tool for rapid manufacturing of thin films devices based on organic conducting and semiconducting inks. LPE is ideally suited to produce graphene inks for inkjet printing. A key property of inks viable for printing is their ability to generate droplets: viscosity, surface tension, density, and nozzle diameter, strongly influence the spreading of the resulting liquid drops. Successful inkjet printing of graphene devices has already been demonstrated by Torrisi *et al*. [23].

The simpler version of inkjet printing is normal drop casting. In this case the drop parameters are less controlled and no special printer machine is needed. However, drop casting of graphene inks suffers of poor coverage and “coffee-ring” effect. It can be improved by simultaneous heating of the substrate or substrate shaking, accelerating solvent drying.

3.3 Graphene electronic properties for FET devices

The application of a transverse electric field to a material (gating) permits to explore its electronic properties by shifting the electrochemical potential level up and down the density of states band diagram towards the zone of interest. Since its discovery, graphene has been investigated by means of gate field-effect making use of standard dielectrics [9]. The gate voltage induces a surface density of states n [cm^{-2}] equal to:

$$n = \frac{Q_i}{e} = \frac{C_i \cdot V_g}{e} = \frac{\varepsilon_0 \varepsilon}{t} \cdot \frac{V_g}{e}$$

3.1,

where Q_i is the charge accumulated per unit of area, e is the electron charge, V_g the gate voltage and C_i is the specific capacitance. Gate field-effect permits to unveil ambipolar transport in graphene and the Dirac point of neutrality separating electrons and holes transport, as illustrated in Figure 3.5. If V_g is negative with respect to the neutrality point, the electrochemical potential (E_F for simplicity) locates in the lower cone of the band diagram and the conduction occurs through holes. If V_g is more positive than the neutrality point, E_F is in the upper cone and majority carriers are electrons. The resistance maximum occurs when E_F passes through the asymptotically null density of states zone of the linear band diagram.

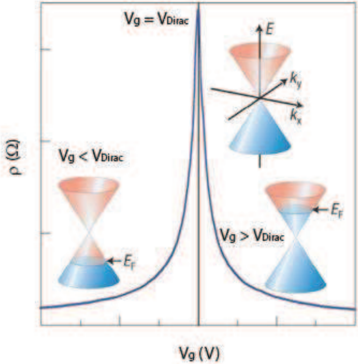

Figure 3.5 Ideal transfer characteristic of a graphene-based field effect transistors showing the ambipolar behavior and highlighting the variation of the Fermi level position with the applied gate bias (reprinted with modification from [1]). V_{Dirac} is not necessarily located at zero gate voltage; its value depends on the intrinsic doping of graphene.

The Dirac point of neutrality (where the numbers of electrons equals the number of holes) does not necessarily correspond to V_g = 0 V. This is why in Figure 3.5 the gate bias at which the Dirac point is located is indicated with general name V_{Dirac}. Its position depends on the intrinsic and extrinsic doping of graphene, so it can vary from flake to flake. Ideal graphene is undoped (V_{Dirac} = 0 V), but the vicinity to the substrate [26] (extrinsic doping) and/or presence of defects (edge-defects, dangling bonds, etc: intrinsic doping) introduce charged impurities that induce additional carriers (electrons or holes). The Dirac maximum of resistance is more pronounced if measurement is carried out at low temperature, because of the Dirac-Fermi distribution around E_F is sharper.

In the linear regime of a graphene-FET, i.e. when the drain bias V_d is much lower than the gate bias V_g, the source-drain current I_{sd} is given by:

$$I_{sd} = \mu \frac{W}{L} C_i V_d (V_g - V_{Dirac})$$

3.2,

where μ is the carrier mobility, W and L respectively the width and length of the device channel and V_d the drain voltage. Hole and electron mobility are thus extracted from the linear regime of the transfer curves as:

$$\mu = \frac{L}{W} \frac{1}{C_i} \frac{1}{V_d} \frac{\Delta I_{sd}}{\Delta V_g}$$

3.3,

where ΔI_{sd} is the current modulation corresponding to a gate bias change equal to $\Delta V_g = V_g - V_{Dirac}$. Examining the $I_{sd} - V_g$ slope in the holes transport part of the curve one obtains μ_h, whereas μ_e is deduced from the slope of the transfer curve in the electron transport regime. For a standard dielectric (SiO_2 for example) C_i is equal to $\varepsilon_0\varepsilon/t$, where ε_0 and ε are respectively the permittivity of vacuum and of the dielectric, and t is the dielectric thickness. Typical specific capacitance values for SiO_2 dielectric are in the nF/cm^{-2} range. Rather high V_g are needed (~100 V) to reach density of carrier above $5{\cdot}10^{12}$ cm^{-2}.

Das *et al*. [27] perform the first electrolyte-gating experiment on a CVD micrometric graphene flake using poly(ethylenoxide)/$LiClO_4$ (PEO/$LiClO_4$) as top-gate. In comparison to standard dielectrics, electrolyte-gating is capable to induce on graphene very high charge carrier density n (up to 10^{13} - 10^{14} cm^{-2}) at low gate bias (few volts), thanks to its extreme polarizability (see Appendix B). Figure 3.6(a) presents the transfer curves obtained by Das *et al*. nicely showing ambipolar behavior within -0.5 V and + 2.0 V of V_g.

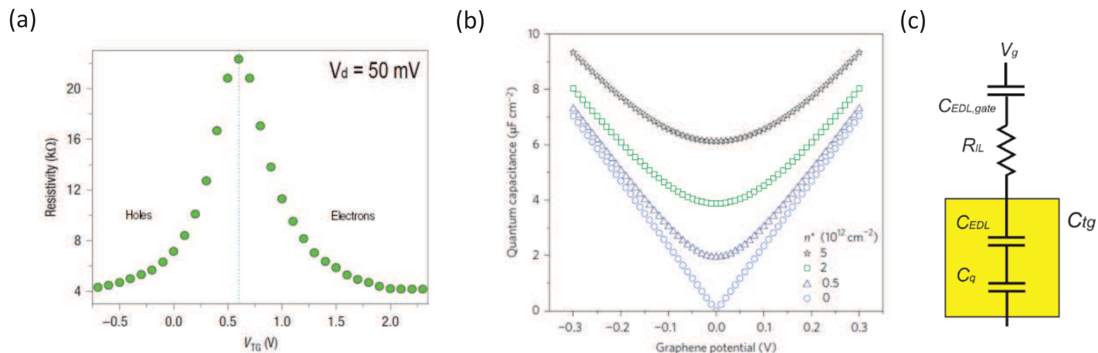

Figure 3.6 a) Transfer curve of the first electrolyte-gated graphene FET (Das *et al.* [27]). b) Estimation of graphene quantum capacitance according to Equation 3.4 (Xia *et al*. [28]) at different densities of charged impurities n^*. c) Equivalent circuit for gate/electrolyte/graphene system, showing the additional quantum capacitance of graphene C_q in series to the electrical double layer capacitance C_{EDL}.

3.3.1 Quantum capacitance of graphene

At such high carrier densities, quantum capacitance of graphene starts to play a role. Quantum capacitance originates for the two-dimensional (2D) geometry of the conductor and it has been firstly postulated for two-dimensional (2DEG) electron gases in quantum wells or inversion layers [29]. It is related to the limited number of available states for charge carriers, which becomes critical for graphene close to the Dirac point of neutrality. A locally gated graphene sheet can be viewed as a two

plate capacitor, with one plate being the top-gate electrode and the other being the graphene sheet. If the density of states on one of the plates is finite, adding a charge carrier costs energy, due to the shift of the Fermi level (charging energy of a capacitance).

Graphene quantum capacitance has been measured for the first time by Xia *et al*. [28] making use of ionic liquid gating (namely [BMIM][PF_6]) and successively by other groups, both by means of electrolyte-gating [30] or high dielectric constant insulators [31]. C_q increases with the square root of the charge density as follows:

$$C_q = \frac{2e^2}{\hbar \upsilon_F \sqrt{\pi}} \sqrt{|n_G| + |n^*|}$$

3.4,

where υ_F is the Fermi velocity, n_G and n^* are carrier concentrations generated by the gate voltage and surface impurity, respectively. Figure 3.6(b) shows calculated values of C_q at different density of charged impurities n^*: C_q tends to zero at Dirac point for ideal graphene, but the presence of impurities increases it up to 8 μF/cm^2. The maximum carrier density physically reachable for graphene at the Dirac point is ~ $1{\cdot}10^{14}$ cm^{-2}.

In a graphene FET, C_q is connected in series with the gate dielectric, as modeled by the equivalent circuit shown in Figure 3.6(c) for an electrolyte-gated graphene FET. Top-gate specific capacitance C_{tg} of the interface electrolyte/graphene is therefore:

$$\frac{1}{C_{tg}} = \frac{1}{C_{EDL}} + \frac{1}{C_q}$$

3.5.

Since the quantum capacitance C_q is comparable to the specific capacitance of the electrical double layer C_{EDL} (they are both in the μF/cm^2 range) and the total capacitance of two capacitor in series is smaller than the capacitance of each single capacitor, the electrical double layer capacitor is less effective than what it could potentially be. Quantum capacitance might therefore become a barrier towards scaling of graphene devices.

3.3.2 Electrical properties of liquid exfoliated graphene

Reports of the electrical characterization of liquid exfoliated graphene are rather scarce in literature. This might be explained by the fact that its transport properties are expected to be poorer than the ones of other types of graphene (mechanically exfoliated or grown by CVD), and because a detailed electrical characterization is maybe unnecessary for the large-scale applications envisioned for graphene 'inks', such as semi-transparent electrodes, supercapacitors, etc.

Torrisi *et al.* [23] report ink-jet printing of graphene obtained by sonicated-assisted exfoliation of graphite in NMP (Figure 3.4(b)). Their optimized devices show a mobility μ ~ 95 cm^2/V·s and an I_{on}/I_{off} ratio of 10. Graphene ink films thicker than 25 nm show sheet resistance R_{sheet} in the 10^4 Ω range and best conductivity σ of 1 S/cm. Parvez *et al.* produce graphene by electrochemical exfoliation with very high yield, in acidic aqueous solutions [17] and inorganic salts aqueous solutions [20]. They obtain an average graphene flake size of 5-10 μm, mostly single or bilayers. Graphene is deposited onto substrates by Langmuir-Blodgett from DMF/chloroform solutions. They study electrical properties of both thin films and single flakes (chasing the largest ones). As visible in Figure 3.7(a,b) films and single flakes are heavily p-doped and the Dirac point of neutrality cannot be detected up to + 100 V of gate bias. The mobility values they report are > 230 cm^2/V·s for single flakes and > 30 cm^2/V·s for thin films. Mobility values given by Torrisi and Parvez are remarkably high for liquid exfoliated graphene.

Kim *et al*. [25] produce graphene by sonicated-assisted exfoliation in NMP and measure electrical properties of thin films deposited by Langmuir-Blodgett. In Figure 3.7(c) we report the transfer curve of their field-effect transistor device built on SiO_2/Si wafer with top source-drain contacts: I_{on}/I_{off} ratio is < 2, even for a large voltage sweep (from – 100 V to 100 V). The film is heavily p-doped with the charge neutrality point located at a gate voltage greater than 40 V. They determine a hole mobility value at room temperature of 0.9 $cm^2/V\cdot s$ and an electron mobility one order of magnitude lower. The conductivity of a 7 nm thick films strongly depends on the average size of the graphene flakes forming the film: it ranges from 100 S/cm (flakes: 220 nm) to $4\cdot10^{-3}$ S/cm (flakes: 80 nm).

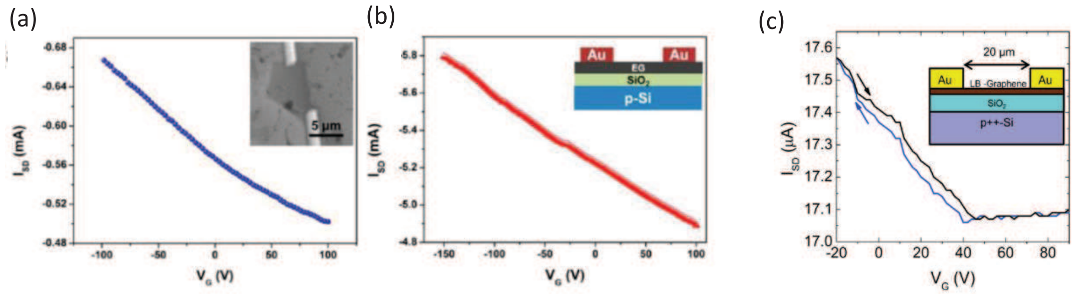

Figure 3.7 a,b) Transfer curves of electrochemically exfoliated graphene obtained by Parvez *et al.* (a) on single micrometric flake (connected by e-beam lithography) and (b) on thin films. c) Transfer curve of LPE-graphene (sonication-assisted exfoliation in NMP) thin film (Kim *et al*. [25]).

LPE-graphene produced in Professor Samori's group (the same we will use in our experiment) has been characterized by the same group making use of commercially available pre-patterned electrodes with interdigitated source-drain electrodes ($L_{channel}$ > 2.5 µm) and 230 nm thick SiO_2 bottom gate [24]. Devices are prepared by drop-casting NMP dispersions, after surface treatment (HMDS or OTS). They extract the sheet resistance of graphene thin films from the two terminal I-V traces, taking into account that the channel coverage is just within 6 and 20 % of the total area (effective channel width, W_{eff}, estimated by optical microscopy). They also measure the gate-dependency. Results are shown in Figure 3.8.

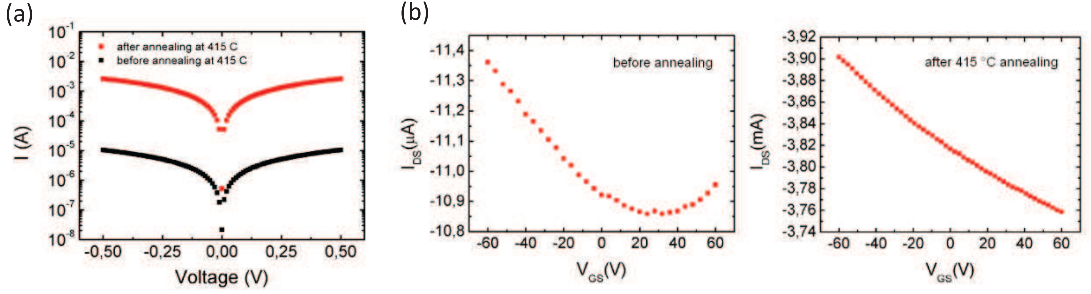

Figure 3.8 Electrical characterization of LPE-graphene thin films produced in prof. Samori's group (Ciesielski *et al*., Suppl. Info [24]). a) I-V curves before and after 415°C annealing [L = 2.5 µm, W_{eff} = 800 µm]. b) Transfer curves of the same device before and after annealing.

Firstly, a 100-fold current increase is observed after an annealing step at 415°C (several hours), attributed to NMP residues removal between the flakes, as already seen by Kim *et al*. [25]. The transfer curve in Figure 3.8(b) reveals ambipolar behavior before the high temperature annealing (left), but disappearing after the annealing step (right). Electron and hole mobilities extracted from the transfer curves range between 0.3 and 1 $cm^2/V\cdot s$. The I_{on}/I_{off} ratio is below 2.

To our knowledge, the only measurement of a single graphene sheet (single GS) with size < 1 µm has been performed by Li *et al*. in their original work reporting exfoliation of graphite in liquid phase [15]. They use a bottom-gate top-contact geometry where source and drain electrodes are placed by electron beam lithography (channel length = 100 nm) after Langmuir-Blodgett deposition of the graphene nanosheets. Figure 3.9(a) shows an AFM image of the device with a single GS bridging the channel (titanium/gold contacts over a 500-nm SiO_2 backgate) between the source (S) and drain (D) electrodes. A typical resistance for a single GS bridging 100-nm-wide gap at room temperature is 10 - 30 kΩ (mean resistance histograms over 10 devices shown in Figure 3.9(b). Graphene-oxide (GO) is much more insulating, as expected (third column of Figure 3.9(b)). Interestingly, the group performs conductivity *vs* temperature measurements (Figure 3.9(c)), but does not show any measurement as a function of gate.

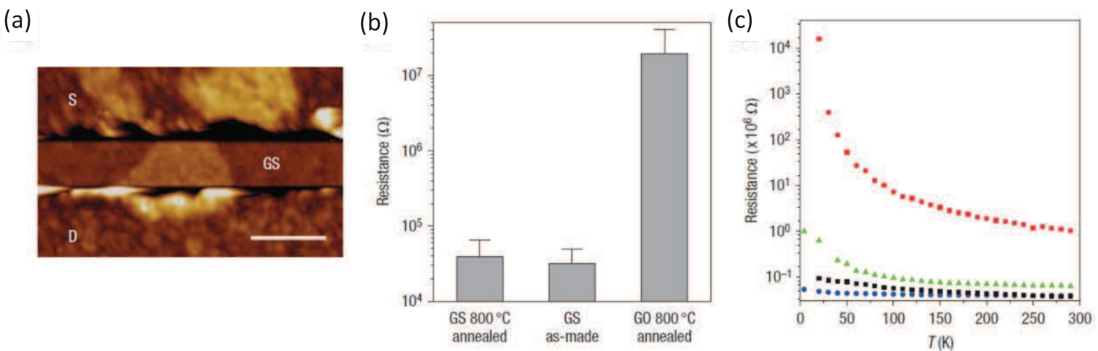

Figure 3.9 a) AFM image of a single graphene sheet connected by source and drain. Scale bar is 200 nm. b) Average resistance for an annealed graphene sheet (GS 800°C annealed), as-made graphene sheet and annealed graphene oxide (GO). c) Temperature-dependence of the resistance for GO 800°C annealed (red), as-made GS (green), GS annealed (black) and GS annealed with palladium contacts (blue). Reprinted from Li *et al*. [15]

To resume the main characteristics of LPE-graphene are:

- Average flake size is < 300 nm (bigger for electrochemically exfoliated graphene).
- Mobility values for LPE-graphene thin films can possibly reach 10 $cm^2/V{\cdot}s$ (exceptionally 10 times higher in some reports).
- Ambipolar properties are undocumented (the only example is Fig. 3.8(b)

The ambipolar behavior peculiar of graphene is almost lost when deposited as thin films and all the exceptional electrical characteristics of graphene such as mobility, conductivity and sheet resistance are strongly reduced by the flake-to-flake hopping.

EXPERIMENTAL

3.4 Electrolyte-gating of suspended LPE-graphene nanosheets

Liquid-phase exfoliated graphene is deposited from solution onto pre-patterned Au electrodes and successively gated by means of an electrolyte top-gate. The aim of our experiment is *i.* to provide a characterization of the electrical transport properties of liquid-phase exfoliated graphene and *ii*. to check whether LPE-graphene possesses the suitable characteristics to be used as active material in organic lateral spinvalves.

We use a quite unique approach that allows us to probe transport in single LPE-graphene flakes of nanometric size. We employ the 'nanotrench' geometry as pre-patterned electrodes, already used in Chapter 2 (see Appendix A for fabrication). The final device for electrolyte-gating of suspended LPE-graphene nanosheets is shown in Figure 3.10.

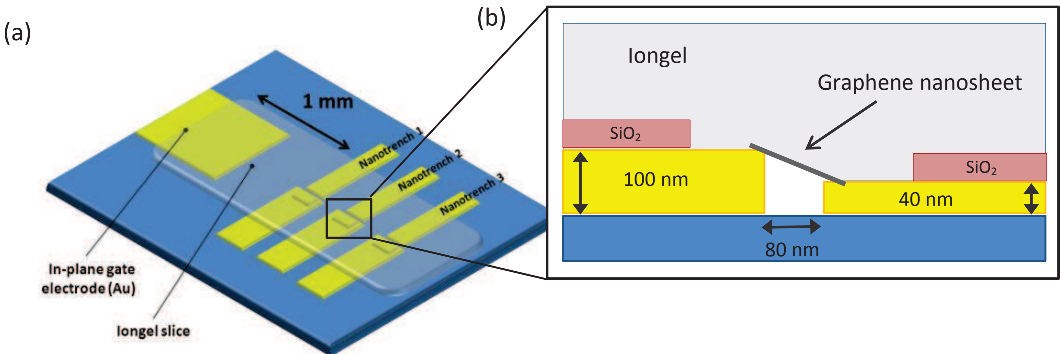

Figure 3.10 Scheme of the device for electrolyte-gating of suspended LPE-graphene nanosheets. a) Perspective view of the sample. 7 nanotrenches are present on the same chip (only 3 are sketched), the iongel slide covers all nanotrenches and in-plane gate electrode. Graphene nanosheets are not shown in this image. b) Profile view of a graphene-bridged nanotrench (80 nm gap). A 50-nm SiO_2 capping layer (in red) protects source and drain metals from direct contact with the iongel.

The key specifics of this experiment are the following:

- *<u>Single</u> and <u>nanometric-sized</u> LPE-graphene flakes are probed*

In paragraph 3.3.2 we have seen that e-beam connected single sheets chosen for single-flake transport characterization are typically in the micrometer size range. However, micrometric flakes do not correspond to the average size of the majority of graphene flakes obtained by liquid exfoliation, that is instead around 200 - 300 nanometers [15],[32]. Measuring exceptionally large flakes extracted by several successive centrifugation steps does not reflect the material under study. On the other hand, evaluating the properties of the material under the form of thin films is interesting for ink-printable circuits, but the intrinsic performances of LPE-graphene, for instance the charge-carrier mobility, will be always affected by the flake-to-flake charge transfer. In contrast, nanotrenches have a gap size shorter than the small flakes dimensions (100 nm), thus they can be easily contacted. The high aspect ratio of nanotrenches (20 µm < W < 100 µm) provides the contact of several nanoflakes with one deposition. A large number of single flakes are connected in parallel all along the width of the nanotrench.

- *Graphene nanosheets are bottom-contacted*

  Examples of bottom-contacted graphene are very rare. One example is the work of Ciesielsky *et al*. (Samori's group), in which LPE-graphene thin films are tested in bottom contact configuration. The bottom-contact geometry is inconvenient for scotch-exfoliated graphene because of the impossibility of positioning the flake in a desired location (above the electrodes). Contact resistance metal/graphene for bottom contact geometry is expected to be much larger than the one in top contact geometry. In fact, evaporation of the metal upon the graphene makes an intimate contact thanks to formation of covalent bonds between metal and carbon atoms [33], whereas simple lying of graphene over metal intuitively leads to poorer contact. However, patterning top contacts by lithography over pre-deposited graphene thin films might be technologically impeded by the film roughness, and stencil mask evaporations might suffer from metallic implantation near the contacts region.

- *Graphene nanosheets are suspended at the top of the nanogap*

  The nanotrenches gap is 80 - 100 nm and the electrodes thickness is > 50 nm. From visual characterization by scanning electron microscopy, it is clear that the nanosheets (slightly larger than the gap itself) are lying on the top of the ridges. We can thus consider the LPE-graphene nanosheets to be suspended, i.e. far from the SiO_2 substrate. It is known that the vicinity to the substrate strongly influences electronic properties of graphene, normally introducing some traps causing a possibly important residual doping. We thus expect this effect to be cancelled out on our devices.

For the first tests experiments, substrates fabrication, graphene deposition and electrical measurements have been carried out in IPCMS by our group, while professor Samori's group (ISIS) provided the exfoliated graphene. Successively, graphene flakes have also been deposited on substrates in ISIS by S. Haar and Dr A. Ciesielsky.

3.4.1 Samples fabrication

In total 8 different samples have been prepared and studied. In what follows we present the results obtained for 3 of them, called sample A, sample B and sample C. They are representative of three different preparation procedures, mainly differing for the presence (or absence) of a SiO_2 layer protecting the source-drain electrodes and for the deposition technique (indirectly influencing the quantity of material deposited). The samples and their characteristics are resumed in Table 3.1.

	Sample A	Sample B	Sample C
SiO_2 covering	NO	YES	YES
Graphene Deposition Method	Dipping directly in NMP	Dipping directly in NMP	Heated drop-casting
Number of deposition steps	3	1	3
Annealing (after each dep. step)	YES (50°C)	YES (50°C)	YES (100°C)

Table 3.1 Main characteristics of the three representative samples presented in this Chapter.

3.4.1.1 Substrate preparation: bottom Au electrodes and SiO_2 cap layer

The bottom electrodes are prepared by optical lithography on standard SiO_2/Si wafers using the angle evaporation technique described in Appendix A. The nanotrench aspect ratio is very high, being

the channel length L = 80 - 100 nm and the channel width W between 20 µm and 100 µm. The electrodes are made of Au, with a Ti adhesion layer of 3 nm. We recall that the two electrodes forming the nanotrench have different heights (thicknesses), respectively around 100 and 50 nm.

Sample A substrate is made by simple metallic bottom contacts evaporation. For sample B and C we introduce an important fabrication step in the substrate preparation: the deposition of a 50 nm thick SiO_2 layer covering the most part of source-drain electrodes. Such improvement is not only respect to sample A, but also respect to all the samples used for experiments with the supramolecular triarylamines nanowires (Chapter 2). The main scope of inserting an insulating barrier is to minimize the area of direct contact metal/electrolyte. An aperture is of course necessary to let access to the electrodes: this opening, centered on the nanotrench, is 20 µm or 150 µm large. In Figure 3.11(a) an optical microscope image of the 20 µm window is reported. We use optical lithography (positive resist process) to draw the aperture, followed by RF-magnetron sputtering of the SiO_2. We will see in paragraph 3.4.3 how the presence of this layer is important for the correct functioning of the device. However, the lift-off process of the sputtered SiO_2 was often unreliable (Figure 3.11(b)), thus strongly reducing the productivity of the sample fabrication process. Using e-beam dielectric evaporator for SiO_2 deposition instead of sputtering and opening the largest window (150 µm) facilitates the lift-off process.

(a)

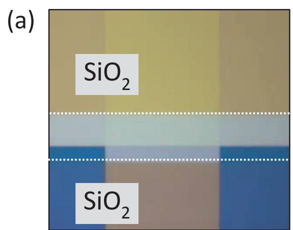

(b)

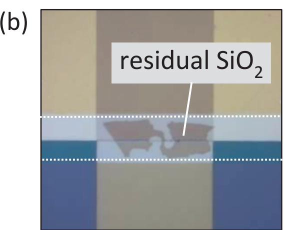

Figure 3.11 Optical microscope images of the 20 µm window in the SiO_2 layer opened on the nanotrench to give access to the gap, (a) well-lifted and (b) not completely lifted (nanogap is lost).

3.4.1.2 LPE-graphene deposition

We have tested several experimental procedures to carry out the deposition of LPE-graphene on substrates. The very first samples have been deposited making use of a Langmuir-Blodgett set-up here in IPCMS, with the help of Professor J.-L. Gallani. The advantage of Langmuir-Blodgett technique is that the quantity of graphene deposited on the substrate is limited and the material is expected to be solvent-free: this allowed us to take clear images of single graphene nanosheets by Scanning Electron Microscopy (see later on, paragraph 3.4.2.1). However, because of the small quantity of graphene deposited, the graphene-bridging of the nanogaps is statistically less probable and the closed gaps are mechanically and electrically fragile (only few flakes bridging the gap are likely subject to electrostatic shock).

We therefore deposited graphene by other techniques, such as direct dipping in NMP dispersion and drop-casting. These were performed by our collaborators in ISIS (S. Haar and Dr. A. Ciesielsky). LPE-graphene has been deposited on Sample A and B by direct dipping in liquid phase dispersion product of the exfoliation (concentration: 80 µg/µL). By means of a motorized set-up, the substrate is immersed in a becher containing 20 mL graphene NMP solution and extracted at a speed of 0.5 mm/s. Each dipping step is followed by a solvent-drying waiting time (~ 20 min) and annealing. For sample A the dipping-drying-annealing process has been repeated 3 times, while just once for sample B. Sample C was instead deposited by heated-substrate drop-casting method. 50 µL of LPE-graphene dispersion in NMP were put on the substrate; substrate was kept heated at 50°C and under mechanical slow oscillation till complete solvent drying. This procedure was repeated 3 times, followed by a 100°C

annealing (1h) at each step. Heated drop-casting deposits on the substrate huge quantities of LPE-graphene, as it can be seen from optical microscope images in Figure 3.12. This deposition technique has been developed to maximize the channel covering for large-scale FETs transistors.

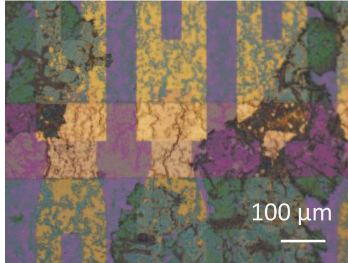

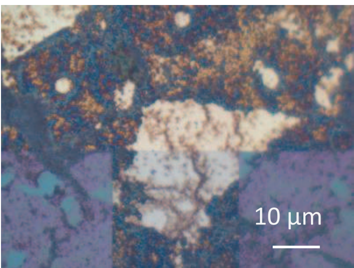

Figure 3.12 Optical microscope images of sample C after heated-substrated drop-casting deposition of LPE-graphene.

At the end of the whole deposition process, a long annealing (24h at least) has been performed for all samples A, B and C, to remove at best NMP residues and improve contact with bottom electrodes.

3.4.1.3 Raman analysis and TEM characterization of LPE-graphene

Micro Raman spectroscopy and High Resolution Transmission Electron Microscopy (HR-TEM) are performed on the LPE-graphene in the work of our collaborators (Ciesielsky *et al*. [24]). We do not perform Raman and TEM analysis directly on our substrates.

Raman spectroscopy is a well-established tool to get quick information about the quality of graphene and the number of carbon layers. A typical Raman spectrum of monolayer graphene shows two main features: the G peak at ~ 1580 cm^{-1} and the 2D peak at ~ 2700 cm^{-1}. In the case of monolayer graphene the 2D peak is single and sharp, while in AB-stacked bilayer it is composed by four bands. Graphite shows a broad and up shifted 2D peak. The 2D peak shape quickly evolves with the number of layers, so that the 2D band of a sample containing more than 8-10 layers is hardly distinguishable from that of bulk graphite. Moreover, in case of disorder, defect-activated features appear in the Raman spectrum: the D peak, first order of the 2D peak, which lies at ~1350 cm^{-1} and the D' peak, which appears at ~ 1620 cm^{-1}.

In Figure 3.13(a) Raman spectra on NMP-exfoliated graphene dispersions drop-cast on silicon substrate are shown. Pristine graphene normally does not have enough structural defects for the D and D' peaks to be Raman active, so they can only be seen at the edges. Since graphene flakes produced by LPE are typically smaller than the laser spot, the D peak is always visible in their Raman spectrum. It can be seen that the 2D peak shape and the intensity of the D peak changes from flake to flake. The percentage of single-layer graphene amounts to approximately 30%. The rest of the material is composed of thin flakes (< 10 layers); they are mostly re-aggregated flakes, since AB stacking was never observed.

For the High Resolution Transmission Electron Microscopy (HR-TEM) analyses, a drop of solution containing graphene flakes was deposited on a TEM grid covered by a lacey carbon membrane. In a number of cases folded monolayer graphene sheet are observed, as shown in Figure 3.13(b). The edges of mono- and bi-layer graphene present some defects, as expected, whereas in the center LPE nanosheets present good crystallinity.

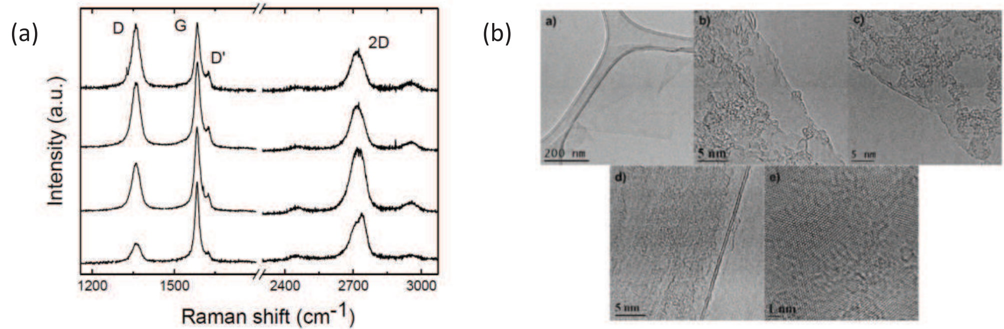

Figure 3.13 a) Raman spectra of the flakes obtained from the graphene/NMP dispersion. b) TEM images of LPE-graphene exfoliated in ISIS: *a.* monolayer graphene flake. *b,c,d*. HR-TEM images taken on the edges of monolayer (*b,c*) and bi-layer (*d*) graphene flakes; *e.* HR-TEM image taken in the center of a bi-layer graphene flake. (reprinted from [24], Suppl. Info)

3.4.2 Optical and electrical characterization after deposition

After the graphene deposition and an annealing step, and before positioning the electrolyte, we characterize each sample electrically and optically, in order to discriminate which and how many nanotrenches are bridged by graphene nanoflakes. Samples are first observed using an optical microscope, as shown in Figure 3.14: we identify at this step the nanotrenches that are expected to show a finite resistance value (bridged with graphene) and the nanotrenches "open" (high resistance, not bridged with graphene).

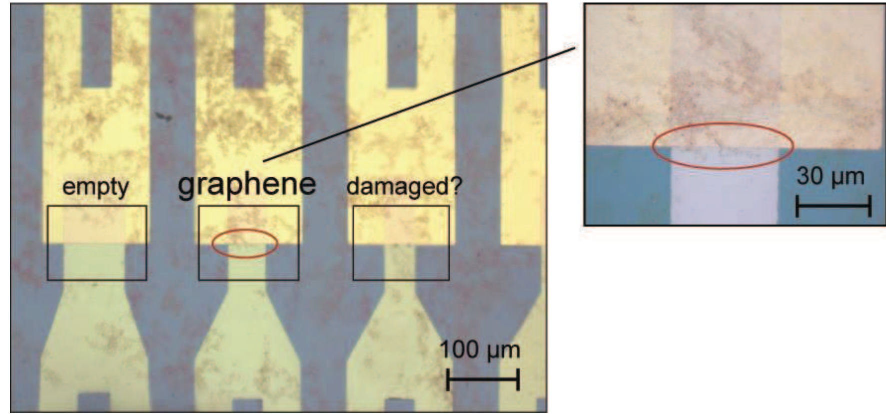

Figure 3.14 Example of optical check of graphene-bridged nanotrenches. The graphene-bridged nanotrench is located inside the red ellipse. Source and drain electrodes have slightly different colors (yellow and greenish) because of the different metal thickness.

This optical check also allows pinpointing nanotrenches eventually damaged during deposition or transportation. These devices are indeed very sensible to electrostatic discharges due to the fact that graphene nanosheets constitutes hot-spots for the current flow (high density of current through a very tiny area); slight electrostatic discharges can cause micro-explosions of the nanogap electrodes in correspondence of the graphene nanoflake (what happened in Figure 3.14 to the nanotrench indicated as "damaged?").

After optical check, electrical characterization is performed. We collect an I-V curve for each nanotrench by applying a source-drain voltage in the range ± 100 mV. I-V curves of samples A, B and

C are shown in Figure 3.15. For low-resistive samples A and C, the metallic pads resistance ($R_{pads} \sim 500$ Ω) has been subtracted from the total resistance R.

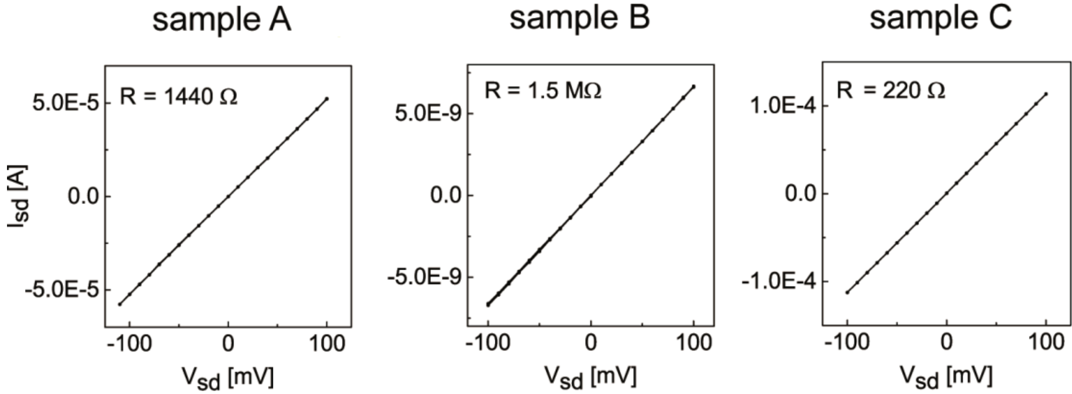

Figure 3.15 I-V traces of sample A, B and C. The curves are measured by means of a probe station, in air and glovebox, at room temperature.

I-V curves are perfectly ohmic for all the three samples, even though they present very different values of resistances. The big difference in resistance R is due to the different quantity of graphene deposited on each sample. We recall that Sample A and B have been deposited by direct dipping in graphene dispersion, but sample A has been dipped-dryed-annealed repeatedly 3 times, whereas sample B only one time. Sample C has instead been deposited by heated-substrate drop-casting method. Heated drop-casting allows the deposition of large quantities of LPE-graphene (Figure 3.12), from this stems the lowest resistance for sample C.

From these I-V curves, some estimates of sheet resistance R_{sheet} and contact resistance R_c can be made. The effective width of the active channel W_{eff} (portion of the nanotrench covered with graphene) is $\sim$ 1.5 µm for sample B and $W_{eff} \sim 20$ µm for samples A and C. If we assume that the interface resistances are negligible, one can deduce an upper bound value of the material sheet resistance R_{sheet}, according to Equation 3.6:

$$R_{sheet} = R \cdot \frac{W_{eff}}{L}$$

3.6.

Best values of R_{sheet} are derived from sample A and C and range between 55 kΩ and 350 kΩ. Our collaborators Ciesielsky *et al*. [24] find $\sim$ 10 kΩ for LPE-graphene bottom-contacted thin films.

In reality, interface resistance is probably the major contribution to the total resistance of our device. If we consider the device resistance R totally due to contact resistance, we obtain an average value of specific contact resistance between 30 kΩ·µm and 5 kΩ·µm (3 Ω·cm - 0.5 Ω·cm). Typical contact resistance for top-contacted graphene is around 0.2 - 0.3 kΩ·µm [34],[35].

The ohmicity of the I-V curves is however remarkable considering that the graphene flakes are bottom-contacted. The annealing step for sure improves the contact resistance, even though our annealing is rather mild (50°C - 100°C). We argue that one possible reason could be that the LPE-graphene flakes are *quasi* end-contacted. Current injection from a metal through the edges of graphene flake has been demonstrated to have low contact resistance [36] and many effort have been devoted to the fabrication of metal/graphene end-contacts. The height asymmetry of source-drain contacts in our angle-evaporated nanogap is such that graphene flakes (of size comparable to the gap length, $\sim$ 100 nm) are not lying parallel to the electrodes, but they are in a tilted position, as schematically represented in Figure 3.10. This might allow for edge-injection into the graphene sheets.

3.4.2.1 Electronic microscope imaging

Samples have been characterized by Scanning Electron Microscopy (SEM), especially for the determination of the effective width W_{eff}. Figure 3.16 shows images of typical single-dipping by Langmuir-Blodgett deposition (at two different magnifications). The coverage is poor, and this allows distinguishing clearly the graphene nanosheets on the bottom Au electrodes. In Figure 3.16(a) it is clear that they organize in some 'islands', probably deriving from their original disposition on the water surface of the Langmuir-Blodgett bath. If one of these assemblies crosses the nanotrench, the gap is electrically closed.

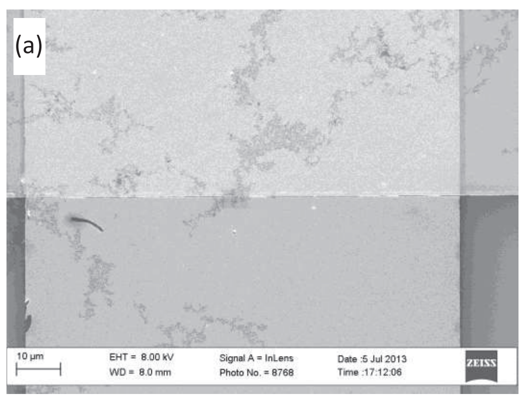

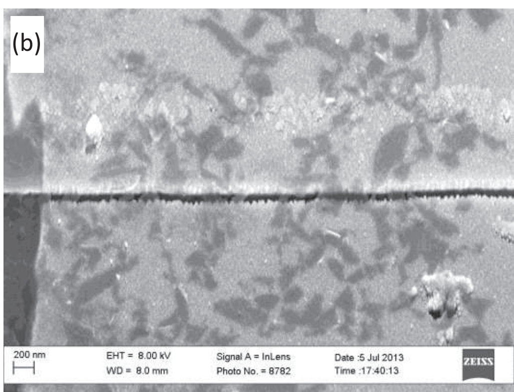

Figure 3.16 SEM images of a nanotrench bridged by LPE-graphene nanosheets, (b) is at higher magnification. Graphene deposited by Langmuir-Blodgett. (Total quantity of LPE-graphene deposited on the water surface was around 35 µg; a short calcination step is performed, 1h at 60°C).

SEM imaging causes a reduction of the resistance, probably due to a local annealing or deposition of carbon based residues after focusing the electron beam on the graphene flakes. For this reason, none of the samples whose electrical characterization is presented has been imaged by SEM before measuring.

Thanks to the possibility of easy removal of the 'cut&stick' iongel (see next paragraph 3.4.3.1), SEM scans could also be taken after measurements. Examples are presented in Figure 3.17. The sample is rinsed with water, dried with nitrogen and put into SEM chamber. Water rinsing does not remove completely iongel residues, but it does not remove graphene nanoflakes from the electrodes.

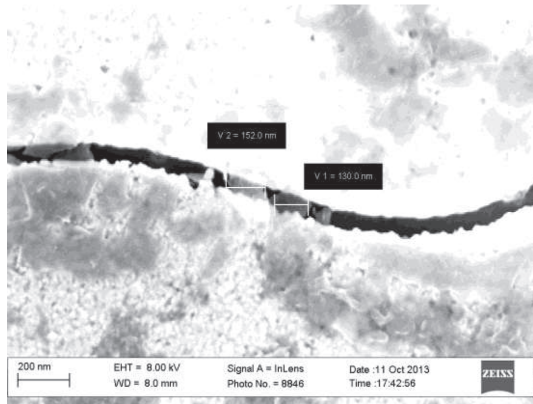

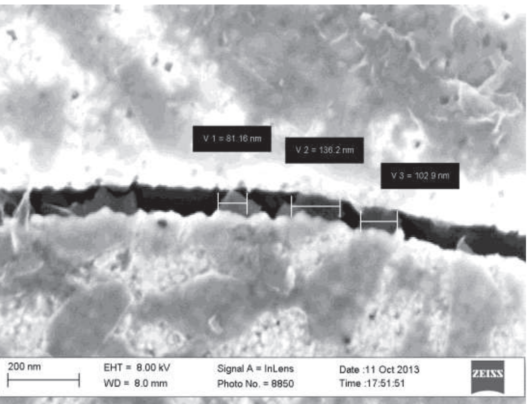

Figure 3.17 SEM images of different zones of the same nanotrench, after measurment. Iongel residues are present, but graphene sheets can be distinguished: we measure them one by one to estimate the effective width W_{eff}.

By scanning along the nanotrench, the graphene nanoflakes bridging the gap can be recognized one by one. Some of them are visibly broken, probably due to the removal of the iongel. By adding up the width of all the graphene nanoflakes that contact both the electrodes, we can estimate the effective width W_{eff} of active graphene channel.

3.4.3 Electrolyte-gating experiment

After optical and electrical check, the samples are put inside glove box, where the electrolyte is stored. There, we finalize the device assembly by placing the electrolyte and we carry out measurements as a function of gate voltage (exceptionally, sample A was measured in air).

3.4.3.1 Iongel preparation

The electrolyte used for this experiment is an iongel composed by a mix of the ionic liquid 1-butyl-3-methylimidazolium, [BMIM][PF_6], and the polymer poly(vinylidene fluoride-*co*hexafluoropropylene), P(VDF-HFP). We follow the recipe of Lee *et al*. [37], using the same polymer matrix with a different ionic liquid (the one we already used for experiments in Chapter 2). The iongel solution for drop-casting is prepared by codissolving P(VDF-HFP) and [BMIM][PF_6] in acetone, with a weight ratio of 1:4:7 between polymer, ionic liquid, and acetone. [BMIM][PF_6] and P(VDF-HFP) are purchased by Sigma-Aldrich. The copolymer P(VDF-HFP) is packaged in the form of pellets: they first need to be smashed in a mortar for long time, for making them properly soluble in acetone. The iongel solution is stirred for several hours and drop-cast on a glass slide. We place the iongel films as-prepared in a vacuum oven at 70°C for 24 h to completely remove residual solvent. The copolymer induces the gelation of the ionic liquid and free-standing iongel layers 2-3 µm thick can be cut with a razor blade, lifted up and transferred on another substrate simply using tweezers. Lee *et al*. report the possibility of spin-coating the iongel solution for the formation of thinner iongel films, but the mechanical robustness of our spin-coated iongel film was not sufficient to permit 'cut&stick' operation. However, since we use a side in-plane gate electrode, the iongel thickness has no influence on our devices. An image of the sample is reported in Figure 3.18. A 'cut&stick' iongel was found to be the most convenient medium for electrolyte-gating, as it is removable from the device after measurement. As already mentioned in the previous paragraph, this has been essential for SEM characterization after measuring.

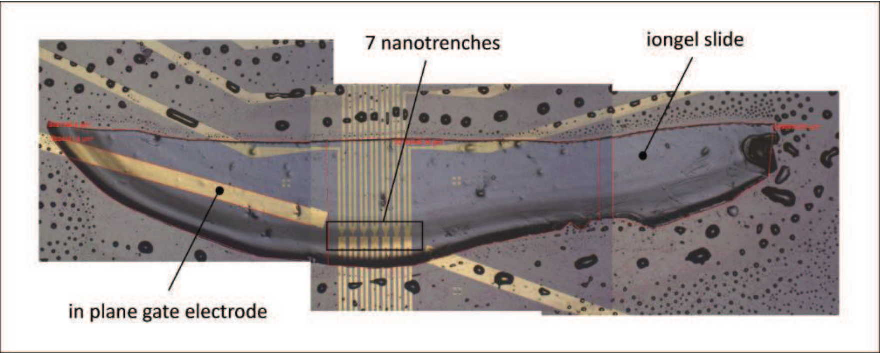

Figure 3.18 Image of the device (collage of different three optical microscope images) showing 7 nanotrenches (in the middle) covered with the iongel slide. On the left it is visible the contact area between the in-plane Au gate electrode and the iongel. Images are taken after measurments. Drops all around are likely ionic liquid that spilled out of the iongel.

3.4.3.2 Transfer curves

We collect I_{sd} – V_g curves by using a two-channel Keithley sourcemeter. The source-drain bias is maintained constant V_d = + 10 mV (E = 10^5 V/m). The gate voltage is swept very slowly (1 mV/s), since *i.* the involved gate-electrodes capacitance are very large and *ii.* the ions mobility in the iongel is limited, thus the charging the electrical double layer at the active channel is not immediate. Figure 3.19 presents the transfer curves of samples A, B and C in terms of source-drain current (I_{sd} - V_g) and resistance (R_{sd} - V_g). We remind that A, B and C correspond to one single nanotrench on a chip. The behavior of other nanotrenches of the same chip has been measured and present similar characteristics.

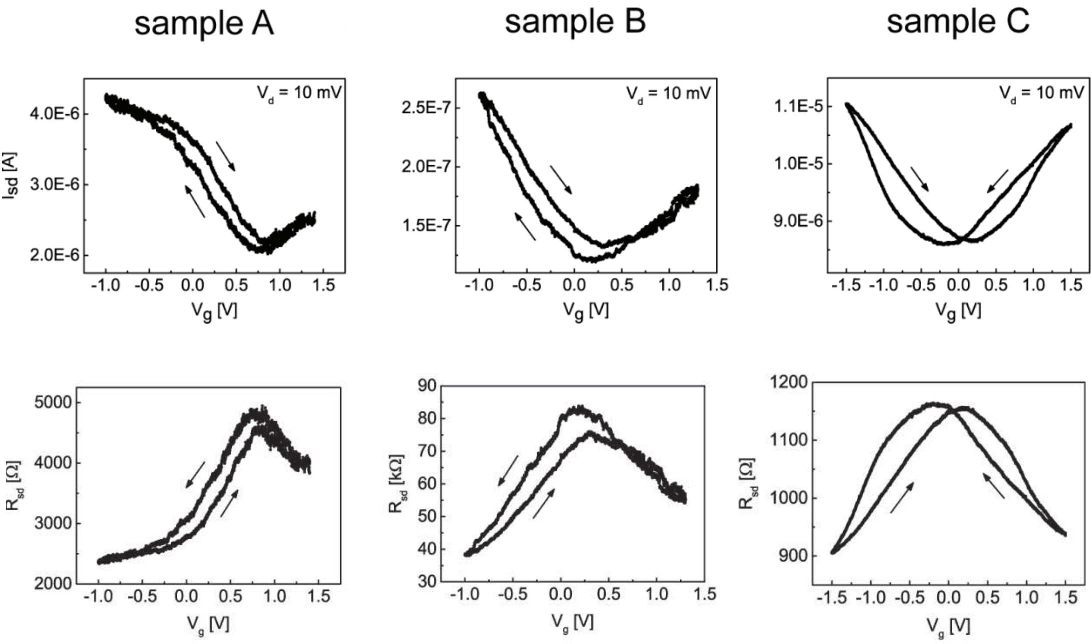

Figure 3.19 I_{sd} - V_g and R_{sd} - V_g curves for sample A, B and C, measured at room temperature.

A clear and systematic ambipolar behavior and Dirac neutrality point emerge for the three samples. Note this is quite remarquable for this type of graphene samples. Prior to quantitative interpretation of the transfer curve, it is necessary to understand and quantify the gating efficiency of the electrolyte. This can be done by analyzing the behavior of the gate current, as discussed below.

3.4.3.3 I_g – V_g curves

We present the associated gate current curves, I_g - V_g, which are fundamental to understand if the electrical double layer charging of the iongel dielectric takes place correctly and to determine its specific capacitance, key for estimate of the mobility. Figure 3.20 illustrates the I_g - V_g curves for the three samples A, B and C. I_g is always 2 orders of magnitude less than the corresponding I_{sd}. However, the diversity between samples A, B and C, proves that the gate/iongel/active channel system follows very different charging mechanisms over the three samples. We explain now the causes of the different behaviors and we elucidate why the most appropriate iongel functioning is represented by sample B.

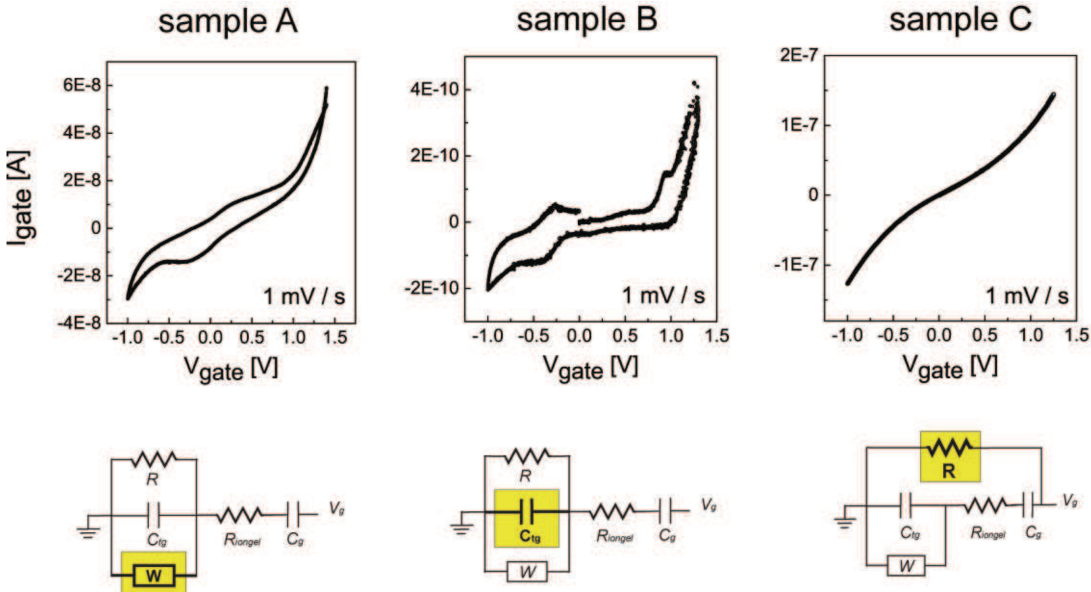

Figure 3.20 I_g - V_g curves for sample A, B and C. Below each plot the assumed equivalent circuit valid for each specific sample is depicted. The yellow box indicates the circuit element that prevails in the circuit.

We presented in Figure 3.6(c) (paragraph 3.3) a simplified circuit model of the iongel, which corresponds to the ideal case in which the electrical double layer at the interface between iongel and active channel is represented by capacitive elements only (C_{tg}). In the real case, an electrical double layer must be modeled by a resistor R, a capacitor C, and a Warburg impedance W in parallel. The resistor R models a parasitic leakage current. The capacitor represents the charge accumulated in the electrical double layer, and the Warburg impedance accounts for charge flowing through the interface due to impurities diffusion to the surface and then being oxidized or reduced. Thus the equivalent circuit of the *iongel/active channel* interface must include a resistor R and a Warburg impedance W elements in parallel to the top-gate capacitor C_{tg} [38], as represented in Figure 3.20. R_{iongel} represents the finite ionic conductivity of the electrolyte.

We believe that the diversity of the I_g – V_g curves between sample A, B and C derives from the prevalence of one or another element of the equivalent circuit. The physical characteristics of sample A, B and C help to explain why one element prevails respect to the others.

Sample A differs from B and C for the absence of the SiO_2 layer covering source and drain electrodes. The iongel is in direct contact with source and drain metallic pads over a very large area, comparable to the gate electrode area ($A_{sd/iongel} \sim A_{gate/iongel}$). The consequences are the following: *i.* the large parasitic source and drain capacitances reduce the effectiveness of the gate potential; *ii.* the charge transfer processes involving reduction/oxidation reactions (represented by the Warburg impedance element) are more probable, owing to the large source-drain metal surface exposed to iongel. Petach *et al*. [38] recently demonstrated that Au surfaces can undergo oxidation and reduction (with formation of few monolayers of Au_2O_3) when exposed to an electrical double layer caused by an ionic liquid polarization at – 2.0 V versus a reference Au electrode. If we perform time integration of the gate current I_g for sample A, we indeed find non-realistic values of total charge accumulated Q and specific capacitance C_i, exceeding by at least one order of magnitude the typical values reported for electrolytes. We conclude that we cannot deduce correctly the charging capacitance of the electrolyte from sample A.

Sample B source and drain metallic pads are covered with 50 nm layer of sputtered SiO_2. A window 150 µm wide is opened at the nanotrench, leaving uncovered an area of $A_{sd/iongel}$ ~ 15000 µm^2 (depending on the nanotrench width, see Figure 3.11). The presence of SiO_2 clearly reduces the parasitic capacitance and surface electrochemical reactions, leading to much lower I_g and clear charging peaks.

Sample C is affected by an excessive quantity of graphene on the substrate due to the heated drop-casting method used for its deposition (Figure 3.12). Consequently, conductive leaking paths connect gate in-plane electrode with source electrode. The gate current I_g of sample C reaches the highest values among the three samples (10^{-7} A); charging effects are completely hidden by the leakage current. The fact that the I_g – V_g curve is not perfectly ohmic and that the corresponding transfer curve shows the ambipolar behavior typical of graphene means that electrical double layer charging is taking place as expected. However, the specific capacitance cannot be calculated from sample C.

This being said, in the next paragraph we will therefore estimate the specific capacitance C_i and the charge accumulated on LPE-graphene by using the I_g – V_g curve of sample B.

3.4.4 Discussion of the results

A clear signature of ambipolar transport and Dirac maximum of resistance is evident for all the three samples, independently of their resistance range. This fact is new for the literature on liquid phase exfoliated graphene, and unique to our device geometry. This likely relates to the remarkable 'efficiency' of electrolyte-gating (high specific capacitance) in terms of creating a large vicinal electric field, and to the fact that we are gating graphene nanoflakes suspended. Li *et al*. [15] do not report any gate-dependency for their e-beam connected single graphene nanosheets, even though they have a gate control available in their device. Their device likely suffers of short-channel effects, i.e. the transverse electric field (gate) is not large enough with respect to the longitudinal one (source-drain) to produce a noticeable I_{sd} modulation as a function of V_g.

3.4.4.1 Electrical double layer specific capacitance C_{EDL}

Specific capacitance measurements of electrolyte-gating by impedance spectroscopy reported in literature for this type of iongels are in the 10 µF/cm^2 range [37] (standard SiO_2 bottom gate, normally in the nF/cm^2 range).

We experimentally calculate the total charge accumulated Q by integration over time of the gate current I_g. This is a common method that has been used by several groups (see Appendix B – Electrolyte-gating). Figure 3.21 shows I_g as a function of gate bias for sample B. Arrows indicate the sweeping direction. In red we point out the two charging peak "shoulders". The 'extra' amount of the current giving rise to the shoulder peaks directly relates to the electrical double layer charging. The peak in the positive I_g region corresponds to the charging of the EDL inducing electrons transport, while the peak in the negative I_g region induces p-type transport. Dividing the total charge Q (calculated by integration of the red area below the shoulder peaks) by the source-drain electrodes area uncovered by SiO_2 (~ 15000 µm^2) leads to an iongel specific capacitance included between 8 µF/cm^2 < C_i < 12 µF/cm^2. The obtained value for C_i is in perfect agreement with results reported in literature.

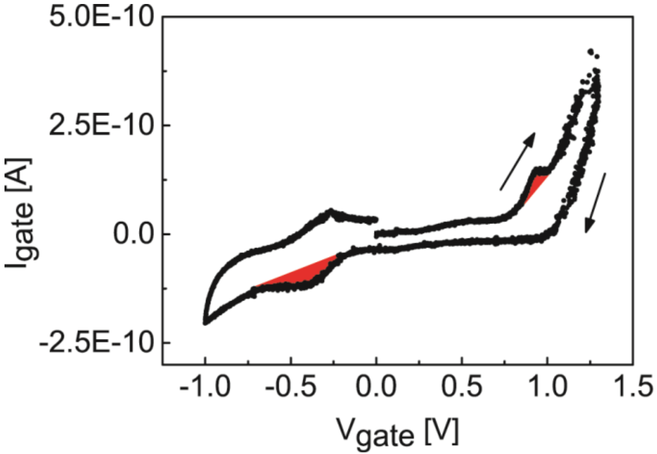

Figure 3.21 Gate current I_g as a function V_g. The colored areas indicate the two shoulder peaks indicating charging of the electrical double layers for electrons (in the positive V_g) and holes transport (in the negative V_g).

By comparing I_g - V_g curves of sample A and B we deduce that the SiO_2 capping layer strongly helps reducing source and drain parasitic capacitance. Thanks to this, the charging of the EDL in the active channel zone can be put into evidence (shoulder peaks integrated in Figure 3.21). Essentially, the 50 nm SiO_2 layer prevents electrochemical reactions at the Au surface, minimizing the Warburg impedance. In order to reduce parasitic capacitance even more, one should be able to shrink the size of the iongel slide, ultimately covering the active channel area only, and not source-drain electrodes. Such request is very challenging in case of nanometric channel device.

3.4.4.2 Mobility estimation

Knowing the top-gate specific capacitance, electron and holes mobility can be extracted from the transfer curve, according to equation:

$$\mu = \frac{L}{W}\frac{1}{C_{tg}}\frac{1}{V_d}\frac{\Delta I_{sd}}{\Delta V_g}$$

3.3.

By integrating the gate current we have obtained an electrical double layer specific capacitance ranging from 8 μC/cm² < C_{EDL} < 12 μC/cm² (also called “geometric” capacitance). Such value is comparable to quantum capacitance of graphene, already discussed in paragraph 3.3.1); hence, we cannot neglect C_q in our mobility estimation. The C_q value from literature ranges from 2 μF/cm² to 10 μF/cm², depending on the vicinity of E_F to the Dirac point of neutrality [28]. We recall that the total top-gate capacitance C_{tg} is:

$$\frac{1}{C_{tg}} = \frac{1}{C_q} + \frac{1}{C_{EDL}}$$

3.5.

In Figure 3.22 we report for clarity the transfer curve of sample B. Red lines represent the range we consider for the estimation of $\Delta I_{sd}/\Delta V_g$. Observing the slopes of the right-branch and left-branch of the transfer curve we expect values of electrons and holes mobility of the same order of magnitude (if we consider the capacitance C_{tg} symmetric on the two sides of the Dirac point).

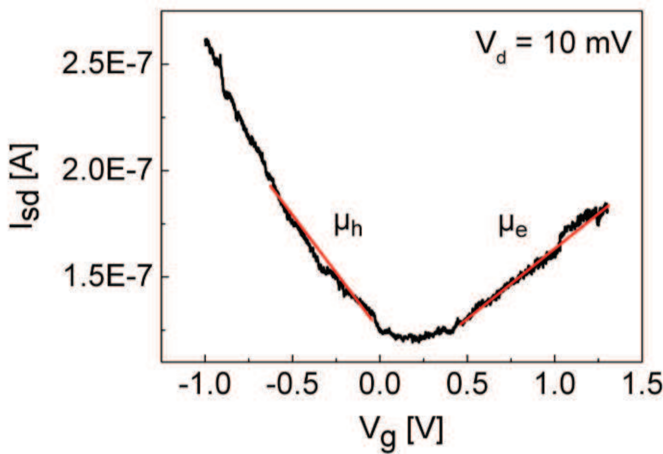

Figure 3.22 Transfer curve $I_{sd} - V_g$ for sample B used for electrons and holes mobility extraction.

We obtain an electron mobility value included between 0.04 cm^2/V·s and 0.12 cm^2/V·s, depending on the quantum capacitance value considered, respectively C_q = 10 μF/cm^2 and 2 μF/cm^2 (for C_{EDL} we take an average value = 10 μF/cm^2). Holes mobility is between 0.06 cm^2/V·s and 0.18 cm^2/V·s. Values are summarized in Table 3.2.

	C_q = 10 μF/cm^2	C_q = 2 μF/cm^2
$\mu_{electron}$	0.04 cm^2/V·s	0.12 cm^2/V·s
μ_{hole}	0.06 cm^2/V·s	0.18 cm^2/V·s

Table 3.2 Mobility estimates for LPE-graphene, derived from the slope of the transfer curves.

Even though it leads to smaller values of mobility, it is realistic to consider a value of quantum capacitance equal to 10 μF/cm^2 in our calculation because the slope of the I_{sd} - V_g curve for the extraction of $\Delta I_{sd}/\Delta V_g$ is not taken exactly at the Dirac point, but ± 0.25 V of V_g apart. Far from the Dirac point the quantum capacitance can reach 8 - 10 μF/cm^2 (see Figure 3.6(b)). Moreover, the quantum capacitance of bi- and tri-layer graphene is little augmented respect to a single layer [39], and we should consider that our LPE-graphene presents a certain percentage of bi and trilayer flakes.

The main incertitude in the mobility estimation is the effective width W_{eff}. For sample B we consider a W_{eff} ~ 1.5 μm, estimated from SEM imaging after measuring (Figure 3.17). Calculated mobility from samples A and C lead to similar values because their lower resistance is due to a major quantity of graphene material (W_{eff} ~ 20 μm).

The mobility values as obtained are disappointing for graphene. We expected to find higher values of mobility respect to LPE-graphene-films, because our devices are supposed not to be affected by the flake-to-flake hopping processes. However, contact resistance strongly limits our devices. The mobility values we provide are certainly lowered by contact resistance. They are two orders of magnitude lower than values reported for ink-jet printed films by Torrisi *et al*. [23] and for Langmuir-Blodgett films by Parvez *et al*. [20],[17]. In any case, they are roughly equal to the results obtained by Kim *et al*. [25] (μ_{hole} 0.9 cm^2/V·s, $\mu_{electron}$ = 0.09 cm^2/V·s) and Ciesielsky *et al*. [24] (0.3 – 1 cm^2/V·s) on LPE-graphene thin films.

3.4.4.1 Position of the Dirac neutrality point, smoothness and hysteresis

The position of the Dirac neutrality point V_{Dirac} usually gives information on the intrinsic and extrinsic doping of graphene. In general, LPE-graphene is often found to be p-doped (paragraph 3.3.2), both in the form of single sheets and thin films.

In our samples, the smoothness of the Dirac maximum of resistance and the hysteresis between the curves backward and forward make difficult the assignment of the Dirac point at a certain value of V_g. However, we can roughly locate the Dirac point for sample A, B and C respectively at V_g = + 0.8 V, + 0.25 V and 0 V. V_{Dirac} resulting for Sample A should not be considered because strongly affected by the absence of the SiO_2 capping layer over source-drain electrodes. For samples B and C, V_{Dirac} is equal or close to V_g = 0 V (since the transfer curves of A and B are hysteretic, V_{Dirac} is taken as the average value between the two Dirac minimum of conductivity). This is in agreement with the fact that suspended graphene should be free of substrate-induced charged impurities, if other factors such as chemical doping or defects are absent. However, it must be considered that the contact with an electrolyte shifts V_{Dirac} towards 0 V [40],[41],[42]. This happens because ions in the iongel neutralize very effectively the charged impurities present on graphene sheets, thus “compensating” their intrinsic doping. In our experiment, we are not able to distinguish which one of these two possible reasons accounts for the V_{Dirac} close to 0 Volts.

Another experimental observation is that the Dirac minimum of conductivity/maximum of resistance is significantly more round than what would be expected from thermal smearing at room temperature. We attribute the smoothness of the Dirac point in our devices to different factors. First of all in our device we measure several single flakes in a parallel configuration, thus the outcome of our measurement is an average of their properties. Evidently, each flake is characterized by a slightly different number of traps and defects, thus the intrinsic doping level varies from one to another, and consequently their V_{Dirac}. Secondly, it has been calculated that the quantum capacitance minimum at the Dirac point is round in presence of a certain density of charged impurities (instead of the sharp theoretical V-shape, when the defect density is negligible, Figure 3.6(b)). Therefore, the shape of the quantum capacitance might be reflected on the Dirac minimum of conductivity.

The hysteresis of the curves for samples B and C is likely due to capacitive coupling. Capacitive coupling mainly involves the presence of residual charges at the graphene/dielectric interface remaining after a certain gate sweep, resulting in a ‘fake’ amount of doping on graphene (enhancement of carrier density): V_{Dirac} moves towards n-type doping if accumulated charges were electrons, and viceversa, giving rise to a negative hysteresis. We observe a small negative hysteresis on sample B ($\Delta V_{hyst} \sim 0.15$ V) and more accentuated on sample C ($\Delta V_{hyst} \sim 0.7$ V). This type of hysteresis is typically observed in electrolyte-gated graphene FETs [43].

3.4.4.1 I_{on}/I_{off} ratio

All the three samples A, B and C present a very poor I_{on}/I_{off} ratio, lower than 2, mainly because the off-current I_{off} value remains always very high. Switching off conduction in graphene is a very well-known problem also for standard dielectrics graphene-FETs [44],[45]. The main reason is the absence of a bandgap in graphene.

3.5 Conclusions

In this Chapter we have demonstrated the successful gating of nanosized (200 – 300 nm) graphene sheets obtained by liquid phase exfoliation of graphite. We are not aware of other reports in which a clear Dirac maximum of resistance and ambipolar behavior have been observed in graphene flakes with nanometric dimensions. The success of our experiment likely results from the high capacitance of the electrolyte used as gating medium.

The deposition of the material itself has also been a challenging part of the experiment, because the behavior of this graphene “ink” on surfaces is not straightforward and it has been initially hard to deposit a quantity of material sufficient for the measurements.

By bridging directly each nanosheet with metallic electrodes, thanks to the use of nanogaps, we were hoping to bypass the limitation related to inter-flake hopping affecting graphene-ink thin film devices and to obtain lower sheet resistance and higher mobility. However, we find out that contact resistance strongly limits the performance of our “graphene nano-FET”. This is probably due to the fact that the graphene flakes are just placed above pre-patterned electrodes, thus the contact is not as intimate as it would be by evaporating metals on pre-deposited graphene. We estimate a contact resistance between 0.5 Ω·cm and 3 Ω·cm, 10- to 100-fold higher than for STANWs (Chapter 2). Although the extracted values of electrons and holes mobility are contact-limited, they are disappointingly small for graphene standards: $\mu_{h/e}$ does not go above 0.2 $cm^2/V \cdot s$.

In order to use this material as organic spacer in lateral spinvalves, one should first find solutions to reduce its contact resistance with electrodes.

BIBLIOGRAPHY

[1] A. K. Geim and K. S. Novoselov, "The rise of graphene," *Nat. Mater.*, vol. 6, no. 3, pp. 183–191, Mar. 2007.

[2] E. W. Hill, A. Geim, K. Novoselov, F. Schedin, and P. Blake, "Graphene Spin Valve Devices," *IEEE Trans. Magn.*, vol. 42, no. 10, pp. 2694–2696, Oct. 2006.

[3] N. Tombros, C. Jozsa, M. Popinciuc, H. T. Jonkman, and B. J. van Wees, "Electronic spin transport and spin precession in single graphene layers at room temperature," *Nature*, vol. 448, no. 7153, pp. 571–574, Aug. 2007.

[4] M. Popinciuc, C. Józsa, P. J. Zomer, N. Tombros, A. Veligura, H. T. Jonkman, and B. J. van Wees, "Electronic spin transport in graphene field-effect transistors," *Phys. Rev. B*, vol. 80, no. 21, p. 214427, Dec. 2009.

[5] A. Avsar, T.-Y. Yang, S. Bae, J. Balakrishnan, F. Volmer, M. Jaiswal, Z. Yi, S. R. Ali, G. Güntherodt, B. H. Hong, B. Beschoten, and B. Özyilmaz, "Toward Wafer Scale Fabrication of Graphene Based Spin Valve Devices," *Nano Lett.*, vol. 11, no. 6, pp. 2363–2368, 2011.

[6] M. V. Kamalakar, A. Dankert, J. Bergsten, T. Ive, and S. P. Dash, "Spintronics with graphene-hexagonal boron nitride van der Waals heterostructures," *Appl. Phys. Lett.*, vol. 105, no. 21, p. 212405, Nov. 2014.

[7] B. Dlubak, M.-B. Martin, C. Deranlot, B. Servet, S. Xavier, R. Mattana, M. Sprinkle, C. Berger, W. A. De Heer, F. Petroff, A. Anane, P. Seneor, and A. Fert, "Highly efficient spin transport in epitaxial graphene on SiC," *Nat. Phys.*, vol. 8, no. 7, pp. 557–561, Jul. 2012.

[8] B. Náfrádi, M. Choucair, and L. Forró, "Spin lifetime of itinerant electrons in chemically synthesized graphene multi-layers," *Carbon*, vol. 74, pp. 346–351, Aug. 2014.

[9] K. S. Novoselov, A. K. Geim, S. V. Morozov, D. Jiang, Y. Zhang, S. V. Dubonos, I. V. Grigorieva, and A. A. Firsov, "Electric Field Effect in Atomically Thin Carbon Films," *Science*, vol. 306, no. 5696, pp. 666–669, Oct. 2004.

[10] X. Li, W. Cai, J. An, S. Kim, J. Nah, D. Yang, R. Piner, A. Velamakanni, I. Jung, E. Tutuc, S. K. Banerjee, L. Colombo, and R. S. Ruoff, "Large-Area Synthesis of High-Quality and Uniform Graphene Films on Copper Foils," *Science*, vol. 324, no. 5932, pp. 1312–1314, Jun. 2009.

[11] S. Bae, H. Kim, Y. Lee, X. Xu, J.-S. Park, Y. Zheng, J. Balakrishnan, T. Lei, H. Ri Kim, Y. I. Song, Y.-J. Kim, K. S. Kim, B. Özyilmaz, J.-H. Ahn, B. H. Hong, and S. Iijima, "Roll-to-roll production of 30-inch graphene films for transparent electrodes," *Nat. Nanotechnol.*, vol. 5, no. 8, pp. 574–578, Aug. 2010.

[12] L. Zhi and K. Müllen, "A bottom-up approach from molecular nanographenes to unconventional carbon materials," *J. Mater. Chem.*, vol. 18, no. 13, p. 1472, 2008.

[13] C. Gómez-Navarro, R. T. Weitz, A. M. Bittner, M. Scolari, A. Mews, M. Burghard, and K. Kern, "Electronic Transport Properties of Individual Chemically Reduced Graphene Oxide Sheets," *Nano Lett.*, vol. 7, no. 11, pp. 3499–3503, 2007.

[14] Y. Hernandez, V. Nicolosi, M. Lotya, F. M. Blighe, Z. Sun, S. De, I. T. McGovern, B. Holland, M. Byrne, Y. K. Gun'Ko, J. J. Boland, P. Niraj, G. Duesberg, S. Krishnamurthy, R. Goodhue, J. Hutchison, V. Scardaci, A. C. Ferrari, and J. N. Coleman, "High-yield production of graphene by liquid-phase exfoliation of graphite," *Nat. Nanotechnol.*, vol. 3, no. 9, pp. 563–568, Sep. 2008.

[15] X. Li, G. Zhang, X. Bai, X. Sun, X. Wang, E. Wang, and H. Dai, "Highly conducting graphene sheets and Langmuir–Blodgett films," *Nat. Nanotechnol.*, vol. 3, no. 9, pp. 538–542, Aug. 2008.

[16] L. Wu, W. Li, P. Li, S. Liao, S. Qiu, M. Chen, Y. Guo, Q. Li, C. Zhu, and L. Liu, "Powder, Paper and Foam of Few-Layer Graphene Prepared in High Yield by Electrochemical Intercalation Exfoliation of Expanded Graphite," *Small*, vol. 10, no. 7, pp. 1421–1429, Apr. 2014.

[17] K. Parvez, Z.-S. Wu, R. Li, X. Liu, R. Graf, X. Feng, and K. Müllen, "Exfoliation of Graphite into Graphene in Aqueous Solutions of Inorganic Salts," *J. Am. Chem. Soc.*, vol. 136, no. 16, pp. 6083–6091, Apr. 2014.

[18] F. Bonaccorso, A. Lombardo, T. Hasan, Z. Sun, L. Colombo, and A. C. Ferrari, "Production and processing of graphene and 2d crystals," *Mater. Today*, vol. 15, no. 12, pp. 564–589, Dec. 2012.

[19] A. Ciesielski and P. Samorì, "Graphene via sonication assisted liquid-phase exfoliation," *Chem. Soc. Rev.*, 2013.

[20] K. Parvez, R. Li, S. R. Puniredd, Y. Hernandez, F. Hinkel, S. Wang, X. Feng, and K. Müllen, “Electrochemically Exfoliated Graphene as Solution-Processable, Highly Conductive Electrodes for Organic Electronics,” *ACS Nano*, vol. 7, no. 4, pp. 3598–3606, Apr. 2013.

[21] M. Choucair, P. Thordarson, and J. A. Stride, “Gram-scale production of graphene based on solvothermal synthesis and sonication,” *Nat. Nanotechnol.*, vol. 4, no. 1, pp. 30–33, Jan. 2009.

[22] W. Qian, R. Hao, Y. Hou, Y. Tian, C. Shen, H. Gao, and X. Liang, “Solvothermal-assisted exfoliation process to produce graphene with high yield and high quality,” *Nano Res.*, vol. 2, no. 9, pp. 706–712, Sep. 2009.

[23] F. Torrisi, T. Hasan, W. Wu, Z. Sun, A. Lombardo, T. S. Kulmala, G.-W. Hsieh, S. Jung, F. Bonaccorso, P. J. Paul, D. Chu, and A. C. Ferrari, “Inkjet-Printed Graphene Electronics,” *ACS Nano*, vol. 6, no. 4, pp. 2992–3006, Apr. 2012.

[24] A. Ciesielski, S. Haar, M. El Gemayel, H. Yang, J. Clough, G. Melinte, M. Gobbi, E. Orgiu, M. V. Nardi, G. Ligorio, V. Palermo, N. Koch, O. Ersen, C. Casiraghi, and P. Samorì, “Harnessing the Liquid-Phase Exfoliation of Graphene Using Aliphatic Compounds: A Supramolecular Approach,” *Angew. Chem. Int. Ed.*, p. n/a–n/a, Jul. 2014.

[25] H. Kim, C. Mattevi, H. J. Kim, A. Mittal, K. A. Mkhoyan, R. E. Riman, and M. Chhowalla, “Optoelectronic properties of graphene thin films deposited by a Langmuir–Blodgett assembly,” *Nanoscale*, vol. 5, no. 24, p. 12365, 2013.

[26] J. Martin, N. Akerman, G. Ulbricht, T. Lohmann, J. H. Smet, K. von Klitzing, and A. Yacoby, “Observation of electron–hole puddles in graphene using a scanning single-electron transistor,” *Nat. Phys.*, vol. 4, no. 2, pp. 144–148, Feb. 2008.

[27] A. Das, S. Pisana, B. Chakraborty, S. Piscanec, S. K. Saha, U. V. Waghmare, K. S. Novoselov, H. R. Krishnamurthy, A. K. Geim, A. C. Ferrari, and A. K. Sood, “Monitoring dopants by Raman scattering in an electrochemically top-gated graphene transistor,” *Nat. Nanotechnol.*, vol. 3, no. 4, pp. 210–215, Mar. 2008.

[28] J. Xia, F. Chen, J. Li, and N. Tao, “Measurement of the quantum capacitance of graphene,” *Nat. Nanotechnol.*, vol. 4, no. 8, pp. 505–509, Jul. 2009.

[29] S. Luryi, “Quantum capacitance devices,” *Appl. Phys. Lett.*, vol. 52, no. 6, pp. 501–503, Feb. 1988.

[30] J. Ye, M. F. Craciun, M. Koshino, S. Russo, S. Inoue, H. Yuan, H. Shimotani, A. F. Morpurgo, and Y. Iwasa, “Accessing the transport properties of graphene and its multilayers at high carrier density,” *Proc. Natl. Acad. Sci.*, vol. 108, no. 32, pp. 13002–13006, 2011.

[31] H. Xu, Z. Zhang, Z. Wang, S. Wang, X. Liang, and L.-M. Peng, “Quantum Capacitance Limited Vertical Scaling of Graphene Field-Effect Transistor,” *ACS Nano*, vol. 5, no. 3, pp. 2340–2347, Mar. 2011.

[32] M. El Gemayel, S. Haar, F. Liscio, A. Schlierf, G. Melinte, S. Milita, O. Ersen, A. Ciesielski, V. Palermo, and P. Samorì, “Leveraging the Ambipolar Transport in Polymeric Field-Effect Transistors via Blending with Liquid-Phase Exfoliated Graphene,” *Adv. Mater.*, vol. 26, no. 28, pp. 4814–4819, Jul. 2014.

[33] C. Gong, S. McDonnell, X. Qin, A. Azcatl, H. Dong, Y. J. Chabal, K. Cho, and R. M. Wallace, “Realistic Metal–Graphene Contact Structures,” *ACS Nano*, vol. 8, no. 1, pp. 642–649, Jan. 2014.

[34] F. Xia, V. Perebeinos, Y. Lin, Y. Wu, and P. Avouris, “The origins and limits of metal–graphene junction resistance,” *Nat. Nanotechnol.*, vol. 6, no. 3, pp. 179–184, Mar. 2011.

[35] W. S. Leong, H. Gong, and J. T. L. Thong, “Low-Contact-Resistance Graphene Devices with Nickel-Etched-Graphene Contacts,” *ACS Nano*, vol. 8, no. 1, pp. 994–1001, Jan. 2014.

[36] L. Wang, I. Meric, P. Y. Huang, Q. Gao, Y. Gao, H. Tran, T. Taniguchi, K. Watanabe, L. M. Campos, D. A. Muller, J. Guo, P. Kim, J. Hone, K. L. Shepard, and C. R. Dean, “One-Dimensional Electrical Contact to a Two-Dimensional Material,” *Science*, vol. 342, no. 6158, pp. 614–617, Nov. 2013.

[37] K. H. Lee, M. S. Kang, S. Zhang, Y. Gu, T. P. Lodge, and C. D. Frisbie, “‘Cut and Stick’ Rubbery Ion Gels as High Capacitance,” *Adv. Mater.*, vol. 24, no. 32, pp. 4457–4462, 2012.

[38] T. A. Petach, M. Lee, R. C. Davis, A. Mehta, and D. Goldhaber-Gordon, “Mechanism for the large conductance modulation in electrolyte-gated thin gold films,” *Phys. Rev. B*, vol. 90, no. 8, p. 081108, Aug. 2014.

[39] E. Uesugi, H. Goto, R. Eguchi, A. Fujiwara, and Y. Kubozono, “Electric double-layer capacitance between an ionic liquid and few-layer graphene,” *Sci. Rep.*, vol. 3, Apr. 2013.

[40] C.-H. Kim and C. D. Frisbie, “Determination of Quantum Capacitance and Band Filling Potential in Graphene Transistors with Dual Electrochemical and Field-Effect Gates,” *J. Phys. Chem. C*, vol. 118, no. 36, pp. 21160–21169, Sep. 2014.
[41] F. Chen, J. Xia, and N. Tao, “Ionic Screening of Charged-Impurity Scattering in Graphene,” *Nano Lett.*, vol. 9, no. 4, pp. 1621–1625, Apr. 2009.
[42] Z. L. Mišković, P. Sharma, and F. O. Goodman, “Ionic screening of charged impurities in electrolytically gated graphene,” *Phys. Rev. B*, vol. 86, no. 11, p. 115437, Sep. 2012.
[43] H. Wang, Y. Wu, C. Cong, J. Shang, and T. Yu, “Hysteresis of Electronic Transport in Graphene Transistors,” *ACS Nano*, vol. 4, no. 12, pp. 7221–7228, Dec. 2010.
[44] M. C. Lemme, T. J. Echtermeyer, M. Baus, and H. Kurz, “A Graphene Field-Effect Device,” *IEEE Electron Device Lett.*, vol. 28, no. 4, pp. 282–284, Apr. 2007.
[45] B. Huard, J. A. Sulpizio, N. Stander, K. Todd, B. Yang, and D. Goldhaber-Gordon, “Transport measurements across a tunable potential barrier in graphene,” *Phys. Rev. Lett.*, vol. 98, no. 23, Jun. 2007.

4. Highly doped polymer semiconductor (PBTTT)

Organic single crystals such as rubrene or pentacene can reach charge carriers mobility μ of 10 - 20 $cm^2/V \cdot s$ thanks to their highly ordered molecular packing, but they lack the ease of processability required for applications in Organic Electronics. For this reason organic polymers and soluble small-molecules semiconductors have been developed, making possible solution processing on large area (flexible) substrates and simple thin films fabrication. Nonetheless, the price to pay for the convenience of solution-processable organic semiconductors is a lower degree of structural order of the material. The degree of structural order and the defects density play a critical role in charge transport of organic semiconductors: disorder and defects are usually synonyms of hopping transport and low carriers mobility, i.e. electric conductivities much lower than inorganic semiconductors.

To overcome this issue and enhance the conductivity of conjugated polymer semiconductors, two main approaches can be used: crystallinity improvement and chemical doping. Conductivity is indeed the product of electronic mobility and number of carriers $\sigma = e \cdot \mu \cdot n$ (where e is the electron charge). The chemical doping acts on the density of carriers n inside the polymeric active channel, increasing it by ions compensation. This approach is well known since a few decades, with bulk polyaniline or polypirrole subject to strong doping (oxidation) reaching conductivities of hundreds S/cm. The other popular approach for enhancing the conductivity is to tune the chemical properties of the monomeric units in order to increase the degree of crystallinity of the thin film. In the last years, tremendous progress has been achieved: new classes of semicrystalline polymer semiconductors with field-effect mobilities μ above 0.5 $cm^2/V \cdot s$, exceeding the one of amorphous silicon (a-Si), have been synthetized, such as polythiophene copolymers ([1], p-type), and naphthalene and perylene diimide copolymers ([2], n-type).

In our work we take advantage of both these approaches. We focus our study on a well known semi-crystalline polythiophene, namely poly(2,5-*bis*(3-dodecyl-2-yl)-thieno[3,2-*b*]thiophene (C12-PBTTT), and we use electrolyte-gating (doping) to enhance its conductivity even further. It must be noted that the electrochemical doping is here gate-controlled and applied to thin films, thus of great relevance for today's organic transistor device applications. We investigate the gate-dependence, temperature-dependence and magnetic field dependence of PBTTT thin films transport properties. The outcomes of this detailed study are very promising: record conductivity values > 1000 S/cm and strong experimental indications of the occurrence of a delocalized transport mechanism.

4.1 Crystalline conjugated polythiophenes

Polythiophenes are made of aromatic thiophene rings, in Figure 4.1(a), coupled together in their 2nd and 5th position to form an extended delocalized electronic π-orbital. Poly(3-hexilthiophene) (P3HT), in Figure 4.1(b), has been the first polythiophene to become a benchmark semiconducting polymer. Along the chain, the thiophene rings are ideally coplanar. Solubility of the polymer is induced through the attachment of aliphatic side units projecting from the backbone, giving rise to the term ''hairy rod'' to describe the conformation of these polymers.

In P3HT, the hexil chains can be all pointing towards the same side of the backbone plane (100% regioregularity), or be randomly oriented. Their orientation depends on the head-to-tail attachments of thiophene monomers during polymerization. A random orientation of the lateral aliphatic chains hampers a good crystalline arrangement of the polymeric fibers, causing twists of the backbone that weaken the conjugation and worsen the carriers mobility (down to 10^{-4} $cm^2/V{\cdot}s$). When regioregular P3HT is instead organized in a lamellar structure, with two-dimensional conjugated sheets perpendicular to the sample plane in an edge-on configuration, as illustrated in Figure 4.1(c), the charge mobility can reach values up to 0.1 $cm^2/V{\cdot}s$. The discovery of the remarkable mobility enhancement in regioregular P3HT [3] has been the starting point for studying how a highly microcrystalline structure of the material is key for optimal electronic performances.

(a)

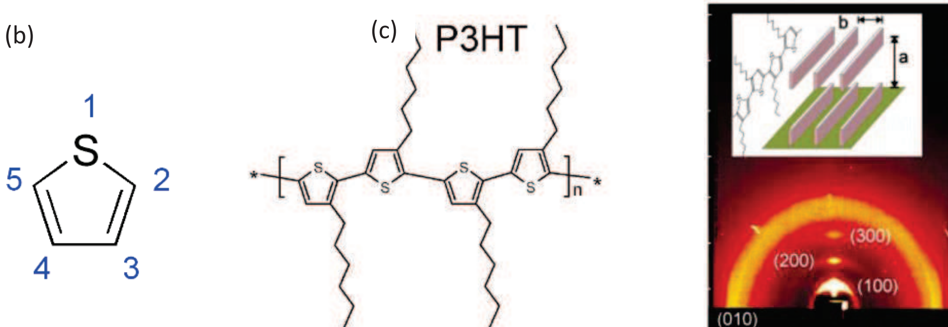

Figure 4.1 a) Thiophene ring monomeric unit and position numbers. b) Poly(3-hexilthiophene), P3HT, "hairy rod" structure. c) Edge-on conformation of highly regioregular P3HT (90% regioregularity), leading to higher mobility value: 0.1 $cm^2/V{\cdot}s$ [3].

4.1.1 Molecular structure and crystalline arrangement of PBTTT

To avoid regio-irregularities, chemists have synthesized polymers using centrosymmetric monomers. Poly(2,5-Bis(3-alkylthiophen-2-yl)thieno[3,2-b]thiophene (PBTTT) is an example of this type of polymers. PBTTT is an alternating copolymer of thieno[3,2-b]thiophene and 4,4-dialkyl 2,2-bithiophene monomer units, synthesized for the first time in 2006 by McCulloch *et al.* [4]. The two monomers and the final PBTTT 'hairy rod' structure are represented in Figure 4.2(a). The density of lateral aliphatic chains is reduced respect to P3HT, favoring their interdigitation inside the lamellae. The typical crystalline arrangement of PBTTT is edge-on, i.e. the rings are perpendicular to the sample plane and polymer backbones lie parallel to the substrate [5], as illustrated in Figure 4.2(b). The conjugation plane is slightly tilted respect to the substrate normal (~ 22°). The dense interdigitation between lateral aliphatic chains of neighboring polymer backbones is visible from the front view in Figure 4.2(c).

The high degree of orientation of the crystalline domains in these films is advantageous for charge transport. In the original paper of PBTTT synthesis, holes mobility up to 0.2 – 0.6 cm2/V·s were reported for bottom-gate FET devices [4]. Since then, PBTTT established as new benchmark conjugated polymer for organic electronics thin films.

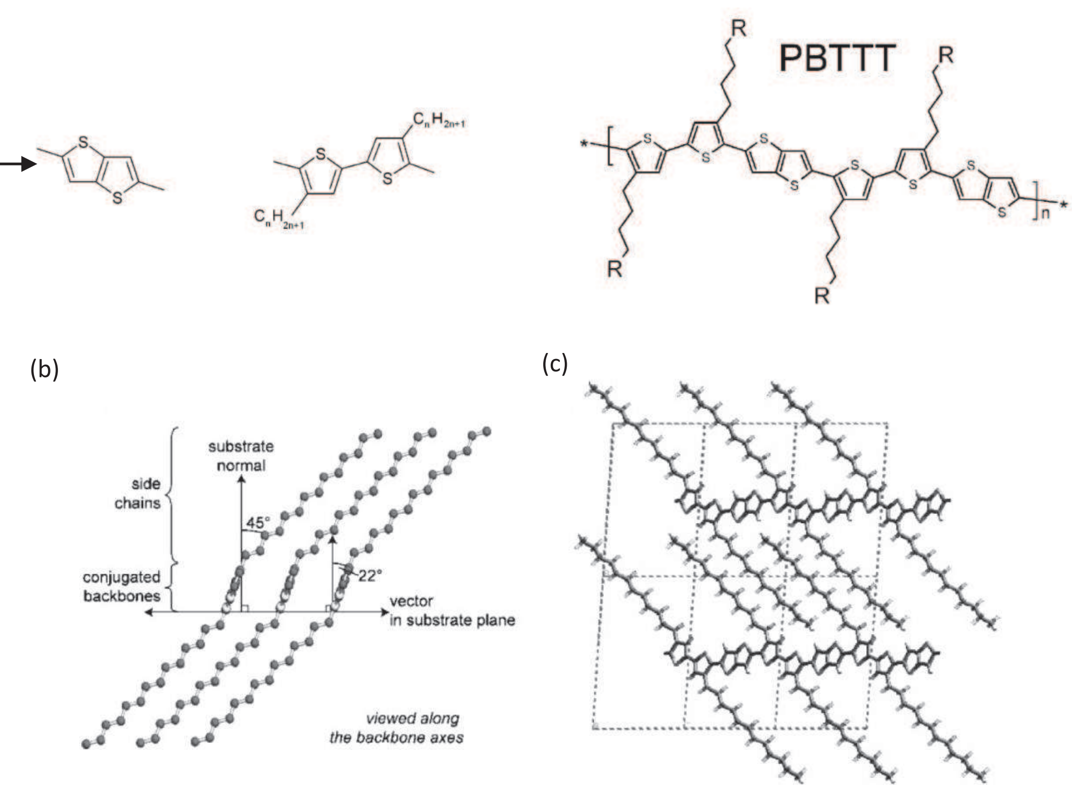

Figure 4.2 a) Centrosymmetric monomers PBTTT and its structure. b,c) Molecular packing of the crystalline domains in a PBTTT thin film.

4.2 Charge transport physics of conjugated polymers (at low carrier densities)

In a conjugated polymer, the strong bonds between sp_2 hybridized atomic orbitals of adjacent carbon atoms yield to bonding σ and antibonding $\sigma*$ molecular orbitals. The remaining p_z orbitals atoms overlap to a smaller degree and result in the frontier bonding π and antibonding π* orbitals of the polymer, respectively the highest occupied molecular orbital (HOMO) and lowest occupied molecular orbital (LUMO). In a hypothetical, infinitely long (and straight) polymer chain, HOMO and LUMO are fully delocalized along the polymer chain. When an additional electron is accommodated in the $\pi*$ antibonding orbital, or removed from the π bonding orbital, for example by injection/extraction from metallic electrodes or reduction/oxidation by a dopant molecule, a charge excited state is formed and charge transport takes place through the polymer. The addition or removal of an electron alters the spatial distribution of the electrons located in the remaining binding orbitals of the polymer, resulting in a different local molecular geometry. This spatial distortion is known as *polaron*, and the energy associated to its formation is called “geometric reorganization energy”. Polarons are direct manifestation of the low dielectric constant of organic semiconductors ($\varepsilon \sim 3$) and they are absent in their inorganic counterpart, where localized charges are more efficiently screened ($\varepsilon \sim 11$) [6].

The electronic structure of a conjugated polymer results from the interplay of the intrinsic π-delocalization along the polymer backbone and the existence of disorder. Strong π-delocalization along the polymer backbone leads to one-dimensional bands with bandwidths of several electron volts [7]. This picture of conjugated polymers electronic properties is close to the approach used for inorganic semiconductors and was used by Su, Schrieffer, and Heeger to explain charge transport in polyacetilene [8]. However, the 1D-semiconductor band model cannot provide the correct description of charge transport in the majority of the conjugated polymers where the effect of disorder is predominant.

The term "disorder" can relate to *dynamic* disorder and *static* disorder. Dynamic disorder is due to intra-chain and inter-chain molecular vibrations. As above-mentioned, a charged excited state in the conjugated polymer is stabilized by a molecular distortion of an amount equal to the reorganization energy (or polaron binding energy). For charge transport to take place (i.e. a charge should 'jump' from one molecular distortion to the neighboring one), this energy needs to be overcome by thermal activation. Such energy is provided by phonons. The transport is thus described as a phonon-assisted hopping process and consequently it is strongly temperature dependent. On one hand molecular vibrations assist the charge transport but, at the same time, they are themselves cause of coherence destruction and shortening of the conjugation length along the chain.

The static disorder often prevails over dynamic disorder. Static disorder is mainly caused by variations of the polymer backbone conformation such as twists or chemical impurities. Ionized dopants in the vicinity of the polymer backbone, or randomly disposed dipoles from a neighboring dielectric (gate dielectric in OFET structure for example) are other important sources of static disorder.

Generally speaking, the presence of disorder breaks the π-conjugation and consequently shortens the length over which a carrier can move coherently. A real polymeric chain does not present orbital wavefunctions delocalized over its whole length (1D semiconductor band picture is inappropriate), but it is rather composed by a series of short conjugated segments extended over few monomers. In the framework of inorganic semiconductors the disorder-concept was developed by Anderson in 1958 [9]. He pointed out that, if disorder is sufficiently strong, the Bloch electronic wavefunctions may become localized (Anderson localization).

If the polymer is rigid and well ordered, the effective conjugation length (also called 'localization length', LL) becomes longer than the one of amorphous polymers and can reach 10 – 15 repeat units [6]. Recently it has been demonstrated that a strong influence on the average effective conjugation length is exercised by torsional displacements of the polymer backbone [10], [11].

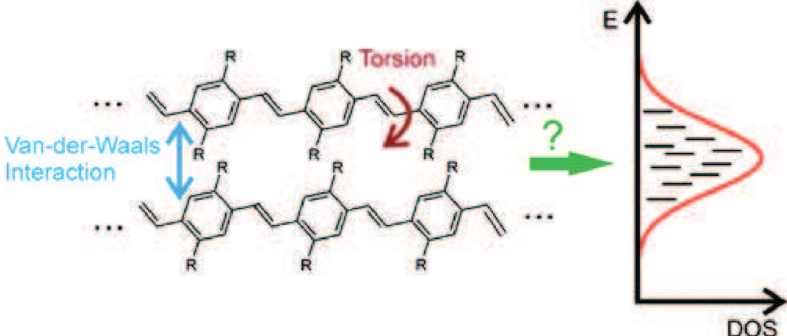

Figure 4.3 Question is : « How do polymer backbone torsions and Van-der-Walls interactions (both sources of static disorder) affect electronic wavefunction localization in conjugated polymers?». The Gaussian density of states (DOS) typical of disordered organic semiconductors is sketched, see next paragraph (Reprinted from [10]).

4.2.1 Gaussian Disorder Model (GDM)

The most quoted charge transport model that accounts for disorder in conjugated polymers devices is the Gaussian Disorder Model (GDM) formulated by Bässler in 1993 [12]. The model was initially formulated to understand transport in the photoconductors used for electrophotolithography. In this model, the presence of disorder gives rise to a Gaussian density of states (DOS) with standard deviations σ, also called 'energetic disorder parameter':

$$DOS = \frac{1}{\sigma\sqrt{2\pi}} \exp\left(-\frac{\varepsilon^2}{2\sigma} \right) \tag{4.1.}$$

The energy ε is measured relative to the center of the DOS. In this picture, all states of the Gaussian DOS are localized, as schematically represented in Figure 4.3. From the experimental point of view, the Gaussian shape of the DOS was suggested by the Gaussian profile of the (excitonic) absorption bands of organic disordered solids. Typical values for the energetic disorder parameter σ are of the order of 100 meV or below [13].

The GDM model also explains the thermal activated hopping transport of charge carriers, and how they "move" in the Gaussian DOS reciprocal space. When a charge carrier is injected in the material, it starts to hop across the localized states. The jump rate among sites i and j is assumed to be of Miller-Abrahams type [14], i.e. it is the product of a prefactor ν_0, an electronic wavefunctions overlap factor, and a Boltzmann factor for jumps upward in energy (or a factor 1 in case of jumps downwards, since they do not require any activation energy):

$$\nu_{ij} = \nu_0 \exp\left(-2\gamma a \frac{r_{ij}}{a} \right) \begin{cases} \exp\left(-\frac{\varepsilon_j - \varepsilon_i}{kT} \right) & \varepsilon_j > \varepsilon_i \\ 1 & \varepsilon_j \le \varepsilon_i \end{cases} \tag{4.2,}$$

where a is the lattice constant, γ a factor related to electronic coupling between adjacent sites and r_{ij}/a is the relative jump distance between sites i and j. By running a Monte Carlo simulation (reproducing a Time-of-Flight experiment), one generates charge carriers at energetically arbitrary sites and follows their hopping motion in the Gaussian DOS under applied electric field. The outcome of the simulation is that the charge carriers relax into tail states, asymptotically approaching an occupational density of states distribution (ODOS) again of Gaussian shape, but displaced below the center of the original DOS of the amount:

$$\langle \varepsilon_\infty \rangle = -\frac{\sigma^2}{kT} \tag{4.3.}$$

This relaxation process is illustrated in Figure 4.4. After relaxation, charge transport occurs by thermally activated jumps from the ODOS to so-called "transport energy". The transport energy is situated above ε_∞, center of the ODOS, because a minimum number of energetically accessible neighboring sites are required from transport and not enough states are available in the tail [15]. We will see in paragraph 4.4 that accessing the transport energy level will be easier in presence of a higher carrier density.

It is important to underline that, contrary to the case of inorganic semiconductors, Fermi statistics is irrelevant in our case, since the carrier is considered to move in an otherwise empty DOS. The right statistics to be used is Boltzmann statistics. The low charge carrier density allows excluding carrier-carrier interactions.

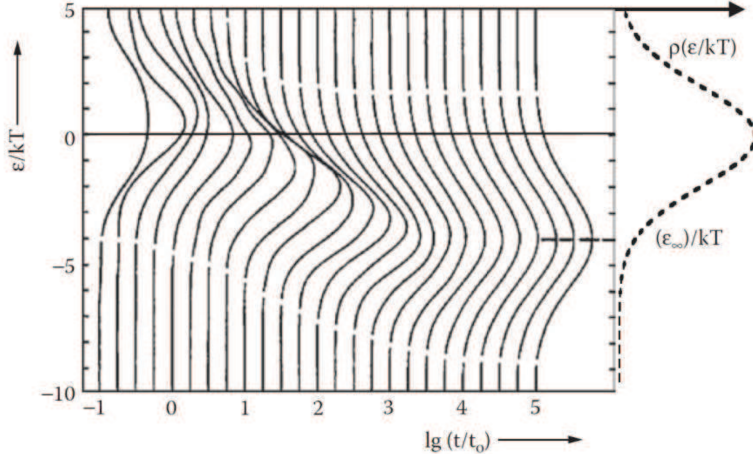

Figure 4.4 Relaxation of the energy distribution of injected charge carriers, hopping in a Gaussian DOS, as a function of time. The DOS is shown as a dashed line on the right. ε_∞ denotes the mean energy in the long-time limit, center of the occupational density of states (ODOS) distribution after relaxation. Reprinted from Bässler (1993) [12].

According to the GDM model, charge carrier mobility depends on the temperature T and the electric field E as:

$$\mu(T,E) = \mu_0 \exp\left[-\left(\frac{2\sigma}{3kT}\right)^2\right]\exp\left\{C\left[\left(\frac{\sigma}{kT}\right)^2 - \Sigma^2\right]E^{1/2}\right\}$$

4.4,

where μ_0, σ is the standard deviation of the Gaussian DOS, C is an empirical constant and Σ the positional disorder parameter. Equation 4.4 predicts a Poole Frenkel-like field dependence of the charge mobility, going as $\ln \mu \propto E^{1/2}$. The temperature dependence is instead of the type $\ln \mu \propto 1/T^2$, i.e. mobility decreases when temperature decreases.

4.2.2 Mobility edge

According to the GDM model, all the electronic wavefunctions inside the Gaussian DOS are localized. In conjugated polymers, the theoretical 1D π-conjugation is disrupted and reduced from the whole polymer length (end-to-end) to few monomers. However, considerable efforts have been done to improve crystallinity in conjugated polymer thin films, with the aim of minimizing static disorder. It is thus reasonable to believe that delocalized electronic wavefunctions exist in organic crystalline or semi-crystalline materials, not necessarily extended over the whole polymer chain, but at least over segments some tens of nanometers long. Hence we believe that it is legitimate to use of the concept of “mobility edge”, as it has been done for example by Menon *et al*. [16] in 1993, and more recently by Wang *et al*. [17].

A mobility edge is defined as the energy level separating localized and non-localized states in the conduction or valence bands of a non-crystalline material. The concept has been introduced by Sir Nevill Mott in 1967 [18] for non-crystalline inorganic semiconductors, namely hydrogenated amorphous silicon, and it follows from the theory of localization developed by Anderson [9].

In Figure 4.5 we schematically illustrate the two mobility edges E_C of a Gaussian DOS, separating localized tail states from extended states in the middle of the band. The same representation is valid for both HOMO (holes) and LUMO (electrons) Gaussian DOS.

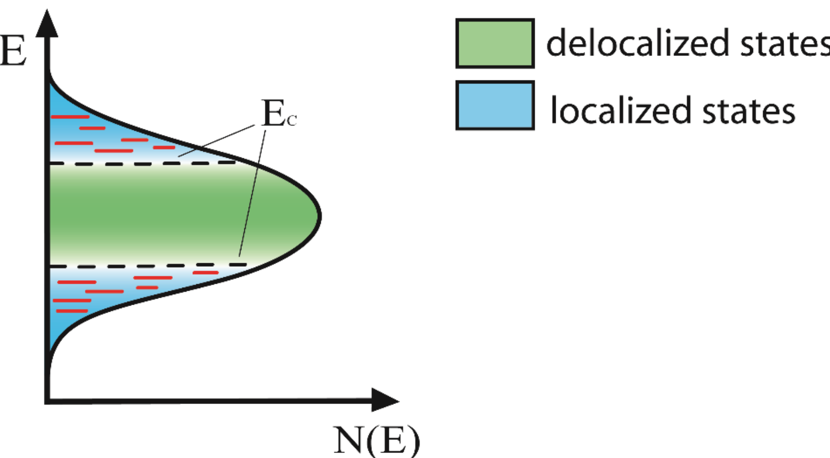

Figure 4.5 Schematic representation of mobility edges E_C in a Gaussian DOS. The picture is valid for both HOMO or LUMO bands of an organic semiconductor characterized by light disorder.

In any case, one must not forget that, in order to access the delocalized states of transport, a very high density of carriers is needed to fill all the localized states up to the mobility edge. One possible method to fill up the DOS beyond the mobility edge is chemical doping, detailed in the next paragraph.

4.3 Chemical doping of conjugated polymers

As previously mentioned, the conductivity of a semiconductor is the product of carriers mobility μ and carriers density n, $\sigma = e \cdot \mu \cdot n$. One can improve σ not only by enhancing μ, but also increasing the density of carriers n inside the material.

This approach has been used very early in the field of organic semiconductors, in the attempt of reaching metallic conductivities and creating the so-called “synthetic metals”. The extensive work in this field, initiated with the synthesis of iodine-doped polyacetylene in 1977 [19], resulted in the awarding of the Nobel Prize in Chemistry in 2000. Nowadays the most conductive polymer thin film is PEDOT-PSS, that indeed constitutes an example of chemical doping, where PSS (polystyrene sulfonate) is the dopant for PEDOT (poly(3,4-ehylenedioxythiophene)).

Optical-quality thin films of metallic polymers can be useful as transparent electrodes. For example they are used as transparent hole-injecting electrodes in polymer light emitting diodes (the initial demonstration of mechanically flexible polymer LED utilized PANI as the anode). Transparent conducting films can also be used as antistatic coatings, or for fabricating electrochromic windows.

4.3.1 Early “synthetic metals”

The early studied conducting polymers are *cis*- and *trans*- polyacetylene $(CH)_x$ [20],[21], poly(*p*-phenylenevinylene) (PPV) [22], polyaniline (PANI) [16] and polypyrrole (PPy) [23]. Their structure is shown in Figure 4.6(a). In the 80’s and early 90’s, exceptional bulk conductivities up to 10^4 S/cm were reported for these polymers when exposed to strong doping.

Basic mechanism of chemical doping is illustrated in Figure 4.6(b). P-type doping consists in the transfer of an electron from the HOMO of the polymer to the dopant molecule, while n-type doping is an electron transfer from the HOMO of the dopant to the LUMO of the polymer. The process is

favorable if the molecular orbitals of the dopant molecule are aligned to the HOMO/LUMO of the polymer accordingly to the figure. Consequently, p-type dopants should be very strong electron-acceptors, with LUMO at least -5 or -6 eV below the vacuum level. N-doping is even more challenging, and it is usually done using alkali metals such as sodium or lithium.

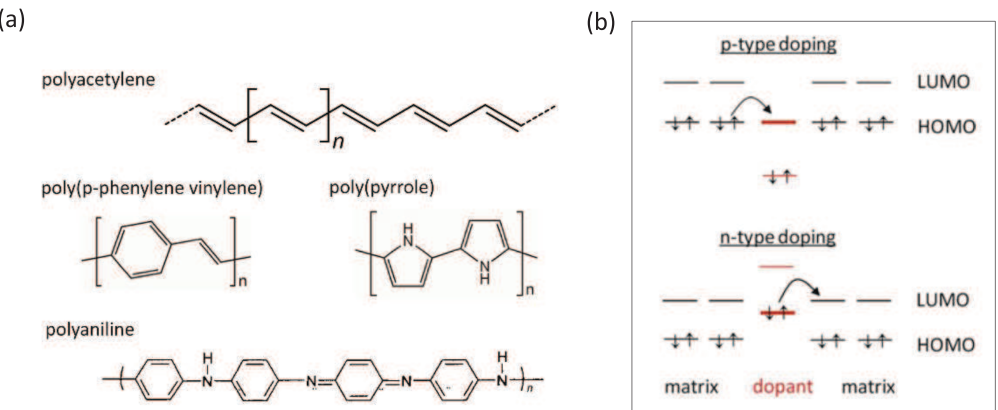

Figure 4.6 a) First generation of conducting conjugated polymers, for which the term “synthetic metals” has been coined. b) Chemical molecular doping mechanism for p-type (top) and for n-type (bottom) doping. HOMO and LUMO of the dopant molecule are in red.

Polyacetylene was usually doped with iodine. Poly(*p*-phenylenevinylene) was doped with sulfuric acid H_2SO_4 and reached conductivities up to 10^2 - 10^3 S/cm [22],[24]. Polypyrrole was often doped with PF_6 ions. Polyaniline was typically doped with camphor sulfonic acid to form the so-called PANI-CSA.

Early experiments on conjugated polymers were performed on macroscopic bulk-shaped samples, in contrast to nowadays (semi)conducting polymers used as thin films for applications. Polymer films after polymerization were tens of microns thick, and electrical measurements were normally performed on bundles of them. Very often their conductivity was further increased by tensile drawing. In such experiments, the polymer “brick” is positioned between two clamps and pulled. This treatment leads to an enhancement of the crystallization of the polymer. In particular, it orients the polymer chains parallel to the pulling direction. Sample is then cut parallel or perpendicular to the pulling direction and the anisotropy of the electrical characteristics in the two directions is measured. A difference of up to 2 orders of magnitude has been found between $\sigma_{//}$ and $\sigma_{\perp}$ values [24]. Even though the conductivity values are comparable to copper or other transition metals thin films, the unambiguous demonstration of their metallicity, with the related band-like delocalized transport, was and remains a real challenge.

4.3.2 Electrolyte-gating: an efficient doping technique

Although chemical doping is an efficient and straightforward process to increase the material conductivity, it is typically inhomogeneous, difficult to control and unstable in time. Very often the dopant molecules diffuse spontaneously outside the polymer thin film, in an uncontrollable de-doping process referred to as “ageing” [24]. These are clearly major drawbacks for the use of doped organic semiconductors in everyday applications, which should instead guarantee acceptable working lifetime.

Electrochemical doping has been introduced to solve issues related to chemical doping [25]. The first electrochemical doping experiment was done on polyacetylene in a solution of KI or $[BuN_4]^+[ClO_4]^-$, and it was run in an electrochemical cell set-up [21]. The principle is the following: the working

electrode is coated with polymer semiconductor and a voltage difference is applied between working and counter electrode (respect to the reference electrode). When the polymer is coated on the anode (cathode), strong p-doping (n-doping) can be achieved by pushing negative (positive) ions inside the polymer film. In electrochemical doping in fact, contrarily to “classical” chemical doping, it is the electrode which supplies additional charges (holes and electrons) to the conducting polymer, while ions diffuse into interchain sites of the polymer from the nearby electrolyte to compensate the added charge. A big advantage is that the doping level can be precisely determined by the voltage between the conducting polymer and the counter electrode. Intermediate doping levels can be achieved by setting the electrochemical cell at a fixed applied voltage and simply waiting as long as necessary for the system to come to electrochemical equilibrium (as indicated by the current through the cell going to zero). The dedoping process is reversible and controllable.

Electrolyte-gating can be used as an electrochemical doping technique in solid-state thin films devices. The gate terminal finely controls the doping level, and source-drain electrodes provide the charge carriers (holes or electrons) to the polymer film. As explained in more detail in Appendix B, there has been an open debate on whether electrolytes ions are penetrating into the organic active material (electrochemical doping) or just creating an electrostatic gate action. Now it is known that electrolyte-gating of soft organic materials (rather than organic single crystals), in combination with “high” gate voltages applied (1 Volt is already considered “high” for electrolyte-gating standards), results in electrochemical doping of the organic semiconductor [26],[27]. The main advantage of electrolyte-gating (respect to doping performed in electrochemical cells) is that it is directly applicable to polymer thin films, relevant for current Organic Electronics applications.

Dhoot *et al*. [28] published in 2006 a very successful example of electrolyte-gating on PBTTT thin films (gated with poly(ethylenoxide)/lithium salt), reporting the achievement of a metallic state of transport at highest doping level.

4.4 Charge transport physics of conjugated polymers (at high carrier density)

The transport model discussed in paragraph 4.2 is based on the condition that the Gaussian density of states for conduction is almost empty (low carrier density) and the interaction between charge carriers is negligible. In the gate-induced accumulation layer of an organic field effect transistor, or in a doped organic semiconductor, these assumptions do not hold anymore. In these cases a non-negligible fraction of tail states of the DOS is occupied. When charge carriers fill up the tail states of the DOS beyond the critical level defined by ε_∞ (see Figure 4.4), the carrier statistics turns from Boltzmann type to Fermi–Dirac type. A quasi-Fermi level is established above ε_∞, thus the activation energy needed for a charge carrier to reach the transport energy level decreases. The phenomenon is described in Figure 4.7. In the case represented in Figure 4.7(b) the transport energy is more easily accessible respect to Figure 4.7(a). It must however be taken into account that, if tail-states filling is obtained by doping, the DOS itself may undergo a broadening due to energetic disorder introduced by the dopants, as represented in Figure 4.7(c). Dopants are charged entities, thus they constitute centers of Coulomb scattering. DOS broadening distances the occupied tail-states from the transport energy level, so it counterbalances the effect of band filling.

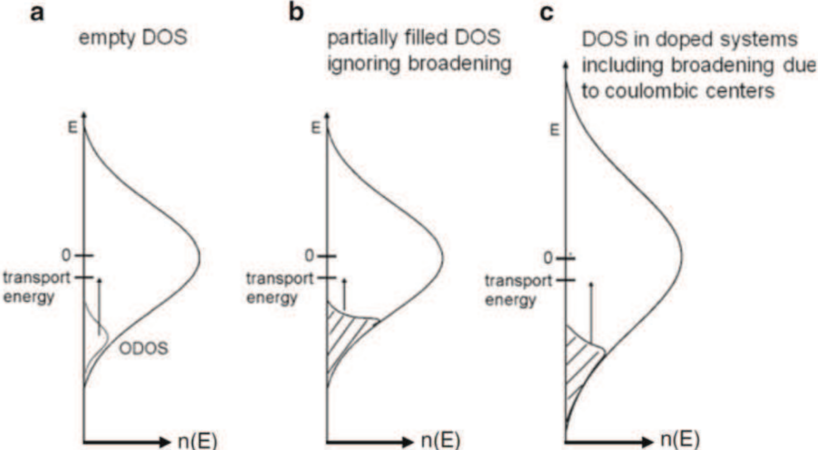

Figure 4.7 Schematic view of the effect of energy states filling in the Gaussian distribution model. a) Charge carrier transport requires thermally activated transitions of a charge carrier from the occupational DOS (ODOS) to the transport energy E_{tr} in the low carrier limit. b) Charge transport in the presence of a partially filled DOS, obeying Fermi-Dirac statistics. c) Charge transport in the presence of a partially filled DOS considering the broadening of the DOS (increase of disorder) due the countercharges generated, e.g., in the course of electrochemical doping. Note the larger width of the DOS. Reprinted from [6].

At high carriers density, the mobility does not depend only on temperature and electric field, but also on the carriers density. If the hopping event is facilitated by more accessible transport energy, conjointly the mobility should also increase. Its temperature-dependence becomes weaker, gradually changing from $\ln \mu \propto 1/T^2$ to Arrhenius type dependence $\ln \mu \propto 1/T$, and the carrier-density dependence $\mu(n)$ enters into play. Omission of the carrier-density dependence in the past has led to an underestimation of the hopping distance and the charge carrier mobility in these polymers. The straightforward verification of this effect is the observation that, for the same material, carrier mobilities measured under FET-conditions (high carrier density) can be up to three orders of magnitude larger than values inferred from ToF experiments (low carrier density) [29]. Considerable efforts to highlight the importance of the carrier density on the transport properties of organic semiconductors have been done by the groups of P. Blom and D.M. de Leeuw [29],[30],[31]. Their formalism, nowadays known as the "extended Gaussian disorder model" (Pasveer *et al*. [30]), proposes a unified description for charge carrier mobility of the form:

$$\mu(T,E,n) = \mu_0(T) g_1(E,T) g_2(n) \quad 4.5,$$

where $\mu_0(T)$ is the temperature dependent mobility in the limit of zero electric field E, $g_1(E,T)$ is the mobility enhancement due to the electric field, and $g_2(n)$ is the mobility gain due to state filling.

In short, for disordered conjugated polymers, the mobility can be enhanced by the presence of a high number of carriers. This feature is absent in inorganic semiconductors. It must be underlined, however, that low to moderate chemical doping levels have the opposite effect: they strongly reduce the mobility. The dopant ions act in fact as Coulomb wells and trap the mobile charges [32]. In the energetic landscape, introducing Coulomb scattering centers causes tail states broadening shown in Figure 4.7(c). This reconciles with the high doping level scenario because, when the Coulomb wells overlap spatially, the energy landscape becomes smoother, improving therefore the mobility value. The effect is documented in Figure 4.8. The black curve corresponds to mobility change induced by electrochemical doping in regioregular P3HT. μ is of the order of 10^{-5} $cm^2/V \cdot s$ for 0.4 % of doping, much

lower than typical values for rr-P3HT in FET (red line). Going from 0.4 % to > 10 % doping percentage brings the mobility from 10^{-5} $cm^2/V{\cdot}s$ up to $5{\cdot}10^{-1}$ $cm^2/V{\cdot}s$.

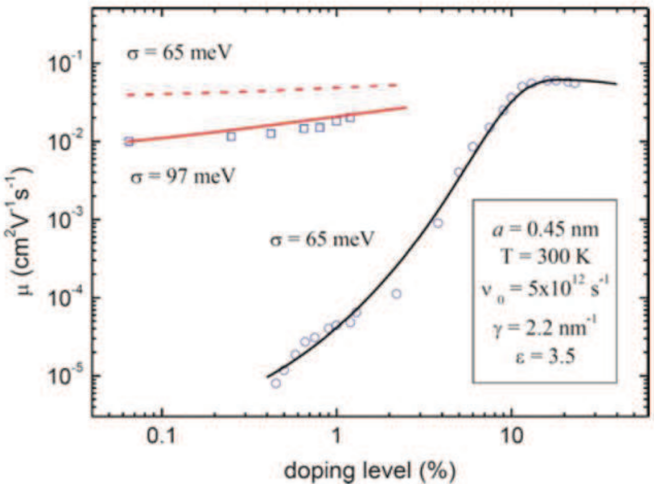

Figure 4.8 Charge carrier mobility in P3HT as a function of the doping level. Points are experimental data taken from [33], while solid and dashed lines are fits according to [32]. Squares refer to experiment performed on an FET, circles refer to an electrochemically doped sample.

4.4.1 Insulator-to-metal transition

When the density of carriers becomes significant, an insulator-to-metal transition can take place and the organic polymer can present typical features of metallicity. Metal-insulator transition (MIT) is a 50-years debated topic, still not completely solved. Many examples of highly doped conjugated polymers have been reported in literature as “synthetic metals” (see paragraph 4.3.1), but the discordance on the definition of “true metallic state” makes them questionable.

The occurrence of an insulator-to-metal transition can be intuitively understood by using the concept of mobility edge. As represented in Figure 4.9 (for a HOMO Gaussian DOS in presence of increasing p-type doping), the transition occurs when the carrier density increases enough so that the Fermi level E_F crosses the mobility edge limit and enters the region of extended electronic wavefunctions.

In the insulating side of the transition the temperature-dependence of the conductivity is well described by the Mott variable range hopping (VHR) model, developed for inorganic semiconductors. The transport occurs between spatially localized wavefunctions, whose electronic density envelope decays in space exponentially. The hopping probability of a charge carrier from one site to the other depends on the spatial and energetic separation between the two states. At high temperatures the thermal energy is sufficient to provide access to several different energetic states and short-range hops are favored. It is the average nearest-neighbor distance between states which determines the overall conductivity.

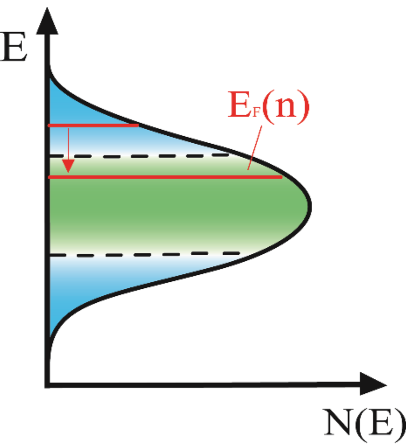

Figure 4.9 The insulator-to-metal transition occurs when the Fermi level E_F moves away from the localized tail-states and it lies in the region of extended states. In the figure the process is represented for HOMO DOS and p-type doping (E_F descends in energy).

Contrarily, at low temperatures, only states very close in energy remain accessible. Nearly degenerate states are in general very far apart in space, thus long-range hops are the most probable at low T. According to this model the conductivity depends exponentially on temperature, with an exponent related to the dimensionality *d* of the system:

$$\sigma(T) = \sigma_0 \exp\left[-\left(\frac{T_{Mott}}{T} \right)^{\frac{1}{d+1}} \right] \tag{4.6.}$$

T_{Mott} is the temperature above which the VHR does not hold anymore (not thermally activated transport). It is usually thousands of Kelvin, thus 'insulating' conjugated polymers are characterized by hopping at room temperature. For 3D systems, the conductivity follow an $\propto \exp -(1/T^4)$ form.

When the transition to a metallic state is approached, the temperature-dependence of the conductivity becomes much weaker and takes a power law T-dependence of the type:

$$\sigma(T) \propto T^{\beta} \tag{4.7,}$$

where the exponent β normally ranges between 0.3 and 1. In this case the conjugated polymer is considered to be in the so-called «critical regime» [16],[24].

4.5 Key experimental insights into metallicity

The identification of a 'true metallic state' in organic semiconductors can be attributed to various experimental signatures, which directly derive from the physical characteristics of transition metals. Metallicity can revealed itself in some special fingerprints in the T-dependence of the conductivity, in the magnetotransport behavior, in the infrared reflectance spectrum R(ω) and in the magnetic susceptibility of the conjugated polymer.

- *T-dependence of the electrical conductivity $\sigma(T)$*

Crystalline metals are characterized by an increase of electrical conductivity while temperature is decreasing. Owing to their disorder, thin metallic films and 'metallic' conducting organic polymers do not show this feature, but they usually present a finite conductivity value σ_0 in the limit $T \rightarrow 0$ K. The main issue related to this experimental fingerprint of metallicity is that it would require measurements down to millikelvins, in order to assure the accuracy of the $T \rightarrow 0$ K extrapolation.

- *Weak localization appearance in the magnetotransport properties*

  Bergmann [34] reported in 1984 the effect disruption of weak localization interferences under application of an external magnetic field on disordered thin film of transition metals. Cancelling the effects of weak localization leads to positive magnetoconductivity (higher conductivity in presence of magnetic field). The appearance of positive magnetoconductivity (normally at low temperatures) in highly doped conjugated polymers has thus been attributed to a metallic state [22],[24].

- *High reflectance of infrared frequencies*

  Metals reflect light at frequencies below the plasma frequency ω_p, which is proportional to the number of electrons per volume unit N, and they are transparent above it. For transition metal ($N \sim 10^{23}$ cm^{-3}), ω_p is usually located in the UV (thus they reflect visible light, from this their typical brilliant aspect), while for organic metals ($N \sim 10^{21}$ cm^{-3}) ω_p is lower and their maximum reflectivity is in the infrared range (IR). For conjugated polymers, an IR reflectance that becomes higher with increasing of doping is interpreted as signature of metallicity [35],[36].

- *T-independent Pauli susceptibility contribution in EPR measurements*

  The paramagnetic susceptibility χ of conduction electrons in a metal is independent of temperature (Pauli susceptibility). Electron Paramagnetic Resonance (EPR) measurements on conjugated polymers can thus provide important information on the nature of the electronic states near the Fermi level. In organic materials near the boundary of the metal-insulator transition, the paramagnetic susceptibility is mainly determined by a temperature independent Pauli contribution at high temperatures and by a temperature dependent Curie contribution below 50 K [37],[38],[39].

EXPERIMENTAL

4.6 CHARGE TRANSPORT STUDY OF HIGHLY DOPED PBTTT THIN FILMS

In our experiment thin films of poly(2,5-*bis*(3-dodecyl-2-yl)-thieno[3,2-*b*]thiophene (C12-PBTTT) are exposed to strong electrochemical doping by means of electrolyte-gating technique (Appendix B). According to paragraph 4.4, our purpose is to accomplish a doping-filling of the localized-tail-states of the Gaussian DOS and have access to the more delocalized electronic states lying in the center of the DOS, beyond the 'mobility edge'. Even though the presence of truly delocalized states in the center of the Gaussian DOS is postulated only for disordered inorganic semiconductors (and not for organic semiconductors), the high degree of crystallinity characterizing PBTTT gives hope for the existence of "extended" states whose effective conjugation length reaches tens of nanometers along the polymer backbone.

Polymer thin films are in general characterized by means of gate-dependent field effect measurements. Such type of measurements are however not sufficient to understand whether the charge transport is "band-like" type or not. We thus carry out in-depth transport measurements of the four-probe conductivity temperature dependence, magnetotransport at low temperatures and search for the appearance of Hall Effect.

The profile and perspective view of the sample geometry are shown in Figure 4.10.

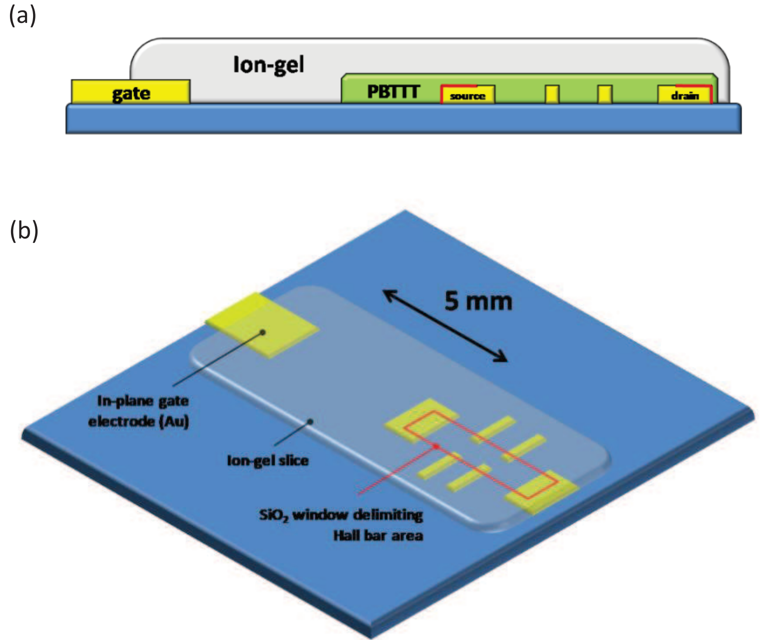

Figure 4.10 Profile (a) and perspective (b) view of the sample. Au electrodes thickness: 30 nm, PBTTT thickness: 25 – 30 nm. The red line represents the contour of the window in the SiO_2 thin capping layer, which is covering bottom electrodes in order to define the Hall bar area. The side in-plane gate electrode is ~ 5 mm apart from the active channel (figure not in scale).

4.6.1 Sample preparation

The sample preparation consists of three phases: a) deposition of the bottom electrodes on the Si/SiO_2 substrate, b) spin coating of the PBTTT thin film and c) preparation and positioning of the iongel electrolyte.

4.6.1.1 Substrate fabrication

Bottom contact electrodes are evaporated on Si/SiO_2 substrates after optical lithography patterning. They are made of 3 nm of Titanium (adhesion layer) and 30 nm of Gold. We use a six fingers Hall bar geometry, conceived for Hall Effect and well suited for four-probe and magnetoconductance measurements (high sensitivity due to the fact that half of the channel voltage potential drops between the two sensing fingers). Having PBTTT deposited over the whole substrate, we define the device active channel area by covering the rest of the non-active area with a SiO_2 sputtered layer (50 nm). Even though this adds a lithography step to the fabrication process, we found it essential to diminish the parasitic gate leakage current and gate-electrodes unwanted capacitance. Two slightly different geometries of Hall bar have been tested for measurements, Figure 4.11. The source-drain distance L is 400 µm for both. The Hall bar width W is instead defined by the SiO_2 layer window and it is either 100 µm (a) or 300 µm (b). In Hall bar (b) the sensing fingers protrude inside the channel (where source-drain current is flowing) whereas they are slightly outside in (a).

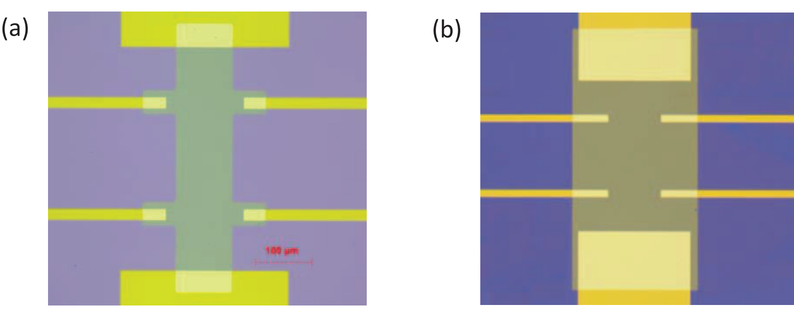

Figure 4.11 Six fingers Hall bar geometry used for measurements. Hall bar area is defined thanks to the aperture in the SiO_2 capping layer (visible with different color).

4.6.1.2 Spin-coating of PBTTT thin films

PBTTT is synthetized by Dr N. Leclerc (ICPEES, Strasbourg) according to the recipe described in literature [4]. A polymer with average molecular weight (M_n) of 27 kDa and a polydispersity index (PDI) of 1.7 has been obtained. The PDI is a measure of the heterogeneity of sizes of polymer chains, it approaches 1 when all polymers chains are identical. The chains of this PBTTT are in average formed by ~ 40 monomers, that would correspond to 50 - 60 nm long chains.

PBTTT solution in orthodichlorobenzene (ODCB) with a concentration of 4 mg/mL is prepared at least 24h before deposition and left overnight at 80°C and under magnetic stirring. 1h before deposition, it is heated at 130°C - 150°C to improve solubility: the color solution changes from bloody red to dark orange. Substrates are cleaned by solvents rinsing (acetone, ethanol, isopropanol) followed by 15 – 30 min of UV-ozone cleaning. PBTTT is then spin-coated (~ 100 µL per substrate) according to the following recipe: a first step at 1000 rpm for 120 s, followed by 2000 rpm for 60 s. No surface treatment is made. The rear side of the substrate, the contact pads far from the central device zone and the in-plane gate electrode are cleaned from PBTTT with a solvent-wet cotton bud. Samples are put into a vacuum chamber (10^{-5} mbar) for a period ≥ 6 h to complete the solvent evaporation.

Thin films have a thickness of 25 - 30 nm (measured with profilometer) and exhibit an edge-on orientation. No X-ray or electron diffraction analysis has been carried out directly on our films, but we consider valid the characterization reported by our collaborators Biniek *et al*. [40] on the same polymer before rubbing. For each samples batch, typically constituted of 2 - 3 samples, one sample was always prepared on commercially available interdigitated transistor geometry and tested in bottom-gate geometry. Mobility values always around 0.1 $cm^2/V{\cdot}s$ are systematically found, even without extra annealing step. A photograph or the sample at this step of preparation is shown in Figure 4.12.

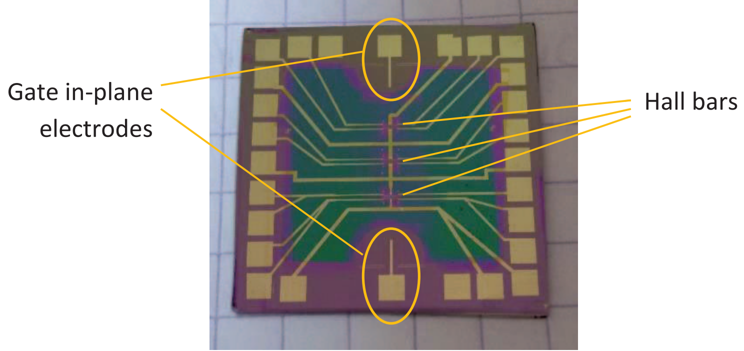

Figure 4.12 Photograph of the full substrate after PBTTT spin coating. Squares size in the background is 0.5 cm. Three different Hall bars and two gate in-plane electrodes are present on each chip. Greenish color is given by PBTTT over SiO_2 capping layer; dark purple is PBTTT in direct contact with the substrate (3 Hall bars for example). Color contrast results from cleaning the contact pads from the PBTTT.

4.6.1.3 Top-gate electrolyte

We have tested several electrolytes for PBTTT top-gating. Different combinations of the ionic species/polymer matrixes have been prepared (listed in Table 4.1), resulting in a polymer electrolyte or an iongel. All chemical products are purchased from Sigma Aldrich.

	$[Li]^+ [ClO_4]^-$	$[BMIM]^+ [PF_6]^-$
PEO	Polymer electrolyte Solvent: acetonitrile Gate electrode: top-evaporated	Iongel Solvent: acetonitrile, dichloromethane Gate electrode: in-plane
PS-PMMA-PS	/	Iongel Solvent: acetonitrile, ethyl acetate Gate electrode: in-plane
P(VDF-HPF)	/	“Cut & stick” iongel Solvent: acetone Gate electrode: in-plane

Table 4.1 Combinations of ionic species and polymer matrixes used to produce electrolytes for top-gating.

Poly(ethylenoxide)/Lithium salt ($PEO/LiClO_4$) has been the first polyelectrolyte used. After drop-casting directly on PBTTT thin film, solidification occurred in ~ 1h. A gold top-gate electrode was successively evaporated through a stencil mask (sample exposed to air to perform this step). Because of the polyelectrolyte roughness, half of the samples were affected by top-electrode cracks, like the

one visible in Figure 4.13(a), and could not be measured. On the other hand, the ionic conductivity of PEO/$LiClO_4$ is too low to use an in-plane gate electrode situated ‘far apart’, because the gate bias would fall along the bulk dielectric and not at the two interfacial electrical double layers. We thus decided to test a more conductive electrolyte (more liquid) which could be gated with an in-plane gate electrode. Using an ionic liquid without a polymer matrix was not compatible with measurement in our cryogenic environment as it prohibited the vertical sample orientation studies. We focus on the preparation of ion-gels. We tried anyhow to evaporate metallic thin films on soft iongels as top-gate electrodes, but the attempt was evidently unsuccessful, as shown in Figure 4.13(b).

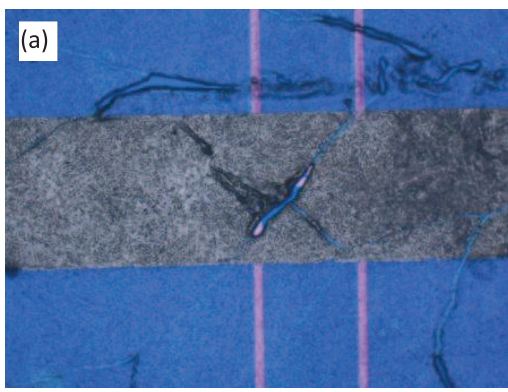

Figure 4.13 Metal evaporation (60 nm of Au) (a) on PEO/$LiClO_4$ and (b) on PEO/[BMIM][PF_6].

We could obtain iongels of PEO/[BMIM][PF_6], but not with the block copolymer poly(styrene-methylmetacrilate-stirene), PS-PMMA-PS, because of its limited solubility (both in acetonitrile and ethyl acetate). However, we found the most convenient electrolyte to be the so-called “cut & stick” iongel, whose synthesis was reported by Lee *et al*. [41]. 1g of polyvinylidene fluoride with hexafluoropropylene, p(VDF-HFP), is mixed with 4g of [BMIM][PF_6] in 10 mL of acetone (weight ratio 1:4:7). Poly(VDF-HFP) is bought under the form of pellets, which need to be smashed in a mortar to obtain a thin layer soluble in the solvent. After several hours of stirring, the iongel is drop-casted on optical microscope glass slides and put at least 12h in the oven at 70 °C under vacuum to remove acetone traces. The iongel layer thickness is several micrometers. We also attempt to spin-coat the iongel to reduce the thickness, but the slice prepared this way was not mechanically stiff enough to be cut and moved elsewhere. Ideally, p(VDF-HFP) milling must be improved to increase iongel homogeneity. After baking, the iongel was cut in slices and carefully transferred over the PBTTT film.

The same iongel solution has been used for all the samples here presented. Another advantage of “cut & stick” iongel, beside its handiness, is avoiding adhesion issues on PBTTT related to idrophobicity. For example, PEO/$LiClO_4$ drop-casted directly on the polymer semiconductor was often peeling-off from the PBTTT during solidification.

4.6.2 Gate-voltage tuning of the conductivity

In Figure 4.14 we report the typical transfer curve of a PBTTT Hall bar device, measured at room temperature inside the glove box. Gate bias is applied to the in-plane Au gate electrode in contact with the iongel slice. Source-drain voltage is fixed at low bias value, V_{sd} = -50 mV, so that ions displacement in the iongel is governed by the gate voltage only and the gating action is uniform over the whole channel length. In terms of electric field such value of V_{sd} corresponds to 10^2 V/m (400 µm long channel), negligible respect to 10^5 V/m range at which typical FETs operate. Drain and gate biases

are negative because PBTTT is a p-type semiconductor and we want to induce holes transport. Gate bias sweeping speed is 1 mV/sec. The direction of sweeping is indicated in Figure 4.14 by the small black arrows.

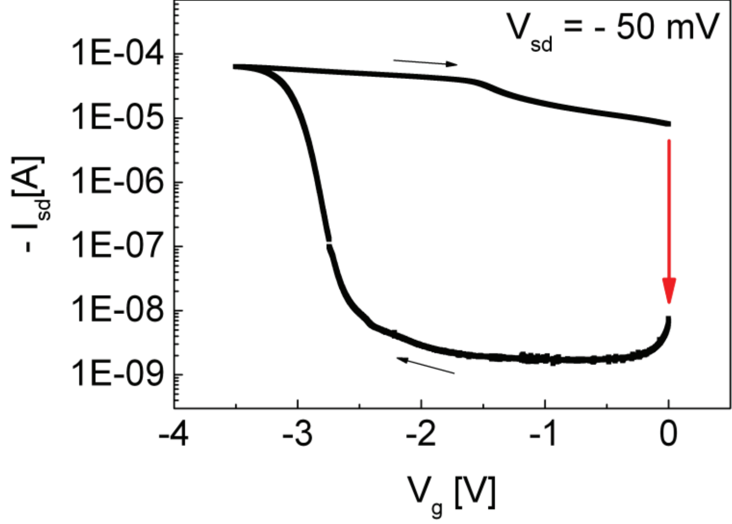

Figure 4.14 Transfer curve of the iongel-gated PBTTT thin film. V_{sd} = -50 mV, V_g sweep speed = 1 mV/s. R_{sheet} at V_g = -3.2 V is 200 Ω. Hysteresis is huge, indication of an important electrochemical doping. Red arrow indicates that applying V_g = 0 V for ~ 2 h makes the source-drain current go back to its initial off-level.

A source-drain current increase of 4 orders of magnitude occurs between -2.5 V and -3.5 V of gate bias (I_{on}/I_{off} ratio of 10^4). The sheet resistance R_{sheet} at the maximum gate voltage is ~200 Ω. The significant threshold voltage (for electrolyte-gating standards) is related to the important voltage drop occurring at the gate electrode, due to its limited area and its distance from the active channel (5 mm). In literature a similar current increase is usually found between 0 V and -1 V. The huge hysteresis of the transfer curve is a strong indication that polarizing the electrolyte results in significant electrochemical doping of the polymer film. Moreover, iongel charging and formation of the electrical double layers are not instantaneous after V_g application: this time delay also contributes to increase the transfer curve hysteresis. The doping process is however reversible, even though the de-doping is very slow. Applying zero gate voltage for around 2 hours, while keeping source-drain bias, brings back the device to the off-state. This de-doping is schematically indicated in Figure 4.14 by the red arrow.

4.6.2.1 Cooling at constant gate bias

When devices are prepared for low temperature measurements, the gating step is performed inside the cryostat chamber, in presence of an atmospheric pressure of He. A source-drain voltage of V_{sd} = -50 mV is applied and channel resistance is monitored in time during application of a constant gate voltage. The gate voltage is kept for at least 30 minutes to assure the complete charge doping associated to that gate level (system in equilibrium). When both I_g and sample resistance reach a plateau, the sample is cooled down.

An example of this gating/cooling process is illustrated in Figure 4.15. Gate-source current I_g and the corresponding drop of total resistance R_{tot} are shown for a sample to which a gate bias of progressively -1.0 V, -2.0 V, -2.3 V and -2.7 V has been applied. A cooling step, and subsequent warming up, is also shown after application of V_g = -2.3 V and before application of -2.7 V. They are respectively highlighted by light blue and red colors on the data background.

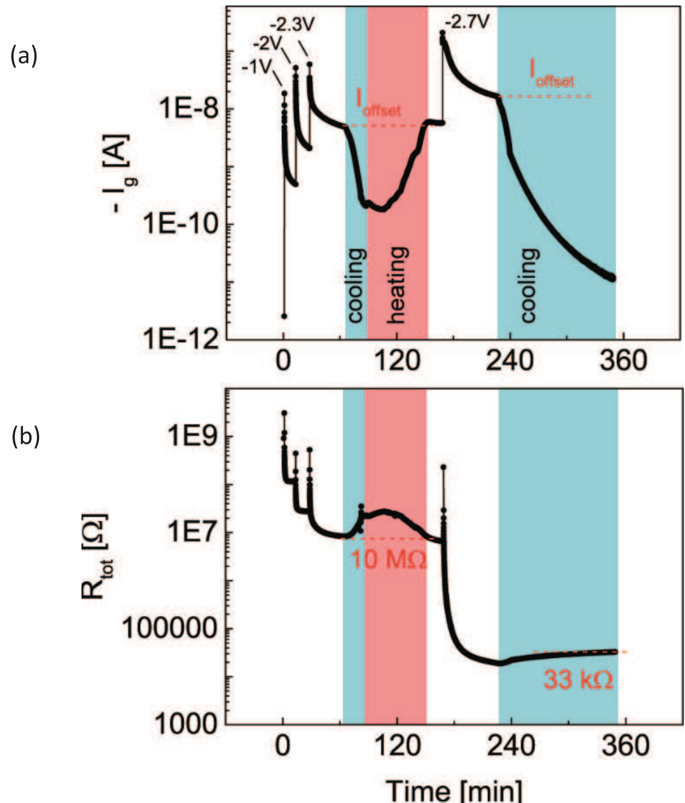

Figure 4.15 Gate current I_g and related source-drain resistance R_{tot} monitored versus time, during consecutive gating steps respectively at V_g = -1.0 V, -2.0 V, -2.3 V and -2.7 V. Cooling and heating are indicated with red and blue colors.

At each change of the gate voltage, I_g shows a peak, Figure 4.15(a). This indicates the immediate start of the iongel capacitive charging process: ions begin to move inside the iongel and create a current. Correspondingly the sample resistance decreases, as in Figure 4.15(b). Ideally I_g should decrease to zero when the electrical double layer charging process is completed. Nevertheless, a residual leakage current remains (we call it I_{offset}) that is subtracted for the calculation of the accumulated charge. I_{offset} goes to zero when the sample is cooled down (< 240 K). Bringing it back at room temperature (at V_g ON) re-establish the same I_{offset} level, as visible in Figure 4.15(a). Some typical I_{offset} values for different gate voltages are 2 - 3 orders of magnitude lower than I_{sd}.

In average we leave the sample at a certain gate bias for at least 30 minutes before starting the cooling. Gate bias equal to -2.7 V leads to a total resistance of 33 kΩ, corresponding to R_{sheet} ~ 8 kΩ, as visible in Figure 4.15(b). R_{sheet} drops at 200 Ω at V_g= -3.2 V.

4.6.2.2 Carrier density estimate

From the integration of the gate-source current I_g, corrected for the residual leakage current I_{offset} that does not contribute to semiconductor doping, we obtain the total accumulated charge in the semiconductor film or at its interface. Values of the order of 80 µC for V_g = -2.7 V, 170 µC for V_g = -3.0 V and 196 µC for V_g = -3.2 V are found, as reported in Table 4.2. For simplicity we consider our gate electrode ideal (zero voltage drop, large capacitance). Integrated Q must thus be divided by the total area A where iongel/PBTTT electrical double layer is formed, in order to obtain Q', the accumulated charge per unit of area [$C \cdot cm^{-2}$]. Subsequently we divide Q' by the electronic charge and the whole thickness of the polymer layer *t*, to deduce the level of electrochemical doping introduced in the PBTTT thin film, according to Equation 4.8:

$$p = \frac{Q'}{e \cdot t} \tag{4.8.}$$

In calculating the doping level p according to Equation 4.8, we assume that the accumulated charge Q' is fully transformed in chemical doping and that the doping is extended over the entire thin film thickness (likely true, the thickness is only 25 nm) and uniformly distributed.

A non-negligible source of error in the doping density estimate is the value of the area A taken to calculate the charge per unit area, Q'. In fact, dividing Q for an area A equal to the Hall bar area only, leads to overestimated and unrealistic values of Q'. Necessarily this means that a major part of the charge accumulates on parasitic capacitors. As shown in Figure 4.16, the iongel slice covers a large area of the bottom metallic pads outside the Hall bars.

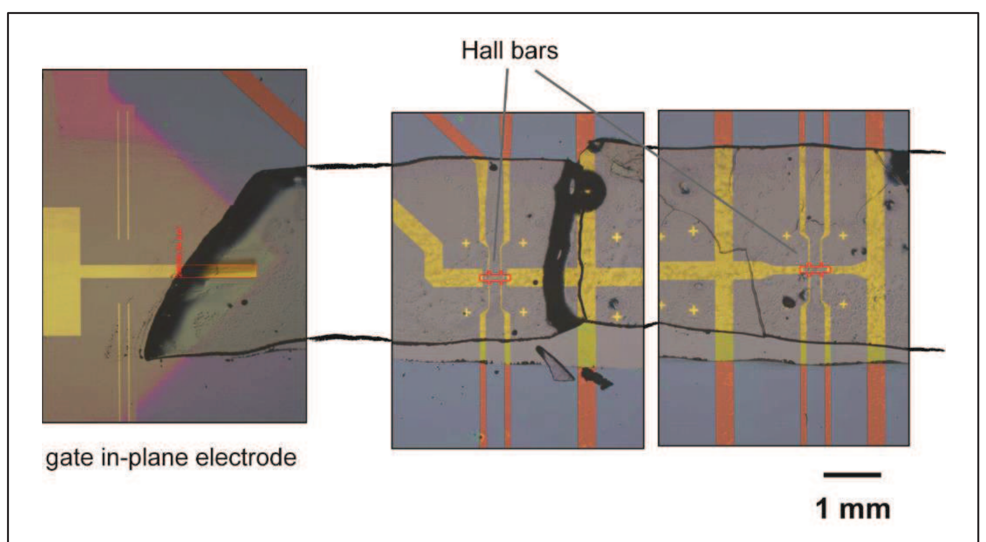

Figure 4.16 Image of a sample after measurement, reconstructed with different optical micrographs. The iongel slice (broken in the middle because of several temperature cycles) is roughly 5 mm * 2 cm in size and covers a large portion of bottom metallic electrodes outside the Hall bars active channel area.

Even though the pads are covered with 50 nm of SiO_2, the electrolyte seems to "feel" their grounded potential underneath the oxide (source is grounded and drain is quasi-grounded) and consequently the electrical double layer is formed there as well. A similar issue is also present in experiments on electrolyte-gated graphene nanosheets (Chapter 3).

For the calculation of the accumulated charge per unit of area Q', we thus use the total area A of the parasitic capacitor source-drain electrodes/SiO_2/PBTTT/electrolyte (~ 0.12 cm^2) instead of the simple Hall bar area. Doping estimates deduced from Equation 4.8 lead to rather high values, in the range of 10^{21} cm^{-3}. Gate biases and corresponding doping levels are reported in the next Table.

Gate voltage	I_{offset} [A]	Q [µC]	p [cm^{-3}]	p [holes per monomer]
V_g = -2.7 V	-1.6 E-8	80	$1.7 \cdot 10^{21}$ cm^{-3}	2.64
V_g = -3.0 V	-5.0 E-8	170	$3.7 \cdot 10^{21}$ cm^{-3}	5.80
V_g = -3.2 V	-1.4 E-7	196	$4.2 \cdot 10^{21}$ cm^{-3}	6.56

Table 4.2 Residual leakage current (I_{offset}), total charge accumulated Q and corresponding carrier density estimates (in units of cm^{-3} and 'holes per monomer') for three different gate biases.

The doping value in terms of 'holes per monomer' (instead of cm^{-3}) is even more astonishing. We obtain the value of 'holes per monomer' by dividing the unit cell volume (1 unit cell = 1 monomer) by the volume of one dopant. According to the crystallographic experimental studies of C14-PBTTT thin films by Cho *et al*. [42], the unit cell present the structure represented in Figure 4.17.

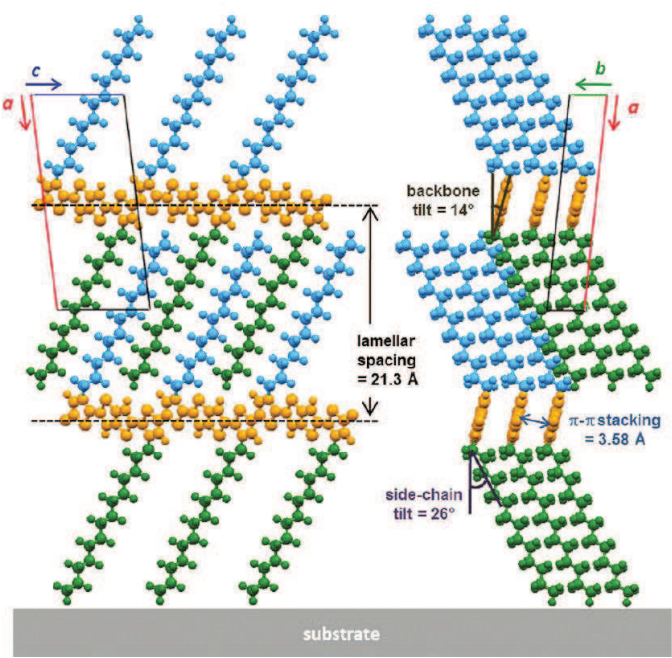

Figure 4.17 Out-of-plane packing motifs for the simulated model of PBTTT-C14 viewed along the b-axis (left) and c-axis (right); the color coding is such that orange represents the polymer backbones and blue and green represent the side chains attached above and below the backbones, respectively. The substrate is shown to indicate the polymer film orientation. Calculated dimensions of the unit cell are: a = 2.15 nm, b = 0.54 nm, c = 1.35 nm.

The unit cell parameters are a = 2.15 nm (~ length of the C14 lateral chain length), b = 0.54 nm (π-π stacking), c = 1.35 nm (monomer length along the backbone), corresponding to a unit cell volume of 1.57 nm^3. We can reasonably consider this unit cell volume valid for our C12-PBTTT as well. Values are reported in the last column of Table 4.2: at the highest doping it goes up to 6.5 holes per monomer.

Very often doping is also reported as 'holes per ring'. Wang *et* al. [17] for example report a value of ~ 0.2 - 0.4 holes per ring for their most doped P3HT thin films, corresponding to $8 \cdot 10^{20}$ cm^{-3}. In our case (each PBTTT unit cell contains 4 thiophene rings) we would extract a 'hole per ring' value higher than 1, for the highest gate voltages. We think that expressing the doping level in terms of 'holes per ring' is not fully appropriate when the unit cell is highly asymmetric, e.g. containing very long lateral chains which are not participating to the transport, like in the case of C12-PBTTT. In fact, if the dopant ion is located between these lateral chains and far from the polymer backbone, it does not influence the conductivity and can be considered inactive.

Some additional errors might be caused by the limited gate in-plane electrode area (non-ideal gate electrode), eventually leading to an overestimation of the accumulated charge density. We hope to be able to deduce the exact carriers density from Hall Effect measurements.

4.7 Conductivity temperature dependence

The temperature dependence of the conductivity is one the main experimental fingerprint of the dominating charge transport mechanism. We therefore carefully analyze it.

Samples are cooled down under constant gate voltage, as explained in the previous paragraph. We observe that sample cooling stability is critical, with a possible observed resistance discontinuity, typically occurring around 220 - 230 K, which makes our room-temperature doping estimates possibly biased at low temperatures. Avoiding cooling under vacuum helps in diminishing this problem, likely related to the adhesion of the ion gel. Such pressure sensitivity has also been reported on ionic liquid gating [43]. He gas at atmosphere pressure is thus introduced in the chamber while cooling.

We present and analyze here the four-probe conductivity as a function of temperature for six different doping levels. The doping levels are identified accordingly to the gate voltage at which the samples have been cooled down, and they are indicated in Figure 4.18. Samples 1 to 6 correspond in reality to 3 distinct devices. The coherence of the results among distinct devices (different substrates, different PBTTT films, and different iongel slices) demonstrates the reproducibility of the preparation method. For all samples the conductivity is measured while the temperature is raised up from 1.6 K to room temperature, under low He pressure. A constant source-drain bias V_{sd} = -0.4 V (electric field ~ 10^3 V/m) is applied between source and drain, and the longitudinal ΔV_{xx} potential drop is measured to deduce the four-probe (contact-free) conductivity σ. As the iongel is frozen, applying larger drain voltage compared to V_{sd} = -50 mV used for gating, is an experimental convenience only, while remaining in low electric field regime for the OFET.

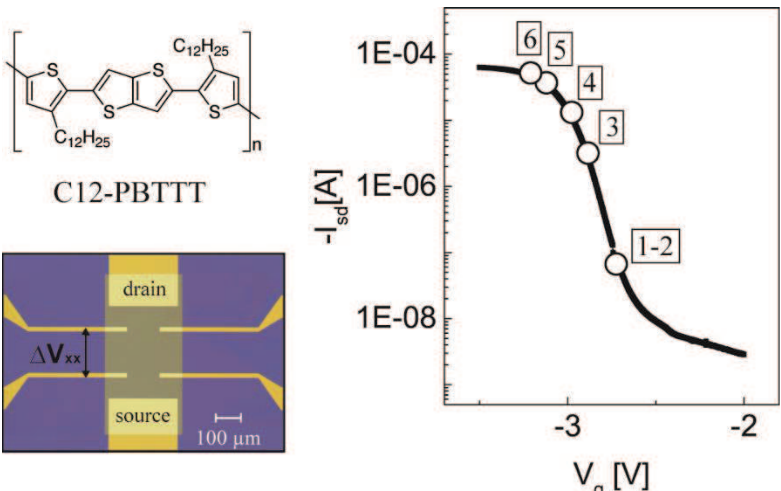

Figure 4.18 Indication of the gate bias of the six samples taken into exam for the study of the temperature dependency of the conductivity as a function of the doping level. Doping is moderate for samples 1 – 2 and maximum for sample 6.

Figure 4.19

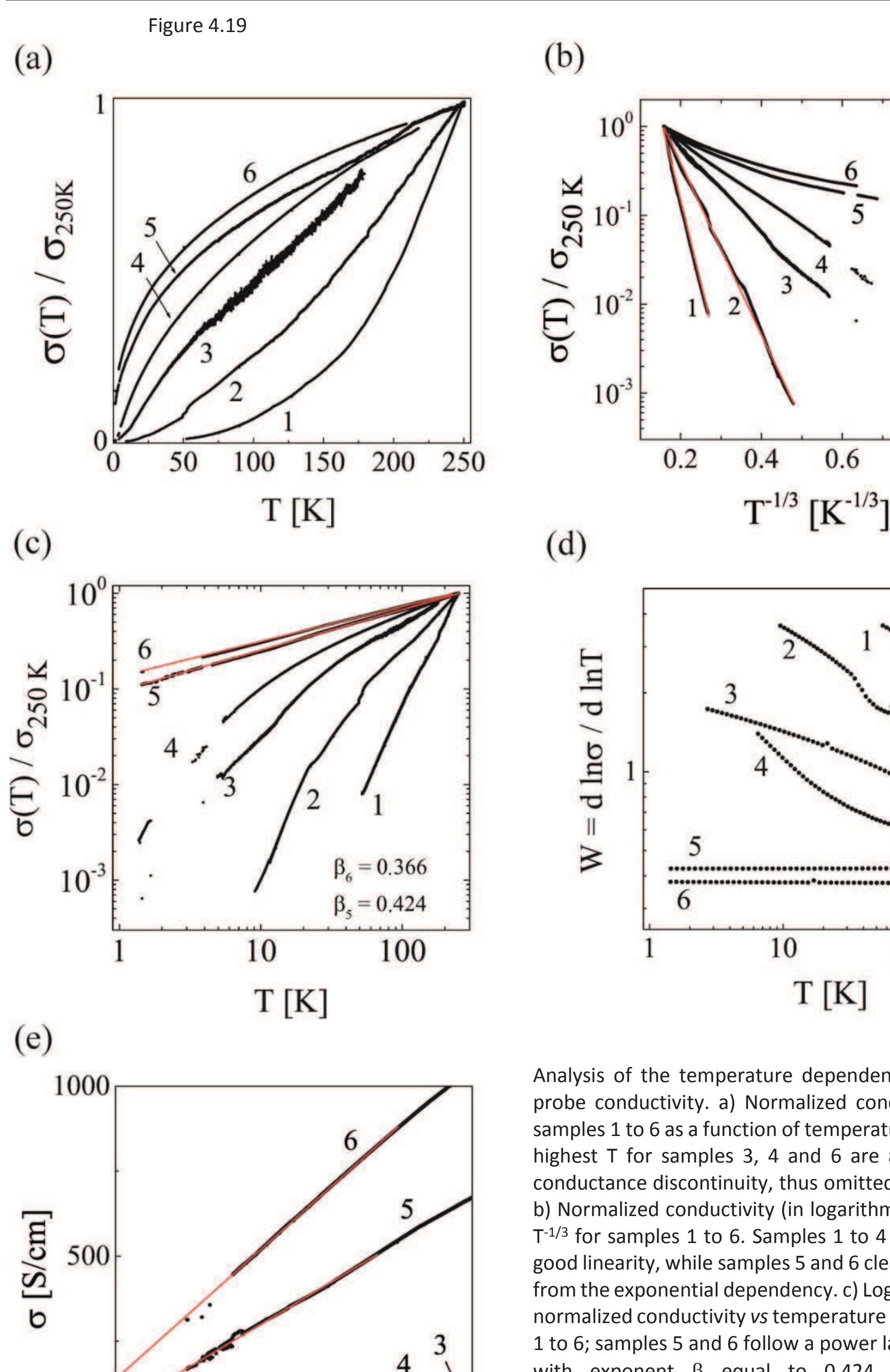

Analysis of the temperature dependence of four-probe conductivity. a) Normalized conductivity of samples 1 to 6 as a function of temperature. Data at highest T for samples 3, 4 and 6 are affected by conductance discontinuity, thus omitted for clarity. b) Normalized conductivity (in logarithmic scale) *vs* $T^{-1/3}$ for samples 1 to 6. Samples 1 to 4 show quite good linearity, while samples 5 and 6 clearly deviate from the exponential dependency. c) Log-Log plot of normalized conductivity *vs* temperature for samples 1 to 6; samples 5 and 6 follow a power law function with exponent β equal to 0.424 and 0.366 respectively. d) Reduced activation energy $W = d \ln\sigma / d \ln T$ for sample 1 to 6. e) Low temperatures conductivity. The horizontal axis scale and zero–temperature extrapolation (in red) follow the power law described by Equ. 4.11.

We plot in Figure 4.19(a) the conductivity normalized at 250 K, σ(T)/σ(250K), for samples 1 to 6. The normalized plot emphasizes the transition from convex conductivity-temperature curves (sample 1 and 2) to concave conductivity-temperature curves (samples 4, 5 and 6). We believe that this change of the second derivative σ''(T) sign is illustrating at best the crossover from insulating-type samples towards metallic-type samples. A similar presentation of the data was used by Chiang *et al*. [20] in an early paper on polyacetylene doped with AsF_5, highlighting the same difference between moderately and highly doped samples. It is interesting to notice that the experimental noise becomes more pronounced for the intermediate sample 3, located exactly at the transition (another sample, not shown in this figure, confirms this observation). Now we proceed at demonstrating our interpretation of insulator-to-metal transition.

Sample 1 and 2 are located in the insulating side of the M-I transition, where the conductivity is governed by the exponential temperature dependence typical of variable range hopping (VHR) between localized states. This is demonstrated in Figure 4.19(b) by the linearity of Log[σ(T)/σ(T=250K)] *vs* $T^{-1/3}$. The exponent of the variable range hopping exponential law depends on the dimensionality *d* of the system, according to:

$$\sigma(T) = \sigma_0 \exp\left[-\left(\frac{T_{Mott}}{T}\right)^{\frac{1}{d+1}}\right] \quad 4.9.$$

For samples 1 and 2, we find an exponent approaching 1/3, that would correspond to *d* = 2 (T_{Mott} temperatures of several thousands Kelvin). This would suggest that our system is *quasi* 2-dimensional (quasi-2D). It is however very hard to distinguish between a temperature dependence going like $exp(T^{-1/2})$, $exp(T^{-1/3})$ or $exp(T^{-1/4})$.

Figure 4.19(c) shows that samples 5 and 6 follow instead a power law dependence of the conductivity, as expected for a conductor in the so-called critical regime, i.e. approaching the metallic side of M-I transition:

$$\sigma(T) = \left(\frac{e^2 p_F}{\hbar^2}\right)\left(\frac{k_B T}{E_F}\right)^{\frac{1}{\eta}} \propto T^{\beta} \quad 4.10,$$

where p_F is the Fermi momentum, and $1 < \eta < 3$ [44]. The latter is consistent with the fitted values we obtain for β: 0,366 for sample 6 and 0,424 for sample 5. It is quite remarkable to observe a simple power law in the whole range of measured temperatures, spanning more than two decades. This strongly suggests that these two samples are at the onset of metallic state.

Indeed, second derivation of the laws in Equation 4.9 (hopping) and 4.10 (if $\beta < 1$, critical regime) leads to a positive and respectively negative sign of the second derivative. This corresponds to the change observed in the normalized conductivity plot in Figure 4.19(a).

Another method extensively used in the past for the determination of metallicity in highly doped conjugated polymers is the analysis of the slope of the reduced activation energy W, defined as the logarithmic derivative of the conductivity: $W = d(\ln\sigma)/d(\ln T)$. The logarithmic derivative method has been initially developed to study metal-insulator transition in highly compensated inorganic semiconductors [45]. According to this method, insulating samples present a negative slope of W *vs* temperature, whereas metallic-type samples are characterized by a positive slope of W *vs* temperature. Between these two classes, samples showing a T-independent logarithmic derivative are considered to belong to the critical regime, i.e. to be located exactly at the insulator-to-metal transition. Figure 4.19(d) presents the reduced activation energy W for the six samples. We observe

that the most insulating samples 1 and 2 exhibit the expected increased W values when cooling down, with a slope of lnW versus lnT of approximately 0.35. This slope is reduced for samples 3 and 4 (except a tail stroke of sample 4 at T < 50 K). A temperature independent behavior becomes dominant for the highest doping samples, with W constant in the whole measured temperature range (1.5 - 200 K) for samples 5 and 6. According to this analysis, a true metallic behavior, with decreasing W under cooling, is not observed here.

The samples behavior when $T \rightarrow 0$ is studied in more details in Figure 4.19(e), revealing that the highest conductivity samples 5 and 6 are characterized by a positive value of the extrapolated T = 0 K value on the y-axis, indicative of a finite zero temperature conductivity. The conductivity temperature dependence for a disordered metal is described by the relationship [46]:

$$\sigma(T) = \sigma_0 + aT^{1/2} + bT^{p/2} \tag{4.11}$$

where the second term is the lowest order correction to the conductivity arising from electron-electron interaction and the third term is determined by the correction to σ_0 due to the weak-localization effects. At low temperatures, phonon scattering is strongly reduced and the main dephasing mechanism is electron - electron interactions. Moreover, theoretical calculations show that the exponent *p* (in the third term) is ~1 when approaching the metallic side of the transition [47], justifying the σ - $T^{1/2}$ approximation in Figure 4.19(d). The intercept with the T = 0 K axis is non-null for the two most conductive samples, respectively σ_0 = 40 S/cm for sample 5 and 150 S/cm, while it is negligible for samples 3 and 4. The finite zero-temperature conductivity is considered to be a key experimental signature of metallicity. It is quite remarkable that samples having a non-decreasing resistivity under cooling (their resistivity is mostly independent under cooling) present finite σ_0, even though we are aware that measurements in the milliKelvin range would be needed to confirm our extrapolation to 0 K.

4.7.1 Interpretation of the conductivity behavior

It has been shown for other systems [48] that metallicity can be due to electric field distortion, caused by measurements at a rather high source-drain voltage V_{sd}. In our experiments source-drain bias is always kept low, thus confirming that the quasi-metallicity of our most doped samples must be caused by the vicinity to the M-I transition.

We interpret the results in terms of doping-filling of the localized states up to the mobility edge, as schematically illustrated in Figure 4.20. As explained in paragraph 4.4, we are in presence of an exceptionally high density of carriers populating the DOS, thus we can consider valid the Fermi-Dirac statistics and define a Fermi level E_F (or electrochemical potential, at $T \neq 0$ K). We are dealing with p-type doping, thus the Fermi level $E_F(n)$ – where *n* indicates carrier density - shifts down (far from the vacuum level) and an increasing number of holes populate the DOS. All states are occupied up to the Fermi level (red zone in Figure 4.20), and empty beyond, in the limit of T = 0 K. Variations of the electrochemical gate voltage allows us to finely tune the position of the Fermi level inside the HOMO band. The withdrawal of the exponential temperature dependence of the conductivity typical of hopping transport and the entrance into a non-thermal-activated transport for samples 5 and 6 demonstrates that we likely have accessed some of the delocalized states present above the mobility edge (green zone).

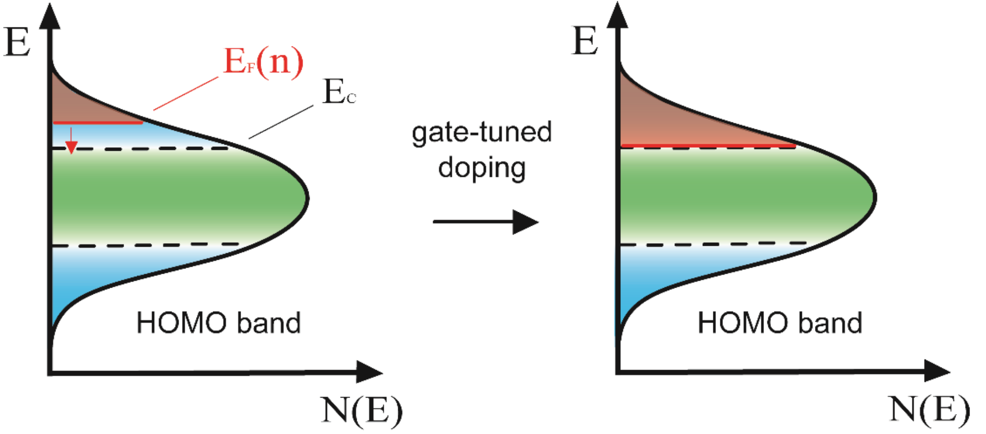

Figure 4.20 Fermi level E_F shifts from the localized tail states to more delocalized states located at the mobility edge E_C by means of electrolyte-gate tuned doping. Red shadow indicates filled holes states.

The main criticism to this interpretation might be that mobility edge model is not appropriate to describe the electronic structure of organic materials, because it has been developed for inorganic semiconductors for which the disorder remains restrained. We also agree that the comparison with the mobility edge model should be taken with caution. We can say that the mobility edge model is correct in the sense that more localized states exist close to the valence band edge, but the separation between localized and delocalized states is not sharp, or at least it is not as sharp as for inorganic semiconductors. The real situation is that the states become gradually more delocalized as we move away from the band edge. This energetic landscape where there is no actual "edge" indeed produces the same qualitative features of mobility edge model (thermal activation and increased mobility with increased charge density).

To sustain our interpretation, several theoretical works have demonstrated the exceptionality of PBTTT respect to other conjugated polymers [49],[50],[51]. In particular, Liu and Troisi [52] clearly show that electronic wavefunctions in PBTTT become very rapidly delocalized, moving 200 – 300 meV from the valence band edge towards its center. We report in Figure 4.21 the calculation for the HOMO DOS and localization length (LL) by Liu and Troisi.

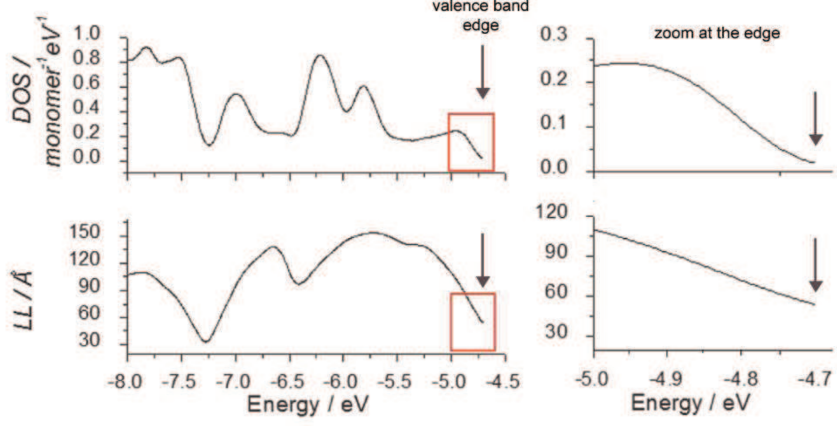

Figure 4.21 Valence band DOS and localization length LL calculated for PBTTT, as a function of orbital energy (left). Zoom at the valence band edge region (right). From Liu and Troisi [52]

The localization length of electron wavefunctions, i.e. the effective conjugation length, reaches a value of ~ 10 nm at -0.3 eV from the valence band edge. A localization length of 10 nm corresponds to ~ 8 repeat unit of PBTTT (1.33 nm each) and it is a remarkable value for conjugated polymers. Moreover, they claim that: *i.* the traps typical lifetime is very short and conformational changes of the polymer backbone leading to easy-detrapping require just a small amount of energy and *ii.* an important inter-chain delocalization is present.

In conclusion, PBTTT seems to present electronic states with long effective conjugation length and a reduced probability of phase-breaking events (incoherent hopping), owing to short-lived intrachain trap states and strong interchain delocalization. This supports our observation of quasi-metallic features of the conductivity for sample 5 and 6 and helps in the understanding of the magnetotransport properties presented below.

4.8 Magnetotransport

Investigation of magnetoconductance (MC), where the conductivity of the material is studied as a function of applied magnetic field, provides additional insight into transport mechanisms at low temperature. We investigate the low temperature magnetoconductance (below 60 K) of the most conductive samples (sample 4, 5 and 6) as a function of temperature, both in the configuration H perpendicular and H parallel to the sample plane. The external magnetic field H is swept between ±7 Teslas, while maintaining the sample temperature constant. A constant source-drain voltage V_{sd} = -0.5 V is applied. Some of the measurements have been carried out sourcing current (I_{sd} = 1 - 100 μA) instead of voltage: magnetoconductance is found equal in the two cases.

Magnetoconductivity $\Delta\sigma$ is defined as:

$$\Delta\sigma = \frac{\sigma(H) - \sigma(0)}{\sigma(0)} \tag{4.12.}$$

We plot the results in terms of percent magnetoconductivity ($\Delta\sigma \cdot 100$). In the following we will abbreviate indistinctly with the acronym “MC” both magnetoconductance and magnetoconductivity.

The results are presented in Figure 4.22, for magnetic field perpendicular (a)-(c) and parallel (b)-(d) to the sample. Different curves correspond to magnetic field scans taken at different temperatures (the corresponding temperature is specified on the right of the curve). Curves are vertically shifted for clarity. We have divided the curves in two temperature ranges, namely T < 4 - 5 K in bottom panels (c)-(d) and 5 K < T < 60 K in top panels (a)-(b), and a different y-axis scale has been used in order to highlight the peculiar features of the magnetoconductivity in each range.

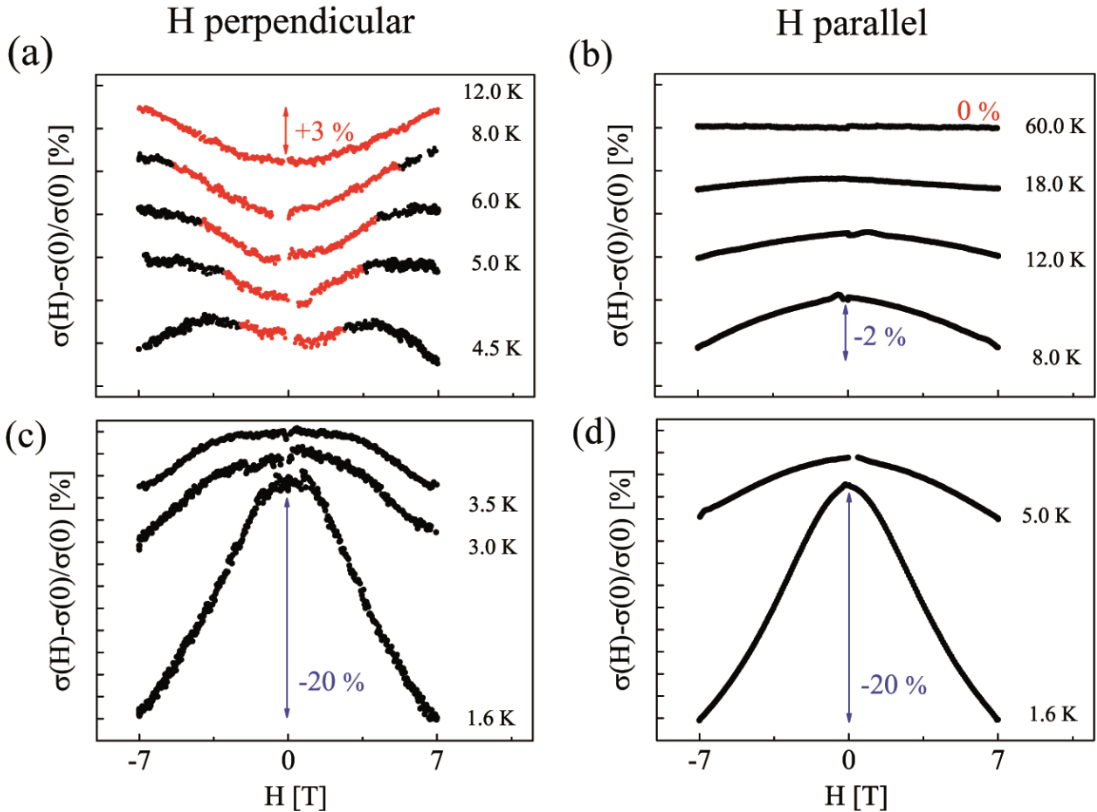

Figure 4.22 Magnetoconductivity for PBTTT thin films straddling the insulator-to-metal transition, studied as a function of temperature for a) magnetic field perpendicular to the film plane and b) parallel to the film plane (parallel to source-drain current). (Curves are vertically shifted for added clarity. Small segments of the curves are sometimes missing due to removal of artifacts due to turning on/off of the electromagnet).

The most remarkable finding is the magnetoconductance behavior in the H $\perp$ case. Figure 4.22(a)-(c) show that the MC changes its sign from negative to positive when the temperature is increased from 1.6 K up to 12 K. Positive MC at 12 K reaches values around 3 %. MC signals close to the transition temperature T_{tr} (4.5 K - 5.0 K) is composed by the superposition of both positive and negative contribution. Negative MC is around 20 % at 1.6 K. The transition from positive to negative magnetoconductivity has been found reproducibly in perpendicular magnetic field also for sample 5 and 6 (not shown here). In particular, the higher the doping level, the lower the transition temperature (positive MC appears at lower T while heating the sample), as resumed in Table 4.3.

	σ(1.6 K)	Neg MC $\rightarrow$ Pos MC
Sample 4	**50 S/cm**	$T_{tr} \sim 4.5$ K
Sample 5	**180 S/cm**	$T_{tr} \sim 4$ K
Sample 6	**300 S/cm**	$T_{tr} \sim 3.5$ K

Table 4.3 Conductivity values at 1.6 K for the most conductive samples and temperatures at which positive MC contribution appears while heating (transition temperatures, T_{tr}).

Comparison between Figure 4.22(a) and Figure 4.22(c) highlights a strong anisotropy of the magnetotransport properties at T > 5 K. When the magnetic field is aligned parallel to the film plane (specifically parallel to the current direction), no trace of positive magnetoconductivity appears (0 %). Only a small negative MC manifests for H // above 5 K, with an intensity of -2 % at 8 K and disappearing when the sample is heated at 60 K.

Negative MC below 4 - 5 K, Figure 4.22(c)-(d), is rather isotropic, presenting a maximum value of $\sim$ 20 % for both H // an H $\perp$.

4.8.1 Interpretation of the magnetotransport properties

The list of mechanisms that can produce positive and negative MC in nominally nonmagnetic systems is extensive. Positive MC (increase of conductance in presence of external magnetic field H) could possibly arise from disruption of weak localization [34],[53]. Negative MC (decrease of conductance in presence of H) might be associated to electron-electron interactions, arising at low temperature in disordered electronic systems [46], or to wave functions shrinkage [54] (in the framework of hopping regime). Quantum corrections in the hopping regime have also been theorized [55],[56], and can produce both positive and negative MC.

4.8.1.1 Positive magnetoconductance: disruption of weak localization

The analysis of the conductivity temperature dependence in paragraph 4.7 demonstrates the departure of samples 4-6 from a temperature-activated hopping regime of transport. The approach to metallicity in our samples makes us conjecture that the $\sim$ 3 % of positive MC at T > 4.5 K in perpendicular H, highlighted in red in Figure 4.22(a), is likely due to magnetic field induced disruption of weak localization.

Weak localization is due to the constructive interference of charge carriers back-scattering events. A back-scattering event can be represented as a series of several scattering events bringing the charge carrier along a self-closing path back to its departure point, as represented in Figure 4.23(a). Since two self-closing paths are possible for the charge carrier with identical phase, clockwise and anti-clockwise, they resonate ("echo"). Consequently, the probability for a scattered conduction electron to return to the initial position is twice as great as in classical diffusion since the amplitudes probabilities add coherently. Closed paths are thus favored and this causes localization. A magnetic field normal to the surface on which these closing paths lie, suppresses their constructive quantum interference, leading therefore to an increase of conductivity (backscattering events are less probable). This phenomenon has been discovered for the first time in metallic thin films by Bergmann [34], Figure 4.23(b). Coherent (elastic) transport is the necessary condition for the occurrence of weak localization, at least for a time τ_0 longer than the time required to complete a self-closing path.

The positive magnetoconductivity observed in Figure 4.22(a) corresponds to sample 4. Clear positive MC of similar amplitude above the respective transition temperature T_{tr} (Table 4.3) has been observed also for the more 'metallic' samples 5 and 6. It worth to notice that positive MC appears already in sample 4, which is not characterized by finite σ_0 at $T \rightarrow 0$ K or constant logarithmic derivative W *vs* temperature. Positive MC has not been observed for the more insulating samples 3, 2 and 1, thus confirming to be a peculiar feature of the highest conductivity samples only.

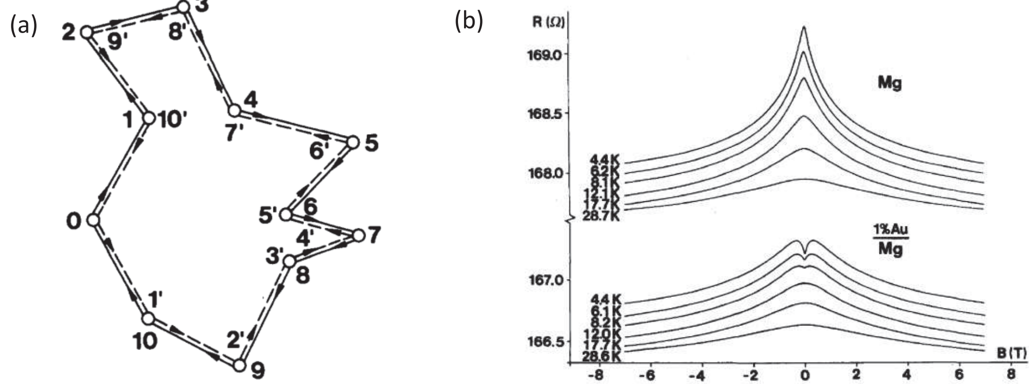

Figure 4.23 a) Constructive quantum interference of a self-closing diffusion path of a conduction electron, leading to weak localization. b) Magneto-resistance curves of a thin Mg film (upper set of curves). Application of an external magnetic field B breaks weak localization and sample resistance decreases. This effect is more pronounced at lower temperatures. The superposition of a Au atomic layer introduces spin-orbit scattering, which rotates the spins of the complementary scattered waves and turns the interference from constructive to destructive (weak anti-localization). Reprinted from Bergmann [34]

Positive MC in metallic-type samples disappears when increasing the temperature above 60 K (not shown here). This also complies with the hypothesis of weak localization, because phonons break the phase coherence. In other words, the inelastic scattering time τ_{in} become shorter at high temperatures. If τ_{in} becomes shorter than τ_0, phase coherence is lost before the circular path is terminated, thus quantum interference effect are null.

The anisotropy of the positive MC, i.e. its absence in the case of H parallel to the film plane, corroborates the theory of weak localization in a quasi-2D system. In such a system, the disruption of weak localization is expected to occur only when the applied field is normal to plane of the circular carrier trajectories: it is in fact much more efficient for breaking the constructive interference of self-closing paths. This is in agreement with our previously discussed 2D nature of the sample. The two-dimensionality derives from the narrowness of the PBTTT layer deposited (~ 25 nm) and from the intrinsic anisotropy of charge transport in a polymer semiconductor.

Positive MC has been previously reported for thick bulk-like chemically doped poly(acetylene) [19], poly(*p*-phenylenevinylene) [22] and PANI-AMPSA [57], all suggesting the occurrence of weak localization. The anisotropy (absence of positive MC in H //) is observed for the PANI-AMPSA system, even though the film thickness is more than 50 µm and they are unoriented. However, to our knowledge, a clear temperature transition between the two regimes has not been reported for organic systems.

We therefore consider that:

i. the anisotropy of the positive MC, and

ii. its limited temperature range occurrence
(limited by phonon-electron coupling at higher temperatures)

strongly point towards the occurrence of weak localization effects. We consider this an additional signature of the fact that the most conductive samples have accessed a metallic-like type of transport.

4.8.1.2 Coherence length estimation

The coherence length is the distance over which the electronic wavefunction of the charge carrier keeps its phase. The coherence length must be at least as long as the effective conjugation length LL of the polymer chain, for the simple reason that a conjugated segment of the polymer backbone constitutes one single electronic wavefunction (with its own phase). If the hop event from one localized state to another is a phase-conserving event, the coherence length is several times the localization length. Otherwise, if the hop is phase-breaking, coherence length and LL correspond. In light of these considerations, and taking into account the long effective conjugation length LL (~ 10 nm) and the coherent-type of intrachain and interchain hopping predicted for PBTTT by Liu and Troisi (results illustrated in Figure 4.21), a coherence length of 25 - 30 nm seems reasonable.

To support this finding, values of very long effective conjugation length LL have been reported for electrochemical-doped PBTTT thin films (27 nm) [58] and regioregular P3HT gated with ferroelectric gate (26 nm) [59]. These values stem from the analysis of current-voltage characteristics as a function of source-drain voltage and temperatures. In both cases the polymers are brought at high carrier densities in order to cancel out the effect of disorder, in analogy with our work.

Such values correspond indeed to the thickness of our PBTTT film. A coherence length of the same order of the thickness of the system would account for the observed quasi-2-dimensionality.

However, we should not forget that the intrinsically anisotropic nature of charge transport in conjugated polymers, where carriers preferentially move along polymeric chains disposed on a plane, could actually be the major responsible of the quasi-2-dimensionality. The coherence length in a conjugated polymer should not be considered isotropic like in normal metals.

4.8.1.3 Negative magnetoconductance: electron-electron interactions

Let us focus now on Figure 4.22 (c) and (d). In the lowest temperature range (below 5 K), for both the magnetic field orientations H $\perp$ and H //, a negative MC appears.

A crossover to negative MC is expected at the lowest temperatures when electron-electron interactions start being dominant respect to electron-phonon interactions. The contribution of electron-electron interactions becomes in fact 'visible' when the inelastic electron-phonon scattering time τ_{in} becomes larger than the electron-electron scattering time τ_{ee}. This condition is satisfied at the lowest T, when the number of phonons is strongly reduced. Electron-electron interactions in disordered electronic systems cause a decrease in the conductivity when an external magnetic field is applied, due to Zeeman splitting of bands [46],[60]. The related change of conductivity $\Delta\sigma$, at a finite temperature T, goes like:

$$\Delta\sigma(H,T) = -0.041\left(\frac{g\mu_B}{k_B}\right)\alpha_d \gamma F_\sigma \cdot T^{-3/2} \cdot H^2, \qquad g\mu_B H << k_B T$$

$$\Delta\sigma(H,T) = \alpha_d \gamma F_\sigma \cdot T^{-1/2} - 0.77\alpha_d\left(\frac{g\mu_B}{k_B}\right)^{1/2} \gamma F_\sigma H^{1/2}, \qquad g\mu_B H >> k_B T \qquad 4.13.$$

According to theory, the dependences of $\Delta\sigma$(H,T) in weak ($g\mu_B H << k_B T$) and strong ($g\mu_B H >> k_B T$) magnetic field should be proportional to H^2 and $H^{1/2}$, respectively. The strength of the magnetic field H is scaled to the thermal energy $k_B T$, so at higher temperatures the crossover from H^2-regime to $H^{1/2}$-regime is expected to occur at a higher field value.

In Figure 4.24 we analyze the isotropy of the negative MC (for the two cases) and its conformity to the e-e interaction model.

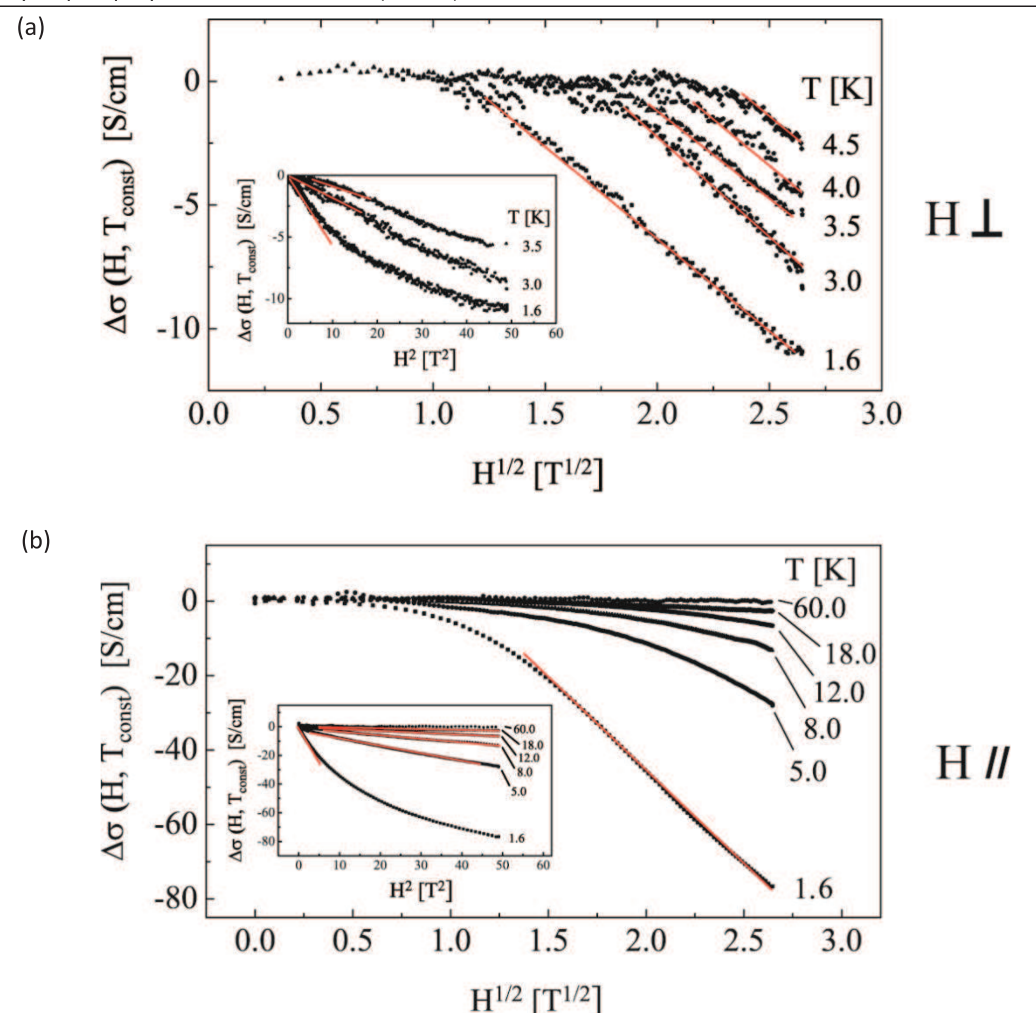

Figure 4.24 Magnetoconductivity as a function of $H^{1/2}$ at several temperatures for magnetic field normal (a) and parallel (b) to the sample plane. (Inset) The same data are plotted as a function of H^2.

Figure 4.24(a) reports the negative magnetoconductivity below 4.5 K in the case of H $\perp$ to the sample plane (same data of Figure 4.22 a-c): the $\Delta\sigma$ dependence nicely follows a $H^{1/2}$ law for the highest values of magnetic field (starting from 1 Tesla for T = 1.6 K), confirming the hypothesis of dominant electron-electron interactions in the strong magnetic field regime. The inset of Figure 4.24(a) also shows the accordance to the H^2 power law in the weak field regime. At T > 4.5 K, the positive and negative MC superpose, but the positive MC is dominant (larger amplitude) and it is the only one observable (Figure 4.22(a)).

Figure 4.24(b) shows the same type of plot in the case of H // for temperatures going from 1.8 K to 60 K. One can see that the $H^{1/2}$ dependency (strong magnetic field limit) is followed at 1.8 K, whereas the curves deviate from this law at higher temperature. From the inset of Figure 4.24(b) one can see that, starting from 5 K, $\Delta\sigma$(H,T) follows a H^2 dependence, typical of e-e interaction in the weak field limit. Objection might be raised regarding the fact that 7 teslas are not a 'weak' magnetic field, but it must be remembered that 'weak' or 'strong' is, in this model, relative to the thermal energy, i.e. $g\mu_B H$ must be scaled with $k_B T$ (Equ. 4.13). At 8 K and 7 Teslas (considering a gyromagnetic ratio g = 2), $g\mu_B H$ and $k_B T$ are comparable. At 30 K and 7 Teslas, $g\mu_B H$ is slightly smaller than $k_B T$, thus the sample is in the weak field limit and a H^2 dependency is justified.

The e-e interactions model has already been adopted to explain magnetic field effect at very low T on highly doped conjugated polymers. For example, Menon *et al*. [16] find good agreement to this model for the magnetoconductivity of PANI:CSA below 4.2 K. Later, Aleshin *et al*. [61] use this interpretation to explain the dependency of the magnetoconductivity of PEDOT doped with PF_6 (10 - 300 µm thick), again below 4.2 K. In both cases, however, magnetotransport at temperatures higher than 4.2 K was not measured.

4.9 Hall Effect

The archetype of a sample used for Hall Effect measurements is made of a uniform slab of electrically conducting material through which a uniform current density flows in the presence of a perpendicular applied magnetic field. The Lorentz force deflects the moving charge carriers to one side of the sample and generates an electric field perpendicular to both the current density and the applied magnetic field. This electric field is measured as a voltage difference, defined as the Hall voltage V_H, equal to:

$$V_H = \frac{R_H I B}{t} \quad 4.14,$$

where R_H is the Hall coefficient, I is the current, B the external magnetic field intensity and t the active material thickness. For a given material, the Hall voltage is directly proportional to B and I and inversely proportional to the sample thickness t. The Hall coefficient R_H reveals the density of free carriers and is equal to:

$$R_H = \frac{1}{e \cdot n} \quad 4.15,$$

where e is the electron charge and n here indicates the electrons or holes carrier density. To be more precise n should be substituted by the difference $(n - p)$ between the density of negative and positive charge carriers. The Hall coefficient, and consequently the Hall voltage V_H, diminish at higher carrier densities, becoming negligible for (inorganic) metals.

Hall measurements may shed light on the occurrence of a diffusive band-like transport in organic semiconductors. For hopping between localized states, it is not possible to introduce a classical velocity of carriers and, thus, a Lorentz force. In the relatively few measurements of the Hall Effect in the hopping regime for conventional semiconductors [62], very small Hall voltages and an anomalous sign for the Hall constant have been observed. We can thus conclude that the observation of a "normal" Hall Effect signal would be a rather convincing signature of delocalized transport.

The first Hall Effect measurements on organic materials have been carried out on single-crystals such as rubrene [63], or pentacene [64],[65] starting from 2005. More recently other molecular crystals have also been studied such as tetramethyltetraselenafulvalene (TMTSF) [66], PDIF-CN_2 [67]. Hall measurement on rubrene/tetracene with improved signal-to-noise ratio has been reported by Lee *et al*. [68] by making use of a polar gate dielectric likely healing the trap states at the surface. Hall measurements reveal that charge transport in the accumulation layer on the surface of organic single-crystals is due to polarons moving diffusively, characterized by a mean free path l that exceeds the intermolecular distance. Starting from these first findings, Hall measurements became increasingly popular for the search of delocalized transport, also for polycrystalline organic semiconductor thin films [69],[70].

For what concerns conjugated polymers, Hall effect has been reported sporadically in bulk polymers on the metallic side of the insulator-metal transition [71], and, to the best of our knowledge,

just one time in a semiconducting polymer thin film [17]. Wang and coworkers [17] report a robust Hall effect in their electrolyte-gated P3HT thin films (60 nm thick, van der Pauw geometry), even though the conductivity temperature dependence of the films clearly fits variable range hopping.

4.9.1 Experiment

Practically, measuring a Hall signal is very challenging. Many non-idealities related to experimental conditions, such as current flow distortion caused by the metallic contacts themselves or by the excitation current used for potential measuring, might short out or “cover” the Hall voltage.

For our experiment we choose to work with the Hall bar geometry represented in Figure 4.25. A DC current flows from source to drain, 5 to 6 in (a), and the face-to-face fingers voltage ΔV_{xy} (couple 1-2 or 3-4) is monitored with a nanovoltmeter for the detection of the Hall voltage V_H. Meanwhile the source-drain voltage V_{sd} is also measured, and in some cases the longitudinal resistance R_{xx} as well. This allows us to exclude ‘artificial’ Hall voltages due to drifts in the channel conductivity and not related to the magnetic field.

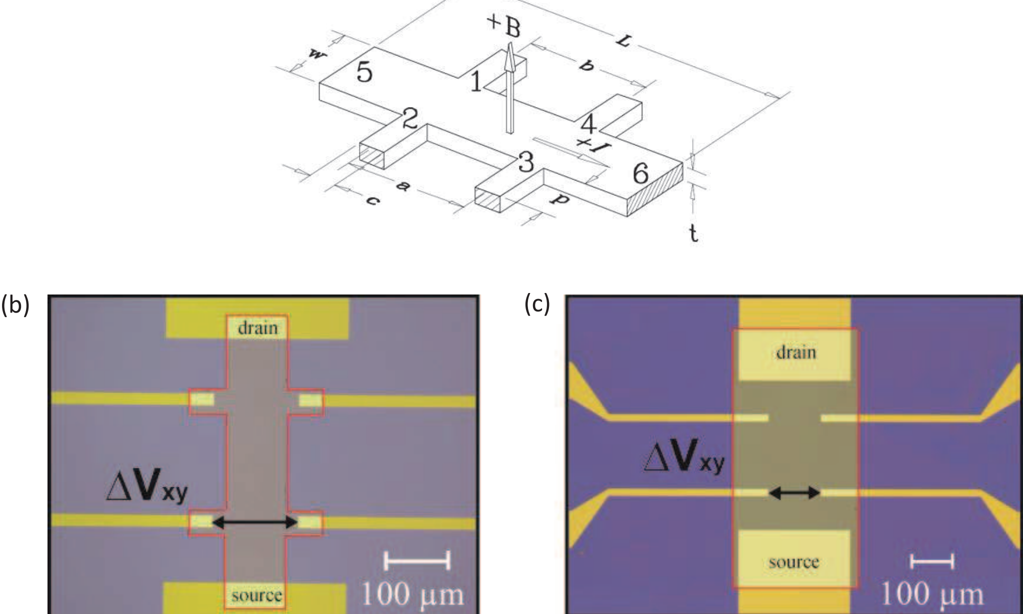

Figure 4.25 Six fingers Hall bar geometry used for Hall Effect measurements on PBTTT thin films. a) Schematic representation of the dimensions playing a role in the measurement. b,c) The two Hall bar geometry used for our experiment with indication of the contacts used to sense the Hall voltage. The main difference is that in (c) fingers largely protrude in the channel, while they are slightly outside in (b).

Hall Effect measurements have been carried out between 180 K and 240 K. At these temperatures the iongel is freezed, thus the leakage current is zero. Magnetic field is applied perpendicular to the sample plane and varied between ±7 Teslas. We source different levels of current I, from -100 nA up to -1 mA. Figure 4.26 (a) and (b) illustrate the outcome of magnetic field scans for seeking Hall Effect on a sample gated at V_g = -2.9 V. The sourced current is respectively -100 µA (a) and -1 µA (b). In Figure 4.26 (c)-(d) the same data are reported, after subtraction of the offset voltage affecting ΔV_{xy}.

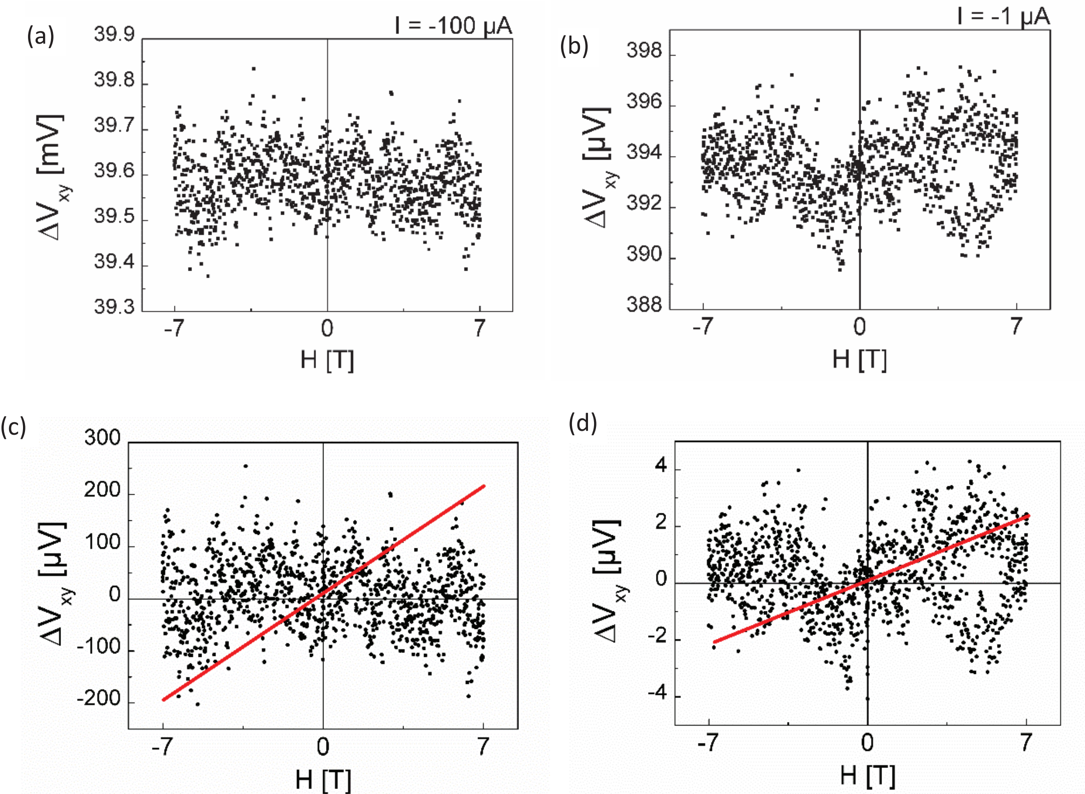

Figure 4.26 Hall Effect measurements of a sample 4, at two different current sourced levels. Data are shown in (a) and (b) before subtraction of the potential offset (~ 39.6 mV for – 100 μA current, and ~ 393 μV for – 1 μA current) and after (c – d). The red line in (c) and (d) indicates the expected Hall voltage calculated from Equ. 4.14 considering $8{\cdot}10^{20}$ cm^{-3} as charge carrier density value.

In both cases the plot is completely flat and extremely noisy. A clear evidence of Hall Voltage has not been found. The cause of the noise might be the vicinity to the insulator-to-metal transition. Red lines in Figure 4.26(c)-(d) indicate the expected Hall voltage calculated for a hypothetical carrier density of $8{\cdot}10^{20}$ cm^{-3}, calculated according to Equation 4.14. The Hall signal might be completely covered by the noise.

The majority of Hall Effect measurements have been carried out with geometry in Figure 4.25(b), where sensing fingers do not protrude in the channel. We now believe that this geometry is not optimized for measuring small signals, since the out-of-channel small segment might add up resistance in the voltage sensing. New tests should be performed with geometry in Figure 4.25(c). AC measurements have also been tested by means of a lock-in instrument, but the noise-to-signal ratio is unvaried. Given the influence of the pressure during the gating step, we also tried to measure Hall Effect keeping atmospheric pressure of He in the cryostat chamber during the magnetic field ramp, but this did not improve the measurement.

However, we must say that probably noise has not been the only issue. Hall Effect measurements have been carried out before (chronologically) the low temperature magnetoconductance study, thus the important piece of information about weak localization was still missing. In light of the low temperature MC results and of some further considerations, we concluded that we have searched for Hall Effect in the wrong range of temperature and doping. In the short term we will probably restart working on it, keeping in mind that to maximize the Hall signal we should measure samples:

i. At T < 60 K (where weak localization also occurs!)

We have chosen to perform Hall Effect measurements in the temperature range 180 K – 220 K in imitation of the first and only report of Hall Effect in a conjugated polymer (Wang *et al*. [17]). However, we have observed at a later stage that positive MC (signature of weak localization and phase-coherent transport) occurs at temperatures much lower than such a range. At lower temperatures phase-breaking events due to phonons are indeed expected to be less relevant and charge carriers maintain their phase coherence for longer time, and distances. Consequently, in our system, the intensity of the Hall Voltage is expected to be higher at lower temperatures.

ii. At maximum doping level

We have attempted to measure Hall Effect on samples at a doping level equal to the one of sample 3 and 4 (not maximized), because the Hall Voltage is inversely proportional to the carriers density (Equ. 4.14). Samples with record conductivities (such as sample 6) have been dedicated to low temperature magnetoconductance measurements only. However, Wang *et al*. [17] emphasize that in electrolyte-gated P3HT, the Hall voltage increases with increasing the doping level. Even though this fact is in disagreement with Hall Effect theory (equ 4.14), the reason is likely the following: in order for the Hall signal to become significant, a high enough density of carriers is required to populate the more delocalized states in the center of the DOS. At low and moderate doping levels the charge transport still occurs through highly localized electronic wavefunctions and the Hall Effect is immeasurably small.

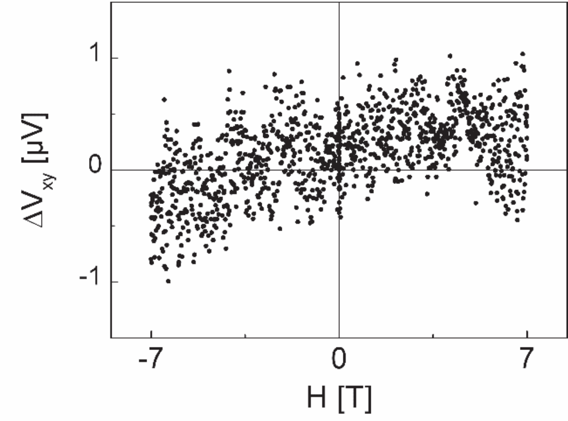

Figure 4.27 Hall Effect magnetic ramp for one of the mostly conducting samples (~ sample 6). Sourced current I = -10 μA, offset potential subtracted ~ 20 μV.

For instance, we performed a quick Hall Effect test run on a very conductive sample (room temperature conductivity ~ 3000 S/cm, similar to sample 6) and we observe the signal reported in Figure 4.27. A linear trend can be perceived although the noise, giving hope for finding Hall Effect signal at very high doping.

The occurrence of Hall Effect would represent a third experimental fingerprint of long electronic wavefunction delocalization and phase-coherent transport in highly doped PBTTT thin films, besides the finite $T \rightarrow 0$ K conductivity and the occurrence of weak localization.

4.10 Mobility calculation

The advantage of PBTTT thin films respect to supramolecular nanowires (Chapter 2) and LPE-graphene nanosheets (Chapter 3) is that we can measure the four-probe conductivity and extract the intrinsic value of mobility of the organic material. Mobility extracted from transfer curves of PBTTT deposited onto SiO_2 bottom gate devices is around 0.1 $cm^2/V \cdot s$.

The mobility of our metallic-type samples 5 and 6 is extracted from the four-probe conductivity according to:

$$\mu = \frac{\sigma_{4p}}{e \cdot p} \quad 4.16.$$

The four-probe conductivity σ_{4p} is calculated by considering the whole thickness of the PBTTT (25 nm) as active channel. Considering the doping levels *p* reported in Table 4.2, we obtain holes mobility at room temperature of $\sim$ 1.6 $cm^2/V \cdot s$ for sample 5 and $\sim$ 3 $cm^2/V \cdot s$ for sample 6. Thanks to the extremely weak conductivity temperature dependence, the mobility at low temperature (1.6 K) remains remarkably higher than 0.1 $cm^2/V \cdot s$ for both samples.

We underline that the doping values we use for the mobility calculation are rather large estimates. Qualitatively, using a common value of $p = 1 \cdot 10^{21}$ cm^{-3}, samples 6 would reach μ values up to 30 $cm^2/V \cdot s$, higher to the best quality organic single crystals. These findings clearly indicate that better estimates of the carrier density are needed.

4.11 Conclusions

In this Chapter we report the successful electrolyte-gating of a semiconductor polymer thin film of C12-PBTTT. Electrolyte-gating causes electrochemical doping of the semiconducting polymer when the gate bias is pushed up to few Volts. Since the 80's, electrochemical doping is used to improve the conductivity of conjugated polymers, such as polyacetylene, polyanyline, polypyrrole, etc. Confronted with these early attempts of creating 'synthetic metal', the advantages of using gate electrolytes to produce electrochemical doping are that:

- Electrolyte-gating can be applied on thin films and in a solid state device;
- Electrolyte-gating allows controlling the doping level by means of a gate potential.

In the most doped samples we could reach remarkable values of conductivity, above 1000 S/cm at room temperature. Such values are comparable to the conductivity of PEDOT:PSS, another conjugated polymer today widely used in its thin film form as contact in photovoltaic cells or other Organic Electronic devices.

Several examples of electrolyte-gated OFET have already been reported in literature. Some of them explicitly share our intention of accessing a metallic-type conductivity, namely Wang *et al*. tried on P3HT [17], Shi *et al*. on C14-PBTTT [43] and Tanaka *et al*. on C16-PBTTT [72], but they could not go beyond a hopping-type of transport. To our knowledge the unique report of metallicity of electrolyte-gated polymer thin films has been published by Dhoot *et al.* [28], but with discontinuous data presented below 80 K.

In this context, our results are thus noteworthy. We provide different experimental signatures demonstrating that the highly doped PBTTT thin films are at the onset of metallicity, namely:

i. the extremely weak temperature dependence of the conductivity;
ii. the extrapolation to a finite σ_0 for $T \rightarrow 0$ K;
iii. the appearance of positive magnetoconductance, related to disruption of weak localization.

These results have been published in the article '*Magnetoconductance anisotropy of a polymer thin film at the onset of metallicity*' [73].

The extracted holes mobility μ_h for the most conductive samples is above 1 cm^2/V·s at room temperature, possibly rising up to 30 cm^2/V·s by considering the incertitude on the doping-induced carriers density *p*. This mobility value is extremely more reliable respect to the estimates given for STANWs and LPE-graphene, because four-probe measurements allow splitting the contact resistance from the intrinsic material conductivity.

Metallicity and very high mobility must stem from a long effective conjugation length along the polymer backbone. We attribute this long conjugation length to the high degree of crystallinity characterizing PBTTT thin films and to the trap-filling effect of doping, which excludes localized electronic states from charge transport. This probably translates into a long coherence length of the system, i.e. a charge carrier should be able to cover a considerable distance (several tens of nanometers) without losing its phase coherence, especially at lower temperatures where phonons scattering is reduced. Phase-coherent transport is likely spin-conserving, thus we can hope for long spin diffusion length λ_s. Under the point of view of the intrinsic transport properties, highly doped PBTTT thin films exceed the supramolecular triarylamines of Chapter 1 and could be very good candidates for the fabrication of organic lateral spinvalves.

BIBLIOGRAPHY

[1] I. McCulloch, M. Heeney, M. L. Chabinyc, D. DeLongchamp, R. J. Kline, M. Cölle, W. Duffy, D. Fischer, D. Gundlach, B. Hamadani, R. Hamilton, L. Richter, A. Salleo, M. Shkunov, D. Sparrowe, S. Tierney, and W. Zhang, "Semiconducting Thienothiophene Copolymers: Design, Synthesis, Morphology, and Performance in Thin-Film Organic Transistors," *Adv. Mater.*, vol. 21, no. 10–11, pp. 1091–1109, Mar. 2009.

[2] S. Vasimalla, S. P. Senanayak, M. Sharma, K. S. Narayan, and P. K. Iyer, "Improved Performance of Solution-Processed n-Type Organic Field-Effect Transistors by Regulating the Intermolecular Interactions and Crystalline Domains on Macroscopic Scale," *Chem. Mater.*, vol. 26, no. 13, pp. 4030–4037, Jul. 2014.

[3] H. Sirringhaus, P. J. Brown, R. H. Friend, M. M. Nielsen, K. Bechgaard, B. M. W. Langeveld-Voss, A. J. H. Spiering, R. a. J. Janssen, E. W. Meijer, P. Herwig, and D. M. de Leeuw, "Two-dimensional charge transport in self-organized, high-mobility conjugated polymers," *Nature*, vol. 401, no. 6754, pp. 685–688, Oct. 1999.

[4] I. McCulloch, M. Heeney, C. Bailey, K. Genevicius, I. MacDonald, M. Shkunov, D. Sparrowe, S. Tierney, R. Wagner, W. Zhang, M. L. Chabinyc, R. J. Kline, M. D. McGehee, and M. F. Toney, "Liquid-crystalline semiconducting polymers with high charge-carrier mobility," *Nat. Mater.*, vol. 5, no. 4, pp. 328–333, Mar. 2006.

[5] D. M. DeLongchamp, R. J. Kline, E. K. Lin, D. A. Fischer, L. J. Richter, L. A. Lucas, M. Heeney, I. McCulloch, and J. E. Northrup, "High Carrier Mobility Polythiophene Thin Films: Structure Determination by Experiment and Theory," *Adv. Mater.*, vol. 19, no. 6, pp. 833–837, Mar. 2007.

[6] H. Bassler, Ed., *Charge Transport in Organic Semiconductors*, vol. 312. Berlin, Heidelberg: Springer Berlin Heidelberg, 2012.

[7] J.-W. van der Horst, P. A. Bobbert, M. A. J. Michels, G. Brocks, and P. J. Kelly, "Ab Initio Calculation of the Electronic and Optical Excitations in Polythiophene: Effects of Intra- and Interchain Screening," *Phys. Rev. Lett.*, vol. 83, no. 21, pp. 4413–4416, Nov. 1999.

[8] W. P. Su, J. R. Schrieffer, and A. J. Heeger, "Solitons in Polyacetylene," *Phys. Rev. Lett.*, vol. 42, no. 25, pp. 1698–1701, Jun. 1979.

[9] P. W. Anderson, "Absence of Diffusion in Certain Random Lattices," *Phys. Rev.*, vol. 109, no. 5, pp. 1492–1505, Mar. 1958.

[10] S. T. Hoffmann, H. Bässler, and A. Köhler, "What Determines Inhomogeneous Broadening of Electronic Transitions in Conjugated Polymers?," *J. Phys. Chem. B*, vol. 114, no. 51, pp. 17037–17048, Dec. 2010.

[11] D. Venkateshvaran, M. Nikolka, A. Sadhanala, V. Lemaur, M. Zelazny, M. Kepa, M. Hurhangee, A. J. Kronemeijer, V. Pecunia, I. Nasrallah, I. Romanov, K. Broch, I. McCulloch, D. Emin, Y. Olivier, J. Cornil, D. Beljonne, and H. Sirringhaus, "Approaching disorder-free transport in high-mobility conjugated polymers," *Nature*, Nov. 2014.

[12] H. Bässler, "Charge Transport in Disordered Organic Photoconductors a Monte Carlo Simulation Study," *Phys. Status Solidi B*, vol. 175, no. 1, pp. 15–56, Jan. 1993.

[13] S. Gambino, I. D. W. Samuel, H. Barcena, and P. L. Burn, "Electric field and temperature dependence of the hole mobility in a bis-fluorene cored dendrimer," *Org. Electron.*, vol. 9, no. 2, pp. 220–226, Apr. 2008.

[14] A. Miller and E. Abrahams, "Impurity conduction at low concentrations," *Phys. Rev.*, vol. 120, no. 3, p. 745, 1960.

[15] V. I. Arkhipov, E. V. Emelianova, and G. J. Adriaenssens, "Effective transport energy versus the energy of most probable jumps in disordered hopping systems," *Phys. Rev. B*, vol. 64, no. 12, p. 125125, Sep. 2001.

[16] R. Menon, C. O. Yoon, D. Moses, A. J. Heeger, and Y. Cao, "Transport in polyaniline near the critical regime of the metal-insulator transition," *Phys. Rev. B*, vol. 48, no. 24, pp. 17685–17694, Dec. 1993.

[17] S. Wang, M. Ha, M. Manno, C. Daniel Frisbie, and C. Leighton, "Hopping transport and the Hall effect near the insulator–metal transition in electrochemically gated poly(3-hexylthiophene) transistors," *Nat. Commun.*, vol. 3, p. 1210, Nov. 2012.

[18] N. F. Mott, *Adv. Phys.*, vol. 16, no. 49.

[19] H. Shirakawa, E. J. Louis, A. G. MacDiarmid, C. K. Chiang, and A. J. Heeger, “Synthesis of electrically conducting organic polymers: halogen derivatives of polyacetylene, (CH)x,” *J. Chem. Soc. Chem. Commun.*, no. 16, pp. 578–580, Jan. 1977.

[20] C. K. Chiang, C. R. Fincher, Y. W. Park, A. J. Heeger, H. Shirakawa, E. J. Louis, S. C. Gau, and A. G. MacDiarmid, “Electrical Conductivity in Doped Polyacetylene,” *Phys. Rev. Lett.*, vol. 39, no. 17, pp. 1098–1101, Oct. 1977.

[21] P. J. Nigrey, A. G. MacDiarmid, and A. J. Heeger, “Electrochemistry of polyacetylene, (CH)x: electrochemical doping of (CH)x films to the metallic state,” *J. Chem. Soc. Chem. Commun.*, no. 14, pp. 594–595, Jan. 1979.

[22] M. Ahlskog, M. Reghu, A. J. Heeger, T. Noguchi, and T. Ohnishi, “Electronic transport in the metallic state of oriented poly (p-phenylenevinylene),” *Phys. Rev. B*, vol. 53, no. 23, p. 15529, 1996.

[23] C. O. Yoon, R. M., D. Moses, and A. J. Heeger, “Transport near the metal-insulator transition: Polypyrrole doped with PF6,” *Phys. Rev. B*, vol. 49, no. 16, pp. 10851–10863, Apr. 1994.

[24] M. Ahlskog, R. Menon, A. J. Heeger, T. Noguchi, and T. Ohnishi, “Metal-insulator transition in oriented poly (p-phenylenevinylene),” *Phys. Rev. B*, vol. 55, no. 11, p. 6777, 1997.

[25] A. J. Heeger, “Semiconducting and Metallic Polymers: The Fourth Generation of Polymeric Materials (Nobel Lecture),” *Angew. Chem. Int. Ed.*, vol. 40, no. 14, pp. 2591–2611, Jul. 2001.

[26] J. D. Yuen, A. S. Dhoot, E. B. Namdas, N. E. Coates, M. Heeney, I. McCulloch, D. Moses, and A. J. Heeger, “Electrochemical Doping in Electrolyte-Gated Polymer Transistors,” *J. Am. Chem. Soc.*, vol. 129, no. 46, pp. 14367–14371, Nov. 2007.

[27] S. H. Kim, K. Hong, W. Xie, K. H. Lee, S. Zhang, T. P. Lodge, and C. D. Frisbie, “Electrolyte-Gated Transistors for Organic and Printed Electronics,” *Adv. Mater.*, p. n/a–n/a, Dec. 2012.

[28] A. S. Dhoot, J. D. Yuen, M. Heeney, I. McCulloch, D. Moses, and A. J. Heeger, “Beyond the metal-insulator transition in polymer electrolyte gated polymer field-effect transistors,” *Proc. Natl. Acad. Sci.*, vol. 103, no. 32, pp. 11834–11837, 2006.

[29] C. Tanase, E. J. Meijer, P. W. M. Blom, and D. M. de Leeuw, “Unification of the Hole Transport in Polymeric Field-Effect Transistors and Light-Emitting Diodes,” *Phys. Rev. Lett.*, vol. 91, no. 21, p. 216601, Nov. 2003.

[30] W. Pasveer, J. Cottaar, C. Tanase, R. Coehoorn, P. Bobbert, P. Blom, D. de Leeuw, and M. Michels, “Unified Description of Charge-Carrier Mobilities in Disordered Semiconducting Polymers,” *Phys. Rev. Lett.*, vol. 94, no. 20, May 2005.

[31] J. J. Brondijk, F. Maddalena, K. Asadi, H. J. van Leijen, M. Heeney, P. W. M. Blom, and D. M. de Leeuw, “Carrier-density dependence of the hole mobility in doped and undoped regioregular poly(3-hexylthiophene),” *Phys. Status Solidi B*, vol. 249, no. 1, pp. 138–141, 2012.

[32] V. I. Arkhipov, E. V. Emelianova, P. Heremans, and H. Bässler, “Analytic model of carrier mobility in doped disordered organic semiconductors,” *Phys. Rev. B*, vol. 72, no. 23, p. 235202, Dec. 2005.

[33] H. Shimotani, G. Diguet, and Y. Iwasa, “Direct comparison of field-effect and electrochemical doping in regioregular poly(3-hexylthiophene),” *Appl. Phys. Lett.*, vol. 86, no. 2, p. 022104, Jan. 2005.

[34] G. Bergmann, “Weak localization in thin films: a time-of-flight experiment with conduction electrons,” *Phys. Rep.*, vol. 107, no. 1, pp. 1–58, May 1984.

[35] K. Lee, A. J. Heeger, and Y. Cao, “Reflectance of polyaniline protonated with camphor sulfonic acid: Disordered metal on the metal-insulator boundary,” *Phys. Rev. B*, vol. 48, no. 20, pp. 14884–14891, Nov. 1993.

[36] K. Lee, R. Menon, C. O. Yoon, and A. J. Heeger, “Reflectance of conducting polypyrrole: Observation of the metal-insulator transition driven by disorder,” *Phys. Rev. B*, vol. 52, no. 7, pp. 4779–4787, Aug. 1995.

[37] N. S. Sariciftci, A. J. Heeger, and Y. Cao, “Paramagnetic susceptibility of highly conducting polyaniline: Disordered metal with weak electron-electron interactions (Fermi glass),” *Phys. Rev. B*, vol. 49, no. 9, pp. 5988–5992, Mar. 1994.

[38] V. I. Krinichnyi, A. L. Konkin, and A. P. Monkman, “Electron paramagnetic resonance study of spin centers related to charge transport in metallic polyaniline,” *Synth. Met.*, vol. 162, no. 13–14, pp. 1147–1155, Aug. 2012.

[39] J. J. Armao, M. Maaloum, T. Ellis, G. Fuks, M. Rawiso, E. Moulin, and N. Giuseppone, "Healable Supramolecular Polymers as Organic Metals," *J. Am. Chem. Soc.*, vol. 136, no. 32, pp. 11382–11388, Aug. 2014.

[40] L. Biniek, N. Leclerc, T. Heiser, R. Bechara, and M. Brinkmann, "Large Scale Alignment and Charge Transport Anisotropy of pBTTT Films Oriented by High Temperature Rubbing," *Macromolecules*, vol. 46, no. 10, pp. 4014–4023, May 2013.

[41] K. H. Lee, M. S. Kang, S. Zhang, Y. Gu, T. P. Lodge, and C. D. Frisbie, "'Cut and Stick' Rubbery Ion Gels as High Capacitance," *Adv. Mater.*, vol. 24, no. 32, pp. 4457–4462, 2012.

[42] E. Cho, C. Risko, D. Kim, R. Gysel, N. Cates Miller, D. W. Breiby, M. D. McGehee, M. F. Toney, R. J. Kline, and J.-L. Bredas, "Three-Dimensional Packing Structure and Electronic Properties of Biaxially Oriented Poly(2,5-bis(3-alkylthiophene-2-yl)thieno[3,2-b]thiophene) Films," *J. Am. Chem. Soc.*, vol. 134, no. 14, pp. 6177–6190, 2012.

[43] W. Shi, J. Ye, J. G. Checkelsky, C. Terakura, and Y. Iwasa, "Transport Properties of Polymer Semiconductor Controlled by Ionic Liquid as a Gate Dielectric and a Pressure Medium," *Adv. Funct. Mater.*, vol. 24, no. 14, pp. 2005–2012, Apr. 2014.

[44] W. L. McMillan, "Scaling theory of the metal-insulator transition in amorphous materials," *Phys. Rev. B*, vol. 24, no. 5, p. 2739, 1981.

[45] A. Zabrodskii and K. Zinov'eva, "Low-temperature conductivity and metal–insulator transition in compensate n-Ge," *Zh Eksp Teor Fiz*, vol. 86, p. 742, 1984.

[46] P. A. Lee and T. V. Ramakrishnan, "Disordered electronic systems," *Rev. Mod. Phys.*, vol. 57, no. 2, pp. 287–337, Apr. 1985.

[47] D. Belitz and K. I. Wysokinski, "Electronic inelastic lifetime near a mobility edge," *Phys. Rev. B*, vol. 36, no. 17, pp. 9333–9336, Dec. 1987.

[48] M. E. Turk, J.-H. Choi, S. J. Oh, A. T. Fafarman, B. T. Diroll, C. B. Murray, C. R. Kagan, and J. M. Kikkawa, "Gate-Induced Carrier Delocalization in Quantum Dot Field Effect Transistors," *Nano Lett.*, vol. 14, no. 10, pp. 5948–5952, Oct. 2014.

[49] J. Northrup, "Atomic and electronic structure of polymer organic semiconductors: P3HT, PQT, and PBTTT," *Phys. Rev. B*, vol. 76, no. 24, p. 245202, Dec. 2007.

[50] C. Poelking, E. Cho, A. Malafeev, V. Ivanov, K. Kremer, C. Risko, J.-L. Brédas, and D. Andrienko, "Characterization of Charge-Carrier Transport in Semicrystalline Polymers: Electronic Couplings, Site Energies, and Charge-Carrier Dynamics in Poly(bithiophene- alt -thienothiophene) [PBTTT]," *J. Phys. Chem. C*, vol. 117, no. 4, pp. 1633–1640, Jan. 2013.

[51] L.-H. Li, O. Y. Kontsevoi, S. H. Rhim, and A. J. Freeman, "Structural, electronic, and linear optical properties of organic photovoltaic PBTTT-C14 crystal," *J. Chem. Phys.*, vol. 138, no. 16, p. 164503, Apr. 2013.

[52] T. Liu and A. Troisi, "Understanding the Microscopic Origin of the Very High Charge Mobility in PBTTT: Tolerance of Thermal Disorder," *Adv. Funct. Mater.*, vol. 24, no. 7, pp. 925–933, 2014.

[53] A. Kawabata, "Theory of negative magnetoresistance in three-dimensional systems," *Solid State Commun.*, vol. 34, no. 6, pp. 431–432, May 1980.

[54] A. L. Efros and B. I. Shklovskii, "Electronic properties of Doped Semiconductors_Shklovskii-Efros.pdf." Springer-Verlag, 1984.

[55] U. Sivan, O. Entin-Wohlman, and Y. Imry, "Orbital magnetoconductance in the variable-range–hopping regime," *Phys. Rev. Lett.*, vol. 60, no. 15, pp. 1566–1569, Apr. 1988.

[56] L. B. Ioffe and B. Z. Spivak, "Giant magnetoresistance in the variable-range hopping regime," *J. Exp. Theor. Phys.*, vol. 117, no. 3, pp. 551–569, Sep. 2013.

[57] A. K. Mukherjee and R. Menon, "Magnetotransport in doped polyaniline," *J. Phys. Condens. Matter*, vol. 17, no. 12, pp. 1947–1960, Mar. 2005.

[58] J. D. Yuen, R. Menon, N. E. Coates, E. B. Namdas, S. Cho, S. T. Hannahs, D. Moses, and A. J. Heeger, "Nonlinear transport in semiconducting polymers at high carrier densities," *Nat. Mater.*, vol. 8, no. 7, pp. 572–575, Jul. 2009.

[59] K. Asadi, A. J. Kronemeijer, T. Cramer, L. Jan Anton Koster, P. W. M. Blom, and D. M. de Leeuw, "Polaron hopping mediated by nuclear tunnelling in semiconducting polymers at high carrier density," *Nat. Commun.*, vol. 4, p. 1710, Apr. 2013.

[60] P. Dai, Y. Zhang, and M. P. Sarachik, "Magnetoconductance of metallic Si:B near the metal-insulator transition," *Phys. Rev. B*, vol. 46, no. 11, pp. 6724–6731, Sep. 1992.

[61] A. Aleshin, R. Kiebooms, R. Menon, F. Wudl, and A. J. Heeger, “Metallic conductivity at low temperatures in poly (3, 4-ethylenedioxythiophene) doped with PF 6,” *Phys. Rev. B*, vol. 56, no. 7, p. 3659, 1997.

[62] D. C. Look, D. C. Walters, M. O. Manasreh, J. R. Sizelove, C. E. Stutz, and K. R. Evans, “Anomalous Hall-effect results in low-temperature molecular-beam-epitaxial GaAs: Hopping in a dense EL2-like band,” *Phys. Rev. B*, vol. 42, no. 6, pp. 3578–3581, Aug. 1990.

[63] V. Podzorov, E. Menard, J. Rogers, and M. Gershenson, “Hall Effect in the Accumulation Layers on the Surface of Organic Semiconductors,” *Phys. Rev. Lett.*, vol. 95, no. 22, Nov. 2005.

[64] T. Uemura, M. Yamagishi, J. Soeda, Y. Takatsuki, Y. Okada, Y. Nakazawa, and J. Takeya, “Temperature dependence of the Hall effect in pentacene field-effect transistors: Possibility of charge decoherence induced by molecular fluctuations,” *Phys. Rev. B*, vol. 85, no. 3, Jan. 2012.

[65] Y. Takamatsu, T. Sekitani, and T. Someya, “Temperature dependence of Hall effects in organic thin-film transistors on plastic films,” *Appl. Phys. Lett.*, vol. 90, no. 13, p. 133516, 2007.

[66] H. Xie, H. Alves, and A. F. Morpurgo, “Quantitative analysis of density-dependent transport in tetramethyltetraselenafulvalene single-crystal transistors: Intrinsic properties and trapping,” *Phys. Rev. B*, vol. 80, no. 24, p. 245305, Dec. 2009.

[67] N. A. Minder, S. Ono, Z. Chen, A. Facchetti, and A. F. Morpurgo, “Band-Like Electron Transport in Organic Transistors and Implication of the Molecular Structure for Performance Optimization,” *Adv. Mater.*, vol. 24, no. 4, pp. 503–508, 2012.

[68] B. Lee, Y. Chen, D. Fu, H. T. Yi, K. Czelen, H. Najafov, and V. Podzorov, “Trap healing and ultralow-noise Hall effect at the surface of organic semiconductors,” *Nat. Mater.*, vol. 12, no. 12, pp. 1125–1129, Dec. 2013.

[69] M. Yamagishi, J. Soeda, T. Uemura, Y. Okada, Y. Takatsuki, T. Nishikawa, Y. Nakazawa, I. Doi, K. Takimiya, and J. Takeya, “Free-electron-like Hall effect in high-mobility organic thin-film transistors,” *Phys. Rev. B*, vol. 81, no. 16, Apr. 2010.

[70] T. Uemura, K. Nakayama, Y. Hirose, J. Soeda, M. Uno, W. Li, M. Yamagishi, Y. Okada, and J. Takeya, “Band-like transport in solution-crystallized organic transistors,” *Curr. Appl. Phys.*, vol. 12, pp. S87–S91, Dec. 2012.

[71] K. Lee, S. Cho, S. Heum Park, A. J. Heeger, C.-W. Lee, and S.-H. Lee, “Metallic transport in polyaniline,” *Nature*, vol. 441, no. 7089, pp. 65–68, May 2006.

[72] H. Tanaka, M. Hirate, S. Watanabe, and S. Kuroda, “Microscopic Signature of Metallic State in Semicrystalline Conjugated Polymers Doped with Fluoroalkylsilane Molecules,” *Adv. Mater.*, vol. 26, no. 15, pp. 2376–2383, Apr. 2014.

[73] S. Zanettini, J. F. Dayen, C. Etrillard, N. Leclerc, M. venkata Kamalakar, B. Doudin, “Magnetoconductance anisotropy of a polymer thin film at the onset of metallicity,” *Appl. Phys. Lett.*, in press.

5. Contact resistance of doped PBTTT with metals

As we already explained in the Introduction, the optimal performance of a spinvalve relies not only on the efficiency of spin transport throughout the non-magnetic spacer, but also on the maximization of spin injection into it and spin detection from it. The spin polarization of the injected electrical current and the capability to detect it with another ferromagnetic electrode depend on the resistivity values of the ferromagnetic electrodes and the non-magnetic channel, as well as on the contact resistances between them.

Our ultimate goal is the fabrication of lateral organic spinvalves. When dealing with ferromagnetic/organic interfaces (or more generally, with metal/organic interfaces), the major issue is the resistance mismatch problem (resistivity metal << resistivity organic semiconductor) which hinders the propagation of the spin current inside the organic semiconductor.

We have presented in the previous chapters three examples of highly conductive materials. For them, the resistance mismatch with metals is strongly reduced. However, in the hypothesis of using one of those as organic spacer in a spinvalve device, we should consider that the contact resistance unavoidably introduced by bringing together two materials very different by nature, such a molecular material and a metal, starts to play a crucial role and could potentially block the flow of spin-polarized currents in our device. In this Chapter we want to verify if this is the case for our highly doped PBTTT thin films. The main advantage of thin films is indeed to provide experimental access to the contact resistance value, in contrast to the two-probe limited information relative to STANWs (Chapter 3) and LPE-graphene nanosheets (Chapter 4).

We first review the theory of spin injection into a semiconductor (quickly explained in the Introduction already) and the nature of metal/organic interfaces, with special attention to the case of solution-processed polymers onto metal bottom electrodes. Later, we report the experimental study on the contact resistance of electrolyte-gated PBTTT on Gold and Nickel electrodes, conducted by means of gated four-probe method (gFP method). This study is tightly related to the findings of Chapter 4. One motivation for the choice of electrolyte-gating was in fact the reported record low values for interface resistance in organic transistors [1]. Finally we discuss the observed contact resistance values in comparison to the ones typically found for standard dielectric Organic Field-Effect Transistors (OFETs) and with respect to the spin injection conditions for Spintronics.

5.1 Semiconductor between spin polarized source-drain: the problem of spin injection and detection

In this paragraph we review the theory of spin injection (and detection) into (from) a semiconductor sandwiched between spin polarized source and drain electrodes. Figure 5.1 represents the prototypical lateral spinvalve for which the spin injection/detection problem is here discussed.

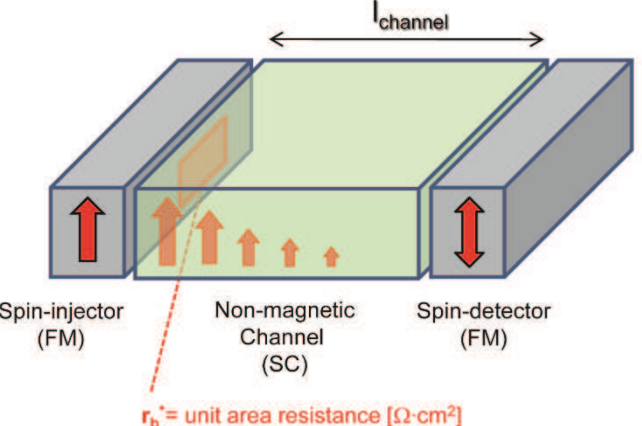

Figure 5.1 Schematic representation of spin-dependent current injection in a lateral spinvalve formed by a non-magnetic semiconductor (SC) between spin-polarized ferromagnetic (FM) source and drain electrodes.

The most common approach for spin injection in semiconductors (SC), inorganic or organic, is injecting an electric current from a transition metal ferromagnet (FM) such as Fe, Co or Ni. These metals exhibit in fact spin-dependent conduction ($j\uparrow \neq j\downarrow$) when magnetized. Alternatives are ferromagnetic semiconductors [2], ferromagnetically-doped semiconductors [3], Heusler alloys or half-metals such as $La_{0.7}Sr_{0.3}MnO_3$ (LSMO) [4],[5], but they are less practical than simple metals (or they are not spin-polarized at room temperature). The spin-dependent conduction in a ferromagnet is due to the magnetic exchange energy that splits significantly the density of state of *d* electrons at the Fermi level. In the two-channels Mott's model of conduction, this splitting implies different scattering probabilities for the two spins populations of conduction electrons, and therefore two different conductivities, with resulting spin polarization of the current $(SP)_I$.

The injection of a spin-polarized current from a material into another is governed by the diffusive behavior of the accumulated spin imbalance $\Delta\mu$ at the interface. The spin accumulation results from the contrast in spin-up and spin-down current in the ferromagnet (FM) and in the non-magnetic material (N, where 'N' stays for "non-ferromagnetic"): at the interface the spin-up/spin-down unbalance of the FM should be accommodated into the equal spin current channels of the SC (Figure 5.2 (a)). This generates a spin accumulation $\Delta\mu = \mu\uparrow - \mu\downarrow$ which relaxes on both sides of the interface as represented in Figure 5.2(b). If the magnetic and non-magnetic materials are both metallic, the spin accumulation also relaxes inside the non-magnetic metal and spin-polarized current is injected (red line in Figure 5.2(c)). As $\Delta\mu$ obeys a diffusive equation the spin current in the material can be interpreted as a current flowing in a material at impedance $\rho\cdot\lambda_s$, where ρ is the material resistivity and λ_s its spin diffusion length.

Problems arise when the non-magnetic material is a semiconductor (SC). The main issue for spin injection at the FM/SC interface is due to the much higher resistivity of the semiconductor respect to the one of the FM metal [6]. This obstacle is generally known as "resistance mismatch problem": the spin current propagation inside the SC with high spin impedance is hindered and therefore escapes by flowing back into the FM electrode ("back-flow"), where it can relax much faster.

(a)

(b)

(c)

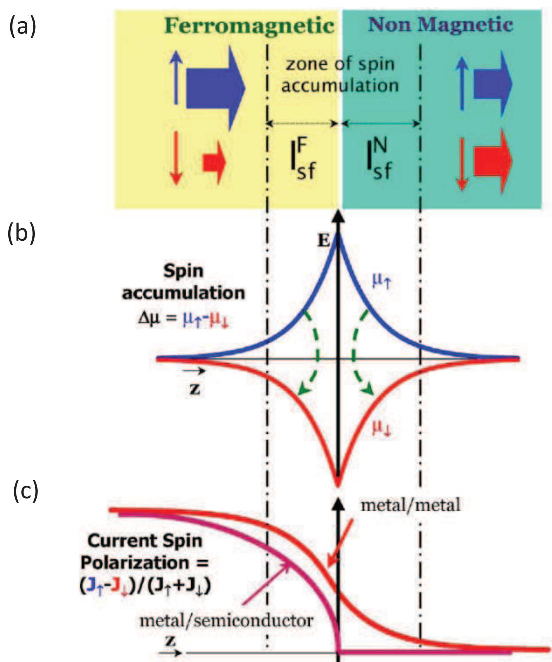

Figure 5.2 a) Spin-up and spin-down current far from an interface between the ferromagnetic and nonmagnetic conductors (outside the spin-accumulation zone). b) Splitting of the chemical potentials μ ↑ and μ ↓ at the interface. c) Variation of the current spin polarization when there is an approximate balance between the spin flips on both sides (metal/metal) and when the spin flips on the left side are predominant (metal/semiconductor for example).

One way to circumvent this mismatch is to have a spin-dependent interface resistance separating FM and SC. If the injected spin current comes from a source made of FM + interface, the related impedance can become comparable (or even lower) to the SC, leading to an optimal injection of the spin current into the SC. This interface resistance has been typically added in the form of a tunnel barrier of oxide.

However, one must also consider the problem of detecting the injected spin-polarized current (decaying along the semiconducting channel) at the second ferromagnet interface. Spin detection is efficient when the outgoing spins have not lost their spin memory at the end of the semiconducting spacer. This requirement imposes a condition not only on the channel length, which should not be too long ($L_{channel} << \lambda_s$), but also on the electrons dwell time. Electrons should not reside in the channel longer than their spin flip time τ_s. In this case, having a too high interface resistance between the semiconductor and the FM spin detector is detrimental for spin detection because it causes electrons bouncing back at the SC/FM interface, thus increasing their residence time in the channel.

Therefore, to obtain optimum spin injection and spin detection in and out of a semiconductor, the interfaces between this and the metallic source and drain must have a contact resistance r_b* per unit of area [$\Omega \cdot cm^2$] included between well-defined boundaries r_1 and r_2:

$$r_1 < r_b^* < r_2 \tag{5.1.}$$

In the next paragraphs, these two boundaries r_1 and r_2 of Equation 5.1 are discussed in more detail.

5.1.1 Lower limit for interface resistance: $r_b^* > r_1$

The difficulty of spin injection in a semiconductor from a metallic ferromagnet has been put forward first by Schmidt *et al.* [6] and subsequently discussed by Fert *et al*. [7]. In this paragraph we follow the notations and modeling of [7] and [8].

The lower limit of Equation 5.1 comes from a single-interface problem. Figure 5.2 in the previous paragraph helps in the understanding. A difference of potential is applied between the ferromagnet F and the non-magnetic conductor N, forcing the current to flow from F to N. Far in the ferromagnetic material, the electron current is spin-polarized ($j\uparrow \neq j\downarrow$), whereas far in the non-magnetic channel the current is not polarized ($j\uparrow = j\downarrow$). At the interface the spin injection takes place thanks to a transfer of current between the same spin channel in the two different materials. This transfer produces spin accumulation, which is a splitting of the electrochemical potential of spin-up and spin-down electrons, $\Delta\mu = \mu\uparrow - \mu\downarrow$ (Figure 5.2(b)). This spin accumulation obeys a diffusion equation, with a characteristic length defined as the spin diffusion length, respectively λ^F_s in the ferromagnet and λ^N_s in the semiconductor, over which it loses its spin memory by spin flipping scattering events. This accumulation therefore decreases exponentially on both sides of the interface, respectively as $\exp(z/\lambda^F_s)$ and $\exp(-z/\lambda^N_s)$, with continuity at the interface (if we suppose zero contact resistance).

The degree of spin polarized current passing through the interface depends on the spin accumulation on the left and on the right of such interface. In particular the spin-polarized current injected at the interface is equal to:

$$(SP)_I = \frac{j_\uparrow - j_\downarrow}{j_\uparrow + j_\downarrow} = \frac{\beta}{1 + r_N / r_F} \qquad 5.2,$$

where β is the bulk ferromagnet spin-dependent conductivities asymmetry coefficient, and r^N and r^F are the spin impedance of the two materials, given by the product of resistivity ρ and spin diffusion length λ_s, i.e. $r^N = \rho^N \cdot \lambda^N_s$ and $r^F = \rho^F \cdot \lambda^F_s$. According to Equation 5.2 the current entering the semiconductor is almost completely depolarized when $r^N >> r^F$, that is usually when a resistivity mismatch exists between F and N, $\rho^N >> \rho^F$, amplified by the long spin diffusion length λ^N_s in case the non-magnetic material is a semiconductor. The concept is illustrated in Figure 5.2(c): spin-polarized current injected is zero in the case metal/semiconductor (purple line). In other words, the spin accumulation at the interface diffuses back into the ferromagnetic metal, owing to a much smaller r_F.

In order to maximize the spin accumulation, it is necessary to add a spin-dependent interface resistance r_b^* (with spin asymmetry γ). A non-zero contact resistance ($r_b^* \neq 0$) leads to a more balanced number of spin flips between F and N, by introducing a spin-dependent discontinuity of $\Delta\mu$ at the interface and impeding back-diffusion of spins. Tunnel barriers are an example of spin-dependent, 'artificially' added, interface resistances. They have been introduced for graphene spin channels [9] and metallic channels [10]. The insulating barrier thickness must be carefully tuned in order to get the proper value interface resistance r_b^* in relation to the semiconductor resistivity ρ.

This concept is represented in Figure 5.3: the polarization of the current entering the semiconductor, indicated as $(J_+ - J_-)/J$ in this figure, is represented for the two cases of *i.* no contact resistance ($r_b^* = 0$) and *ii.* contact resistance equal to r^N, $r_b^* = r^N$. The introduction of a spin-dependent contact resistance greatly enhances the degree of polarization (blue line) that would be otherwise zero (red line).

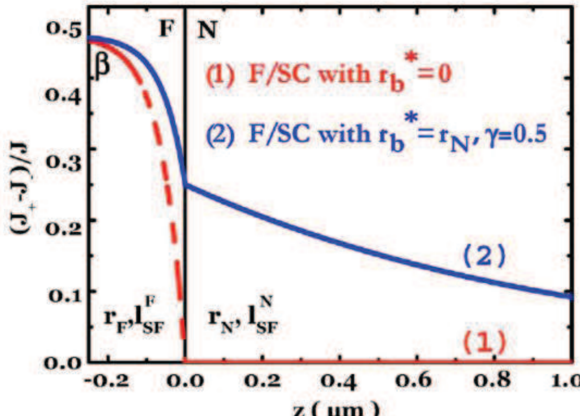

Figure 5.3 Current spin polarization at a ferromagnetic metal/semiconductor F/SC interface in the two cases of zero contact resistance $r_b^* = 0$ (red line) and contact resistance equal to r^N. Reprinted from [8].

Therefore, a too transparent interface is not beneficial for spin injection. A minimum value of interface resistance r_1 (lower limit of Equ. 5.1) helps to enhance the proportion of spin flips on the semiconductor side and to promote spin injection.

5.1.2 Upper limit for interface resistance: $r_b^* < r_2$

The upper edge of Equation 5.1 originates instead from considering the complete device formed by a semiconductor sandwiched between ferromagnetic source and drain, F_1/SC/F_2 (two-interface problem), and searching for the condition that maximizes the resistance difference between the parallel (P) and antiparallel (AP) configuration $\Delta R/R_P = (R_{AP}-R_P)/R_P$ of the magnetization of the two magnetic electrodes F_1 and F_2 [11]. In other words, the upper boundary derives by considering also the problem of spin detection at a second interface.

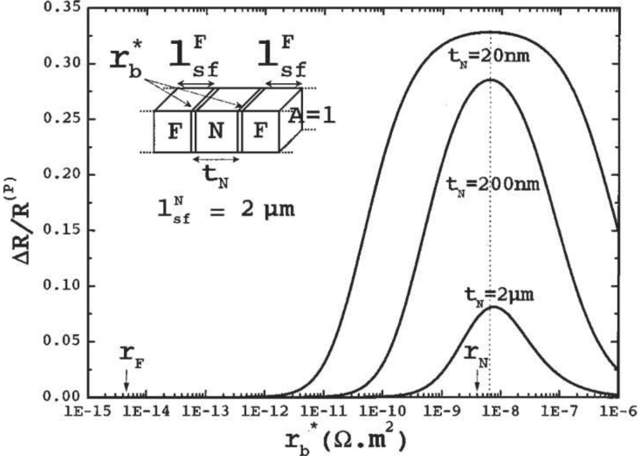

Figure 5.4 Magnetoresistance versus interface resistance r_b^* of a F_1/N/F_2 structure. In the calculation the authors consider $F_1 = F_2$ = Co with $r^F = 7.5 \cdot 10^{-6}$ Ω·cm, l^F_{sf} = 60 nm, β = 0.46 and a semiconductor N with r^N = 0.2 Ω·cm, l^F_{sf} = 2 µm. Three different semiconductor thicknesses t_N are considered: 20 nm, 200 nm and 2 µm. The geometry of the structure is shown in the left top of the figure. Reprinted from [7]

Figure 5.4 represents the magnetoresistance signal ($\Delta R/R_P$) as a function of the interface resistance r_b^* for three different values of semiconductor thickness t_N, namely 20 nm, 200 nm and 2 µm, for a given spin diffusion length of the semiconductor λ^N_s. The two interfaces are supposed to be identical. A channel thickness longer than the semiconductor spin diffusion length ($t_N / l^N_{sf} > 1$) is not even considered, because it would correspond to spin memory lost along the cannel. In the calculation, typical values of ρ^F, λ^F_s for metals and ρ^N, λ^N_s for semiconductors are chosen, and noted in the capture of Figure 5.4. The main information deductibles from Figure 5.4 are that:

i. a channel length t_N much smaller than λ^N_s is favorable, and it gives rise to the highest MR signal for the larger r_b^* window;

ii. the magnetoresistance maximum implies an interface resistance of the same order as r^N.

The highest MR signal is obtained for $t_N / l^N_{sf} = 10^{-2}$ (t_N = 20 nm and l^N_{sf} = 2 µm) and it spreads over the larger r_b^*/r^N ratio window (almost 2 decades of r_b^* around r^N). To obtain a detectable spinvalve MR signal the contact resistance r_b^* should not be much larger than the product $r^N = \rho^N \cdot \lambda^N_s$.

The lower and upper limits of Equation 5.1 can thus be more specifically expressed as:

$$r_N \frac{t_N}{[\lambda_s^N]} = \rho_N t_N = r_1 < r_b^* < r_2 = \rho_N \frac{[\lambda_s^N]^2}{t_N} = r_N \frac{[\lambda_s^N]}{t_N} \quad 5.3,$$

$$r_N \frac{t_N}{[\lambda_s^N]} < r_b^* < r_N \frac{[\lambda_s^N]}{t_N} \quad 5.4.$$

In conclusion, Equation 5.4 (which corresponds to Equ. 5.1) is satisfied if $r_b^* \cong r^N$. The window of optimal values of interface resistance is centered at r^N. The ratio between t_N and λ^N_s defines the breadth of the window.

Reasonable processing requires a typical separation between electrodes t_N of minimum 100 nm. In fact, in the vertical geometry, this is necessary to ensure that the top electrode does not perforate the 'soft' organic spacer. In the lateral geometry, making reliable and reproducible electrodes distance by less than 30 nm is highly challenging. On the other hand, if the spin diffusion length λ^N_s in organic semiconductors is short, owing to low mobility values and transport governed by short-distances hopping conduction, the boundaries of Equation 5.4 are expected to shrink.

The major obstacle in Organic Spintronics is the existence of the upper limit of Equation 5.4, owing to the fact that contact resistances between metals and organics are inherently very large, due to the very different nature between these materials. Ideally, one would like to have an interface resistance much smaller than the SC impedance, so that it can then be increased 'by design', typically by using a dielectric tunnel barrier, in order to create a spin-dependent interface resistance.

Highly conductive organic semiconductors, where delocalized transport dominates, give hope for longer spin diffusion lengths λ^N_s, thus extending the window of 'permitted' values. At the same time, occurrence of delocalized transport is expected to facilitate charge injection at the interface between the metal and the organic SC, therefore lowering the contact resistance r_b^*.

5.1.3 Gate-tuning of the r_b^*/r^N ratio

It is worth to underline that, for a given t_N / λ^N_s ratio (t_N established by the fabrication process and λ^N_s by the choice of the non-magnetic semiconductor), the application of a gate voltage could allow the tuning of the r_b^*/r^N ratio. This advantage of a gate terminal has been already illustrated in the Introduction, we report here for clarity the associated figure. A gate changes the carrier density in

the semiconductor and this directly modifies the resistivity of the channel ρ^N and indirectly its spin diffusion length $\lambda^N{}_s$. This leads to a variation of r^N and, consequently, a shift of the ratio $r_b{}^*/r^N$ with respect to the window of Figure 5.5. The effect of a gate on the interface resistance is expected to be smaller. The possibility to insert a gate terminal is one of the main advantages of lateral geometry that we are currently exploiting.

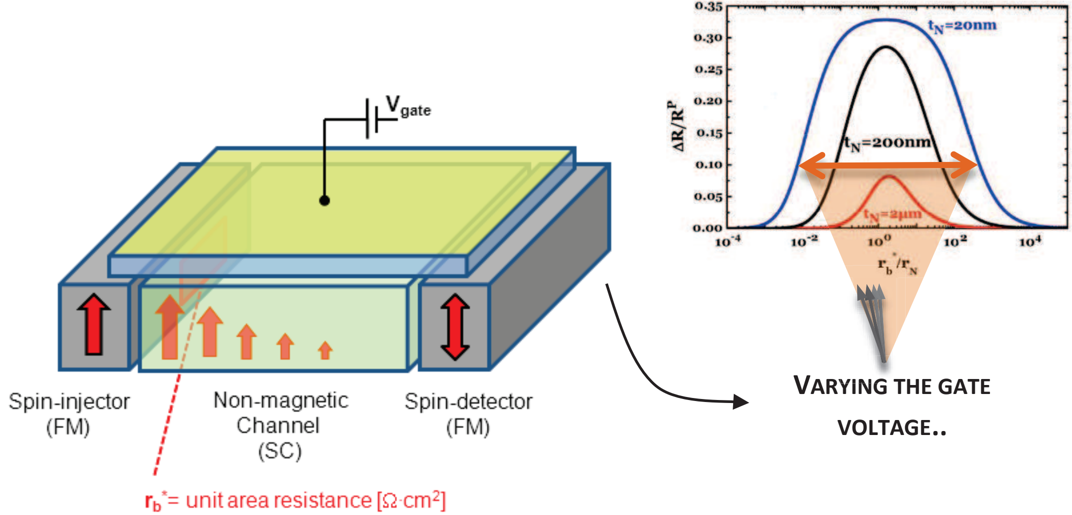

Figure 5.5 Principle of gate modulation of the $r_b{}^*/r^N$ ratio. A prototypical top-gated lateral spinvalve is represented. The gate is potentially able to tune both the semiconductor resistivity and the interface resistance, and the possible change in the $r_b{}^*/r_N$ ratio results in a displacement along the orange arrow in the MR plot.

5.2 The metal/semiconductor interface

In this section we overview the main characteristics of a metal/semiconductor interface. We first revise the archetypical Schottky barrier that nicely describes the carriers injection mechanism from metals to inorganic semiconductors, and later we explain the reasons why the metal/organic interface differs from it. Given the vastness of the topic, we will just focus on the aspects relevant for the material we use (conjugated polymer) and for our purpose (making spin-dependent ferromagnet/organic interfaces for lateral spinvalves).

5.2.1 Metal/inorganic semiconductor interface: the Schottky barrier

When an inorganic semiconductor is brought into contact with a metal, their chemical potentials should necessarily align at the interface, in order to reach equilibrium. The alignment occurs by a transfer of charge from one material to the other. In particular, electrons flow from the material with lower work function (i.e. chemical potential closer to vacuum level), towards the material with higher work function. The charge transfer gives rise to an energy barrier across the interface, equal to the difference of the Fermi levels of the isolated materials. This energy barrier forming (referred to as “band bending”) is indeed what balances the initial carriers diffusion and prevents extra transfer of charge. For instance, if the chemical potentials of the two materials lie initially at the same level, no charge transfer happens, and no potential drop arises at the interface.

At thermal equilibrium, injection due to diffusion and backflow due to barrier potential drift cancel out. Upon application of external voltage (V_{sd}), the energy maximum of the barrier gets lower and closer to the interface, thus favoring injection with respect to backflow, in the framework of a field-enhanced diffusion process [12],[13]. The lowering of the interface potential maximum thanks to the application of an external electric field (similar to polarizing directly a *pn* junction) is known as Schottky effect. Figure 5.6(a) represents qualitatively a Schottky barrier. It must be noted that a quite high electric field is needed (10^6 V/m) to produce a relevant drop of the barrier.

In conventional crystalline inorganic semiconductors a charge carrier can cross the Schottky barrier in two possible ways: either by Richardson–Schottky thermoionic emission [14] or by Fowler–Nordheim tunneling. The two processes are represented in Figure 5.6(b).

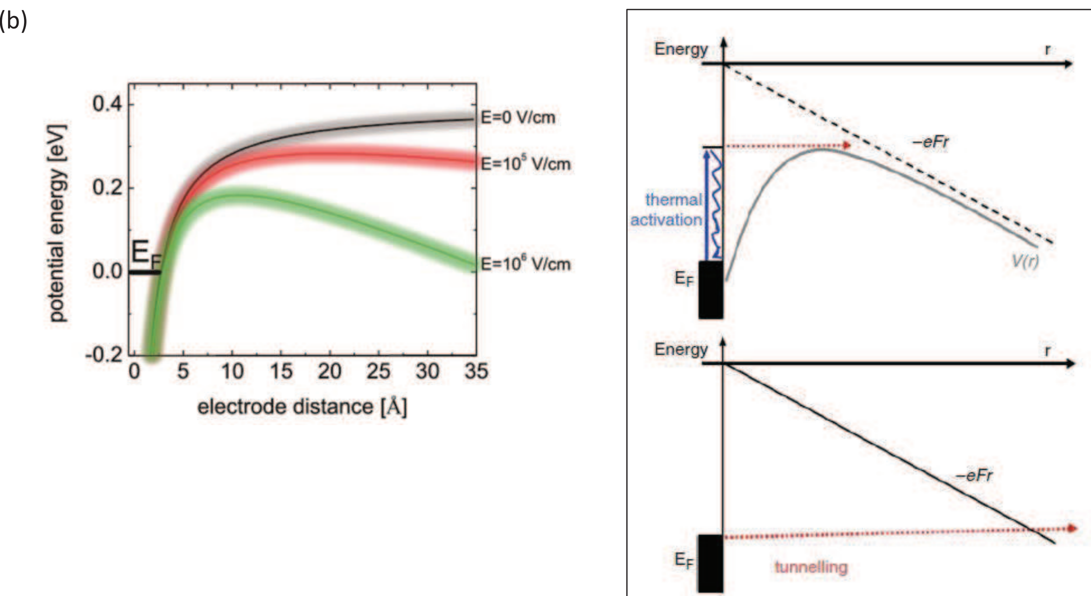

Figure 5.6 Representation of a Schottky barrier. a) Potential energy distribution at the metal-semiconductor interface for three values of the externally applied electric field (nominal barrier ϕ_B = 0.4 eV). The larger the external electric filed, the lower the maximum of the potential energy becomes (Schottky effect). (reprinted from [12], based on simulation from [13]). b) Sketch of the thermionic emission mechanism (top) and of the tunneling mechanism (bottom). Reprinted from [15].

Thermionic emission is defined as the heat-induced flow of charge carriers over a potential energy barrier from a surface to vacuum or into another material. When the emission is towards another material (in this case called "injection"), the current density depends on the Schottky barrier height ϕ_B lowered by the field-effect of the quantity $\Delta\phi_B = (e^3E/4\pi\varepsilon_0)^{1/2}$:

$$J = A^* T^2 \exp\left(-\frac{\phi_B - \Delta\phi_B}{k_B T} \right) \quad 5.5.$$

The thermally excited carrier travels across the maximum of potential without being scattered. This gives rise to an Arrehenius-type of temperature dependence of the current injected $\ln j \propto T$.

In the case of tunneling the electron at the Fermi level of the metal tunnels through a triangular potential barrier. Normally the depletion width associated with the Schottky barrier is generally too large to allow tunneling to occur. Values of barrier widths for *n*-doped GaAs, for example, are 100 nm for a doping level of $\sim 10^{17}$ cm^{-3} and 40 nm for $n \sim 10^{18}$ cm^{-3}. However this width can be tailored, and in particular reduced, by varying the doping profile at the semiconductor interface. Heavily doping the

surface region can reduce the depletion width to few nanometers, so that tunneling from the metal to semiconductor becomes a highly probable process. Several examples of Schottky barrier tailoring have been demonstrated for inorganic semiconductors [14]. This approach has been exploited as an alternative to the physical insertion of a discrete insulating layer to improve the spin injection in inorganic semiconductors spintronic devices [16].

5.2.2 Metal/organic semiconductor interface

The situation for metal/organic interfaces is different because the condition of collision-free charge injection across the maximum of the electrostatic potential, implied by Schottky theory, is violated. An experimental signature of the classical injection models failure for metal/organic interfaces is that the temperature dependence of the injection current is weaker than expected based upon the estimated energy barriers. Great efforts to find a more suited approach to describe charge injection from metal to organics have been done by Bässler and coworkers [17],[18],[19] (mostly simulation and theory).

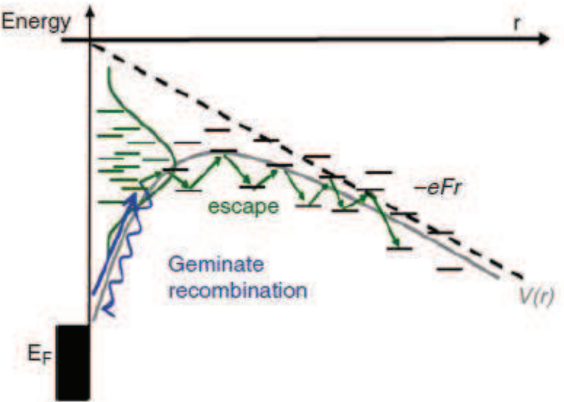

Figure 5.7 Charge injection mechanism from a metal to an organic semiconductor [15].

The proposed model for charge injection from a metal into an organic material, represented in Figure 5.7, describes charge injection as a thermally activated jump that raises the carrier, an electron for example, from the Fermi level of the electrode to a tail state of the Gaussian density of states distribution. To ensure that the primarily injected carrier can continue its motion away from the interface, rather than recombine with its image charge in the electrode, it is necessary the presence of another hopping transport site at equal or even lower energy. Subsequently the carrier executes a diffusive random walk in the combined coulomb potential of the image charge and the externally applied potential, getting away from the interface. Essentially the presence of disorder and of a Gaussian DOS distribution of hopping sites lowers the injection barrier. A clear experimental proof of the weak temperature dependence of charge injection from Ag and Al into a conjugated polymer, p-phenylene vinylene (PPV), has been given for example by Woudenbergh *et al*. [20].

Although charge injection is facilitated for the above-mentioned reason, the limiting parameter becomes the transport within the bulk of the semiconductor, i.e. the velocity at which the excess of injected carriers is neutralized by diffusion away from the contact zone. Since the diffusion coefficient is proportional to the mobility, $D = \mu \cdot k_B T/e$, low mobilities of the organic semiconductor are also responsible for poor injection. In this case the injection is categorized as space-charge-limited (SCL), or diffusion-limited (*versus* contact- or emission-limited). The crowding effect of injected carriers at

the interface is schematically represented in Figure 5.8(a). Consequently, to a lower mobility corresponds a higher contact resistance, as shown in Figure 5.8(b), reprinted from the review of Natali and Caironi [12].

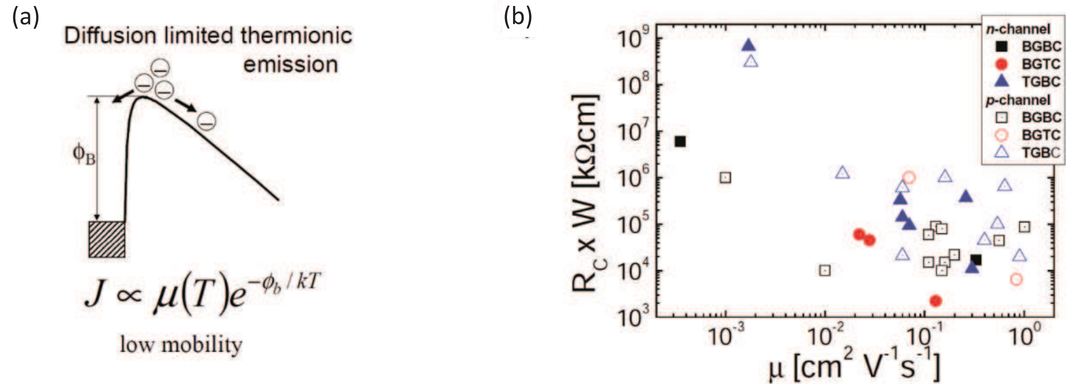

Figure 5.8 a) Sketch of diffusion-limited or space-charge-limited current injection mechanism. The semiconductor is unable to disperse injected carriers fast enough, thus they tend to be back-scattered into the metal. b) Specific contact resistance R_c (in unit of kΩ·cm) as a function of the charge carriers μ. The general trend is a smaller R_c for higher μ. Reprinted from [12].

In general the presence of charge accumulation layer in a gated device (zone of higher available density of states) helps reducing the space-charge limitation simply by creating a faster "exit path" for carriers towards the semiconductor bulk. This is why normally Organic Field-Effect Transistors (OFETs) are contact-limited devices [21], while Organic Light Emitting Diodes (OLEDs) are space charge limited current devices (no gate, no accumulation layer).

Contrarily to metal/inorganic interfaces which are always characterized by strong bonding between the two materials, the metal/organic interface can vary among different degrees of interaction, going from simple physisorption to chemisorption (weak or strong), depending on the specific materials used and on the preparation process [12]. Physisorbed interfaces do not present any covalent bond or hybridized state between the molecular orbitals of the organic material and the electron wavefunctions of the metal. When metal-hybridization of the molecular orbitals occurs instead, we are in the range of weak chemisorption: this happen for evaporation of organics on ultra-clean metal surfaces prepared in vacuum [22]. Self-assembled monolayers (SAMs) constitute one of the strongest possible binding between M/O and they are an example of chemisorption. However, their average binding energy is still not comparable to normal covalent bonds between atoms in molecules.

In conclusion, metallic electrodes and semiconductor molecular materials have very different electronic properties, and this is at the origin of the complex and slow process of transfer of charges from one to the other. Large contact resistance values are a serious limitation in Organic Electronics devices. Electrically poor contacts severely degrade charge injection as well as charge transport in the channel [21].

High mobility organic materials can allow the fabrication of devices with more efficient charge injection and lower contact resistance (as already experimentally demonstrated, Figure 5.8(b)). Furthermore, high doping of the organic material, filling the trap states of the Gaussian DOS, may accelerate the hopping process when injecting charges.

5.3 Contact resistance of solution-processed organic semiconductors onto metals

We discuss now in major detail the interface between metallic electrodes and solution-processed organic semiconductors. This preliminary discussion will put in perspective results obtained for doped PBTTT/Au and PBTTT/Ni contacts presented in the experimental part of this Chapter.

The nature of the interface between an organic semiconductor deposited from solution onto a pre-existing metal surface in ambient conditions is to be considered physisorbed, or weakly chemisorbed. Typical contact resistance values for solution-processed semiconductors with metals (generally reported for Au contacts) are in the tens of kΩ·cm range.

The commonly used unit measure for contact resistance in Organic Electronics is a resistance per unit of length, Ω·cm or Ω·m. The reason is that the conductive active channel in field effect geometry is very often a few nanometers thick only (even for OSCs of much larger thickness), making the charge-injection interface essentially independent of the metal electrode thickness. Charge injection occurs through a very tiny area, along the width W of the channel and of negligibly short thickness, which can be considered a line. In a profile view (Figure 5.9) such "line" is a point. The specific contact resistance is thus usually calculated multiplying the total contact resistance [Ω] by the channel width W [cm].

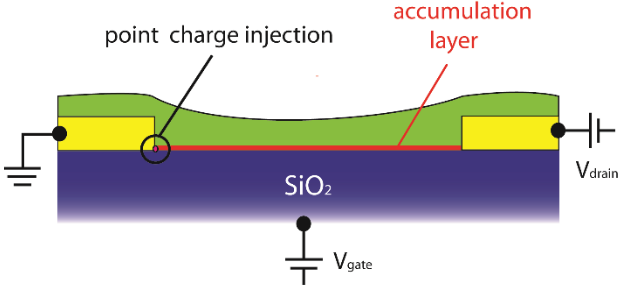

Figure 5.9 Schematic illustration of the few nanometers thick accumulation layer in OFET structure, explaining why the specific contact resistance is usually expressed per unit of length Ω·cm (R_c·W).

Contact resistance values between solution-processable organic semiconductors and metals are reported in Table 5.1 for different polymer semiconductors, device structures, metal contacts and measurement methods [12]. Obviously a scattering of the results exists due to the different extraction methods and device architectures, but 10 kΩ·cm remains the lower limit for specific contact resistance R_c obtained for OFETs operating with standard gate dielectrics. Since our condition for an adequate contact resistance r_b^* for Spintronics is expressed in terms of resistance per unit of area, we 'translate' this values by simple multiplication for the accumulation layer thickness (~ 3 nm): 10 kΩ·cm corresponds roughly to a surface contact resistance of $3{\cdot}10^{-3}$ Ω·cm^2.

	Semiconductor	Structure	Contacts	μ [$cm^2V^{-1}s^{-1}$]	R_C [Ω·cm]	Method
p channel						
	TES-ADT	BGTC	Au	0.07	1×10^6	SKPM
		BGBC	Au	0.11	5.9×10^4	
	P3HT	BGBC	Au/ naphtalene	0.001	1×10^6	TLM
	P3HT	BGBC	Au	0.01	1×10^4	SKPM
	P3HT	BGBC	Pt	0.16	1.5×10^4	TLM
	P3HT	BGBC	Au	0.11	1.5×10^4	TLM
		BGBC	Recessed Au	0.15	1.0×10^4	TLM
	P3HT	BGBC	Au	0.15	8.0×10^4	
	PTVPhI-Eh	TGBC	Au	0.54	1×10^5	TLM
	F8T2	TGBC	PEDOT:PSS	0.015	1.2×10^6	TLM
	TIPS-p	BGBC	MWCNT:PSS blend	0.13	9×10^4	TLM
	TIPS-p	BGBC	Au	0.20	2.2×10^4	SKPM
	TIPS-p: PS [a]	BGBC	Au	1.01	8.7×10^4	SKPM
	TIPS-p	TGBC	Ag printed	0.06	6×10^5	TLM
			Ag printed/ F4TCNQ	0.9	2×10^4	
	TIPS-p	TGBC	Au/ PFDT	0.64	6.5×10^5	TLM
	TIPS-p	TGBC	Au	0.16	1×10^6	TLM
			Au/ PFDT	0.06	2.1×10^4	
	pBTTT	TGBC	Au/ PFDT	0.4	4.5×10^4	gFPP
	F8BT [b]	TGBC	Au/ PFDT	0.0018	3×10^8	gFPP
	pBTTT	BGBC	Au	0.56	4.4×10^4	TLM
		BGTC	Au	0.84	6.5×10^3	

Table 5.1 Typical values of contact resistance for solution-processable organic semiconductors with metal electrodes (reviewed from Natali and Caironi in 2012, [12]). In the last column: SKPM is Scanning Kelvin Probe Microscopy, TLM is Transmission Line Method, and gFPP is gated four-probe method.

5.3.1 The highly doped polymer semiconductor case

A high doping level of an inorganic semiconductor leads to a very narrow depletion layer associated to the Schottky barrier (paragraph 5.2.1). In organic semiconductors, chemical doping improves the mobility (see Chapter 4), and consequently it strongly reduces the space-charge limitation. The contact between a highly doped organic semiconductor and a metal is consequently 'contact-limited', not space-charge limited. The absence of space charge limitation leads to a contact ohmic at room temperature and characterized by exceptionally low values of contact resistance, with respect to the ones of undoped polymers.

In light of their working principle based on doping, electrolyte-gated OFETs (EGOFETs) hold the record with three orders of magnitude lower R_c than standard dielectrics ones. In 2010 Braga *et al.* [1] reported values as low as 4 Ω·cm for P3HT/Au contacts in a top-gate bottom-contact (TGBC) architecture gated with an iongel formed by a triblock copolymer swollen with a room temperature ionic liquid. In the first report of electrolyte-gated PBTTT thin film, Dhoot *et al*. [23] quickly refer to a value of PBTTT/Au contact resistance around 20 Ω·cm (electrolyte: PEO/$LiClO_4$).

The reason for such a low contact resistance value is the occurrence of electrochemical doping at the contact zone. The doping assists charge injection by reducing the carriers crowding at the interface, thanks to compensation operated by the ions. This explanation is confirmed in the work of Fabiano *et al*. [24] where an EGOFET is made with a specific polyelectrolyte unable to dope electrochemically the semiconductor P3HT: in this experiment the R_c values remain in the 10^4 range, similarly to standard dielectric OFETs. The value found by Braga and coworkers, 4 Ω·cm, corresponds

to a surface contact resistance in the range of 10^{-5} $\Omega\cdot cm^2$, still almost two orders of magnitude lower than the contact resistance values without interfacial doping. This value already takes into account the fact that in EGOFETs the charge injection area extends over the whole semiconductor thickness, if the semiconductor film is uniformly doped across its volume.

Supported by this finding, we believe that highly doped polymer semiconductors in contact with ferromagnetic metals may provide the suitable contact resistance value for efficient spin injection/extraction and be the favorable combination to overcome the resistance mismatch problem.

To the best of our knowledge no other accurate studies of contact resistance in EGOFETs with polymer semiconductors as active channel (with ion penetrating in the polymer) have been carried out except the work of Braga *et al* [1]. We will present in the experimental part of the Chapter a study on the contact resistance of PBTTT on Gold as a function of gate bias (doping) and temperature. Since our ultimate purpose is the fabrication of spinvalves (ferromagnetic electrodes), we will also examine contact resistance with Nickel.

5.3.2 Few attempts of lateral organic spinvalves with highly doped polymers

We overview in this paragraph the two tentative realizations of non-local lateral spinvalves measurements made with a highly doped conjugated polymer (PEDOT:PSS). These two works have been published during the period of this thesis (in 2013) by Kawasugi *et al*. [25] and Oliveira *et al*. [26]. Both the attempts report unsuccessful results. We discuss the experimental results and the conclusions proposed by each group to explain the absence of spin signal in their respective work.

The choice of PEDOT:PSS, i.e. poly(3,4-ethylenedioxythiophene):polystyrene sulfonate, as organic spacer for organic spinvalves is motivated by reasons similar to the ones driving our group toward electrochemically doped PBTTT thin films: high conductivity (up to 1000 S/cm) gives hope for long spin diffusion lengths, low interface resistances, and the possibility to perform successful non-local spinvalve measurements. Note that we did not consider PEDOT:PSS as a candidate for our studies because it can be highly inhomogeneous (zones more or less doped in PSS) and, moreover, we are not aware of successful field-effect gating on this material. Figure 5.10 resumes the device geometry and the main results of the two reports we want to discuss.

Kawasugi *et al*. [25] perform non-local spinvalve measurements on lateral devices with $Ni_{80}Fe_{20}$ (Py) electrodes evaporated onto the PEDOT:PSS film (top contact geometry) after e-beam lithography patterning process. They do not observe any magnetoresistance signal. Their explanation is that the contact resistance value is too high and is the cause of an extreme reduction of spin polarization at the electrode/polymer interface, causing the absence of spin signal. The interface resistance value they report is roughly $5\cdot10^{-6}$ $\Omega\cdot cm^2$. Note however that defining a contact resistance with top-evaporated electrodes is a difficult task because the inclusions of the evaporated metal in the soft material can be misleading for the estimate of the real contact area. They also fabricate Py/SiO_2(2nm)/PEDOT:PSS contacts, but evidently the contact resistance is even higher and leads to non-measurable magnetoresistance.

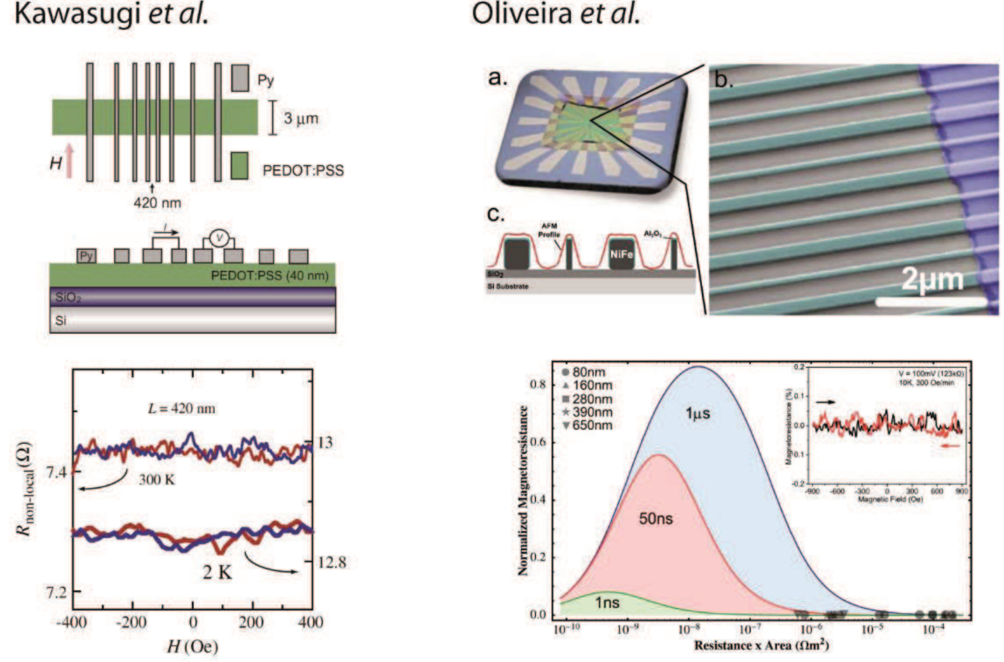

Figure 5.10 Schematic representation of the lateral PEDOT:PSS spinvalve made by Kawasugi *et al*. (top-left) [25] and Oliveira *et al*. (top-right) [26]. In both cases electrodes are made of Py; Oliveira and coworkers also add a thin Al_2O_3 barrier. Below, the respective magnetoresistance curves completely flat, indicating absence of spin signal. Oliveira (bottom-right) also analyze their result in the light of the interface resistance value.

Oliveira *et al*. [26] have made $Ni_{80}Fe_{20}/AlO_x$/PEDOT:PSS/AlO_x/ $Ni_{80}Fe_{20}$ two-terminal (local) spin valves by spin-coating the polymer from aqueous solution after e-beam electrodes patterning (bottom contact geometry). AlO_x tunnel barrier is introduced intentionally in order to avoid native oxidation of the Py electrodes surface in air and to improve its chemical stability towards the very acidic PEDOT:PSS solution (pH 1.8). AlO_x thickness is varied from 1 to 1.3 nm and the corresponding contact resistance value spans from $6{\cdot}10^{-3}\ \Omega{\cdot}cm^2$ to $6\ \Omega{\cdot}cm^2$. In their case, the detection of spin transport signal remains elusive even for devices with the smallest electrode spacing, namely 80 nm. The insertion of alumina tunnel barrier is first claimed to enhance spin polarization at the interface, whereas later it is judged responsible for a too high contact resistance preventing the possibility to observe a spin signal.

5.4 Gated four-probe method for contact resistance measurements

The contact resistance in a given device can be extracted by using direct or indirect methods [12]. Indirect methods consist in exploiting the dependence of I_{sd} (source-drain current) on the channel length L, on the V_g (gate voltage) or on V_{sd} (source-drain voltage). Transfer (or Transmission) Line Method (TLM) is the most used indirect technique (Figure 5.11(a)). It is based on the hypothesis that the contact resistance of a device does not depend on the channel length L, while the total resistance R_{tot} obviously scales with it. Consequently the y-axis extrapolation of the expected linear $R_{tot}(L)$ plot for a set of FETs with different channel lengths corresponds to the total contact resistance of the device.

Whereas indirect methods rely on some assumptions, whose validity needs to be verified, direct methods provide the contact resistance value experimentally. Direct methods are divided in two

groups: *i.* four-probe measurements, in which the potential along the channel is probed at some specific position by means of additional electrodes, and *ii*. scanning probes techniques, where the full potential profile from source to drain is investigated by mapping the local voltage, scanning between source and drain electrodes (Scanning Kelvin Probe Microscopy - Figure 5.11(b) - or Contact Atomic Force Microscopy).

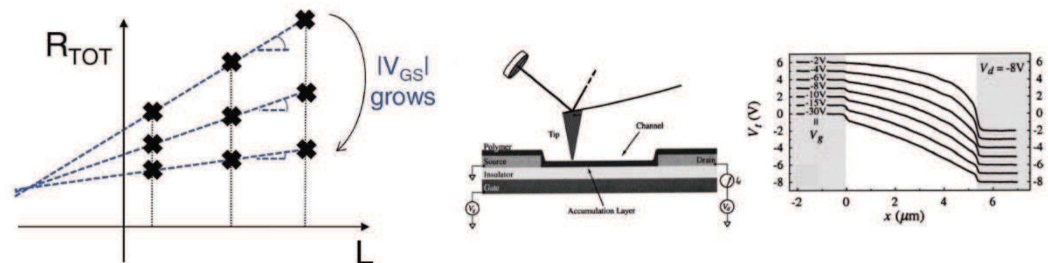

Figure 5.11 a) Transmission Line Method (TLM), indirect technique for the measurement of the contact resistance. R_c of the device is extracted from the y-axis intercept of the R_{TOT} vs L (channel length) plot. b) Scanning Kelvin probe microscopy, direct technique. Schematic representation of the set-up (left) and examples of potential profiles acquired on a bottom-gate bottom contact field effect transistor.

For our investigation we adopt the direct method known as *gated four-probe method* (gFP). This technique is a variation of the very common four-point probe technique used for sheet resistivity measurements, with the difference that the absolute potential of the two sensing fingers V_1 and V_2 are independently referred to the source voltage, not just their difference ΔV_{12}. This is possible by connecting the sensing fingers independently to two high impedance voltmeters. A schematic representation of gFP is given in Figure 5.12.

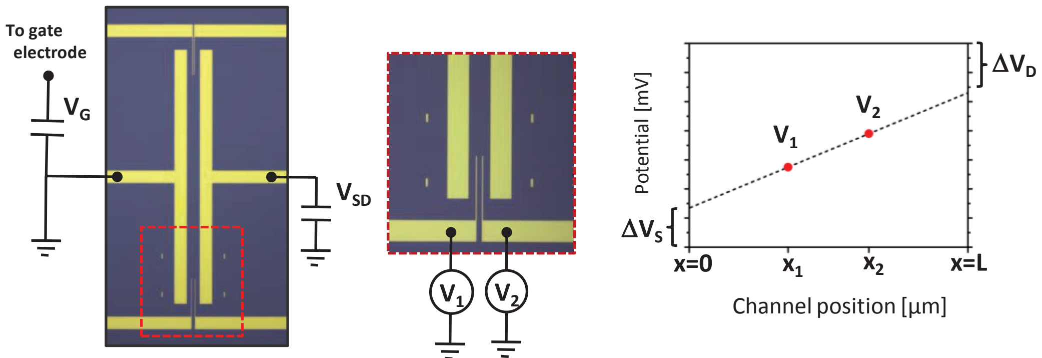

Figure 5.12 a) Schematic drawing of the measuring circuit for gFP method on transistor geometry. b) Potential profile along the channel of an FET working in linear regime, illustrating the potential drops at the source and drain electrodes due to contact resistances.

The *gated four-probe method* is valid when the field-effect transistor is in the linear regime of operation, namely when $V_g >> V_{sd}$ and the potential profile along the channel is linear. We opt for gated four-probe method instead of TLM because of the following advantages: one device is in principle enough to extract the contact resistance information and source and drain contact resistance

are known separately. Scanning probes techniques like Kelvin probe microscopy require direct access to the accumulation layer thus they are incompatible with top-gate device structures like ours.

Figure 5.12 includes the optical microscope image of one of our samples for gFP contact resistance measurement. It is a transistor geometry featuring two sensing fingers positioned at equal distances from source and drain electrodes. Channel width W is 1 mm, channel length L varies from 12 μm to 50 μm. The fingers width (2.5 μm) is negligible respect to the channel length and they protrude into the channel for a limited length (100 μm) in order to limits the source-drain current uniformity perturbation of the device during operation. gFP measurements have been performed on Hall bar geometry as well (see Chapter 4). In case the contact resistances of source and drain electrodes are similar, the average value is given.

According to the methods explained in the paragraph, the contact resistance between two materials can be measured only if: i. the channel length can be varied (TLM) or ii. the active material can be connected with two additional probes besides source and drain (gFP). In Chapter 2 and Chapter 3 we have presented a study on the transport properties respectively of supramolecular nanowires of triarylamines (STANWs) and nanosheets of graphene exfoliated by liquid phase (LPE-graphene nanosheets): both these systems are characterized by the impossibility of direct measuring of the contact resistance with the metal electrodes owing to the very short channel lengths.

EXPERIMENTAL

One of the main advantages of studying organic semiconductor thin films as candidates for Spintronics is the possibility to know their contact resistance with electrodes. In this section we present our experimental findings on contact resistance of PBTTT, poly(2,5-bis(3-alkylthiophen-2-yl)thieno[3,2-*b*]thiophene), onto metal electrodes and we discuss them on the basis of the necessary conditions for Spintronics explained in paragraph 5.1. The contact resistance study here presented is complementary to the investigation on the intrinsic transport properties carried out for PBTTT in Chapter 4.

5.5 Contact resistance of PBTTT with metals (Au, Ni)

PBTTT contact resistance with Au electrodes is in the range of 80 - 40 kΩ·cm for bottom-contact devices (SiO_2 bottom-gate [27], PMMA top-gate [28]) and 6.5 kΩ·cm for top-contact ones [27]. Au Fermi level and PBTTT HOMO (Highest Occupied Molecular Orbital) are aligned around -5.1 eV from the vacuum level [29]: this favors holes injection and makes PBTTT a p-type semiconductor.

We measure the contact resistance with Gold and Nickel bottom electrodes by means of gated four-probe method, as a function of the gate voltage V_g (doping) and temperature. The values will be first given in linear units (Ω·cm) to allow a fast comparison to the ones typically reported in Organic Electronics. They will be subsequently transformed in ohms per square centimeters for the discussion about the Spintronics condition.

5.5.1 PBTTT/Gold electrodes

Measurements for gold electrodes are carried out in the cryogenic set up using the Hall bar geometry.

5.5.1.1 Contact resistance as a function of doping

Figure 5.13 presents the contact resistance of PBTTT/Au bottom electrodes for different gate voltages. In this case, we do not perform a direct sweep of the gate voltage, but we reconstruct the curve by plotting the specific contact resistance R_c for samples discussed in Chapter 4 (from 2 to 6). The source and drain contact resistance values reported are taken at 250 K of the σ(T) curve. At this temperature the iongel is freezed and we avoid artifacts related to gate leakage current.

The error on the contact resistance value estimation comes from the noise on the fingers voltage potentials V_1 and V_2 (± 0.5 mV) and to the non-zero width of the fingers electrodes (25 µm, over $L_{channel}$ = 400 µm). We estimate this error to be around ± 5%. Data relative to gate values $|V_g| < -2.7$ V are not presented because the iongel dielectric is not completely charged, as already explained in Chapter 4.

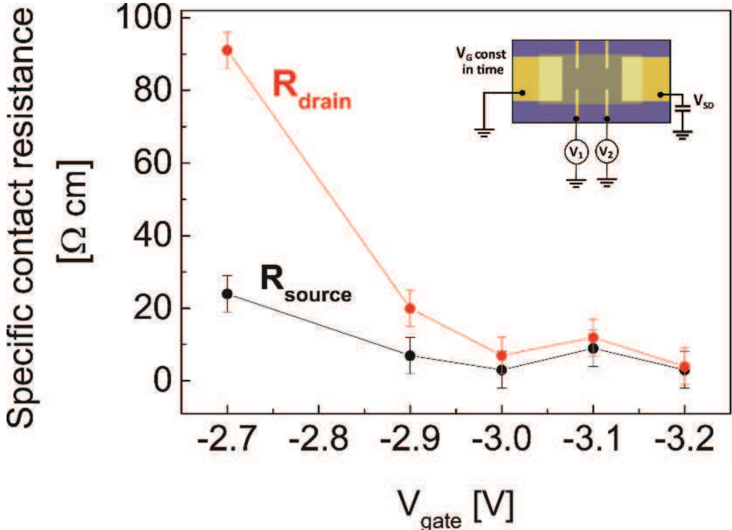

Figure 5.13 Specific source and drain contact resistance R_{source} and R_{drain} for PBTTT/Au at different gate voltages V_g = -2.7 V, -2.9 V, -3.0 V, -3.1 V and -3.2 V. The drain voltage is V_{sd} = -0.4 V for all measurements. (Inset) Hall bar device geometry used for measurements (L = 400 μm).

V_{gate}	Specific source resistance R_{source} (T=250K)	Specific drain resistance R_{drain} (T=250K)
-2.7 V	24 ± 1.2 Ω·cm	91 ± 4.5 Ω·cm
-2.9 V	7 ± 0.35 Ω·cm	20 ± 1 Ω·cm
-3.0 V	3 ± 0.15 Ω·cm	7 ± 0.35 Ω·cm
-3.1 V	9 ± 0.45 Ω·cm	12 ± 0.6 Ω·cm
-3.2 V	3 ± 0.15 Ω·cm	4 ± 0.2 Ω·cm

Table 5.2 Values of source and drain specific contact resistance at 250 K, as reported in Figure 5.13.

Our measurements confirm an absolute value of R_c extremely low, three orders of magnitude lower than standard dielectric OFETs. Such values are in accordance to the ones reported for Dhoot *et al*. [30] for PBTTT gated with PEO/$LiClO_4$ polymer electrolyte. Both R_{source} and R_{drain} diminish while increasing the gate voltage. This is typical for every type of OFETs: higher gate bias corresponds to a higher available density of states in the channel (stronger accumulation); it reduces the space-charge-limitation and improves the charge injection process. R_{source} is lower than R_{drain} at low gate bias (V_g - V_T), in accordance with Braga *et al* [1]. At higher (V_g - V_T) the resistances of the two contacts become comparable. R_{drain} decreases almost two orders of magnitude within few hundreds of millivolt of gate bias, going from ~ 100 Ω·cm at V_g = -2.7 V down to 4 Ω·cm when V_g = -3.2 V. Standard gate dielectrics can usually decrease R_c less than a factor 10 over several tens of Volts [27],[28].

We argue here that the strong influence of the gate bias and the record low contact resistance values are due to the electrochemical doping action of the gate. Electrochemical p-type doping consists in an oxidation of the semiconducting polymer (an electron is removed from the polymer through the source or drain electrode and a hole polaron is generated) and a simultaneous penetration of an anion from the electrolyte into the bulk of the polymer into an interchain site (reduction reaction). Essentially, the anions compensate the charge carriers (holes) entering from the source-drain electrodes. Intra-chain chemical bonds are not disrupted during electrochemical doping, which is reversible (as discussed in Chapter 4, paragraph 4.6.2). The anions simply "sit" in between the chains in order to compensate the charge of the carriers entering from the source/drain electrodes.

Consequently, doping near the contacts drastically reduce the space charge limitation to current injection. At high doping levels, the conjugated polymer is well compensated by counterions from the electrolyte, leading to quasi-ohmic contacts.

Moreover, since the doping is three-dimensional and occurs over all the thickness of the PBTTT thin film (25 - 30 nm), the typical parasitic resistance of a bottom contact tog-gate device due to a depleted zone along the semiconductor film thickness is absent.

5.5.1.2 Contact resistance as a function of temperature

From the same set of data we analyze also the PBTTT/Au contact resistance dependence on temperature. Figure 5.14 reports the contact resistance values extracted from σ(T) curves for samples 2, 4 and 5. Curves derive from heating ramps from 1.6 K to 250 K (overnight) at V_g constant (iongel frozen). Source and drain contact resistances are almost identical all along the temperature scan, so we report their average value.

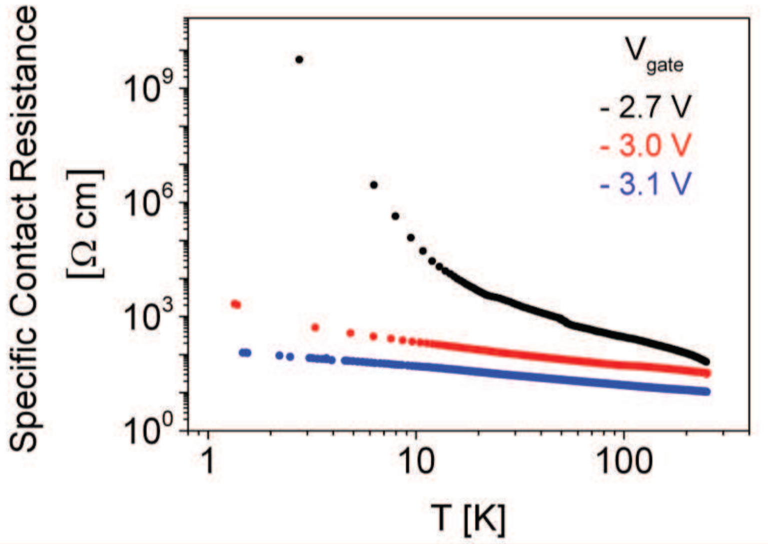

Figure 5.14 Specific contact resistance R_c PBTTT/Au as a function of temperature for three films gated respectively at V_g = -2.7 V (black), -3.0 V (red) and -3.1 V (blue). R_c is the average value of R_{source} and R_{drain} (V_{sd} = -0.4 V).

We observe that the temperature dependence of the contact resistance mimics exactly the channel conductivity temperature dependence (see Chapter 4). R_c for samples gated at -3.0 V and -3.1 V presents power law temperature dependence (1 order of magnitude difference from room temperature to 1.6 K), while R_c for the sample at lower gate bias (V_g = -2.7 V) follows an exponential dependence and becomes very large at low temperature. At high temperatures (T > 150 K) R_c is below 200 Ω·cm for all samples, in accordance with Figure 5.13 and Table 5.2.

The correspondence in the temperature dependence of intrinsic conductivity and contact resistance is not surprising. A higher charge carrier mobility of PBTTT, both in the channel and close to the contact zone, implies a faster diffusion/drift of the injected charge to the bulk. We should however mention that our result is different from the finding of Lee *et al* [31], reporting a T-independent contact resistance (30 Ω·cm) for another electrolyte-gated thiophene-based polymer semiconductor (PQT-12) versus Au electrodes.

5.5.1.3 Contact resistance versus channel resistance at high doping

We underline the fact that, when the doping of the polymer semiconductor start to be considerable and the channel conductivity elevated, the contact resistance (R_{source} + R_{drain}, [Ω]) reaches up to the 70 % of the total resistance R_{tot} of the device. For a device with a channel length of 400 µm (our Hall bar) such contact resistance is enormous!

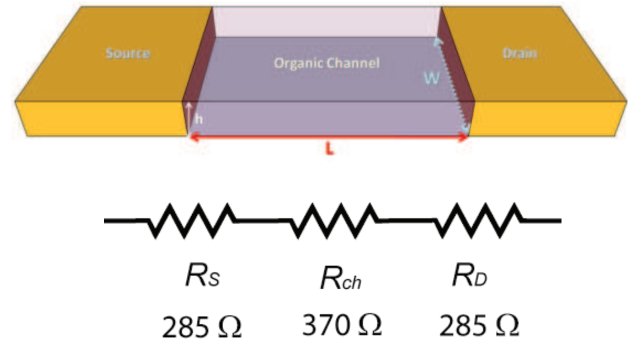

Figure 5.15 Schematic representation of the equivalent circuit of a general device with the different contributions to the total resistance R_{tot}. Typical values of R_S, R_D and R_{ch} of the most conductive sample are given (V_g = -3.2 V).

In Figure 5.15 we report the values of the different contributions to R_{tot} for the most conductive (V_g = -3.2 V, sample 6 in Chapter 4), at 250 K. The sum of drain and source contact resistances, (R_S + R_D) = 570 Ω, is 1.5 times the whole channel resistance R_{ch}, even though the channel length is 400 µm long! This is due to the fact that doping brings the conjugated polymer to incredibly low values of sheet resistance (< 300 Ω) and resistivity (< $1 \cdot 10^{-3}$ Ω·cm), thus R_{ch} becomes negligible also for macroscopic piece of material.

In other words, these estimates indicate that the improvement in polymer conductivity due to high doping exceeds the improvements in interface resistance value. The weight of contact resistance remains considerable even if the organic material presents an extremely high conductivity.

5.5.2 PBTTT/Nickel electrodes

We also investigate contact resistance with a ferromagnetic transition metal, Nickel, as this will be the archetype candidate for spin injection/detection metal. Measurements of contact resistance have been performed with gated four-probe method, at room temperature, inside a glove box. We use a transistor geometry with W >> L, instead of the Hall bar geometry of PBTTT/Au studies. Due to the exposition of Ni electrodes to air before the semiconductor deposition, the presence of a thin native layer of Nickel oxide at the surface is unavoidable.

The in-plane gate electrode of gold is evaporated separately, before PBTTT spin-coating, making use of a stencil mask. Since it has been demonstrated by Fabiano *et al*. [24] that in electrolyte-gated devices the work function of the gate electrode influences the source charge injection, it is important to use the same gate metal in order to compare PBTTT/Au and PBTTT/Ni contact resistance values.

5.5.2.1 Contact resistance as a function of doping

The gate-dependence of the specific contact resistance R'_c for PBTTT/Ni interfaces is shown in Figure 5.16. Five different transistors are present on the same chip, having identical width (W = 1 mm) and different lengths L, varying from 12 µm to 50 µm (aspect ratio W/L always > 20). Even though one

transistor is enough to know source/drain contact resistance values when using the gFP method, the presence of several devices on the same chip allows statistical comparison of the data collected for different channel lengths. In this case, no remarkable differences in R'_c have been traced among transistor different channel lengths.

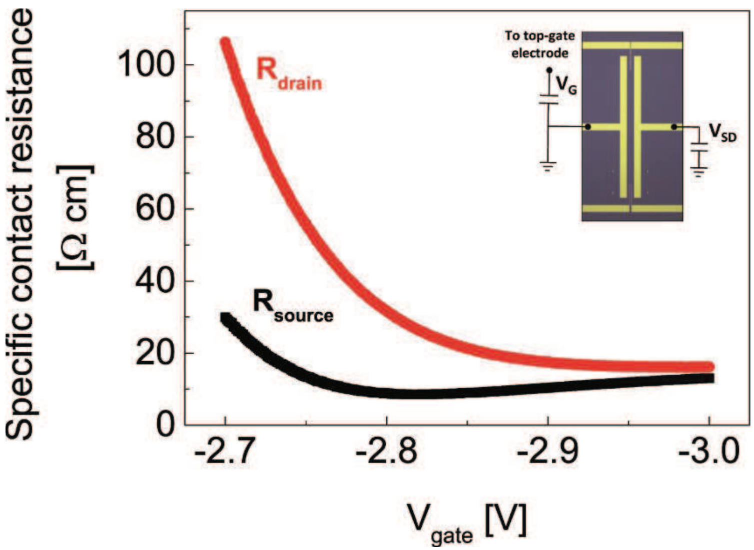

Figure 5.16 Specific source and drain contact resistance R_{source} and R_{drain} for PBTTT/Ni as a function of the gate voltage. The drain voltage is V_{sd} = -0.4 V for all measurements. (Inset) Transistor geometry used for measurements (L = 50 µm, W = 1 mm).

A direct comparison of Figure 5.16 (PBTTT/Ni) with Figure 5.13 (PBTTT/Au) shows that source and drain contact resistances behave in a very similar way for the two different metals, Ni and Au. R_{source} and R_{drain} diminish with increasing gating (doping). Similarly to PBTTT/Au, at V_g = -3.0 V the contact resistance of both contacts saturate at values below 20 Ω·cm. For instance, in the experiments with Ni electrodes, we did not increase the gate bias up to -3.2 V like for PBTTT/Au devices.

The weight of the contact resistance on R_{tot} at $|V_g|$ > -2.8 V is quite important, around 60 %.

5.6 Conclusions

We investigated the contact resistance of PBTTT thin films with gold and nickel electrodes for the purpose of testing if it satisfies the conditions required for an efficient spin injection and spin accumulation conservation, as described at the beginning of the Chapter. We remind that the condition requires the surface interface resistance r_b^* to be of the order of the spin impedance of the non-magnetic semiconductor r^N, where r^N is the product of ρ^N and λ^N_s. As explained in paragraph 5.1.3, the main motivation for implementing a gate electrode in lateral spinvalves was indeed the opportunity to tune the channel resistivity ρ^N and the interface resistance in order to manipulate the ratio r_b^*/r^N, as represented in Figure 5.5.

In the experimental part we have expressed all the contact resistance values in linear units [Ω·cm]. Here we simply multiply R'_c by the electrode thickness (30 nm = $30 \cdot 10^{-7}$ cm), for both Au and Ni, in order to express it as surface contact resistance r_b^* [$\Omega \cdot cm^2$]. This is reasonable, as the thickness of the active channel covers the whole semiconductor thickness (bulk doping). We obtain values in the 10^{-5} $\Omega \cdot cm^2$ range.

In Figure 5.17 we illustrate a direct comparison between surface contact resistance $r_b^*$and r^N as a function of gate bias (a) and temperature (b). Gate-dependent data are taken for Ni electrodes while temperature-dependent data are taken for Au electrodes. We have already underlined that the contact resistance values in two cases are similar, thus we present them together.

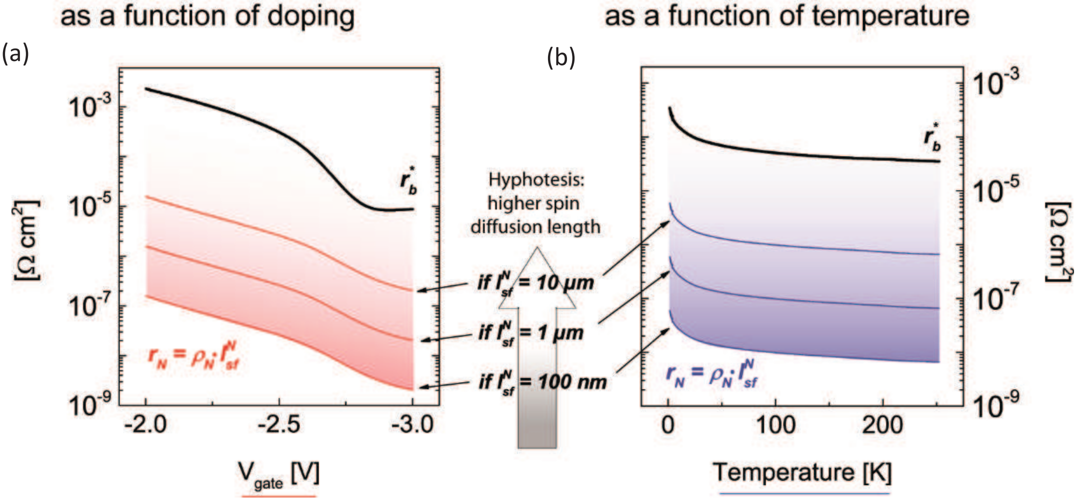

Figure 5.17 Direct comparison of surface contact resistance r_b^* and r^N a) as a function of doping (gate bias V_g) and b) of temperature, for PBTTT thin films onto bottom metal electrodes. r_b^* is experimentally measured, r^N is calculated multiplying ρ^N by three hypothetical spin diffusion length values of the polymer semiconductor: 100 nm, 1 μm and 10 μm. Red and blue lines never intersect black line, meaning that the r_b^*/r^N ratio never approaches the unity.

Figure 5.17(a) reports in black the interface resistance measured for PBTTT/Ni electrodes (as reported in Figure 5.16, with a slightly wider V_g window) together with the four-probe PBTTT resistivity ρ^N in red. The resistivity ρ^N has been multiplied for three hypothetical spin diffusion lengths λ^N_s of 100 nm, 1 μm and 10 μm. In order to fulfill the condition $r_b^* \approx r^N$, the black curve and the red curve should superpose. It is clear from Figure 5.17(a) that, even supposing an exceptionally long spin diffusion length (unlikely to be true), the surface interface resistance remains always too high respect to r^N.

If gate-tuning of r_b^*/r^N ratio is not as expected, one may wonder whether the r_b^*/r^N ratio can be varied by changing the temperature. According to Figure 5.17(b), this is not the case. None of the blue lines crosses the black line. Data are taken form PBTTT/Au contact resistance measurements, but we expect the same behavior for PBTTT/ferromagnetic electrodes.

The outcome of the study is disappointing. Independently of the metal electrode (Au or Ni) and of the variable (gate bias or temperature), results lead to the same conclusion: the gate potential changes r^N and the contact resistance r_b^* by similar amounts, keeping the ratio r_b^*/r^N unvaried and far from unity.

Even though the contact resistance drop is remarkable, and the values attained are exceptionally low if compared to other standard gate dielectric devices (10 Ω·cm *versus* 10 kΩ·cm), it still remains too high when compared to the channel conductivity. We believe our result for highly doped PBTTT with Au and Ni electrodes can be generalized to other polymer semiconductors, thus confirming the absence of spin signal reported by Kawasugi *et al*. [25] and Oliveira *et al*. [26] in their lateral spinvalves made with PEDOT:PSS (paragraph 5.3.2). Spin injection issues will not be solved by simply enhancing charge carrier mobility of the organic spacer, but require innovative approaches to decrease specifically the contact resistance.

The predominance of contact resistance, severely limiting the successful spin injection in organics, must be taken into account in the interpretation of the magnetoresistance signal of organic spinvalves. The origin of the magnetic-field-sensitive signal found in organic spinvalves remains indeed controversial, especially considering the absence of measurable spin signals in non-local measurements. Recently it has been demonstrated that a magnetoresistance signal can be generated by magnetic fringe fields emitted from a nearby ferromagnetic electrode [34],[35]. The fringe field is a residual magnetic field present outside the ferromagnetic electrode (up to 50 nm apart), due to its multi-domain structure. Since it can create a non-negligible local magnetic field close to the electrodes, one should take care not to confuse the flow of a spin current through the channel with fringe field effects at the interfaces, especially in a device in which interfaces (contact resistances) play such an important role. The positive aspect is that this "fringe-field" magnetoresistance could also be exploited and tuned to match a desired application [36].

5.7 Possible solutions and perspectives

- *To control the contact resistance*

In the light of these conclusions, the only solution to satisfy the condition $r_b^* \approx r^N$ is using a tool able to reduce the contact resistance without varying the channel conductivity. The Organic Electronics community pursues this objective since long time, especially in the attempt of reducing the contribution of contact resistance over the total device resistance in order to lower the operating voltage of devices and allow the channel length scalability.

The most straightforward solution is the use of interface-modification techniques. The so-called charge injection layers (CILs), such as thiol-based self-assembled monolayers (SAMs), are widely used. For instance, our group has already experience with contact-modification by means of zwitterionic molecules chemisorbed on gold electrodes. Zwitterions are short thiol-ended molecules characterized by a permanent internal dipole that, if properly positioned (in the right direction with respect to the interfacial dipole forming), can help reducing the potential barrier due to space charge transfer at the interface. While thiol anchoring on gold is now well documented, the equivalent for ferromagnetic metals needs to be found and characterized.

In general terms, one could envision a system metal/organic chemisorbed/organic physisorbed on which the chemically absorbed material acts as a "buffer layer" to help reducing the contact resistance.

- *To control the interface spin-dependence*

In addition to the value of contact resistance, one should not forget that the organic/ferromagnet interface also needs to be spin-dependent. This means that the mechanism of charge injection (thermoionic, tunneling, etc) should not mix the spin states of the charge carriers.

Extensive studies have been carried out for spin injection at FM/inorganic semiconductors interfaces mostly using optical investigation techniques. Table 5.3, taken from ref. [37], resumes the main reports on topic. In several cases Schottky barriers between ferromagnets and inorganic semiconductors have thus been demonstrated to be spin dependent interfaces, thanks to the tunnelling across the depleted space charge region at the semiconductor/ferromagnet interface.

Summary of major results on optical investigation of electrical spin injection				
Authors	Spin injector	Spin detector	Spin current polarization (%)	Operation temperature (K)
H.J.Zhu et al. (2001)	Fe/GaAs Schottky contact	(In,Ga)As/GaAs	2	300
A.T. Hanbicki et al. (2002)	Fe/AlGaAs Schottky contact	(Al,Ga)As/GaAs	30	240
V.F. Motsnyi et al. (2002)	CoFe/Al_2O_3/AlGaAs MIS diode	(Al,Ga)As/GaAs	9	80
M. Ramsteiner et al. (2002)	MnAs/GaAs Schottky contact	(In,Ga)As/GaAs	6	80
V.F. Motsnyi et al. (2003)	CoFe/Al_2O_3/AlGaAs MIS diode	(Al,Ga)As/GaAs	16	300
A.Kawaharazuka et al. (2004)	Fe_3Si/GaAs Schottky contact	(In,Ga)As/GaAs	10	25
Y. Ohno et al. (1999)	GaMnAs	(In,Ga)As/GaAs	~ 2	6
R. Fiederling et al. (1999)	BeMnZnSe	(Al,Ga)As/GaAs	90	5

Table 5.3 Main findings of electrical spin injection into inorganic semiconductors from ferromagnetic metals and magnetic semiconductors. Reprinted from [37].

However, similar studies have not been carried out for FM/organic interfaces yet. Chemical modification of interfaces could possibly be used to increase the spin-dependency of the interface. The extensive work carried out by different groups in the 'Spinterface' domain for the manipulation of single molecules or monolayers at the interface of magnetic or non-magnetic metals, goes exactly in this direction [38]. It would be interesting to take advantage of this new knowledge about chemically adsorbed molecules on surfaces not only to improve spin dependency, but also to reduce the metal/organic contact resistance.

In our case, one of the main obstacles to the spin-polarization conservation at the interface is the formation of the native oxidation layer at the surface of magnetic metals. Native oxide could be avoided by careful ultra-high-vacuum preparation method (see for example the all-in-vacuum fabrication technique developed by Grunenwald *et al*. [39]), but this approach does not retain the advantages of wet chemistry deposition, of key importance for large-scale applications. To avoid the oxidation of ferromagnetic electrodes, and keep compatibility with solution process, a graphene-passivation approach of the ferromagnetic electrodes is a candidate of interest. This approach has been presented by Dlubak *et al*. [40] in 2012: the chemical vapor growth of graphene directly on Nickel has the capability to preserve the Nickel surface unoxidized upon air exposure. We are currently working on the graphene-passivation of pre-patterned Nickel electrodes in collaboration with KRICT (Daejeon, Korea). The project foresees not only surface analysis of the graphene-passivated Ni electrodes, but also the measurement of their contact resistance with different organic semiconductors (PhD thesis in codirection with P. Samori, ISIS, Strasbourg).

BIBLIOGRAPHY

[1] D. Braga, M. Ha, W. Xie, and C. D. Frisbie, “Ultralow contact resistance in electrolyte-gated organic thin film transistors,” Appl. Phys. Lett., vol. 97, no. 19, p. 193311, 2010.

[2] R. Fiederling, M. Keim, G. Reuscher, W. Ossau, G. Schmidt, A. Waag, and L. W. Molenkamp, “Injection and detection of a spin-polarized current in a light-emitting diode,” Nature, vol. 402, no. 6763, pp. 787–790, Dec. 1999.

[3] Y. Ohno, D. K. Young, B. Beschoten, F. Matsukura, H. Ohno, and D. D. Awschalom, “Electrical spin injection in a ferromagnetic semiconductor heterostructure,” Nature, vol. 402, no. 6763, pp. 790–792, Dec. 1999.

[4] Z. H. Xiong, D. Wu, Z. Valy Vardeny, and J. Shi, “Giant magnetoresistance in organic spin-valves,” Nature, vol. 427, no. 6977, pp. 821–824, Feb. 2004.

[5] V. Dediu, M. Murgia, F. C. Matacotta, C. Taliani, and S. Barbanera, “Room temperature spin polarized injection in organic semiconductor,” Solid State Commun., vol. 122, no. 3–4, pp. 181–184, Apr. 2002.

[6] G. Schmidt, D. Ferrand, L. W. Molenkamp, A. T. Filip, and B. J. van Wees, “Fundamental obstacle for electrical spin injection from a ferromagnetic metal into a diffusive semiconductor,” Phys. Rev. B, vol. 62, no. 8, pp. R4790–R4793, Aug. 2000.

[7] A. Fert and H. Jaffrès, “Conditions for efficient spin injection from a ferromagnetic metal into a semiconductor,” Phys. Rev. B, vol. 64, no. 18, p. 184420, Oct. 2001.

[8] A. Fert, J.-M. George, H. Jaffres, and R. Mattana, “Semiconductors Between Spin-Polarized Sources and Drains,” IEEE Trans. Electron Devices, vol. 54, no. 5, pp. 921 –932, May 2007.

[9] M. Popinciuc, C. Józsa, P. J. Zomer, N. Tombros, A. Veligura, H. T. Jonkman, and B. J. van Wees, “Electronic spin transport in graphene field-effect transistors,” Phys. Rev. B, vol. 80, no. 21, p. 214427, Dec. 2009.

[10] Y. Fukuma, L. Wang, H. Idzuchi, S. Takahashi, S. Maekawa, and Y. Otani, “Giant enhancement of spin accumulation and long-distance spin precession in metallic lateral spin valves,” Nat. Mater., vol. 10, no. 7, pp. 527–531, Jun. 2011.

[11] A. Fert and H. Jaffrès, “Conditions for efficient spin injection from a ferromagnetic metal into a semiconductor,” Phys. Rev. B, vol. 64, no. 18, p. 184420, Oct. 2001.

[12] D. Natali and M. Caironi, “Charge Injection in Solution-Processed Organic Field-Effect Transistors: Physics, Models and Characterization Methods,” Adv. Mater., vol. 24, no. 11, pp. 1357–1387, 2012.

[13] V. I. Arkhipov, U. Wolf, and H. Bässler, “Current injection from a metal to a disordered hopping system. II. Comparison between analytic theory and simulation,” Phys. Rev. B, vol. 59, no. 11, pp. 7514–7520, Mar. 1999.

[14] S. M. Sze, Physics of semiconductor devices. Wiley-Interscience, 1981.

[15] H. Bassler, Ed., Charge Transport in Organic Semiconductors, vol. 312. Berlin, Heidelberg: Springer Berlin Heidelberg, 2012.

[16] E. Y. Tsymbal and I. Zutic, Handbook of spin transport and magnetism. Taylor & Francis Group, 2012.

[17] U. Wolf, V. I. Arkhipov, and H. Bassler, “Current injection from a metal to a disordered hopping system. I. Monte Carlo simulation,” Phys. Rev. B, vol. 59, no. 11, pp. 7507–7513, Mar. 1999.

[18] V. I. Arkhipov, U. Wolf, and H. Bassler, “Current injection from a metal to a disordered hopping system. II. Comparison between analytic theory and simulation,” Phys. Rev. B, vol. 59, no. 11, pp. 7514–7520, Mar. 1999.

[19] S. Barth, U. Wolf, H. Bassler, P. Muller, H. Riel, H. Vestweber, P. F. Seidler, and W. Riess, “Current injection from a metal to a disordered hopping system. III. Comparison between experiment and Monte Carlo simulation,” Phys. Rev. B, vol. 60, no. 12, pp. 8791–8797, Sep. 1999.

[20] T. van Woudenbergh, P. W. M. Blom, M. C. J. M. Vissenberg, and J. N. Huiberts, “Temperature dependence of the charge injection in poly-dialkoxy-p-phenylene vinylene,” Appl. Phys. Lett., vol. 79, no. 11, pp. 1697–1699, Sep. 2001.

[21] L. Bürgi, T. J. Richards, R. H. Friend, and H. Sirringhaus, “Close look at charge carrier injection in polymer field-effect transistors,” J. Appl. Phys., vol. 94, no. 9, p. 6129, 2003.

[22] N. A. Morley, A. J. Drew, H. Zhang, K. Scott, S. Hudziak, and D. J. Morgan, “Study of the magnetic–Alq3 interface in organic spin-valves,” Appl. Surf. Sci., vol. 313, pp. 850–857, Sep. 2014.
[23] A. S. Dhoot, J. D. Yuen, M. Heeney, I. McCulloch, D. Moses, and A. J. Heeger, “Beyond the metal-insulator transition in polymer electrolyte gated polymer field-effect transistors,” Proc. Natl. Acad. Sci., vol. 103, no. 32, pp. 11834–11837, 2006.
[24] S. Fabiano, S. Braun, M. Fahlman, X. Crispin, and M. Berggren, “Effect of Gate Electrode Work-Function on Source Charge Injection in Electrolyte-Gated Organic Field-Effect Transistors,” Adv. Funct. Mater., vol. 24, no. 5, pp. 695–700, Feb. 2014.
[25] Y. Kawasugi, M. Ara, H. Ushirokita, T. Kamiya, and H. Tada, “Preparation of lateral spin-valve structure using doped conducting polymer poly(3,4-ethylenedioxythiophene) poly(styrenesulfonate),” Org. Electron., vol. 14, no. 7, pp. 1869–1873, Jul. 2013.
[26] T. V. A. G. de Oliveira, M. Gobbi, J. M. Porro, L. E. Hueso, and A. M. Bittner, “Charge and spin transport in PEDOT:PSS nanoscale lateral devices,” Nanotechnology, vol. 24, no. 47, p. 475201, Nov. 2013.
[27] T. Umeda, D. Kumaki, and S. Tokito, “Surface-energy-dependent field-effect mobilities up to 1 cm2/V s for polymer thin-film transistor,” J. Appl. Phys., vol. 105, no. 2, p. 024516, Jan. 2009.
[28] Y.-Y. Noh, X. Cheng, M. Tello, M.-J. Lee, and H. Sirringhaus, “Controlling contact resistance in top-gate polythiophene-based field-effect transistors by molecular engineering,” Semicond. Sci. Technol., vol. 26, no. 3, p. 034003, Mar. 2011.
[29] Q. Sun, K. Park, and L. Dai, “Liquid Crystalline Polymers for Efficient Bilayer-Bulk-Heterojunction Solar Cells,” J. Phys. Chem. C, vol. 113, no. 18, pp. 7892–7897, May 2009.
[30] A. S. Dhoot, J. D. Yuen, M. Heeney, I. McCulloch, D. Moses, and A. J. Heeger, “Beyond the metal-insulator transition in polymer electrolyte gated polymer field-effect transistors,” Proc. Natl. Acad. Sci., vol. 103, no. 32, pp. 11834–11837, 2006.
[31] J. Lee, B. Cho, J. Won Chung, and M. Sung Kang, “Reduction and transition in thermal activation for charge transport through electrolyte-gated polythiophene thin films with high hole densities,” Appl. Phys. Lett., vol. 103, no. 16, p. 163302, 2013.
[32] M. J. Panzer and C. D. Frisbie, “Polymer electrolyte gate dielectric reveals finite windows of high conductivity in organic thin film transistors at high charge carrier densities,” J. Am. Chem. Soc., vol. 127, no. 19, pp. 6960–6961, 2005.
[33] W. Xie and C. D. Frisbie, “Organic Electrical Double Layer Transistors Based on Rubrene Single Crystals: Examining Transport at High Surface Charge Densities above 1013 cm–2,” J. Phys. Chem. C, vol. 115, no. 29, pp. 14360–14368, Jul. 2011.
[34] F. Wang, F. Macià, M. Wohlgenannt, A. D. Kent, and M. E. Flatté, “Magnetic Fringe-Field Control of Electronic Transport in an Organic Film,” Phys. Rev. X, vol. 2, no. 2, Jun. 2012.
[35] N. Harmon, F. Macià, F. Wang, M. Wohlgenannt, A. Kent, and M. Flatté, “Including fringe fields from a nearby ferromagnet in a percolation theory of organic magnetoresistance,” Phys. Rev. B, vol. 87, no. 12, Mar. 2013.
[36] M. Wohlgenannt, P. A. Bobbert, and B. Koopmans, “Intrinsic magnetic field effects in organic semiconductors,” MRS Bull., vol. 39, no. 07, pp. 590–595, Jul. 2014.
[37] A. Bsiesy, “Spin injection into semiconductors: towards a semiconductor-based spintronic device,” Comptes Rendus Phys., vol. 6, no. 9, pp. 1022–1026, Nov. 2005.
[38] N. Atodiresei and K. V. Raman, “Interface-assisted spintronics: Tailoring at the molecular scale,” MRS Bull., vol. 39, no. 07, pp. 596–601, Jul. 2014.
[39] M. Grünewald, J. Kleinlein, F. Syrowatka, F. Würthner, L. W. Molenkamp, and G. Schmidt, “Large room-temperature magnetoresistance in lateral organic spin valves fabricated by in situ shadow evaporation,” Org. Electron., vol. 14, no. 8, pp. 2082–2086, Aug. 2013.
[40] B. Dlubak, M.-B. Martin, R. S. Weatherup, H. Yang, C. Deranlot, R. Blume, R. Schloegl, A. Fert, A. Anane, S. Hofmann, P. Seneor, and J. Robertson, “Graphene-Passivated Nickel as an Oxidation-Resistant Electrode for Spintronics,” ACS Nano, 6 (12), pp. 10930–10934, Nov. 2012.

Conclusions

In this thesis we have studied the charge transport properties of three organic materials with high conductivity as candidates for the fabrication of organic lateral spinvalves. The three materials investigated are I. supramolecular self-assembled nanowires of triarylamines molecules (STANWs), II. graphene nanoflakes obtained by liquid phase exfoliation of graphite (LPE-graphene), and III. highly doped thin films of a conjugated polymer semiconductor (Doped PBTTT).

In the Introduction we explained that the suitable organic material for Organic Spintronics must be characterized by:

1) a long spin diffusion length λ_s;
2) a low interface resistance with metallic electrodes.

The issue related to condition 1) is that the value of the spin diffusion length λ_s can be precisely known only from non-local spinvalve measurements, which have not been performed yet in literature on organic materials. Values of λ_s on organics are essentially estimates based on spin lifetimes and mobility values, until non-local measurements will be successful. One can therefore only conjecture that an organic material with higher carrier mobility (higher than the typical 10^{-3} - 10^{-2} $cm^2/V\cdot s$ value for organics) presents a longer spin diffusion length, owing to the simple consideration that a 'faster' charge (and spin!) carrier will be able to travel longer distances without losing its spin memory. This hypothesis 'high mobility - high spin diffusion length' has been indeed one of the motivation behind our search for organic materials with a 'delocalized' (or 'band-like') type of transport, with the related ansatz that hopping transport is detrimental to mobility and increases the spin flip probability. To confirm the correctness of this conjecture one should know if *a)* a spin carrier residing for a certain time in a trap state loses its spin memory or not, and if *b)* a hop event of a spin carrier from one trap state to another causes spin-flip or not. We are aware that during the period of the development of this thesis, experimental [1] and theoretical results [2] indicated that λ_s could be potentially long also in organic materials characterized by a hopping type of transport and a high density of traps.

The only way to verify these hypothesis is to measure λ_s experimentally by non-local measurements: this will be possible only when a correct injection/detection of a spin polarized electrical current into/from an organic material will be achieved (N.B. in [1] the spin current is injected by optical method). Efficient electrical spin injection (and detection) will be possible only by reducing the interface resistance between the organic material and the ferromagnetic metal electrode, i.e. by satisfying condition 2). As long as large organic/metal contact resistances prevent the optimal relaxation of spin accumulation inside the semiconductor, and hinder the transfer into the spin detecting electrode, the measurement of λ_s values will be unattainable.

Hence, condition 2) is, in some sense, primary and propaedeutic. For this reason, the final comparison between the three materials investigated mostly relies on their fulfillment of the second condition. The surface interface resistance r_b^* is evaluated 'low' or 'high' with respect to the 'spin impedance' of the two materials forming the interface ($r_{FM} = \rho_{FM}\cdot\lambda_s^{FM}$ and $r_{SC} = \rho_{SC}\cdot\lambda_s^{SC}$). More simply, one can compare the resistivity of the material $\rho_{FM/SC}$ with the linear contact resistance R_c' (both expressed in $\Omega\cdot cm$). The condition for optimal spin injection is to have an FM/SC linear contact resistance of the same order of magnitude of the injecting FM electrode resistivity, while the condition for optimal spin detection is to have a SC/FM linear contact resistance corresponding to the SC

resistivity. Generally, this means asking for a reduced contact resistance with respect to typical values of metal/organic interfaces, which are always too high.

In Table A we thus report resistivity and contact resistance estimates for the three materials.

	Resistivity ρ [Ω · cm]		**Contact resistance R_c' [Ω · cm]**	
	min	**max**	**min**	**max**
STANWs	$3 \cdot 10^{-3}$	3	$5 \cdot 10^{-2}$	$5 \cdot 10^{-1}$
LPE-graphene	10^{-6}	10^{-4}	$5 \cdot 10^{-1}$	3
Doped PBTTT	$5 \cdot 10^{-4}$	Doping dependent	4	Doping dependent

Table A Values of resistivity ρ and linear contact resistance R_c' for STANWs, graphene nanosheets and doped PBTTT.

First of all, it must be recalled that a basic difference exist between values reported for doped PBTTT and for STANWs/LPE-graphene: ρ and R_c' for PBTTT thin films have been measured experimentally, whereas they are only estimates for STANWs and graphene nanoflakes. This fact already confers an 'advantage' to PBTTT, based on the solidity of the experimental result, compared to the large incertitude on the values for the other two materials.

This being said, we can draw the following conclusions:

- *Contact resistance R_c' of highly doped PBTTT thin films with metals remains an issue.*

The achievement of conductivity values approaching those of metallic thin films (highly doped PBTTT: 500 μΩ·cm, Co-Ni thin films 10-20 μΩ·cm) gives hope for the fabrication of a spinvalve with no resistance mismatch between ferromagnetic electrodes and organic channel. However, the metal/PBTTT contact resistance remains four orders of magnitude higher than the four-probe resistivity of PBTTT. For none of the gate bias of electrolyte-gating ρ and R_c' are similar, owing to the fact that doping lowers both quantities with the same order of magnitude. If we translate these values in terms of areal contact resistance r_b^* ($1 \cdot 10^{-5}$ $\Omega \cdot cm^2$) and spin impedance $r_N = \rho \cdot \lambda_s$, an unlikely spin diffusion length value λ_s larger than 100 μm would be required to achieve the equivalency.

The condition on low organic/metal interface resistance is extremely hard to satisfy because of the extreme dissimilarity of the two type of materials, which introduces an unavoidable obstacle to the flow of charge (and spin!) carriers from one to the other. Under the point of view of contact resistance:

- *Supramolecular Triarylamines Nanowires present the lowest contact resistance with metals (among the three materials studied).*

The major difference of STANWs with respect to graphene and PBTTT is the in-loco 'construction' of the material. In the case of graphene and PBTTT the material already exist in solution and it is deposited onto the metallic electrodes. 'Building' the organic spacer starting from the metal electrode itself seems to be key factor for achieving a very low interface resistance. Evidently, it is important that the conductive channel of the organic structure (the π delocalized path, for example) is in direct contact with the electronic reservoir of the metal, otherwise charge injection remains hindered. Even though a r_b^*/r_N ratio closer to 1 (respect to doped PBTTT) might be possible for STANWs, unfortunately

other practical issues prevent the possibility of fabricating lateral spinvalves, in particular the short time stability of the fibers between magnetic-only electrodes.

It is very complicated to find a 'best choice' among the three materials investigated, because each of them has advantages and disadvantages; perhaps, it is not even reasonable to provide a ranking. The solution-processable 'ink' of graphene nanosheets is also a potential good candidate for the fabrication of lateral organic spinvalves. Graphene is the only material among the three for which the spin diffusion length λ_s is experimentally known (from non-local measurements), and it exceeds 1 micrometer (condition n.1 is fulfilled!). Unfortunately, the interface resistance is too elevated also for this liquid-exfoliated graphene nanoflakes ink. One could for example try to reduce it by evaporating metallic contacts onto the graphene thin film, instead of depositing the film on pre-patterned electrodes.

It is now clear to the Organic Spintronic community that the magnetoresistance in two-terminal spin-valves cannot be considered a fingerprint for spin injection, and that a different piece of evidence is needed (non-local measurements, Hanle effect, etc) [3]. One of the main outcomes of this work is that, until now, the difficulty in matching the interface resistance with the spin impedance of electrodes and channel has been underestimated and it is probably the main cause why the 'different piece of evidence' is still missing.

One way to circumvent the resistance mismatch in a diffusive model would be to rely 'only' on tunneling (TMR devices), but this would mean to completely bypass the problem, and consequently to miss the opportunities deriving from being able to inject a spin polarized current in an organic material, such as manipulating it through external stimuli. The constructive way to face the problem is to find new approaches to reduce interface resistance to a large extent, for example by inducing strong chemisorption of the organic channel on the electrodes and/or introducing chemisorbed intermediate layers. Organic electronics is working hard on that since 10 – 15 years already, and progresses have been made. A considerable effort for understanding the way in which molecules couple magnetically with surfaces of ferromagnetic metals is also ongoing from the groups of the Organic Spintronics community working in the so-called 'Spinterface' area [4]. These efforts will hopefully lead to the creation of spin-dependent organic/inorganic interfaces possessing the adequate characteristics for successful devices fabrication. Several challenges however remain in both device performance and fundamental understanding before organic semiconductors can compete with inorganic semiconductors or metals in the development of realistic spintronic applications.

Despite the unresolved issue above discussed, the scientific path we followed to come to such conclusion has been challenging and fascinating by itself, and it has brought to several important discoveries, summarized below.

- *Metallicity of supramolecular all-organic nanofibers*

To understand the impact of this finding, one should consider that metallicity in organic materials has been for long a 'holy grail' (and still is, because of its rarity). The possibility of unifying the benefit of a highly efficient electrical conductivity with the advantages characterizing organic materials (solution-processability, low temperature treatments, low cost and abundance of the raw materials) would allow substituting inorganic materials in various applications. Our result constitutes a breakthrough within the shared scientific effort of Organic Electronics community towards organic materials with higher mobility and a 'band-like' type of transport.

- *Ambipolar transport in graphene nano-flakes made by liquid-phase exfoliation of graphite*

We present a method to sense the electrical transport properties of single nano-flakes which compose graphene inks and we demonstrate that they preserve the ambipolar charge transport intrinsic of graphene, which is instead 'lost' when the material is tested in the form of thin films. Ambipolar transport is perhaps unnecessary when graphene inks are used as printable transparent electrodes or large specific area electrodes for capacitors, but it could be exploited in other types of applications.

- *Delocalized transport in a highly doped conjugated polymer semiconductor*

The analysis of electrical properties of doped thin film of PBTTT has revealed different fingerprints of a charge transport mechanism almost temperature-independent and occurring through more 'delocalized' states respect to typical trap states present in the tail of the Gaussian DOS. Different reports recently published by the group of H. Sirringhaus [5] and P. Blom – D. de Leeuw [6] highlight that a completely new physics of charge transport can emerge in polymer semiconductors if the influence of disorder is cancelled out. In [5] the effect of disorder is 'neutralized' by using a semiconductor specifically designed to present a torsion-free polymer backbone; in [6] the authors exploit more 'classical' approaches like chemical doping and ferroelectric gates. Our result also confirms the crossover to a 'metallic' quasi-2-dimensional type of transport, up to the point of proving the occurrence of weak localization phenomena, which until now has been exclusively attributed to inorganic metals.

The study of the response of PBTTT thin films to the presence of an external magnetic field has also been carried out as preparatory study in view of tentative spinvalve fabrication. In fact, as above mentioned, the reproducible magnetoresistance found in two-terminal spinvalves is not necessarily due to injection and diffusion of a spin polarized current inside the semiconducting spacer. Each non-magnetic material has its own intrinsic magnetoresistance response to the application of a magnetic field [7], thus in principle one should first study MR on the bulk material to be sure to avoid artifacts during spinvalve measurements. We believe it is now essential to perform control experiments in 'spin valves' involving organic spacers to check if the MR signal comes from the injection-detection of a spin current, or if it realtes to the intrinsic response of an organic material to the magnetic field. For example, simple experiments where one, or both electrodes are non-ferromagnetic should provide a simple discrimination between the two model. One important message from this presented work is that the creation of a spin current, or the adequacy of a diffusive model inspired by results on inorganic materials, are unlikely to apply.

BIBLIOGRAPHY

[1] S. Watanabe, K. Ando, K. Kang, S. Mooser, Y. Vaynzof, H. Kurebayashi, E. Saitoh, and H. Sirringhaus, "Polaron spin current transport in organic semiconductors," *Nat. Phys.*, Mar. 2014.

[2] R. C. Roundy and M. E. Raikh, "Spin transport with dispersive traps: Narrowing of the Hanle curve," *Phys. Rev. B*, vol. 90, no. 24, p. 241202, Dec. 2014.

[3] S. Sanvito and V. A. Dediu, "Spintronics: News from the organic arena," *Nat. Nanotechnol.*, vol. 7, no. 11, pp. 696–697, Nov. 2012.

[4] S. Sanvito, "Molecular spintronics: The rise of spinterface science," *Nat. Phys.*, vol. 6, no. 8, pp. 562–564, 2010.

[5] D. Venkateshvaran, M. Nikolka, A. Sadhanala, V. Lemaur, M. Zelazny, M. Kepa, M. Hurhangee, A. J. Kronemeijer, V. Pecunia, I. Nasrallah, I. Romanov, K. Broch, I. McCulloch, D. Emin, Y. Olivier, J. Cornil, D. Beljonne, and H. Sirringhaus, "Approaching disorder-free transport in high-mobility conjugated polymers," *Nature*, Nov. 2014.

[6] K. Asadi, A. J. Kronemeijer, T. Cramer, L. Jan Anton Koster, P. W. M. Blom, and D. M. de Leeuw, "Polaron hopping mediated by nuclear tunnelling in semiconducting polymers at high carrier density," *Nat. Commun.*, vol. 4, p. 1710, Apr. 2013.

[7] M. Wohlgenannt, P. Bobbert, B. Koopmans, "Intrinsic magnetic field effects in organic semiconductors" *MRS Bullettin.*, issue 39, vol. 07, p. 590-595, Jul. 2014

Appendix A - Nanotrenches fabrication

In 2010 our group presented a simple and versatile lithographic procedure to pattern high aspect ratio (W/L > 100) nanogaps [1], characterized by gap size (L) down to ~ 50 nm and gap width (W) of several tens of microns (W). High aspect ratio devices are very useful when highly resistive materials are investigated, or in order to minimize the contact resistance effect on the device performance. Because of this very high aspect ratio, we called this type of electrical interconnects "nano-trenches".

Gap size below 1 µm is normally fabricated by electron beam (e-beam) lithography or by using sacrificial layers. E-beam lithography of sub-100 nm gaps with aspect ratio > 10 is very challenging (problems of "proximity effect"). The use of a sacrificial layer of oxide (insulating layer successively etched to create a nanogap) might suffer of residues contaminating the gap.

Our fabrication process makes use of standard optical lithography to create a sub-100 nanometers gap. It is an edge-mediated shadow masking under angle evaporation. Details are explained in the following. The easiness of the geometrical effect exploited in this nanofabrication process allows us to realize reproducible nanotrenches, uniform all along the micrometric width of the gap and without resist contamination into the gap area. The productivity is drastically augmented respect to e-beam lithography. This method allows parallel processing of many junctions, making it easily scalable and industrially relevant. We can obtain 28 nanotrenches (distributed over 4 chips) each run of nanofabrication.

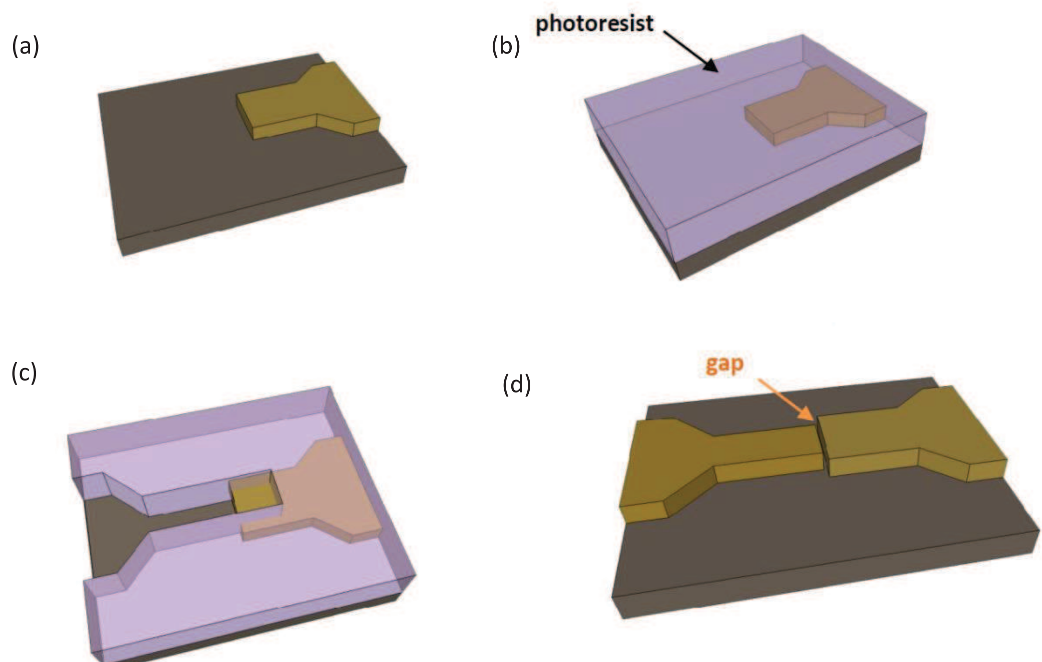

Figure I. Schematic of the edge-mediated shadow mask lithography process. (a) The first electrode is patterned and deposited; in (b) and (c) the photoresist is patterned partially superpositioned on the first electrode; (d) metal deposition with the sample tilted at a specific angle (see next figure) form the second electrode and the nanotrench in between.

The procedure is composed by two optical lithography step and consequent metal evaporation, as schematically represented in Figure I.

The first step of lithography consists in patterning and evaporating the first electrode (a). With the second lithography step we pattern the photoresist for second electrode deposition, leaving a window that superposes in some area with the first eslectrode, as clear in Figure I (c). The width W of the gap is defined with this second step. Then the second electrode is evaporated mantaining the sample tilted of an angle θ (between the substrate normal and the metal evaporation direction), as shown in Figure II. The shadow effect of the nanometric thick first electrode allows the aperture of the nanometric gap.

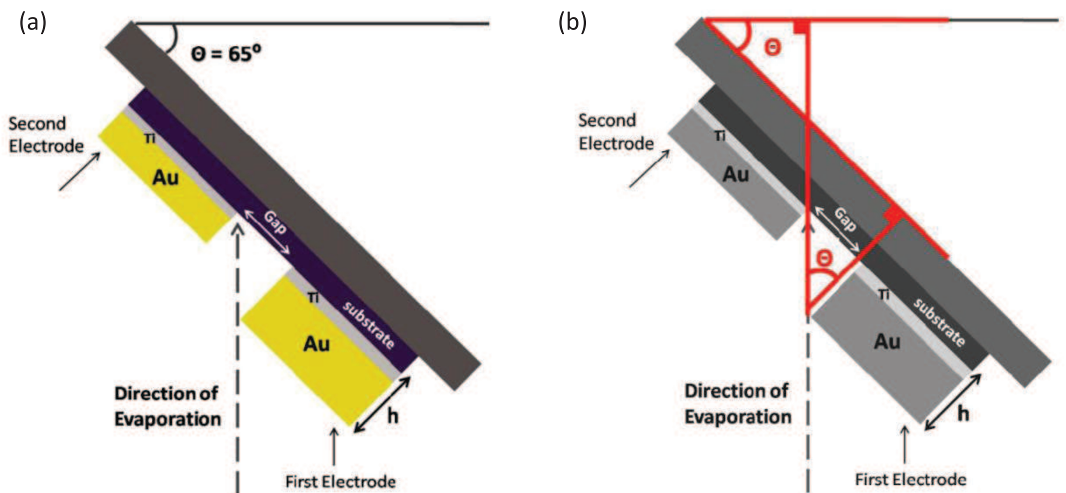

Figure II. Representations of the principle of the edge-mediated shadow mask lithography process. The gap size L is determined by the height of the first electrode h and the angle θ. The gap is created thanks to the shadowing effect of the first electrode.

The gap size L depends on the height *h* of the first electrode and on the angle θ according to:

$$L = h \cdot tg\theta \, .$$

We typically use a deposition angle θ of 65° and a first electrode thickness of 60 nm. This would give a theoretical gap size of ~ 130 nm. Pratically these parameters lead to a gap of ~ 80 nm.

The thickness of the second electrode is reduced respect to the actual quantity of metal deposited (and weighted by the quartz balance inside the evaporator) because of the tilted evaporation. In particular, the height of the two electrodes is very different because the second electrode is also evaporated above the first, resulting in a small area of double thickness. For some applications or special measurements or imaging, the height difference might be a drawback.

Critical for the success of the fabrication procedure is the cleanliness and perfection of the first electrode edge. Presence of resist residues or zigzaged edges strongly affect the quality of the final gap.

Nanotrenches have already been used in our group for photoconductivity measurements of spin-crossover nanocrystals [2], electrical detection of optically switchable molecular junctions [3] and electrical transport in nanoparticles networks [4],[5].

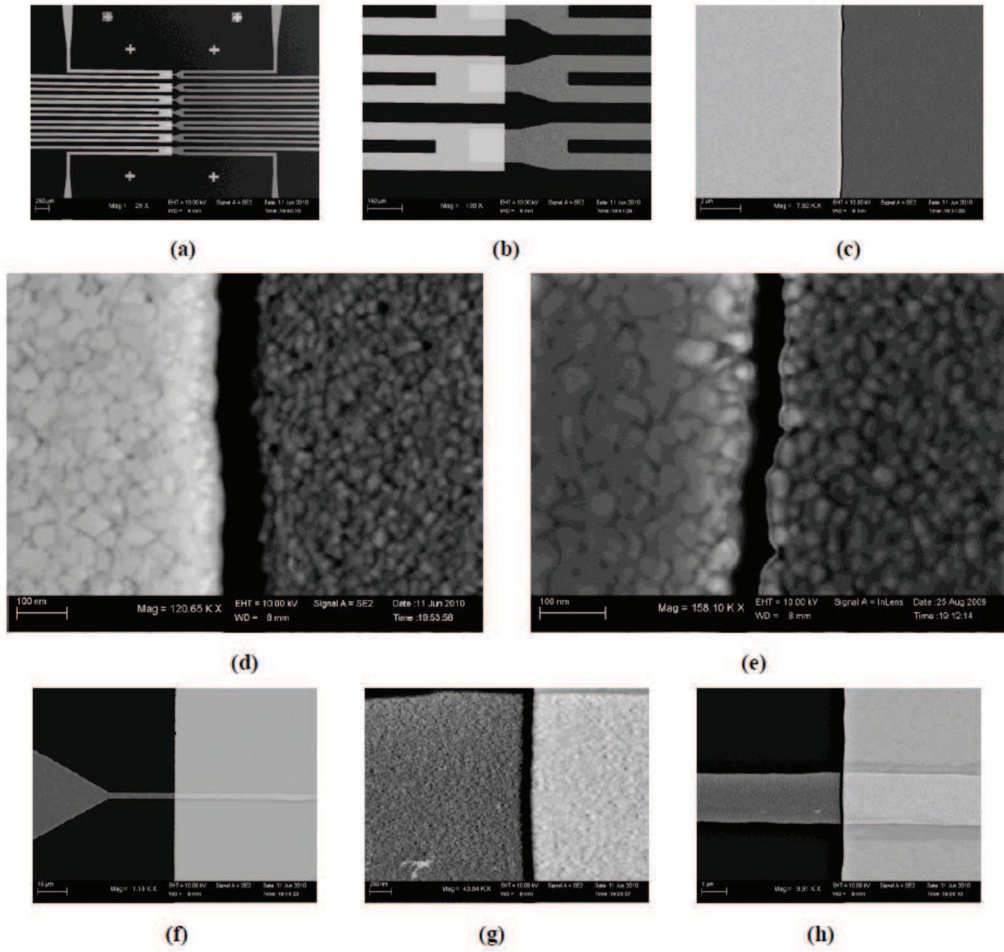

Figure III. a) SEM image of the 7 nanotrenches present on one chip, each connected by four pads. b) Zoom on the 100 µm and 80 µm wide nanotrenches. The different color of the two electrodes is due to the different metal thickness. c,d,e) Zoom on the 80 nm gap. f,g,h) Images of a 3 µm wide nanotrench.

[1] J. F. Dayen, V. Faramarzi, M. Pauly, N. T. Kemp, M. Barbero, B. P. Pichon, H. Majjad, S. Begin-Colin, and B. Doudin, “Nanotrench for nano and microparticle electrical interconnects,” *Nanotechnology*, vol. 21, p. 335303, 2010.

[2] C. Etrillard, V. Faramarzi, J.-F. Dayen, J.-F. Letard, and B. Doudin, “Photoconduction in [Fe(Htrz)2(trz)](BF4)·H2O nanocrystals,” *Chem. Commun.*, vol. 47, no. 34, p. 9663, 2011.

[3] V. Faramarzi, C. Raimondo, F. Reinders, M. Mayor, P. Samori, and B. Doudin, “Optically switchable molecular device using microsphere based junctions,” *Appl. Phys. Lett.*, vol. 99, no. 23, pp. 233104–233104–3, Dec. 2011.

[4] J.-F. Dayen, E. Devid, M. V. Kamalakar, D. Golubev, C. Guédon, V. Faramarzi, B. Doudin, and S. J. van der Molen, “Enhancing the Molecular Signature in Molecule-Nanoparticle Networks Via Inelastic Cotunneling,” *Adv. Mater.*, vol. 25, no. 3, pp. 400–404, 2013.

[5] M. Pauly, J.-F. Dayen, D. Golubev, J.-B. Beaufrand, B. P. Pichon, B. Doudin, and S. Bégin-Colin, “Co-tunneling Enhancement of the Electrical Response of Nanoparticle Networks,” *Small*, vol. 8, no. 1, pp. 108–115, 2012.

Appendix B – Electrolyte-gating

The extensive use of electolytes as gating media starts around the years 2001 - 2002 with the works of Kruger *et al*. [1] and Rosenblatt *et al*. [2] for the fabrication of carbon nanotubes transistors. Beside the higher performances (higher transconductance, lower operating voltage), the main advantage of these transistors was their compatibility with biological sensing (salty water is an electrolyte). After the first application of electrolyte gating on pentacene transistors realized by the group of Prof. C. Frisbie [3],[4] in 2005, the use of this technique in Organic Electronics rapidly gained popularity.

In addition to their use as gating media, nowadays electrolytes are now employed in a wide range of electronics applications, such as thin-film batteries, electrochromic displays, fuel cells and supercapacitors.

Electrolytes versus conventional insulators

In field-effect transistors with standard dielectric gates (inorganic oxides or organic insulating polymers), the application of a voltage potential to the gate electrode produces the polarization of the dielectric material, which consists in a small displacement of positive and negative charges inside the dielectric respect to their equilibrium positions. A dielectric material is by definition a material in which there are no free charges; all electrons are bound, thus no current flow occurs upon exposure to an electric field. The induced dipole moments caused by polarization are temporary and they should disappear when the electric field is removed. If permanent dipoles are present in the material, the electric field simply orients them. The polarization of a parallel-plate capacitor with a dielectric material as insulating layer is shown in Figure I.

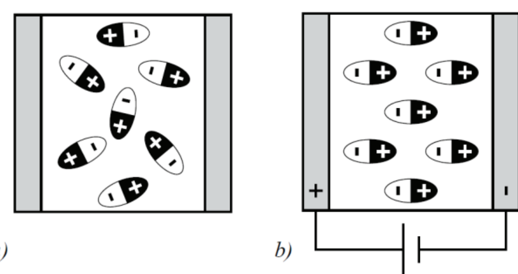

Figure I. Illustration of the polarization in a conventional dielectric capacitor. a) With no voltage applied, the permanent dipole moments are randomly oriented. b) with a voltage applied, the dipole moments align with the electric field. Reproduced from [5].

The capacitance of a parallel-plate capacitor with a dielectric material as the insulating layer is given by:

$$C = \frac{\varepsilon_0 \varepsilon_r}{d} \cdot A$$

where ε_0 and ε_r are respectively the dielectric constant of vacuum and of the insulating material, A is the capacitor plate area and d is the thickness of the dielectric. Typical values of specific

capacitance (capacitance per unit of area) for 200 - 300 nm thick SiO_2 gates are in the range of few nanofarads per square centimeter (nF/cm^2). High-ε thin oxides such as ZrO_2, Ta_2O_5 or HfO_2 can reach up to 0.1 µF/cm^2.

In contrast to dielectric materials, electrolytes have free (ionic) charges that can move in an electric field. An illustration of a parallel-plate capacitor consisting of an electronically insulating but ion-conducting electrolyte sandwiched between two metal electrodes is given in Figure II. When a voltage is applied to the capacitor, Figure II(b), redistribution of ions takes place in the electrolyte. Positively charged ions (cations) migrate towards the negatively charged electrode while negatively charged ions (anions) migrate towards the positively charged electrode, as in Figure II(c). At the end of the charging process, electric double layers (EDLs) are formed at each electrolyte-electrode interface, Figure II(d).

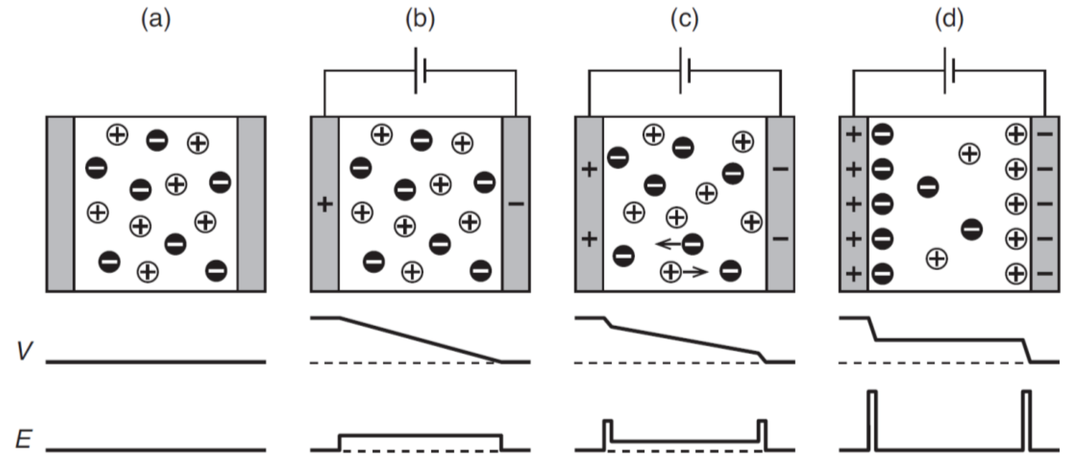

Figure II. Schematic illustrations of the charge distribution, electric potential (V) and electric field (E) in the electrolyte layer of an electrolytic capacitor during charging. a) The ions are evenly distributed when no voltage is applied. b) An applied voltage will induce a redistribution of the charges in the electrolyte. The situation in the electrolyte (b) before, (c) during and (d) after ionic relaxation is shown. Reproduced from [6].

Provided that no electrochemical redox reactions occurs at the double layer formed at the electrolyte-active channel interface, the ionic nature of an electrolyte allows electrons or holes to be induced at much lower operating voltages when compared to traditional FET dielectric materials. Electrical double layers are characterized by a very large specific capacitance C' [F/cm^2] due to the nanometric thickness of the accumulated charge. In fact, the specific capacitance of an EDL may be estimated by Helmoltz formula:

$$C' = \frac{\varepsilon_0 \varepsilon_r}{\lambda_D}$$

which resembles the formula previously reported for normal dielectrics, with Debye screening length λ_D (or EDL thickness) replacing the dielectric thickness. EDLs typically present specific capacitance in the 1 - 10 µF/cm^2 range, around 3 orders of magnitude higher respect to classical SiO_2 bottom gates.

Electrolyte-gated OFET

In Figure III a schematic of an electrolyte-gated OFET under bias is represented. The gate voltage V_G and the drain voltage V_D are applied relative to the grounded source electrode. For a hole conducting organic semiconductor, applying a negative V_g causes ion migration within the electrolyte dielectric layer, resulting in the formation of electric double layers at the gate/electrolyte and electrolyte/semiconductor interfaces, which consist of electrons/cations and anions/holes, respectively. The charge-neutral electrolyte region forces nearly all of the V_G potential applied to drop across these two double-layer capacitors.

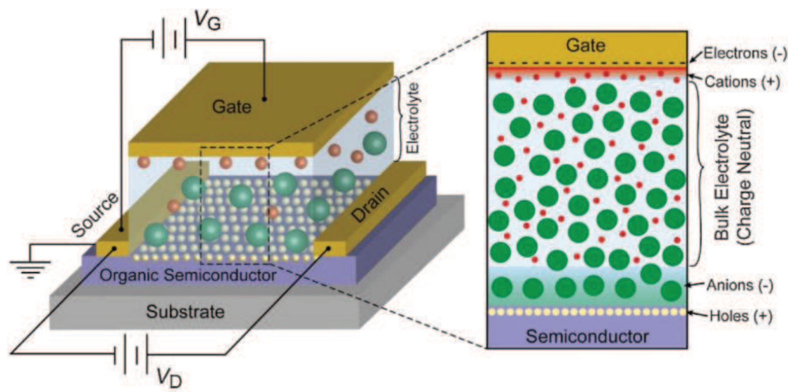

Figure III. Electrolyte-gated OFET under drain and gate bias. The picture is not in scale in order to better show the formation of the two electrical double layers forming at the gate/electrolyte and electrolyte/semiconductor interfaces. Gate bias is negative. Reprinted from [7].

An important figure of merit for gate dielectrics is their specific capacitance C', because it determines how much charge can be induced in the semiconductor channel of an OFET for a given applied gate voltage; higher capacitance translates into higher induced charge densities and therefore both higher ON currents and lower operating voltages (< 2 V) [8],[9]. Large specific capacitances have been achieved also by means of other gate dielectrics other than electrolytes, namely ferroelectric polymers [10] and ultrathin self-assembled monolayers [11]. The capacitances of these systems also approach 1 $\mu F/cm^2$.

Thanks to the record levels of induced charge density on the active channel, electrolyte-gating has already been a key factor for important discoveries of some fundamental physical properties of different materials, among which: the measurement of quantum capacitance of graphene [12], the superconductivity in $SrTiO_2$ [13] and other materials [14],[15], and the occurrence of insulator-to-metal transitions in ZnO [16] and in a thin film conjugated polymer [17].

The applicable gate voltage for transistor operation is limited by the electrochemical stability window of the electrolyte, i.e. the window of voltage potential inside which no redox reactions occur at the gate electrode. The electrochemical window of many electrolytes extends over 4 - 5 Volts around 0 V. For instance, the presence of water/moisture inside the electrolyte can reduce its electrochemical window because of the appearance of hydrolysis reaction.

Different types of electrolytes

Different types of electrolytes exist and they are schematically illustrated in Figure IV: electrolyte solutions, ionic liquids, iongels, polyelectrolytes, polymer electrolytes (listed in order of increased

viscosity). **Electrolyte solutions** are the simplest type of electrolytes, constituted of a salt (e.g. NaCl, $LiClO_4$) dissolved in a liquid medium. Common dissolving medium are water or other polar solvents (e.g. alcohols, acetonitrile). Pure water is itself an electrolyte solution, even though of limited usable gate voltage range, because of water molecules dissociation in ions OH^- and H^+; it has indeed been used as gating medium [18]. **Ionic liquids** are salts which are liquid at room temperature. They are formed by anions and cations that are tightly attracted by electrostatic forces, but they are not arranged in a crystalline packing because of their relatively large size. Typically one of the two ions has a delocalized charge and is organic. To overcome the fact that ionic liquids are impractical to use in solid-state devices, it exist the possibility to blend them with polymers in order to make them stiffer and more convenient to handle. In this case the electrolyte is defined as **ion gel**, i.e. a polymer network swollen by an ionic liquid. The amount of polymer however remains very low (< % in weight).

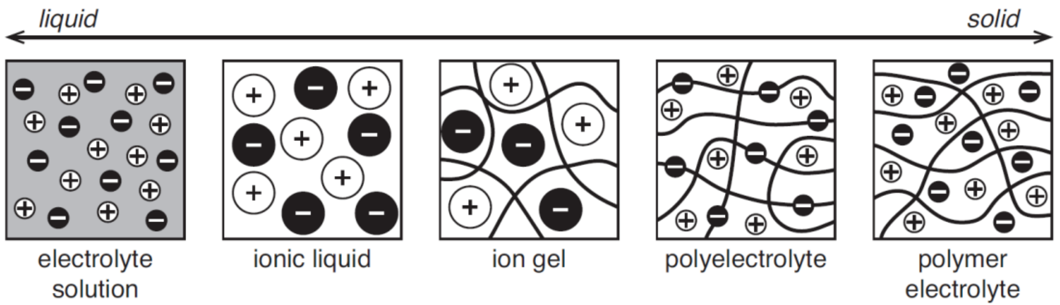

Figure IV. Different classes of electrolytes in order of solidity from left to right. Reprinted from [6].

Polyelectrolytes are polymers that have an electrolyte group in the repeat unit along the molecular backbone. A small quantity of polar solvent is present to allow the groups dissociation under the application of a voltage potential. Polyelectrolytes that are positively (negatively) charged are called polycations (polyanions). The main advantage of polyelectrolytes is that ions of only one polarity are mobile. Finally, **polymer electrolytes** are composed of a salt dissolved in a polymer matrix. Both ions are mobile and no solvent is present. One of the firstly used polymer electrolytes is poly(ethylene oxide) blended with a sodium or lithium salt [19],[20],[3] ($PEO/LiClO_4$).

Polyelectrolytes and polymer electrolytes have been introduced for their convenience in fabricating solid-state devices, while ionic liquids and iongels are used in applications in which a liquid medium is preferred.

Due to their inherent liquid state, ionic liquids can exhibit high ionic conductivities, often up to 0.1 S/cm. Ionic conductivity of ion gels is comparable to that of pure ionic liquids, i.e. in the range of 10^{-4} to 10^{-2} S/cm. Polyelectrolytes typically exhibit an ionic conductivity in the range from 10^{-6} to 10^{-3} S/cm, while for polymer electrolytes it is even lower (10^{-8} to 10^{-4} S/cm), owing to the presence of a relevant amount of polymer matrix. Typical values of ionic conductivity are shown in Figure V(a).

The polarization time delay in response to the application of a voltage potential to the electrolyte directly depends on its ionic conductivity. Charging of polyelectrolytes and polymer electrolytes is longer than for ionic liquids and gels because ions movement is slowed down by the presence of the polymer matrix. Impedance spectroscopy analysis shows that, in general, electrolytes exhibit capacitive behavior up to frequencies around 10^4 Hertz, as shown in Figure V(b) for the iongel PS-PMMA-PS/[EMI][TFSA]. At higher frequencies the iongel behavior becomes resistive, thus unable to exploit its gating function. This constitutes one of the major limits to the cutoff frequency at which electrolyte-gated devices can be used.

(a)

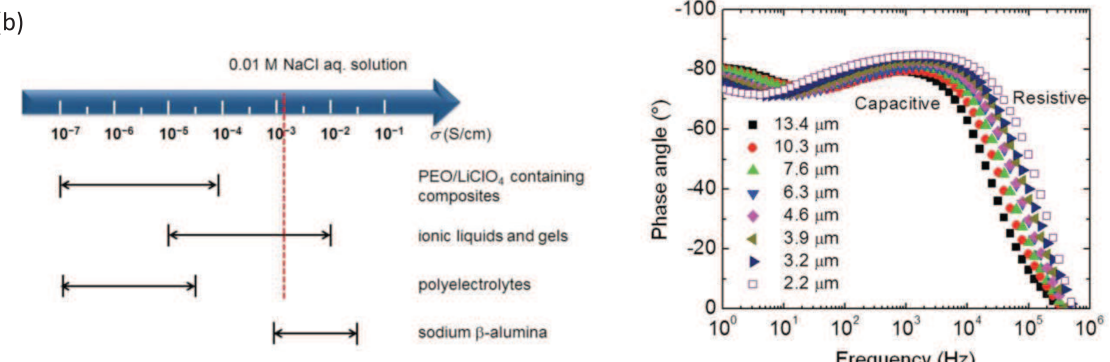

Figure V. a) Ionic conductivity ranges for common electrolytes at room temperature [21]. b) Phase angle versus frequency for ion gel electrolyte capacitors with different thicknesses. The ion gel electrolyte consists of a gelating triblock copolymer and an ionic liquid, in this case poly(styrene-*b*-methyl methacrylate-*b*-styrene) and [EMI][TFSA]. Reproduced from [22].

Electrolytes on OSCs: electrostatic gating or chemical doping?

A debate remained open for some years whether electrolyte-gating on OSCs was a simple electrostatic effect (as in conventional FETs) or if ions penetrate in the semiconductor and dope it chemically, as illustrated in Figure VI. The type of mechanism associated to electrolyte-gating strongly depends on the "permeability" of the OSCs to the electrolyte ions. With an impermeable semiconductor, the gating action of the EDL charging at the surface is merely electrostatic, thus it exerts a large transverse electric field onto the semiconductor that produces charge carrier accumulation (or depletion). With ion permeable semiconductors, EDL ions diffuse from the electrolyte into the semiconductor film. This process, called electrochemical doping, creates a compensation of the induced charge carriers (entering in from the source and drain contacts). Electrochemical doping was among the first methods used to dope polymer semiconductors, even though early experiments were carried out in electrochemical cells, not in OFETs architectures. Electrochemical doping of the organic semiconductor in ECTs is however reversible (de-doping) upon removal of the gate bias. Recent consensus is to refer to devices with impermeable semiconductors as 'electric double layer transistors', or EDLTs, and as 'electrochemical transistors', or ECTs, for transistors that employ permeable semiconductors. If electrolyte-gating correspond to reduction/oxidation of conjugated polymer thin films, the values of specific capacitance can reach up to 100 – 200 µF/cm^2, simply because the accumulated charge distributes within a volume.

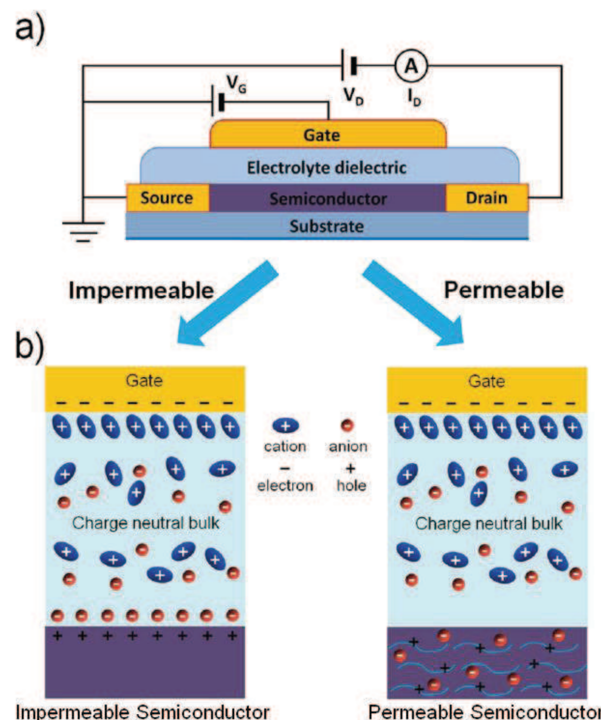

Figure VI. a) Cross-section of an electrolyte-gated transistor. b) Representation of the two possible operation principles for un-doped ion-impermeable (left) and permeable semiconductor (right).

However, the differentiation between these two types of gating mechanism is not straightforward. Permeability of the OSC towards the electrolyte ions depends on many different factors, such as the crystallinity degree of the OSC, its hydrophobic/hydrophilic affinity, and the nature of electrolyte ions. A 'mixed' regime exist between the pure electrostatic and the 3D chemical doping, as demonstrated by Laiho *et al*. [23]. The three regimes are represented in Figure VII.

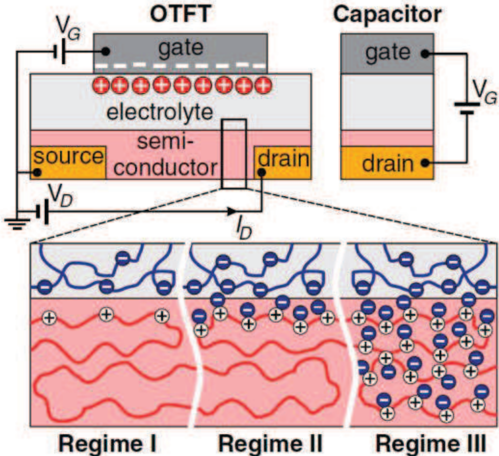

Figure VII. Three regimes of operation of an electrolyte-gated OFET (accumulation mode in a p-type semiconductor). Regime II is 'mixed': not purely electrostatic gating effect (as Regime I), but the doping is limited to the first monolayer close to the interface (it is not a 3D doping as Regime III). Reprinted from [23].

At low gate bias, the OFET operate similarly to a conventional field-effect transistor (Regime I). At higher gate bias, electrochemical doping dominates, but the extent of doping can be controlled by the duration of the applied gate bias. A fast application of the gate bias leads to an intermediate regime in which few monolayers only are involved in charge transport (Regime II), whereas a long application of the gate bias causes a 3D doping and charge transport occurs through the bulk of the semiconductor (Regime III).

Determination of the accumulated charge density

The determination of charge density Q induced on electrolyte-gated organic semiconductors is not as simple as in standard dielectrics OFETs. For standard dielectrics OFETs one can estimate the charge density simply from the gate dielectric capacitance and the applied gate voltage, $Q = C \cdot (V_{gate} - V_{threshold})$. The specific capacitance of conventional dielectrics is easily known as the ratio of dielectric constant to layer thickness ($C' = \varepsilon_0\varepsilon_r/d$).

On the contrary, the capacitance of an electrolyte layer is independent of the electrolyte thickness and typically depends on both operating frequency and gate voltage. The capacitance of an electrolyte gating medium can be determined by means of two main techniques:

- Impedance spectroscopy, which can measure capacitance as a function of frequency (C−*f*) and gate voltage (C−V).
- Measure and integration of the gate-source current I_g. Integrating I_g, measured while sweeping the gate voltage, gives the total Q accumulated. This essentially corresponds to the gate displacement current method, with the difference that in this latter source and drain contacts are both grounded. Normally distinct charging and discharging regions can be identified, similar to the behavior of charging an ideal capacitor.

[1] M. Krüger, M. R. Buitelaar, T. Nussbaumer, C. Schönenberger, and L. Forró, “Electrochemical carbon nanotube field-effect transistor,” *Appl. Phys. Lett.*, vol. 78, no. 9, pp. 1291–1293, Feb. 2001.

[2] S. Rosenblatt, Y. Yaish, J. Park, J. Gore, V. Sazonova, and P. L. McEuen, “High Performance Electrolyte Gated Carbon Nanotube Transistors,” *Nano Lett.*, vol. 2, no. 8, pp. 869–872, 2002.

[3] M. J. Panzer, C. R. Newman, and C. D. Frisbie, “Low-voltage operation of a pentacene field-effect transistor with a polymer electrolyte gate dielectric,” *Appl. Phys. Lett.*, vol. 86, no. 10, p. 103503, 2005.

[4] M. J. Panzer and C. D. Frisbie, “Polymer electrolyte gate dielectric reveals finite windows of high conductivity in organic thin film transistors at high charge carrier densities,” *J. Am. Chem. Soc.*, vol. 127, no. 19, pp. 6960–6961, 2005.

[5] O. Larsson, “Polyelectrolyte-Based Capacitors and Transistors,” Linköping, 2011.

[6] L. Herlogsson, “Electrolyte-Gated Organic Thin-Film Transistors,” Linköping, 2011.

[7] M. J. Panzer and C. D. Frisbie, “Exploiting Ionic Coupling in Electronic Devices: Electrolyte-Gated Organic Field-Effect Transistors,” *Adv. Mater.*, vol. 20, no. 16, pp. 3177–3180, Aug. 2008.

[8] J. H. Cho, J. Lee, Y. Xia, B. Kim, Y. He, M. J. Renn, T. P. Lodge, and C. Daniel Frisbie, “Printable ion-gel gate dielectrics for low-voltage polymer thin-film transistors on plastic,” *Nat. Mater.*, vol. 7, no. 11, pp. 900–906, Oct. 2008.

[9] Y. Xia, W. Zhang, M. Ha, J. H. Cho, M. J. Renn, C. H. Kim, and C. D. Frisbie, “Printed Sub-2 V Gel-Electrolyte-Gated Polymer Transistors and Circuits,” *Adv. Funct. Mater.*, vol. 20, no. 4, pp. 587–594, Feb. 2010.

[10] R. C. G. Naber, C. Tanase, P. W. M. Blom, G. H. Gelinck, A. W. Marsman, F. J. Touwslager, S. Setayesh, and D. M. de Leeuw, "High-performance solution-processed polymer ferroelectric field-effect transistors," *Nat. Mater.*, vol. 4, no. 3, pp. 243–248, Mar. 2005.

[11] M. Halik, H. Klauk, U. Zschieschang, G. Schmid, C. Dehm, M. Schütz, S. Maisch, F. Effenberger, M. Brunnbauer, and F. Stellacci, "Low-voltage organic transistors with an amorphous molecular gate dielectric," *Nature*, vol. 431, no. 7011, pp. 963–966, Oct. 2004.

[12] J. Xia, F. Chen, J. Li, and N. Tao, "Measurement of the quantum capacitance of graphene," *Nat. Nanotechnol.*, vol. 4, no. 8, pp. 505–509, Jul. 2009.

[13] K. Ueno, S. Nakamura, H. Shimotani, A. Ohtomo, N. Kimura, T. Nojima, H. Aoki, Y. Iwasa, and M. Kawasaki, "Electric-field-induced superconductivity in an insulator," *Nat. Mater.*, vol. 7, no. 11, pp. 855–858, Nov. 2008.

[14] A. T. Bollinger, G. Dubuis, J. Yoon, D. Pavuna, J. Misewich, and I. Božović, "Superconductor-insulator transition in La2 - xSrxCuO4 at the pair quantum resistance," *Nature*, vol. 472, no. 7344, pp. 458–460, Apr. 2011.

[15] J. T. Ye, S. Inoue, K. Kobayashi, Y. Kasahara, H. T. Yuan, H. Shimotani, and Y. Iwasa, "Liquid-gated interface superconductivity on an atomically flat film," *Nat. Mater.*, vol. 9, no. 2, pp. 125–128, Feb. 2010.

[16] H. Shimotani, H. Asanuma, A. Tsukazaki, A. Ohtomo, M. Kawasaki, and Y. Iwasa, "Insulator-to-metal transition in ZnO by electric double layer gating," *Appl. Phys. Lett.*, vol. 91, no. 8, p. 082106, 2007.

[17] A. S. Dhoot, J. D. Yuen, M. Heeney, I. McCulloch, D. Moses, and A. J. Heeger, "Beyond the metal-insulator transition in polymer electrolyte gated polymer field-effect transistors," *Proc. Natl. Acad. Sci.*, vol. 103, no. 32, pp. 11834–11837, 2006.

[18] L. Kergoat, L. Herlogsson, D. Braga, B. Piro, M.-C. Pham, X. Crispin, M. Berggren, and G. Horowitz, "A Water-Gate Organic Field-Effect Transistor," *Adv. Mater.*, vol. 22, no. 23, pp. 2565–2569, May 2010.

[19] C. Lu, Q. Fu, S. Huang, and J. Liu, "Polymer Electrolyte-Gated Carbon Nanotube Field-Effect Transistor," *Nano Lett.*, vol. 4, no. 4, pp. 623–627, 2004.

[20] G. P. Siddons, D. Merchin, J. H. Back, J. K. Jeong, and M. Shim, "Highly Efficient Gating and Doping of Carbon Nanotubes with Polymer Electrolytes," *Nano Lett.*, vol. 4, no. 5, pp. 927–931, 2004.

[21] S. H. Kim, K. Hong, W. Xie, K. H. Lee, S. Zhang, T. P. Lodge, and C. D. Frisbie, "Electrolyte-Gated Transistors for Organic and Printed Electronics," *Adv. Mater.*, vol. 25, issue 13, p. 1822 - 1846, Apr. 2013.

[22] K. H. Lee, S. Zhang, T. P. Lodge, and C. D. Frisbie, "Electrical Impedance of Spin-Coatable Ion Gel Films," *J. Phys. Chem. B*, vol. 115, no. 13, pp. 3315–3321, Apr. 2011.

[23] A. Laiho, L. Herlogsson, R. Forchheimer, X. Crispin, and M. Berggren, "Controlling the dimensionality of charge transport in organic thin-film transistors," *Proc. Natl. Acad. Sci.*, vol. 108, no. 37, pp. 15069–15073, Aug. 2011.

Silvia ZANETTINI

High mobility materials for Organic Spintronic applications

Résumé

Ce travail de thèse est porté sur l'étude du transport électronique dans différents matériaux organiques conducteurs, considérés comme candidats potentiels pour des applications en Electronique de Spin Organique. Pour rendre possible la diffusion d'un courant polarisée en spin à l'intérieur d'un canal semi-conducteur organique (injection-transport-détection), le mécanisme de transport de charge et la mobilité des porteurs, ainsi que la nature et la valeur de la résistance de contact de l'interface séparant matériau organique et électrodes métalliques ferromagnétiques, doivent répondre à des critères très stricts. Tous les dispositifs sont en géométrie latérale, que nous considérons la plus adaptée pour le développement de dispositifs pour l'électronique de spin. Nous étudions trois matériaux organiques différents, présentant des techniques de mises en forme à partir de molécules en solution: des fibres supramoléculaires auto-assemblées, une encre de nano-flocons de graphene exfolié en phase liquide et un polymère semi-conducteur fortement dopé en forme de couche mince. Nos résultats montrent que les conditions sont partiellement respectées, mais que des défis demeurent.

Mots-clés: polymères semi-conducteurs, auto-assemblage, transport, Electronique de Spin.

Summary

In this thesis, we study the electronic charge transport properties in different high mobility organic materials considered as possible candidates for applications in Organic Spintronics. Stringent conditions are needed to make possible the diffusive transport of a spin-polarized current through an organic spacer (injection-transport-detection): both the intrinsic characteristics of the organic semiconductor (mechanism of charge transport, carriers mobility) and the interface between the organic semiconductor and the ferromagnetic metallic electrodes should meet special criteria. Our devices are in lateral geometry, which we consider best suited to implement interesting spin-based devices. We investigate three organic materials, all compatible with wet processing of organic electronics: supramolecular fibers self-assembled by light irradiation, an ink of liquid-phase exfoliated graphene nano-sheets and a conjugated polymer semiconductor thin film exposed to strong electrochemical doping. We observe that the criteria are partially matched, but some challenges are still present.

Keywords: conjugated polymers, self-assembly, high mobility, transport, Spintronics.